Title
Monitoring the internal dynamics of proteins in the time domain of μs-ms using SDSL-EPR via the exploration of novel spin labels with restricted motions

Author
Chen, Mengzhen

Publication Date
2022

Peer reviewed|Thesis/dissertation

UNIVERSITY OF CALIFORNIA

Los Angeles

Monitoring the internal dynamics of proteins in the time domain of μs-ms using SDSL-EPR *via* the exploration of novel spin labels with restricted motions

A dissertation submitted in partial satisfaction of the

requirements for the degree Doctor of Philosophy

in Chemistry

by

Mengzhen Chen

2022

ABSTRACT OF THE DISSERTATION

Monitoring the internal dynamics of proteins in the time domain of μs-ms using SDSL-EPR *via* the exploration of novel spin labels with restricted motions

by

Mengzhen Chen

Doctor of Philosophy in Chemistry

University of California, Los Angeles, 2022

Professor Wayne L. Hubbell, Chair

Although many functionally important processes occur in the μs-ms timescale, few spectroscopic techniques can report direct dynamic information of biological systems in this time domain. One of these is SDSL-EPR (Site-Directed Spin Labeling Electron Paramagnetic Resonance). In the versatile toolbox of EPR methods, ST (Saturation Transfer)-EPR is uniquely capable of extending the motional-sensitivity range of EPR to as long as 10^{-3}s, which is particularly attractive for studying protein dynamics. However, the method has not previously been generalized for the study of the internal dynamics of ordinary proteins. The development of methodologies that enable the ST-EPR technique to probe μs-ms internal protein dynamics under ambient conditions is the central aim of the work presented in this dissertation.

The fast rotational diffusion of small soluble proteins and side chain internal motions limit the utility of ST-EPR to monitor conformational dynamics in the μs-ms range. To reduce the

interference of these fast motions and extend the applicability of ST-EPR, we combine both stationary-phase techniques for protein immobilization and novel nitroxide spin labels with highly restricted internal motions. In all cases reported, the spin label is attached to a cysteine residue introduced by site-directed mutagenesis. The results from this work demonstrate that: (1) The applicability of SDSL ST-EPR for monitoring protein internal modes can, in general, be extended to ordinary soluble and membrane proteins via the use of a disulfide-linked bifunctional spin label side chain (RX) together with immobilization of the protein on a Sepharose solid support. Using the well-characterized proteins (T4 Lysozyme and Myoglobin), various contributions to the slow motions measured by RX and ST-EPR were dissected and the feasibility, versatility, and sensitivity of ST-EPR for monitoring protein internal dynamics were demonstrated. (2) To overcome potential perturbations to structure and dynamics caused by the cross-linking bifunctional RX side chain, two disulfide-linked spin label side chains attached at a single cysteine and having highly restricted internal motions were characterized and shown to be comparable to RX for the detection of slow protein motions. (3) Finally, a novel highly immobilized spin label side chain attached via a thioether linkage at a single cysteine was characterized. Unlike the disulfide-linked side chains, the new side chain, designated R9, reacts preferentially with solvent-exposed cysteine residues and is non-reducible by common reagents used in protein studies. R9 has great potential for describing the magnitude of structural changes and probing protein dynamics.

Collectively, this work advances and broadens significantly the SDSL-EPR methodology for monitoring protein motions, making the direct measurement of internal dynamics possible within the important μs-ms time domain by providing new experimental tools and strategies. The results lay the foundation for the use of new spin labels in complex systems, including membrane proteins.

The dissertation of Mengzhen Chen is approved.

James U. Bowie

William M. Gelbart

Emil Reisler

Wayne L. Hubbell, Committee Chair

University of California, Los Angeles

2022

上高楼，望天涯路，犹未不悔，仍得憔悴。众里寻他易，未可终回首。

愿为灯火，与君重逢。

I climb the lofty tower to gaze at the endless roads, I still cannot live without regrets as I am getting old. Across the mountains and the oceans, searching for her a thousand times, but I might never be that fortunate, to turn around, to discover her there.

All I hope to become is the torch, the lantern, to see you again where the lights are dim.

TABLE OF CONTENTS

LIST OF FIGURES

Chapter 1

Chapter 2

Chapter 3

Chapter 4

Chapter 5

Chapter 6

Chapter 7

LIST OF TABLES

ACKNOWLEDGEMENTS

I would like to express my gratitude to Dr. Wayne L. Hubbell for his guidance and support, and for sharing his scientific knowledge and wisdom with me throughout these years. I will never forget that it is the decision he made as my advisor in the CSST program that really opens the door to this whole journey for me. I will always appreciate the time and energy he put into our projects and my education of being a better researcher. I am also grateful to the members of my committee for their guidance and insightful questions.

I am grateful to past and current members of the Hubbell laboratory for their contribution to my scientific development and just all the generous help over all these years. I owe them a great deal of gratitude. I would like to thank Dr. Matthias Elgeti for sharing his exceptional technical expertise, invaluable scientific discussions and career advice, and his genuine care for everyone in the lab including me. I would like to thank Kevin Eden for always sharing his outstanding knowledge of molecular biology and protein science selflessly with me and for all the inspiring and interesting discussions. I would like to thank Dr. Margaux Kreitman for sharing the graduate school life and office with me and for your friendship, and Dr. Michael Bridges for your time and patience for me, who kindly measured and provided the SR-EPR data used in this dissertation. I would also like to thank Dr. Christian Altenbach for providing his excellent EPR software, the barbecue, and all the fun.

Dr. Támás Kálai's laboratory synthesized all of the nitroxide spin labels used in this dissertation; I really appreciate his work and dedication. A special thanks to Dr. Duilio Cascio for significant technical assistance with the X-ray diffraction experiments in this dissertation. Another special thanks to Dr. Julian P. Whitelegge for his technical assistance in the Mass spectrometer experiments. I would also like to express my gratitude to Drs. Carlos López and Mark Fleissner

for establishing solid foundations of the work in this dissertation. And Evan Brooks for providing technical assistance in the expression and purification of myoglobin.

Dr. Bridges and Dr. Elgeti carefully reviewed this dissertation, I am indebted to them for their generous devotion of time, and countless enlightening revision suggestions. I am grateful for the funding sources that have supported the work presented in this dissertation: this work was supported by NIH/NEI grant 5R01 EY05216 and the Jules Stein Professor Endowment.

I thank my friends and families, although gratitude is such an incapable term to describe my unspoken emotion for them. I am also hoping for a future where the mother language of everyone could be equally used and understood by everyone.

I know all of you will be happier for not seeing your actual names here, but I know you know that I am talking about you (wink). Thank you for all those hours-long phone talks and chats, and thank you for always being my emotional tree holes and my gas stations across the Pacific Ocean. I would never be able to accomplish this without you.

Finally, Dear Dr. and Prof. Lv, and Prof. Chen (sorry dad), thank you for being my parents, my academic examples, my shield and mirror, my weakness and backup. Grandma, thank you for staying healthy and thank you for constantly pushing me by always asking when I will be finishing. It has been longer than I thought, but I am finally getting there, where all my doctoral cousins have been waiting for me for a while. I know there is still another long way to go.

The project presented in chapters 5-6 is a modified version of a manuscript under revision. Kevin Eden generated new T4L mutants modified at N-terminal for solid-support attachments and prepared these proteins. Dr. López, Evan Brooks, and I prepared the other proteins for experiments. Dr. Bridges performed the SR-EPR experiments. I performed CW-EPR and ST-EPR experiments

and analyzed the data under the guidance of Professor Hubbell. I wrote the manuscript with Professor Hubbell.

Chapters 5-6 include the EPR data from "Molecular Motion of Spin Labeled Side Chains in α-Helices: Analysis by Variation of Side Chain Structure" by Linda Columbus, Támás Kálai, József Jekö, Kálmán Hideg, and Wayne L. Hubbell (2001). *Biochemistry.* 40:3828-3846.

The project presented in chapter 7 is a modified version of a manuscript under revision. Evan Brooks and I prepared proteins for experiments. I set up the crystallization trays with Génesis Falcon in the X-Ray and EM structure determination core, UCLA-DOE IGP. Dr. Cascio performed the X-ray diffraction experiments, the crystal structure data collection, and refinements. Dr. Whitelegge performed the Mass spectrometer experiments. Dr. Bridges performed the SR-EPR experiments. I performed CW-EPR, ST-EPR, and DEER experiments, and analyzed the data under the guidance of Professor Hubbell. I wrote the manuscript with Professor Hubbell.

Chapter 7 includes the EPR data from "Motion of Spin-Labeled Side Chains in T4 Lysozyme. Correlation with Protein Structure and Dynamics" by Hassane S. Mchaourab, Michael A. Lietzow, Kálmán Hideg, and Wayne L. Hubbell (1996). *Biochemistry*. 24:7692–7704.

VITA

2015	Second-Grade Prize Scholarships Taishan College Shandong University
2015	CSST Scholarships University of California, Los Angeles
2016	Taishan College President Award Taishan College Shandong University
2016	B.Sc., Chemistry Taishan College Shandong University
2016	Teaching Assistant Department of Chemistry and Biochemistry University of California, Los Angeles
2017	Teaching Assistant Department of Chemistry and Biochemistry University of California, Los Angeles

PUBLICATION

Hongfang Yang, **Mengzhen Chen**, Xinyu Song* and Yuxiang Bu (2015), Structural Fluctuation governed Dynamic Diradical Character in Pentacene, *Phys. Chem. Chem. Phys.*, **17**, 13904

Chapter 1: Protein dynamics

1.1 The energy landscape and protein function

Proteins in solution are dynamic macromolecules, exhibiting hierarchical flexibility across a wide range of both length and time scales[1,2]. While a thermodynamically stable 'native' state typically predominates under physiological conditions, by the late 1950's it had become clear that, in order to perform their functions, proteins cannot exist as static, rigid systems[3]. The lock-and-key model[4] proposed by Emil Fisher in the 19th century was thus shown to be a poor descriptor of enzyme-substrate binding and enzymatic function. Daniel Koshland proposed a new mechanism of molecular recognition, known as the induced-fit model[5] where, upon binding of a substrate, conformational change of the enzyme is induced, whereby specific functional groups of the enzyme relocate into positions required to establish necessary stabilizing interactions, thus allowing the enzymatic reactions to be catalyzed.

However, unfortunately neither lock-and-key nor induced-fit models are adequate descriptors of reality, as both mechanisms consider only a single conformation in their functional enzymatic events. Further, a different view has come to light, with a growing body of experimental evidence, from techniques such as fluorescence[6], nuclear magnetic resonance[7], and hydrogen exchange experiments[8 9,10]. In 1976, Cooper[11] reported that transient fluctuations are an intrinsic property of proteins at thermodynamic equilibrium. Studies on myoglobin soon thereafter lead to a new paradigm proposed by Frauenfelder and coworkers[12–18], introducing the concept of hierarchical dynamics to describe the molecular mechanism of protein function.

The concept of the 'energy landscape' is used to describe the existence of multiple conformational states in equilibrium, separated by multiple energetic barriers; this landscape is

dynamic and coupled to a particular set of parameters, including temperature, pressure, solvent, etc. The population distribution of the various conformational substates in the energy landscape is determined by their relative free energy and by the energy barriers that separate them. On a funnel-shaped[19,20] energy landscape (Figure 1.1 (B)), excited states possessing higher configurational entropy[21,22] co-exist with the stabilized native state, as the latter's free energy is often only a few kcal/mol lower[2,23,24].

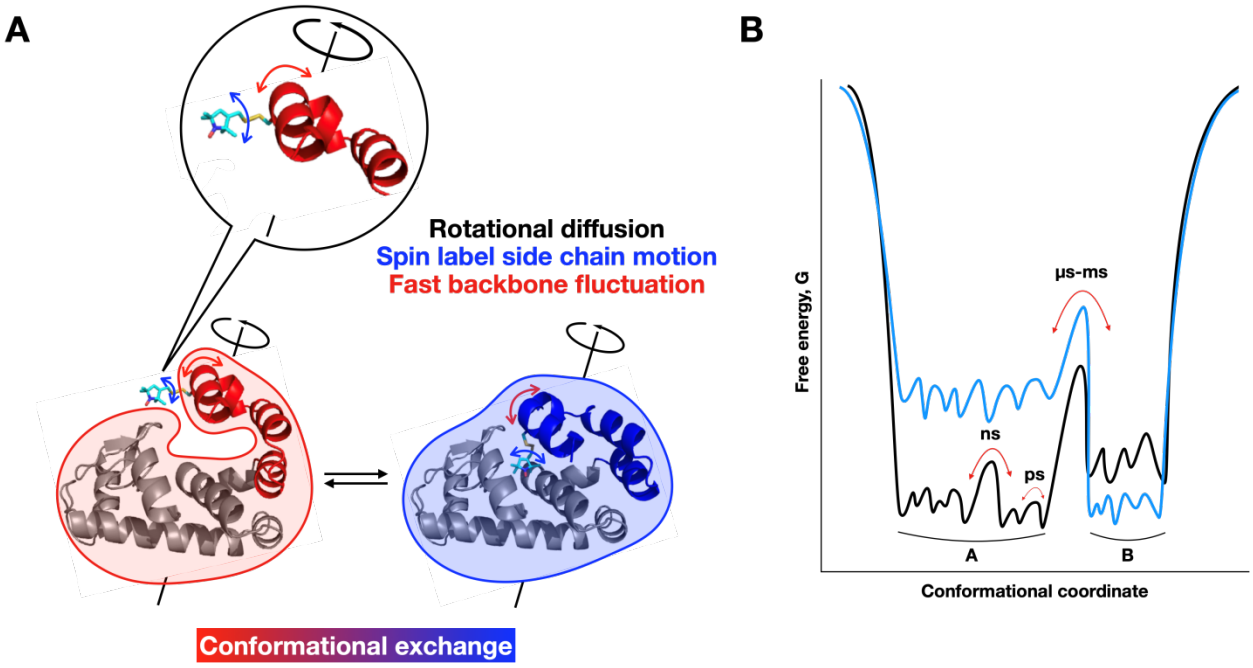

Figure 1.1 (A) Characteristic protein dynamics involved in this dissertation; (B) corresponding time scales of protein dynamics depicted in the energy landscape (based on the description introduced by Frauenfelder and co-workers).

Close analysis of the energy profile reveals that these native state-adjacent excited states are sparsely populated and may thus be inaccessible to traditional spectroscopic detection. Perturbations in the surrounding environment, however, can redistribute the relative populations of these substates, and transitions from native to excited states can occur more readily. Both the structural changes and the time scale of exchange accompanying such perturbations may contribute to the execution of protein functions[22,25–27].

1.2 Timescales of protein dynamics

In the context of a dynamic energy landscape, the motions of proteins (Figure 1.1 (A)) can be divided into two major classes: (1) conformational changes (i.e., conformational rearrangement), and (2) fluctuations around a ground state structure (i.e., breathing modes), which may not necessarily be the native state. Characterized by their motional amplitude and frequency (or timescale), different protein motions are often correlated to specific dynamical classes. While the amplitude of motion can be large or small for conformational changes, fluctuations tend to be smaller in amplitude. The extreme of motional processes[28,29] lead to complete unfolding of the protein into disordered coils, resulting in a loss of three-dimensional tertiary structure and thus function.

1.2.1 Conformational changes (μs-ms)

A high activation barrier usually separates two states undergoing a conformational change[30–32]; as such, the time domain of their exchange is often found in the μs-ms range. Conventional X-ray diffraction experiments on crystallized proteins cannot characterize the majority of these conformational rearrangements directly in solution, because of the characteristics of this preparation method. Rather, evidence of motions can only be inferred from the comparison of multiple static crystal structures of the same protein in slightly different conditions. Progress has been made in the development of methods for the direct time-resolved detection of conformational changes. Nuclear magnetic resonance (NMR) spectroscopy has made significant contributions in identifying and characterizing protein conformational changes in solution[23,26,27].

However, NMR methods are also limited in several aspects, one of which is their poor sensitivity in the microsecond time domain. In this timescale, typically two discrete states are observed and then exchange information is indirectly extracted; further discussions of NMR can be found in Chapter 2.

In 1962, Perutz[33] determined the X-ray crystal structure of deoxy- and oxyhemoglobin aiming at providing a structural explanation that accounted for Haurowitz's 1938 observation[34] , that the entrance of oxygen-induced a conformational change large enough to disrupt crystal packing. X-ray crystal structures showed structural differences between deoxy- and oxyhemoglobin, but failed to identify a clear route for the binding of the oxygen molecule to the heme group (i.e., the oxygen binding site). This result again confirms that fluctuations in the tertiary structure of proteins are required for their functionality, and more importantly it also shows the benefit of characterizing conformational changes in solution, i.e., in biologically relevant or native physiological conditions.

Functionally important conformational changes have been widely identified in many systems[35–39]. An often-cited example[30] refers to the exchange between 'open' and 'closed' conformational states related to ligand binding and dissociation in protein-ligand systems. Characterization of conformational 'switches' involved in signal transduction has made a magnificent contribution to understanding the role of proteins in such processes. Various conformational states and substates are possible, and often correspond to specific structural or kinetic intermediates where nonspecific binding (so-called promiscuity) enables a diversity of ligand recognition and protein-protein interactions.

Shear[40] and hinge[41] motions are the most common types of conformational changes, while more complicated collective motions[42], coupling multiple structural elements and dynamic steps,

also exist, where non-covalent interactions, e.g., hydrogen bonding, salt bridges, and van der Waals forces, are all found to be relevant. Shear motions are sliding motions that occur at interfaces between well-packed elements and maintain the integrity of the interface throughout the course of the motion. Accumulated small torsions of side chains contribute to the overall shear motion of a secondary element or domain. Such motions[43] are normally found in the global movement of larger domains, which may, for example, create an active site cleft. Hinge motions[44], on the other hand, involve larger torsional changes and result from movements between two relatively static and compact domains connected by a highly flexible 'hinge'—— often a few short alpha-helices or beta strands.

1.2.2 Fluctuations (ps-ns)

Although backbone fluctuations may seem to play a less significant role to the functionality and stability of folded proteins, large-scale motions associated with conformational changes actually depend upon such fluctuational processes. Frauenfelder[45,46] suggested that coordinated motions with surrounding solvent molecules are essential for conformational change in proteins, a process he described as 'solvent slaving'. Backbone fluctuations are small-scale structural excitations induced by thermal fluctuations of the solvent[47,48], leading to a series of high-frequency, stochastic motions of the protein. Over longer timescales, these fluctuational motions in concert eventually result in large-scale conformational motions. Moreover, peptide backbone modes in proteins result in local plasticity, which is required for transitions between statistical substates on the ps-ns time scale, i.e., for modulating entropic changes associated with functional processes, and providing flexible regions dynamic degrees of freedom to populate function-relevant excited states[49–52].

Backbone dynamics also play a key role in providing ligand access to protein interiors. Oftentimes, functional binding sites are buried within the protein core and appear inaccessible to solvent through the lens of the crystal structure. The aforementioned example of deoxy- and oxyhemoglobin provides a good example[53], namely that according to the crystal structure there is no clear pathway for small molecules (oxygen, carbon monoxide, etc.) to reach its binding pocket, where the heme group is bonded to the protein. Certain dynamics are required to provide such a pathway, either a large-scale conformational change or a series of smaller, coordinated backbone motions. However, for the reasons described above, these dynamics are not easily identified in the static crystal structure and at most shown as unresolved in the electron density maps.

Results from hydrogen exchange experiments[8,54,55] demonstrated that even hydrogen atoms buried within the core of a protein undergo a slow, but finite, isotopic exchange with deuterated solvent, serving as clear evidence of the occurrence of protein fluctuations. Further characterization using NMR and various chemical modification techniques revealed that the essence of such protein fluctuations are small amplitude motions in the folded state and/or local unfolding of particular regions to expose buried sites[49,52]. These two characteristic processes occur over different time scales: Structural or thermal fluctuations involve motions on the ps-ns time scale with small amplitudes, while larger amplitude motions that require activation to cross an energetic maximum occur in the μs-ms time domain.

For the work presented in this dissertation, it should be mentioned that because the detection of motions with NMR often replies on the atom-H bond vectors, particularly the N-H vector which is collinear with the helical axis, this technique is orientationally less sensitive to the ‘rocking’ mode of a helix. Rather, the motional mode of N-H vectors is modulated by a

'crankshaft'[56] kind of fluctuation. SDSL-EPR serves as a perfect complement in monitoring rotational modes as the spin label is averagely orientated perpendicular to the helix, which will be introduced with more details in chapters 2-4.

1.2.3 Side chain dynamics

With its capability briefly mentioned above, it is reasonable to believe that NMR techniques[57–59] have an optimal observation scheme for detecting protein side chain dynamics. A combined NMR ^{13}C relaxation and time-resolved fluorescence study[60] reported the rotamer lifetimes of valine, leucine, isoleucine, histidine, phenylalanine, and tyrosine as approximately 2 ns. However, the timescales of side chain dynamics can vary greatly even within the same protein——from this study, side chain bond rotation lifetimes ranged from 10 to 1000 ps.

Comparisons between side chains revealed that the mobility of side chains is correlated with the local steric packing. For side chains at solvent-exposed, surface sites of the protein, their dynamics are found at the fast end of the range. According to the results of NMR relaxation dispersion by Kay and Dahlquist[61–64], 'slower' motions were observed for 'interior' side chains. For a protein modified to have an unnatural cavity ('cavity mutant'), the side chains of valine, leucine, isoleucine, alanine, methionine, asparagine, and glutamine were reported to be slowed to even the μs-ms range. Ishima et al. also reported slow, millisecond side chain motions in partially-deuterated HIV-1 protease *via* ^{13}C relaxation experiments[65,66]. Unlike the fast dynamics originating from low-amplitude bond librational motions on surface sites, slower rotameric exchanges observed for buried hydrophobic side chains might be more functionally important, as such processes are likely to be involved in the structural rearrangement of protein and/or ligand binding to the cavity[61].

In this dissertation, discussions regarding side chain dynamics will primarily focus on the internal motion of spin label side chains, which is essentially modulated by the surrounding environment, interactions with nearby side chains, and local and global protein dynamics. Chapter 4 will provide an in-depth discussion in this regard.

1.3 References

1. Henzler-Wildman, K. & Kern, D. Dynamic personalities of proteins. *Nature* **450**, 964–972 (2007).
2. Kitahara, R. *et al.* A Delicate Interplay of Structure, Dynamics, and Thermodynamics for Function: A High Pressure NMR Study of Outer Surface Protein A. *Biophys. J.* **102**, 916–926 (2012).
3. Linderstrom-Lang, K. Enzymes. *Annu. Rev. Biochem.* **6**, 43–72 (1937).
4. Fischer, E. Einfluss der Configuration auf die Wirkung der Enzyme. *Berichte Dtsch. Chem. Ges.* **27**, 2985–2993 (1894).
5. Koshland, D. E. Application of a Theory of Enzyme Specificity to Protein Synthesis*. *Proc. Natl. Acad. Sci.* **44**, 98–104 (1958).
6. Lakowicz, J. R. & Weber, G. Quenching of fluorescence by oxygen. Probe for structural fluctuations in macromolecules. *Biochemistry* **12**, 4161–4170 (1973).
7. Allerhand, A. *et al.* Conformation and segmental motion of native and denatured ribonuclease A in solution. Application of natural-abundance carbon-13 partially relaxed Fourier transform nuclear magnetic resonance. *J. Am. Chem. Soc.* **93**, 544–546 (1971).

8. Hvidt, A. & Nielsen, S. O. Hydrogen Exchange in Proteins. in *Advances in Protein Chemistry* (eds. Anfinsen, C. B., Anson, M. L., Edsall, J. T. & Richards, F. M.) vol. 21 287–386 (Academic Press, 1966).
9. Weber, G. Energetics of Ligand Binding to Proteins. in *Advances in Protein Chemistry* (eds. Anfinsen, C. B., Edsall, J. T. & Richards, F. M.) vol. 29 1–83 (Academic Press, 1975).
10. Cooper, A. Protein fluctuations and the thermodynamic uncertainty principle. *Prog. Biophys. Mol. Biol.* **44**, 181–214 (1984).
11. Cooper, A. Thermodynamic fluctuations in protein molecules. *Proc. Natl. Acad. Sci.* **73**, 2740–2741 (1976).
12. Frauenfelder, H., Petsko, G. A. & Tsernoglou, D. Temperature-dependent X-ray diffraction as a probe of protein structural dynamics. *Nature* **280**, 558–563 (1979).
13. Frauenfelder, H. Proteins: Paradigms of complexity. *Proc. Natl. Acad. Sci.* **99**, 2479–2480 (2002).
14. Frauenfelder, H., McMahon, B. H., Austin, R. H., Chu, K. & Groves, J. T. The role of structure, energy landscape, dynamics, and allostery in the enzymatic function of myoglobin. *Proc. Natl. Acad. Sci.* **98**, 2370–2374 (2001).
15. Kumar, S., Ma, B., Tsai, C.-J., Sinha, N. & Nussinov, R. Folding and binding cascades: Dynamic landscapes and population shifts. *Protein Sci.* **9**, 10–19 (2000).
16. Tsai, C.-J., Kumar, S., Ma, B. & Nussinov, R. Folding funnels, binding funnels, and protein function. *Protein Sci.* **8**, 1181–1190 (1999).
17. Frauenfelder, H., McMahon, B. H. & Fenimore, P. W. Myoglobin: The hydrogen atom of biology and a paradigm of complexity. *Proc. Natl. Acad. Sci.* **100**, 8615–8617 (2003).

18. Austin, R. H., Beeson, K. W., Eisenstein, L., Frauenfelder, H. & Gunsalus, I. C. Dynamics of ligand binding to myoglobin. *Biochemistry* **14**, 5355–5373 (1975).
19. Onuchic, J. N., Luthey-Schulten, Z. & Wolynes, P. G. THEORY OF PROTEIN FOLDING: The Energy Landscape Perspective. *Annu. Rev. Phys. Chem.* **48**, 545–600 (1997).
20. Leopold, P. E., Montal, M. & Onuchic, J. N. Protein folding funnels: a kinetic approach to the sequence-structure relationship. *Proc. Natl. Acad. Sci.* **89**, 8721–8725 (1992).
21. Ma, B., Shatsky, M., Wolfson, H. J. & Nussinov, R. Multiple diverse ligands binding at a single protein site: A matter of pre-existing populations. *Protein Sci.* **11**, 184–197 (2002).
22. Boehr, D. D., Nussinov, R. & Wright, P. E. The role of dynamic conformational ensembles in biomolecular recognition. *Nat. Chem. Biol.* **5**, 789–796 (2009).
23. Baldwin, A. J. & Kay, L. E. NMR spectroscopy brings invisible protein states into focus. *Nat. Chem. Biol.* **5**, 808–814 (2009).
24. Neudecker, P. *et al.* Structure of an Intermediate State in Protein Folding and Aggregation. *Science* **336**, 362–366 (2012).
25. Manglik, A. *et al.* Structural Insights into the Dynamic Process of β2-Adrenergic Receptor Signaling. *Cell* **161**, 1101–1111 (2015).
26. Korzhnev, D. M., Religa, T. L., Banachewicz, W., Fersht, A. R. & Kay, L. E. A Transient and Low-Populated Protein-Folding Intermediate at Atomic Resolution. *Science* **329**, 1312–1316 (2010).
27. Bouvignies, G. *et al.* Solution structure of a minor and transiently formed state of a T4 lysozyme mutant. *Nature* **477**, 111–114 (2011).
28. Fink, A. L. Natively unfolded proteins. *Curr. Opin. Struct. Biol.* **15**, 35–41 (2005).

29. Dunker, A. K., Silman, I., Uversky, V. N. & Sussman, J. L. Function and structure of inherently disordered proteins. *Curr. Opin. Struct. Biol.* **18**, 756–764 (2008).

30. Nicholson, L. K. *et al.* Flexibility and function in HIV-1 protease. *Nat. Struct. Biol.* **2**, 274–280 (1995).

31. Jardetzky, O. Protein dynamics and conformational transitions in allosteric proteins. *Prog. Biophys. Mol. Biol.* **65**, 171–219 (1996).

32. Gerstein, M. & Krebs, W. A database of macromolecular motions. *Nucleic Acids Res.* **26**, 4280–4290 (1998).

33. Perutz, M. F. *Proteins and nucleic acids: structure and function*. (Elsevier Pub. Co., 1962).

34. Haurowitz, F. Das Gleichgewicht zwischen Hämoglobin und Sauerstoff. **254**, 266–274 (1938).

35. Huang, Y.-L., Hsu, Y.-H., Han, Y.-T. & Meng, M. mRNA Guanylation Catalyzed by the S-Adenosylmethionine-dependent Guanylyltransferase of Bamboo Mosaic Virus *. *J. Biol. Chem.* **280**, 13153–13162 (2005).

36. James, L. C., Roversi, P. & Tawfik, D. S. Antibody Multispecificity Mediated by Conformational Diversity. *Science* **299**, 1362–1367 (2003).

37. Keskin, O. Binding induced conformational changes of proteins correlate with their intrinsic fluctuations: a case study of antibodies. *BMC Struct. Biol.* **7**, 31 (2007).

38. Ma, Y.-C. & Huang, X.-Y. Novel regulation and function of Src tyrosine kinase. *Cell. Mol. Life Sci. CMLS* **59**, 456–462 (2002).

39. Woodside, D. G. *et al.* The N-terminal SH2 Domains of Syk and ZAP-70 Mediate Phosphotyrosine-independent Binding to Integrin β Cytoplasmic Domains *. *J. Biol. Chem.* **277**, 39401–39408 (2002).

40. Lesk, A. M. & Chothia, C. Mechanisms of domain closure in proteins. *J. Mol. Biol.* **174**, 175–191 (1984).

41. Vyas, N. K., Vyas, M. N. & Quiocho, F. A. Sugar and Signal-Transducer Binding Sites of the *Escherichia coli* Galactose Chemoreceptor Protein. *Science* **242**, 1290–1295 (1988).

42. Li, Y., Li, H., Smith-Gill, S. J. & Mariuzza, R. A. Three-Dimensional Structures of the Free and Antigen-Bound Fab from Monoclonal Antilysozyme Antibody HyHEL-63,. *Biochemistry* **39**, 6296–6309 (2000).

43. Remington, S., Wiegand, G. & Huber, R. Crystallographic refinement and atomic models of two different forms of citrate synthase at 2·7 and 1·7 Å resolution. *J. Mol. Biol.* **158**, 111–152 (1982).

44. Xu, Z., Horwich, A. L. & Sigler, P. B. The crystal structure of the asymmetric GroEL–GroES–(ADP)7 chaperonin complex. *Nature* **388**, 741–750 (1997).

45. Fenimore, P. W., Frauenfelder, H., McMahon, B. H. & Parak, F. G. Slaving: Solvent fluctuations dominate protein dynamics and functions. *Proc. Natl. Acad. Sci.* **99**, 16047–16051 (2002).

46. Frauenfelder, H. *et al.* A unified model of protein dynamics. *Proc. Natl. Acad. Sci.* **106**, 5129–5134 (2009).

47. Ansari, A. *et al.* Protein states and proteinquakes. *Proc. Natl. Acad. Sci.* **82**, 5000–5004 (1985).

48. Barbato, G., Ikura, M., Kay, L. E., Pastor, R. W. & Bax, A. Backbone dynamics of calmodulin studied by nitrogen-15 relaxation using inverse detected two-dimensional NMR spectroscopy: the central helix is flexible. *Biochemistry* **31**, 5269–5278 (1992).

49. Palmer, A. G., Williams, J. & McDermott, A. Nuclear Magnetic Resonance Studies of Biopolymer Dynamics. *J. Phys. Chem.* **100**, 13293–13310 (1996).

50. Adams, P. D., Loh, A. P. & Oswald, R. E. Backbone Dynamics of an Oncogenic Mutant of Cdc42Hs Shows Increased Flexibility at the Nucleotide-Binding Site. *Biochemistry* **43**, 9968–9977 (2004).

51. Duggan, B. M., Dyson, H. J. & Wright, P. E. Inherent flexibility in a potent inhibitor of blood coagulation, recombinant nematode anticoagulant protein c2. *Eur. J. Biochem.* **265**, 539–548 (1999).

52. Palmer, A. G. Probing molecular motion by NMR. *Curr. Opin. Struct. Biol.* **7**, 732–737 (1997).

53. Kneipp, J. *et al.* Dynamics of Allostery in Hemoglobin: Roles of the Penultimate Tyrosine H bonds. *J. Mol. Biol.* **356**, 335–353 (2006).

54. Hvidt, A. & Linderstrom-Lang, K. Exchange of deuterium and 18O between water and other substances. III. Deuterium exchange of short peptides, Sanger's A-chain and insulin. *Comptes Rendus Trav. Lab. Carlsberg Ser. Chim.* **29**, 385–402 (1955).

55. Englander, S. W., Downer, N. W. & Teitelbaum, H. Hydrogen Exchange. *Annu. Rev. Biochem.* **41**, 903–924 (1972).

56. Fadel, A. R., Jin, D. Q., Montelione, G. T. & Levy, R. M. Crankshaft motions of the polypeptide backbone in molecular dynamics simulations of human type-α transforming growth factor. *J. Biomol. NMR* **6**, 221–226 (1995).

57. Trbovic, N. *et al.* Protein Side-Chain Dynamics and Residual Conformational Entropy. *J. Am. Chem. Soc.* **131**, 615–622 (2009).

58. Chou, J. J., Case, D. A. & Bax, A. Insights into the Mobility of Methyl-Bearing Side Chains in Proteins from 3JCC and 3JCN Couplings. *J. Am. Chem. Soc.* **125**, 8959–8966 (2003).

59. Lee, K.-C., Huo, S. & Cross, T. A. Lipid-Peptide Interface: Valine Conformation and Dynamics in the Gramicidin Channel. *Biochemistry* **34**, 857–867 (1995).

60. Palmer, A. G. I., Hochstrasser, R. A., Millar, D. P., Rance, M. & Wright, P. E. Characterization of amino acid side chain dynamics in a zinc-finger peptide using carbon-13 NMR spectroscopy and time-resolved fluorescence spectroscopy. *J. Am. Chem. Soc.* **115**, 6333–6345 (1993).

61. Cavanagh, J. & Venters, R. A. Protein dynamic studies move to a new time slot. *Nat. Struct. Biol.* **8**, 912–914 (2001).

62. Skrynnikov, N. R., Mulder, F. A. A., Hon, B., Dahlquist, F. W. & Kay, L. E. Probing Slow Time Scale Dynamics at Methyl-Containing Side Chains in Proteins by Relaxation Dispersion NMR Measurements: Application to Methionine Residues in a Cavity Mutant of T4 Lysozyme. *J. Am. Chem. Soc.* **123**, 4556–4566 (2001).

63. Mulder, F. A. A., Skrynnikov, N. R., Hon, B., Dahlquist, F. W. & Kay, L. E. Measurement of Slow (μs−ms) Time Scale Dynamics in Protein Side Chains by 15N Relaxation Dispersion NMR Spectroscopy: Application to Asn and Gln Residues in a Cavity Mutant of T4 Lysozyme. *J. Am. Chem. Soc.* **123**, 967–975 (2001).

64. Mulder, F. A. A., Hon, B., Mittermaier, A., Dahlquist, F. W. & Kay, L. E. Slow Internal Dynamics in Proteins: Application of NMR Relaxation Dispersion Spectroscopy to Methyl Groups in a Cavity Mutant of T4 Lysozyme. *J. Am. Chem. Soc.* **124**, 1443–1451 (2002).

65. Ishima, R., Louis, J. M. & Torchia, D. A. Transverse 13C Relaxation of CHD2 Methyl Isotopmers To Detect Slow Conformational Changes of Protein Side Chains [J. Am. Chem. Soc. 1999, 121, 11589−11590]. *J. Am. Chem. Soc.* **122**, 548–548 (2000).
66. Ishima, R. & Torchia, D. A. Protein dynamics from NMR. *Nat. Struct. Biol.* **7**, 740–743 (2000).

Chapter 2: Introduction to Electron Paramagnetic Resonance Spectroscopy (EPR) Theory and Instrumentation

2.1 Introduction to magnetic resonance and EPR spectroscopy

2.1.1 Spectroscopy

The determination of macromolecular structures by X-ray crystallography has enormously advanced our knowledge of protein science over the last century[1]. As the most energetically stable conformation, the crystal structure of a protein in its native state directly reveals the structural basis for biological function and physicochemical properties at atomic resolution[2–6]. However, with time it became clear the importance of elucidating not only the static structure of a protein but also the equilibrium that exists between its various conformations[7–9]. With the advent and advancement of cross-disciplinary methodologies, another innovative chapter of protein science has started. By incorporating methods of molecular biology and spectroscopies that are capable of detecting dynamics in a range of time scales, the field of protein science has grown dramatically in the past decades. Widely utilized methods include Nuclei Magnetic Resonance (NMR) spectroscopy, Fluorescence spectroscopy, Infrared (IR) and Ultraviolet-visible (UV-Vis) spectroscopy, and many others, [10–14] each of which plays a role in revealing the unique and non-negligible role of dynamics in protein function.

Deepened understanding of interactions between matter and electromagnetic radiation has further established the spectroscopic methods as one of the fundamental exploratory tools in the study of protein function, structure, and dynamics. In general, spectroscopic methods probe the interaction between atoms or molecules and corresponding electromagnetic radiation that meets the resonance condition to induce transitions between two energy levels. The resonance

condition means that such transitions are quantum-mechanically allowed by photon emission or absorption and occur at a frequency ν, defined by the energy level difference between the two states according to Planck's law:

$$\Delta E = h\nu \tag{2.1}$$

where $h = 6.626069 \times 10^{-34} J \cdot s$ is Planck's constant.

The wavelength of radiative energy in each process decides the characteristics and capacities of each kind of spectroscopy (Table 2.1), ranging from the high-frequency region of the electromagnetic spectrum (e.g., X-, gamma rays) to the low-frequency region (e.g., radio-, microwaves). Across this broad range in the electromagnetic spectrum, spectroscopies can reveal the finer details of rotational, vibrational, electronic, and nuclear structure, probing at the (sub-nanometer) atomic level and in the sub-nanosecond time scale.

Among the various spectroscopic methods listed above, NMR spectroscopy[15–17] has contributed many of the most important results in protein science, particularly following the development of pulsed radiofrequency technologies. By reporting residue-specific information on protein dynamics, NMR methods have revealed the conformational flexibility of proteins, and the importance of such flexibility in protein function[18–21]. Therefore, protein structure (an ensemble of conformations in many cases) as determined by NMR is typically considered as a complementary method of structural characterization to that obtained by X-ray diffraction.

Unfortunately, typical solution-phase NMR methods have relatively low sensitivity to samples of sub-millimolar concentration and/or samples in rather complicated conditions, for example, membrane proteins in their native lipid environments. Indeed, the fact that proteins exhibit hierarchical flexibility across a wide range of both length and time scales presents a significant challenge to many experimental methods, including NMR. Regardless of its ability to

map residue-specific structure, the use of solution-phase NMR to measure internuclear distances is limited to a relatively short range, while direct measurements of dynamics are only possible for those on the sub-millisecond time scale, which is unfortunate as many functionally important biological processes occur outside of this range.

The shortcomings of other spectroscopic techniques in the study of protein structure and dynamics provide the foundation for the development and use of Electron Paramagnetic Resonance (EPR, or ESR, Electron Spin Resonance) spectroscopy[22,23] and SDSL[24,25] (Site-Directed Spin Labeling) as a complementary method to NMR and X-ray diffraction of protein crystals, which have been widely recognized as having unique strengths for detecting rather complex biological systems.

Table 2.1 Electromagnetic spectrum region (by wavelength), type of energy transition, and the associated spectroscopic technique.

Wavelength	**Energy type**	**Origin**	**Spectroscopy**
< 0.1 nm	γ-rays	Atomic nuclei	Mössbauer spectroscopy
0.01-2.0 nm	X-rays	Inner shell electrons	X-ray absorption spectroscopy
2.0-200 nm	UV	Ionization	Vacuum UV spectroscopy
200-800 nm	UV-Vis	Valency electrons	UV-Vis spectroscopy
Emission			Fluorescence spectroscopy
0.8-300 μm	Infrared	Molecular vibration	IR and Raman spectroscopy
1 mm-30 cm	Microwave	Molecular rotation	Microwave rotational spectroscopy
		Electron spin	EPR spectroscopy
0.6-10 m	Radio waves	Nuclei spin	NMR spectroscopy

Electron paramagnetic resonance was first observed and reported by Yevgeny Zavoisky in 1944; the EPR spectroscopy technique is sensitive to the motion and environment around molecular species containing one or more unpaired electrons. Due to the relative rareness of stable, unpaired electron spins in biological systems, EPR is highly selective spectroscopy. There are three major types of paramagnetic species that are of biological significance: free radicals, transition metal compounds, and a few paramagnetic molecules such as oxygen. Before the development of specific molecular biology techniques such as site-directed mutagenesis[26] and recombinant protein expression, the applications of EPR in protein science were largely limited by the practical difficulty of incorporating unpaired electrons into proteins. Pioneered by Hubbell and McConnell[27], the technique of site-directed spin labeling (SDSL) vastly broadens the horizon of EPR for use in protein science. In short, SDSL-EPR involves the incorporation of stable free radicals into protein sites specifically selected by site-directed mutagenesis methods; these radicals, so-called 'spin labels', serve as reporters of motion and local environment for EPR[28]. Nearly all spin labels in common use are nitroxides in which the unpaired electron is localized on the N-O bond (see Figure 2.2 and chapter 4).

Since the first application of SDSL-EPR, substantial progress has been made in methodology, instrumentation, relevant molecular biology techniques, and the chemical and physical understanding of spin labels. Both the ability to resolve dynamics over a wide range of timescales (Figure. 2.1) and the sensitivity across sample types[29–33] make SDSL-EPR a particularly ideal tool for exploring protein internal dynamics.

Throughout the following sections of this chapter and Chapters 3 and 4, the relevant background, magnetic resonance theory, and instrumental techniques, are presented using the formalism of the following authors: Marsh[34]; Poole[35]; Carrington and McLachlan[36]; Berliner[37,38];

Bridges, Columbus, Fleissner, Guo, Lerch, Lopez, McCoy, and Warshaviak who summarized and commented associative materials in their respective dissertation works[39–46]. The organizational framework of their derivations, as well as some content, were drawn upon in the writing of this dissertation.

There are many excellent publications on the theory and application of EPR methods, and a more quantitative description can be found in the above references. The aim of this chapter and Chapter 3 is only to provide a brief introduction and a general sufficient background on EPR spectroscopy, which will help the Reader in navigating subsequent chapters. Also, as the spin label is a crucial part of this dissertation, the development of SDSL-EPR will be separately introduced with more details in Chapter 4.

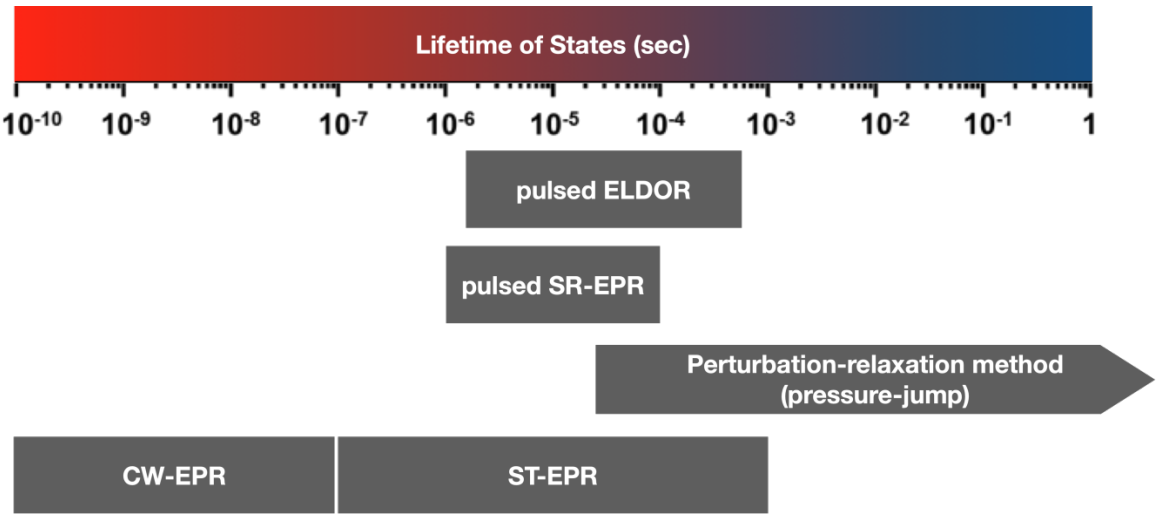

Figure 2.1 Intrinsic timescales of SDSL-EPR spectroscopic methods[47] for detecting protein dynamics and selected protein motions. CW-EPR: Continuous-wave EPR; ST-EPR: Saturation-transfer EPR; SR-EPR: Saturation recovery EPR; ELDOR: Electron-electron double resonance.

2.1.2 Electron paramagnetic resonance

An unpaired electron placed in an external magnetic field (**B**) possesses a magnetic

moment, $\boldsymbol{\mu_e}$, which is associated with the electron angular momentum, **S**:

$$\boldsymbol{\mu_e} = \gamma_e \hbar \mathbf{S} \tag{2.2}$$

$$\boldsymbol{\mu_e} = -g\beta_e \mathbf{S} \tag{2.3}$$

where $\hbar \equiv h/2\pi$, and γ_e is the electron gyromagnetic ratio. The second equality is a more commonly used, equivalent expression in EPR, given in terms of the electron g-value ($g \approx 2.002319$ for a free electron) and the Bohr magneton $\beta_e (= e\hbar/2m_e = 9.274009 \times 10^{-24} J \cdot T^{-1})$.

The interaction energy of an electron with the field is determined by their relative spin orientations, where $\widehat{H}$ is the electron Hamiltonian operator, the eigenvalues of which are the energies of the states:

$$\widehat{H} = -\boldsymbol{\mu_e} \cdot \mathbf{B} \tag{2.4}$$

Conventionally, one defines the direction of the static magnetic field in the z-direction, and as such the Hamiltonian is:

$$\widehat{H} = g\beta_e B_z S_z \tag{2.5}$$

This constitutes what is known as the Zeeman interaction. It has been shown by experiments that an unpaired electron has a spin $\mathbf{S} = \frac{1}{2}$, which is quantized to two allowed energy states in the z-direction and thus two eigenvalues, $M_S = \pm\frac{1}{2}$; often, α and β are used to represent the $M_S = +\frac{1}{2}$ state and the $M_S = -\frac{1}{2}$ state, respectively. According to Eq. 2.1 and Eq. 2.5, the energy difference, ΔE, between two states separated by the static magnetic field can be written as:

$$\Delta E = g\beta_e B_0 = h\nu \tag{2.6}$$

where B_0 is the static magnetic field strength. This is known as the resonance condition for EPR absorption. Transitions between the two spin states of the electron can be induced by applying

electromagnetic radiation of frequency ν such that the incident photon energy matches the energy difference $\Delta E = h\nu$. In practice, conventional continuous-wave (CW) EPR spectroscopy employs a fixed microwave frequency while scanning the magnetic field to achieve resonance.

Table 2.2 lists commonly used microwave frequency bands and magnetic fields matching their resonance conditions in commercial EPR spectrometers. The most widely used frequency in EPR is the X-band, and is the primary frequency technique reported in this dissertation, unless otherwise specified (like Q-band applications in pulsed EPR spectroscopy).

Table 2.2. Calculated fields of resonance (with equation 2.6) at different frequencies.

Frequency (GHz)	Microwave band	Magnetic Field of Resonance (Gauss)
1.1 (1-2)	L	392
4.0 (2-4)	S	1439
9.40 (8-12)	X	3350
24.0 (18-26.5)	K	8633
35.0 (33-50)	Q	12470
94.0 (75-110)	W	33811

2.2 Nitroxide EPR spectrum

2.2.1 Hyperfine interactions and nitroxide spin Hamiltonian

As mentioned in 2.1, the most common types of spin labels used in biological studies are stable nitroxide derivatives (Figure 2.2), in which the unpaired electron is localized on a nitrogen atom, e.g., N-oxyl derivatives of secondary amines in heterocyclic rings.

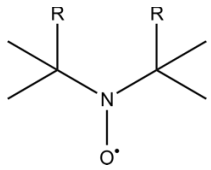

Figure 2.2. The general form of nitroxide radicals for use in spin labeling studies.

Since the unpaired electron is localized at the nitrogen ^{14}N, which has a nuclear spin angular momentum $\mathbf{I} = 1$, an interaction exists between the electron and nitrogen nuclear spins, resulting in what is known as the hyperfine interaction. By including the hyperfine interaction in consideration of the electron energy levels, the nitroxide spin Hamiltonian in the z-direction contains two principal energy terms:

$$\widehat{H} = g\beta_e B_z S_z + A I_Z S_Z \tag{2.7}$$

where A is the strength of hyperfine interaction. Placed in the external magnetic field, the nitrogen nucleus has three quantized energy states in the z-direction and three eigenvalues, $m_I = +1, 0,$ and -1. Dictated by the selection rules of quantum mechanics ($\Delta M_S = \pm 1, \Delta m_I = 0$), there are three allowed transitions involving electron spin transitions, and therefore three separated absorption lines in a nitroxide spin label EPR spectrum, corresponding to the interaction of the electron with each nitrogen nuclear spin state (Figure 2.3).

Theoretically, any nucleus with non-zero spin angular momentum ($\mathbf{I} \neq 0$) in nearby atoms can interact through the hyperfine mechanism with the unpaired electron, resulting in the splitting of a single EPR absorption line into many ($2\mathbf{I} + 1$). In general, ^{1}H and ^{13}C are commonly known to also cause line-splittings for nitroxide spin labels. The energy difference between these lines ($A/g\beta_e$) in magnetic field units is called hyperfine splitting, and it can offer explicit details about structures and dynamics experienced by the radical. In fact, in the analysis of SDSL-EPR spectra, it is one of the most important parameters and will be discussed in more

detail. While the splitting caused by ^{14}N is a major feature in nitroxide EPR spectra, whether other separations can be resolved in lineshapes depends on both the microwave frequency (which determines the energy separation level in the field) and the potential overlap of linewidth broadening contributed from other factors.; thus, they are not always easily separable. Some examples will be mentioned in section 2.2.3 and chapter 5.

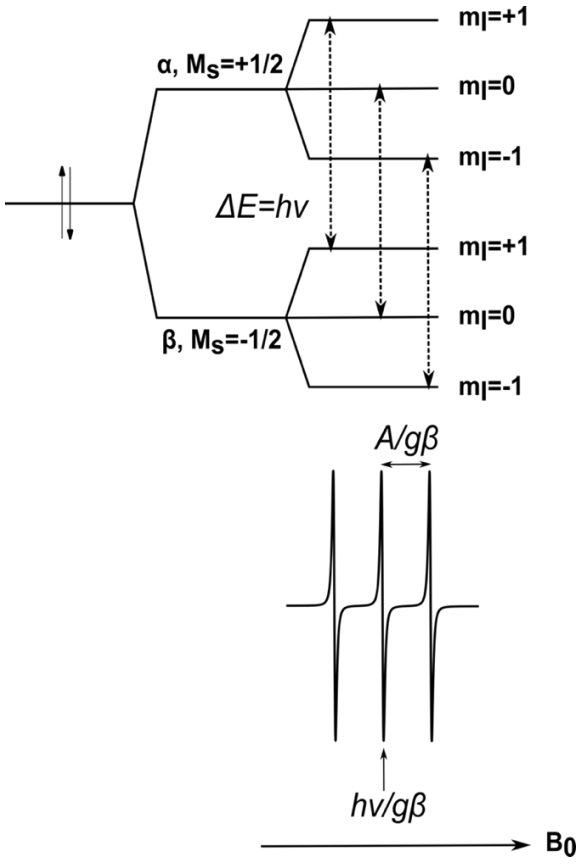

Figure 2.3. Allowed energetic transitions for an electron interacting with a nuclear spin of $\mathbf{I} = 1$. In a magnetic field, the spin state of an electron is split into two distinct energetic states, α, and β. Those states are further split by hyperfine interactions, which are dependent on the nuclear spin state m_I, in this example, the nitrogen is considered, a nucleus that has three spin states: $m_I = +1, 0,$ and -1. Allowed transitions (ΔE) are shown by dashed arrows, corresponding to three first-derivative absorption peaks shown in the EPR spectrum below, with their resonance positions at $h\nu/g\beta_e$ and the splitting as $A/g\beta_e$.

Following from Eqs. 2.6 and 2.7, considering the hyperfine interaction, the resonance

condition for EPR absorption becomes:

$$\Delta E = g\beta_e B_0 + Am_I = h\nu \tag{2.8}$$

2.2.2 Angular anisotropy and powder spectrum

As mentioned above, the unpaired electron in nitroxide spin labels mainly resides near the nitrogen atom, namely, in the two-center π-molecular orbitals formed by $2p_Z$ atomic orbitals of nitrogen and oxygen. This highly localized, anisotropic electron distribution results in an angular dependence and thus, in the absence of rapid motional averaging, in an anisotropic nitroxide EPR spectrum. It is the spectral anisotropy of spin labels that imparts their sensitivity to molecular orientation and local surroundings, which enables the unique sensitivity of SDSL-EPR spectroscopy to structures and dynamics.

Both the g-value and the hyperfine coupling parameter A can be expressed as direction-dependent tensors (**g** and **A**) that depend on relative orientation in the magnetic field. The spin Hamiltonian can be rewritten as:

$$\widehat{H} = \beta_e \mathbf{B} \cdot \mathbf{g} \cdot \mathbf{S} + \mathbf{I} \cdot \mathbf{A} \cdot \mathbf{S} \tag{2.9}$$

The anisotropic part of the g-tensor arises from the spin-orbit coupling[48,49] of the unpaired electron. Due to the non-spherical symmetry of the p-orbital, its contributions to the orbital angular momentum of the electron lead to nitroxide g-values that deviate from the free-electron (spherically symmetric) g-value.

While the Fermi contact interaction[50] between the unpaired electron and the nitrogen nucleus leads to an isotropic component of the hyperfine interaction, the anisotropic part of the A-tensor arises from the magnetic dipolar contribution of the electron in the axially symmetric $2p_Z$ atomic orbital and its interaction with the nitrogen nuclear magnetic moment. In considering the

magnetic and spatial structure of the nitroxide, there is very little difference between the molecule in the x- and y-axes, while the z-axis is significantly different. Therefore, the nitroxide is often approximated as having axial symmetry, where the properties along two axes (the perpendicular ones in our case) are considered equivalent and very different from the third axis (the parallel axis in our case): for both the hyperfine and g tensors, the value measuring along the z-axis is significantly different from (much larger) the values observed along the x- or y-axis that are approximately equivalent.

At X-band, the hyperfine anisotropy dominates the EPR spectral anisotropy. The effect of g-tensor anisotropy is relatively unimportant at any frequency lower than 94 GHz. At higher frequencies, with enhanced energy separation, the g-tensor anisotropy can be resolved as different resonance field centers about which the absorption line is split (Figure 2.4), and hyperfine splitting is less pronounced.

With the principal axes coincident with the nitroxide frame shown in Figure 2.5 (A), the g- and A-tensors can be expressed in terms of these principal elements: $g_{xx},\ g_{yy},\ g_{zz}, A_{xx}, A_{yy}, A_{zz}$. The spin Hamiltonian then becomes:

$$\widehat{H} = \beta_e\left(g_{xx}B_xS_x + g_{yy}B_yS_y + g_{zz}B_zS_z\right) + A_{xx}I_xS_x + A_{yy}I_yS_y + A_{zz}I_zS_z \quad (2.10)$$

where $B_x, B_y,$ and B_z are the orientational components of the magnetic field vector **B** as shown in Figure 2.5 (B). In practical measurements, the isotropic g- and A-value: $g_0 = \frac{1}{3}\left(g_{xx} + g_{yy} + g_{zz}\right);\ a_0 = \frac{1}{3}\left(A_{xx} + A_{yy} + A_{zz}\right)$ can also be expressed.

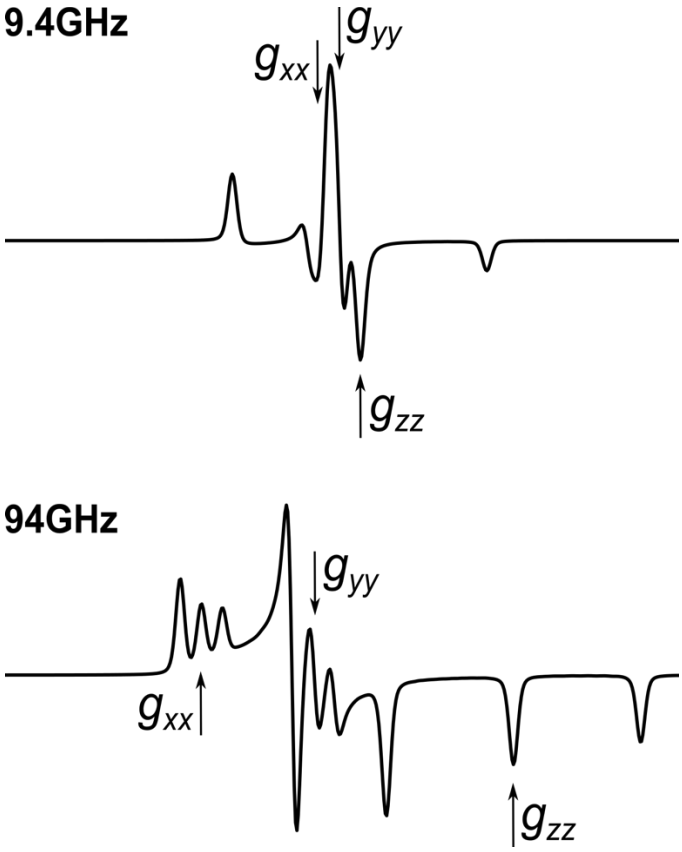

Figure 2.4. The spectra of randomly-orientated powder samples using ^{14}N-nitroxide spin labels at EPR frequencies of 9.4 GHz (top panel, X-band) and 94 GHz (bottom panel, W-band), and g-values g_{xx}, g_{yy}, and g_{zz} that indicate corresponding resonance-field positions are noted. Field width: 200 Gauss or 20 mT.

Conveniently, the magnetic field direction can be re-expressed in terms of the polar angles: θ and ϕ. The angular dependence of the nitroxide EPR resonance in field units $B_{m_I}(\theta, \phi)$ is then given by:

$$B_{m_I}(\theta, \phi) = \frac{h\nu}{g(\theta,\phi)\beta_e} - \frac{A(\theta,\phi)}{g(\theta,\phi)\beta_e} m_I \tag{2.11}$$

where the explicit angular dependence of the field relative to the nitroxide principal axes is defined by the angular dependence of effective g-value and hyperfine coupling on the polar angles θ and ϕ :

$$g(\theta, \phi) = \left(g_{xx}cos^2\phi + g_{yy}sin^2\phi\right)sin^2\theta + g_{zz}cos^2\theta \tag{2.12}$$

$$A(\theta,\phi) = \sqrt{\left(A_{xx}^2 cos^2\phi + A_{yy}^2 sin^2\phi\right) sin^2\theta + A_{zz}^2 cos^2\theta} \tag{2.13}$$

In practice, considering the axial symmetry of nitroxides, the g-values and hyperfine couplings are often expressed by the parallel and perpendicular components instead:

$$g(\theta) = g_{\parallel} cos^2\theta + g_{\perp} sin^2\theta \tag{2.14}$$

$$A(\theta) = \sqrt{\left(A_{\parallel}^2 cos^2\theta + A_{\perp}^2 sin^2\theta\right)} \tag{2.15}$$

where the z-axis is designated ∥, and both the x- and y-axis are both designated ⊥.

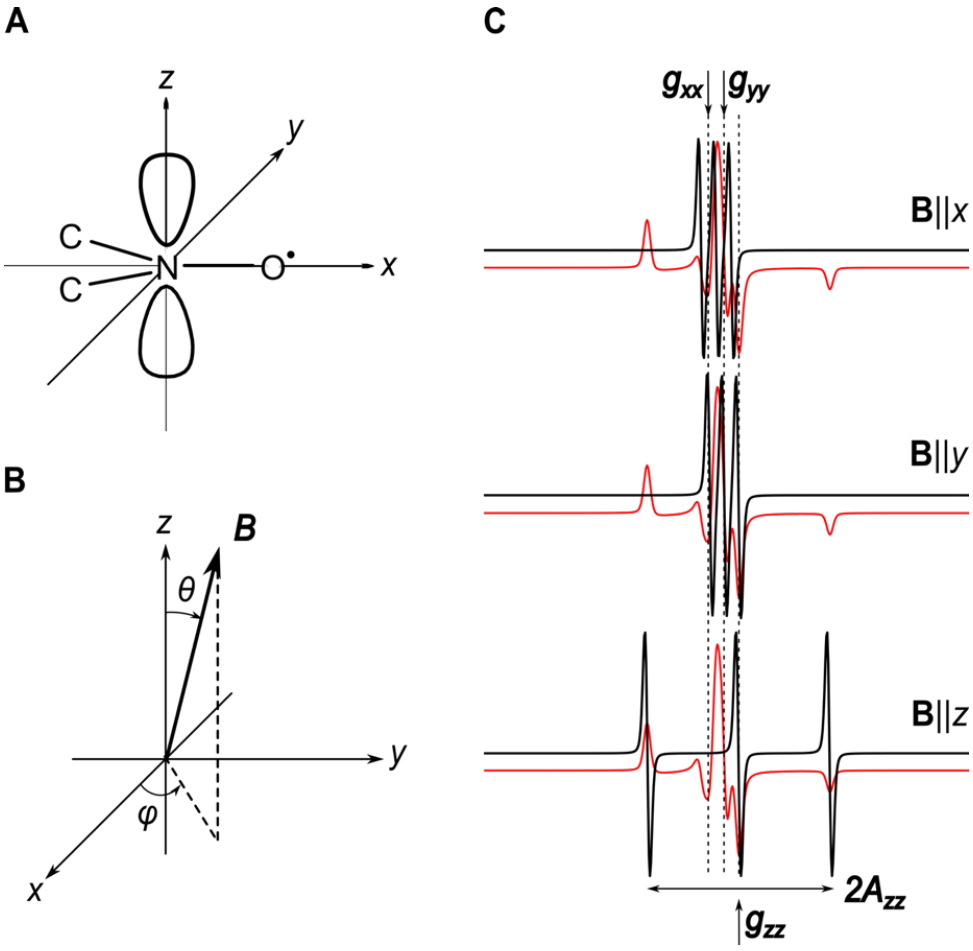

Figure 2.5 (A) Principal axis system for a nitroxide. z-axis lies along the nitrogen 2p atomic orbital, which participates in the nitroxide pπ-bond that contains the unpaired electron; the x-axis lies along the N–O bond; the y-axis lies in C–NO–C plane. (B) Orientation of magnetic-field vector **B** to the nitroxide principal axis system. (C)

The first-derivative CW-EPR spectra of uniformly-orientated samples using nitroxide spin labels, with the magnetic field B directed along the x-, y-, or z-axis of the nitroxide principal axis system. The spectrum of a randomly-oriented powder sample is also included as the red curve for comparison. The dotted lines indicating the principal g-values and the hyperfine splitting are used to help guide the eye. Field width: 200 Gauss or 20 mT.

By positioning a uniformly-oriented sample[51], like a single crystal, such that the magnetic field is aligned with the nitroxide axis system, we can resolve separate components along each direction of the hyperfine interaction (in the principle axis system) at the X-band (Figure 2.5 (C)). However, in most cases, such a single crystal-type experiment is impractical or impossible. Biological systems under physiological conditions usually are randomly oriented and are in constant Brownian motion. In these samples, subspectra for the nitroxide at all possible orientations relative to the field are present, and the EPR spectrum is a superposition of all such components.

In cases where such re-orientational motion is severely reduced or completely absent (e.g., for a frozen solution, or a finely-crushed crystal), a so-called powder spectrum is produced and it reflects the orientational distribution of the sample. Analysis of this type of spectrum is useful since the orientational distribution relates strongly to the intrinsic anisotropy of spins (nitroxide in most cases) as we have been demonstrating above. The powder spectrum can be simulated with different models of angular dependence to offer detailed orientation information on the sample, and so principal A and g values (as well as natural linewidths) can be extracted from them with ease because they specify turning points of spectral lineshapes as shown in Figures 2.4 and 2.5.

2.2.3 Polarity dependence and inhomogeneous linewidth broadening

As discussed above, the chemical structure[52] (and associated molecular orbitals and local polarity) of spin labels, namely the ring structure and substituents in the ring of nitroxides, influences the g-factor and hyperfine anisotropy, and thus their EPR spectra. Some specific examples reflective of such effects will be shown and discussed in the chapters to follow.

Apart from the dependence on intrinsic molecular properties, spectral parameters of nitroxide spin labels also show a solvent polarity dependence[53–57], making them excellent probes[58–60] of the local environment, particularly for biological systems in which non-covalent interactions play important roles. Both experimental and computational work[61–63] has been done to understand the polarity dependence in EPR, for the practical aims of interpreting spectral lineshapes (see Chapter 3 for discussion of lineshape simulations) and for a better understanding of spin labels. For the nitroxide spin labels that are widely used in biological studies, two kinds of solvent effects[63,64] affecting g- and A-tensor components are usually considered: electrostatic effects due to the polarity of the solvent, and hydrogen bonding to the nitroxide.

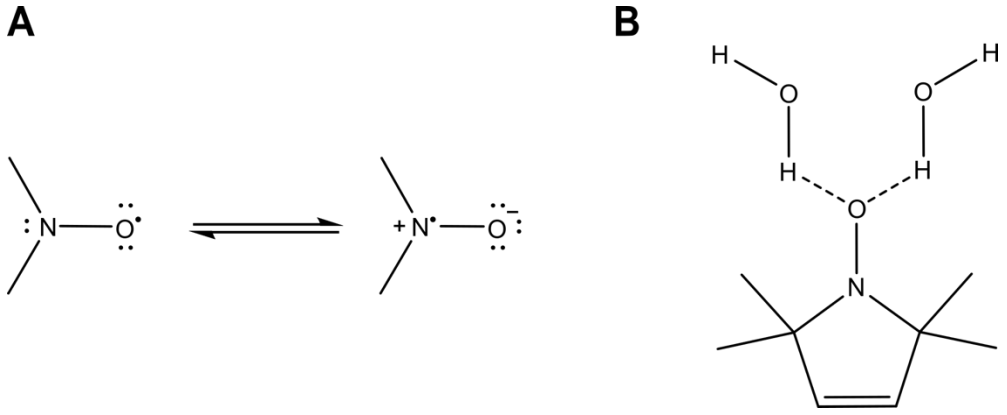

Figure 2.6. (A) The distribution of unpaired electron spin density in the nitroxide in terms of the two resonance-hybrid structures; (B) An example[66] of the pattern of hydrogen bonding between H_2O molecules and a nitroxide ring.

The distribution of unpaired electron density in the nitroxide molecule is usually shown as two electronic structures in resonance (Figure 2.6 (A)). It has been determined that the structure

in which the unpaired electron is localized on the nitrogen atom is favored in polar environments[61]. Consequently, with increasing solvent polarity, the strength of the nitrogen hyperfine interaction is stronger, and thus so does the magnitude of the A-tensor[65]. In practice, twice the 'effective hyperfine splitting' can be directly measured from spectral extrema ($2A_{zz\prime}$), and can be used as a quantitative parameter to evaluate the polarity of environments, which is particularly useful in the studies of biological membranes.

On the other hand, the hydrogen bonding to the nitroxyl oxygen in protic media (e.g., Figure 2.6 (B)) can induce profound shifts (as compared to the change brought by polarity) in spin density off oxygen onto nitrogen, which can be visualized in crystals of nitroxide molecules. In protic environments, both isotropic hyperfine couplings and g-values have a linear dependence on the concentration of hydroxyl groups:

$$a^N = a_0^N + \left(\frac{\partial a^N}{\partial [\mathrm{OH}]}\right) \cdot [\mathrm{OH}] \tag{2.16}$$

where a_0^N is spin label specific. Such shifts markedly increase the strength of nitrogen hyperfine coupling and thus the magnitude of the A-tensor[67,68].

Another spectral parameter that is sensitive to both the chemical structure of the spin label and the surroundings is the spectral linewidth. Theoretically, each absorption line in a spectrum corresponds to a quantum-mechanically allowed transition between energy states. As for the EPR powder spectrum, different resonance positions correspond to different angular orientations of nitroxide in the magnetic field. However, a spectral line extends over a range of frequencies in practice, not a single frequency; in other words, it has a nonzero natural linewidth. Moreover, the center of each absorption line may be shifted from its nominal frequency position due to the mixing of states or exchange averaging between states of similar energies.

Two major categories of linewidth broadening in EPR spectroscopy exist and are usually

referred to as homogeneous and inhomogeneous broadening. The former is determined by the lifetime of states based on the Heisenberg uncertainty principle, resulting in an unshifted Lorentzian lineshape (see Chapter 3). The latter, on the other hand, generally arises when the ensemble of free radicals (nitroxides in our case) occupies a variety of local environments; yielding a distribution of unresolved, energetically-similar Lorentzian components. In EPR spectra, the common source of inhomogeneous broadening is the unresolved hyperfine structure from surrounding atoms. For the ^{14}N-nitroxide, such broadening arises mostly from unresolved hyperfine coupling to nearby protons or trace ^{13}C in the radical. Therefore, inhomogeneous broadening depends not only on the nitroxide molecular structure, but also on solvent polarity and temperature.

It should be noted that although both the hyperfine splitting and linewidth directly reflect the electronic structure of the spin label, in many cases their apparent values may be subject to exchange narrowing due to rapid dynamics, and Heisenberg spin exchange due to collisions with another existing paramagnetic species. For example, the equivalent twelve ^{1}H nuclei from the four methyl groups of a typical nitroxide ring give a hyperfine splitting of approximately 0.2 Gauss at X-band, and the single ^{1}H on atom C_4 gives a hyperfine splitting of approximately 0.5 Gauss[69]. Such splitting is incredibly small compared to the dominant ^{14}N hyperfine splitting and is not typically observed relative to the natural linewidth. However, the presence of ambient oxygen dissolved in the solution (0.18 mM for protein solutions, 0.26 mM for pure water, absorbed from the atmosphere) is sufficient to broaden the EPR linewidth far beyond that seen due to coupling with methyl and ring protons on the nitroxide[70].

In the aqueous solution and under room temperature, the mobility dependence of these parameters is usually the more significant contributor. In the following chapter, the effects of

rotational diffusion on spectral lineshapes will be explained in detail, and some applications involving these parameters will be introduced. Even in the absence of thermal fluctuation and Heisenberg exchange from paramagnetic species, such as measurements taken at cryogenic temperature, the energy limitation of X-band as well as instrumental design (specifically the field modulation, see next section 2.3) usually leads to an observed broadening of linewidths originated from these refined proton hyperfine structures, instead of splitting of resonance lines. Some actual spectra will be shown in Chapters 5&6.

2.3 EPR instrumentation

Based on the principles of EPR spectroscopy introduced above, in particular, those relating to nitroxide spin labels, this section aims to describe the instrumental details of a typical commercial EPR spectrometer. Unlike NMR spectroscopy, where CW (field-swept) methods have fallen out of favor with the advent of pulsed technology, the traditional continuous-wave EPR method still plays an important role in SDSL-EPR studies. Pulsed methods in EPR were significantly slower to develop than for NMR; it was in the 1980s, almost 30 years after the first observation of EPR, when pulsed EPR and high-field EPR spectroscopy began rapid development and such commercial spectrometers first came on the market[71,72]. Nowadays, high-frequency pulsed EPR is a very active field, with the main emphasis on measuring molecular-scale distances in biological systems (see chapter 3 for ‘DEER spectroscopy’).

When compared to other forms of spectroscopy, there are two major differences for the common EPR methods. First, the unmatched bandwidth between microwave resonators and microwave sources leads to difficulty in tuning the hardware adequately, which has decided that in the scheme of EPR spectroscopy, the electromagnetic radiation frequency is kept fixed while

the magnetic field is scanned to match the resonance condition. Second, due to the relatively weak signals arising from the small population difference between the two energy levels of spins, and the naturally weaker magnetic dipole transitions, the detector in the EPR spectrometer is tasked with measuring the amount of radiation reflected back from a standing wave, rather than the direct transmission of excitation power through the sample. Several efforts in design have been made to obtain better signal-to-noise spectra, which will be introduced below.

2.3.1 Resonator

The microwave resonator is designed to house a paramagnetic sample in its center, and to maintain a standing wave of incident microwaves inside it around that sample. Until the resonance condition is met (*via* field sweep) and thus the microwave radiation is absorbed by the sample, the resonator sustains the microwave oscillations and the amount of energy reflected back to the detector remains constant.

One of the quantitative characteristics of resonators is their quality factor, Q, which indicates how efficiently they store microwave energy[73]. In general, a higher Q factor for a resonator results in a higher sensitivity in measurement. Figure 2.7 shows the frequency-dependent microwave reflection of a resonator, in which the 'dip' at ν_{res} (resonance frequency) corresponds to minimal reflection from the resonator of incident radiation, and $\Delta\nu$ is the full width at half maximum (FWHM) at resonance. The Q factor can be expressed based on these parameters:

$$Q = \frac{\upsilon_{res}}{\Delta\upsilon} \tag{2.17}$$

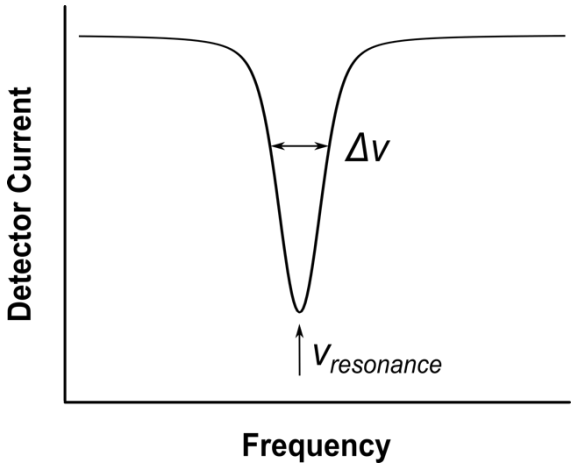

Figure 2.7 The electromagnetic reflection of a resonator as a function of incident microwave radiation frequency.

Inside the resonator, the 'stored' standing electromagnetic waves have both electric and magnetic field components. To minimize the non-resonance microwave absorption by the sample *via* the electric field (which causes energy dissipation by generating heat and therefore degrades the Q), different resonators have been designed to optimize the spatial distribution of the amplitudes of electric and magnetic fields. In a standard cavity resonator[74], which is widely used in basic EPR spectrometers, the electric and magnetic components are exactly out of phase with each other, i.e. where the magnetic field is maximum, the electric field is minimum, and *vice versa*. Therefore, the sample is placed in the electric field minimum and the magnetic field maximum to obtain the highest sensitivity.

Most of the experiments reported in this dissertation, however, were performed with a loop-gap resonator (LGR), in particular, a 2-Loop-1-Gap resonator[75], first described by Froncisz, Hubbell, and Hyde in 1987. Loop-gap resonators have wider resonant frequency profiles than those of cavity resonators, thus leading to a smaller (*ca*. ten times lower) Q value. While the signal-to-noise ratio (SNR) for a resonator is proportional to the Q value, it is also proportional to its filing factor, η, which is defined as[73]:

$$\eta = \frac{\int B_1^2 dV_{sample}}{\int B_1^2 dV_{resonator}} \tag{2.18}$$

where B_1 is the magnitude of the circularly polarized component of the microwave magnetic field (see Chapter 3).

The filling factor describes the amount of energy stored in the sample relative to the energy sustained by the resonator, which depends on the sample arrangement in the resonator. For LGRs, the filling factor is approximately 100 times higher than those of cavity resonators, which means that LGRs have order-of-magnitude signal per spin improvement over cavities regardless of the lower Q. This feature makes LGRs more suitable for samples of small volumes (on the order of 2-10μL), and thus the ideal choice for biological samples. Figure 2.8 shows a top-down view of the 2-loop-1-gap resonator used, the design of which maximizes the electric field in the narrow slit and minimizes it in the two loops. When placed in either loop, a sample is largely free from the dielectric absorption and the accompanied heating and thermal background noise, another advantage for biological applications.

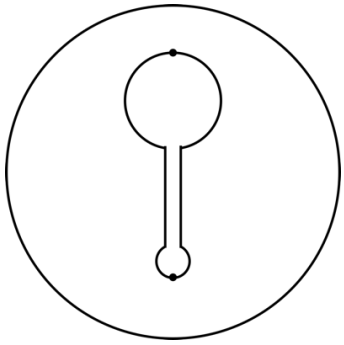

Figure 2.8 The 2-loop-1-gap resonator used in the studies of this dissertation. Electric field potential is a maximum in the gap and exactly zero at the two dots.

LGRs are reported to have another characteristic that is particularly useful for studies in this dissertation, and which will be explained in more detail in chapter 3. In short, its efficiency parameter, Λ, is defined as[74]:

$$\Lambda = \frac{B_1}{\sqrt{P}} \tag{2.19}$$

where the microwave P is the power into the resonator. A typical value of Λ for cavity resonators is ~1 Gauss/$W^{1/2}$, while LGRs[73] usually have Λ values as high as 10 Gauss/$W^{1/2}$. In addition to the fact that a higher efficiency parameter results in a larger B_1 magnetic field strength, it is also believed that there is better uniformity of the B_1 magnetic field over the sample in LGRs[22,72,76]. Both characteristics provide LGRs significant advantages in experiments involving high power levels of incident microwave radiation (e.g., in saturating conditions).

In pulsed EPR experiments, a resonator with an intrinsically lower Q is preferred. The amount of time that the energy in a resonator takes to decay to 1/e of its initial pulse intensity is defined as the resonator ringdown time, τ_{RD}, which is proportional to the Q value[77]. Counter to the pursuit of better energy utilization in CW-EPR measurements, pulse methods are optimized to minimize ringdown in part because visible ringing in the resonator can obscure the weak signals obtained in pulsed EPR, making LGRs the more promising candidate. Besides, the broader resonant frequency profile (larger bandwidth/lower Q) of LGRs allows for the simultaneous irradiation of two or more frequencies in the same resonator, which is intrinsically useful for pulsed ELDOR (electron double resonance) experiments measuring spectral diffusion.

As mentioned above, the architecture of a particular resonator determines the electromagnetic field distributions inside, and thus its usefulness for a specific sample and measurement type. In summary, the loop-gap resonator is ideal for both CW (including both measurements at low power levels or under saturating conditions, see chapter 3) and pulsed EPR experiments that were used and reported in this dissertation.

2.3.2 Continuous-wave (CW) EPR spectroscopy

As briefly introduced above, for CW-EPR experiments, microwave radiation incident upon the sample is maintained at a constant frequency while the static magnetic field (B_0) is slowly swept through the resonance condition of the spins in the sample[36]. From time-dependent perturbation theory in quantum mechanics, the fluctuating microwave radiation field B_1 must be perpendicular to the static magnetic field B_0 to induce the transition between corresponding energy levels. Under these conditions, the sample absorbs the microwave energy and an EPR signal is observed.

A CW-EPR spectrometer consists of four main components: the resonator, the magnet, the microwave bridge including both the microwave source and the signal detector, and associated electronics contained in a console for signal processing and display. This section describes the general instrumental setup primarily for obtaining a low-power (unsaturated), first-derivative absorption spectrum *via* conventional continuous-wave EPR experiments. Some details will be revisited and expanded upon in Chapter 3 specifically for the saturation transfer EPR method that also uses continuous-wave techniques.

2.3.2.1 Magnet and field modulation

Controlled by a Hall-probe attached to a pole piece near the center of the field, the magnet produces homogeneous and stable magnetic fields B_0 in the desired range, e.g., ~3.3 kilogauss for X-band (~9.4 GHz) and ~13 kilogauss for Q-band (~35 GHz) measurements. The homogeneity and stability of the B_0 field are necessary to acquire accurate EPR spectral lineshapes, in which the linewidth is an important parameter for analysis and highly sensitive to the applied field.

For most paramagnetic samples, their signal is not strong enough for direct detection (i.e., for direct measurement of resonant absorption, as is possible in NMR spectroscopy). Therefore, magnetic field modulation is employed as a method to enhance signal sensitivity in measurements. Small modulation coils are usually mounted on the outside of the resonator body, providing a secondary oscillating magnetic field ($\frac{1}{2} B_m \sin \omega_m t$) superimposed on the 'static' magnetic field B_0, which is ordinarily swept linearly over the range ΔB_0. The magnetic field is thus modulated at the angular frequency ω_m and amplitude B_m, which selectively amplifies the desired EPR signal at a particularly high modulating frequency, while filtering out the non-resonant noise at each resonant field position. As a practical result of this method, the recorded CW-EPR spectrum is detected as the first derivative of the absorption spectrum.

This use of high-amplitude field modulation can distort CW spectra dramatically, so it is important to employ modulation amplitudes comparable to or smaller than the spectral linewidth, so that the maximum sensitivity can be achieved without distorting the intrinsic lineshapes. Similarly, but more complicated, the modulation frequency needs to be high enough relative to the field scan during the 'passage' (the sweep of modulated magnetic field) between each resonant line so that the effective magnetic field can be considered constant and there are many cycles of the modulation accomplished. Such a setup is usually defined as the 'slow passage' experiment at the modulation frequency of 100 kHz. There are other specific situations in which a 'rapid/adiabatic passage' experiment with a different modulation frequency would instead be needed; further details are given in Chapter 3.

2.3.2.2 Microwave bridge and phase-sensitive detector

Figure 2.9 schematically shows a diagram of the main components of a microwave bridge.

There are two essential parts among them all that play a central role in the acquisition of the EPR signal: the microwave source (Figure. 2.9-1), and the reference arm that includes the phase-sensitive detector (Figure. 2.9-6).

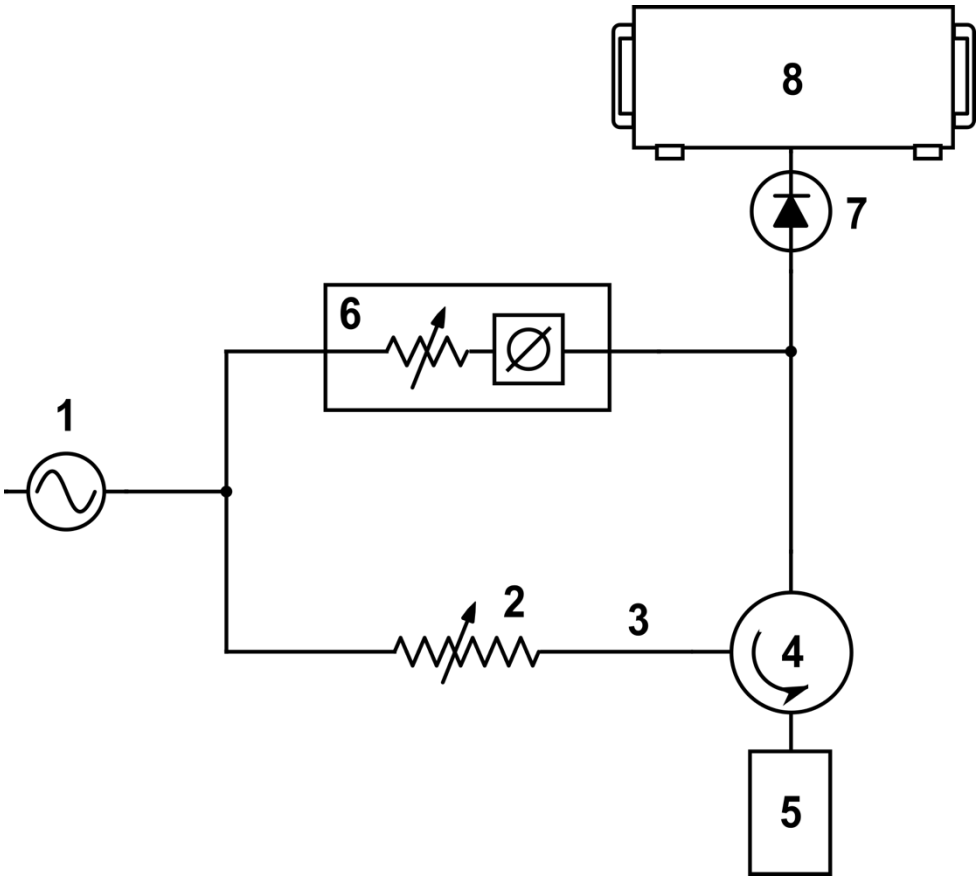

Figure 2.9 Diagram of the main components of the microwave bridge. 1: Microwave source; 2: Power attenuator; 3: Waveguide; 4: Circulator; 5: Resonator and modulation coil; 6: Reference arm with the phase-sensitive detector; 7: Schottky barrier diode detector; 8: Electronics within the console.

The electromagnetic radiation source can be either a klystron vacuum tube or a Gunn diode. A frequency stabilizer is required for the radiation source to respond to all frequency changes by a mechanism that returns the frequency to its initial value, so that uncertainty in the determination of magnetic properties (i.e., A-, g-tensors) is minimized. The attenuator controllably reduces the power of the microwaves before they are transmitted to the resonator

through a tube known as a waveguide, whose dimensions are in the order of the microwave wavelength (~3 cm for X-band frequency). The incident microwave radiation is fed to the sample in the resonator after passing through the circulator, and then reflected energy from the resonator is fed to the detector through the circulator again without mixing the two.

A phase-sensitive ('lock-in') detector compares the EPR signal reflected back to a reference signal and only passes through the components of the former that properly correspond to the reference frequency and phase. The reference voltage comes from the same oscillator that produced the field modulation voltage, and this allows the modulated EPR signal to pass through while noise is suppressed. In traditional experiments, the frequency and phase of the detector are set equal to that of the modulated EPR signal, but by adjusting these parameters (out-of-phase or in quadrature), first or second derivatives of signals can instead be recorded, as will be further discussed in Chapter 3.

The microwave radiation is then converted to an electrical current *via* a Schottky barrier diode, and is sent to the electronics housed within the console. Generally, the console digitizes the signal, monitors the response from the Hall probe, and controls the microwave field (both the field sweep and the modulation). Optimizing sensitivity and absolute signal intensity requires that the detector diode be operated at power levels greater than 1mW, so that the diode itself operates within its linear sensitivity range.

2.3.2.3 Absorption and dispersion mode

With the magnetic field being swept, when the resonance condition is satisfied, the sample absorbs the incident microwaves, which manifests itself as a Q change or a frequency change in the resonator. Most EPR spectrometers detect only the Q change that results from the energy

absorption or the change of the imaginary part of the magnetic susceptibility χ''. Some spectrometers can operate in both modes, including the detection of dispersion that corresponds to the frequency change that results from the change of the real part of the magnetic susceptibility χ'.

In typical CW-EPR experiments, the insertion of samples into the resonator causes a shift in the resonant frequency of the resonator. The microwave source is required to be stabilized by a mechanism on the resonator frequency, thus it will 'follow' the change of frequency upon the placement of the sample, leaving the change of χ' in resonators stabilized out. In other words, the dispersion signal is usually not detectable, unless a phase shifter may be placed between the circulator and resonator to vary the effective length of the waveguide and thus adjust the phase of the microwave incident on the resonator. It thus permits one to observe either the real part or the imaginary part of the magnetic susceptibility. This will have the effect of producing absorption, dispersion, or a combination of both shapes of the signal.

Due to the higher noise level and more strict hardware requirements of dispersion mode, it is rarely used compared to absorption detection. However, dispersion spectra can provide unique information about slow dynamics in the important μs-ms time range, which will be discussed in Chapter 3, section 3.4.

2.3.3 Pulsed EPR spectroscopy

Most components needed to set up a pulsed EPR system are the same as those of the CW system, including the microwave source, the circulator, the magnet, and (often) the resonator, detector, and console. It has been historically difficult, however, to develop microwave electronics that are fast enough for signal detection across a range of signal intensities (nanowatt

to milliwatt), immediately following a high-power excitation pulse (kilowatt), as well as to protect the sensitive detector from being destroyed by such high-powered pulses. Eventually, three key components have been added to the microwave bridge designed for pulsed EPR experiments: a pulse programmer, a pulse amplifier, and a quadrature detector that enables signal acquisition in both real and imaginary channels simultaneously.

Specific descriptions of the pulse excitation arm typically include the microwave pulse forming unit (MPFU) and the TWT; this hardware is typically installed separately in the EPR bridge so that the low-power CW measurements can still be performed when needed. The pulse programmer coordinates the complex series of events required for a pulse experiment to be successful, including the basic pre-amplification excitation pulse and defense pulse, and the more complicated designs of pulse sequences required for exotic experiments such as DEER, saturation recovery, or ELDOR. The microwave amplifier, often of the 'traveling wave tube' (TWT) variety but can also be solid state, produces kilowatt excitation pulses. A short, low-power pulse is generated first by the MPFU and is then amplified by the TWT to reach a higher power level (~1 kW). The pulse is then sent to the resonator to excite the sample spins.

The pulse programmer is responsible for coordinating these events with appropriate timing (and preamplifier/detector 'defense'). The TWT must be powered on prior to the microwave pulse generated from the MPFU, while the diode that is responsible for the defense pulse must be active whenever the TWT is on, to protect the signal preamplifier and detector. Further details on pulsed techniques will be provided in the following chapters when discussing specific pulsed EPR methods, such as SR-EPR and DEER.

2.4 References

1. Ewald, P. P. *Fifty years of X-ray diffraction: dedicated to the International Union of Crystallography on the occasion of the commemoration meeting in Munich, July 1962*. (Springer, 2014).
2. Tanford, Charles. Contribution of Hydrophobic Interactions to the Stability of the Globular Conformation of Proteins. *J. Am. Chem. Soc.* **84**, 4240–4247 (1962).
3. Perutz, M. F. *et al.* Structure of Hæmoglobin: A Three-Dimensional Fourier Synthesis at 5.5-Å. Resolution, Obtained by X-Ray Analysis. *Nature* **185**, 416–422 (1960).
4. Kendrew, J. C. *et al.* Structure of Myoglobin: A Three-Dimensional Fourier Synthesis at 2 Å. Resolution. *Nature* **185**, 422–427 (1960).
5. Kendrew, J. C. *et al.* A Three-Dimensional Model of the Myoglobin Molecule Obtained by X-Ray Analysis. *Nature* **181**, 662–666 (1958).
6. Green, D. W., Ingram, V. M., Perutz, M. F. & Bragg, W. L. The structure of haemoglobin - IV. Sign determination by the isomorphous replacement method. *Proc. R. Soc. Lond. Ser. Math. Phys. Sci.* **225**, 287–307 (1954).
7. Henzler-Wildman, K. & Kern, D. Dynamic personalities of proteins. *Nature* **450**, 964–972 (2007).
8. Frauenfelder, H., Sligar, S. G. & Wolynes, P. G. The Energy Landscapes and Motions of Proteins. *Science* **254**, 1598–1603 (1991).
9. Henzler-Wildman, K. A. *et al.* A hierarchy of timescales in protein dynamics is linked to enzyme catalysis. *Nature* **450**, 913–916 (2007).
10. Englander, S. W., Downer, N. W. & Teitelbaum, H. Hydrogen Exchange. *Annu. Rev. Biochem.* **41**, 903–924 (1972).

11. Molday, R. S., Englander, S. W. & Kallen, R. G. Primary structure effects on peptide group hydrogen exchange. *Biochemistry* **11**, 150–158 (1972).
12. Lakowicz, J. R. & Weber, G. Quenching of protein fluorescence by oxygen. Detection of structural fluctuations in proteins on the nanosecond time scale. *Biochemistry* **12**, 4171–4179 (1973).
13. Grinvald, A. & Steinberg, I. Z. Fast relaxation processes in a protein revealed by the decay kinetics of tryptophan fluorescence. *Biochemistry* **13**, 5170–5178 (1974).
14. Austin, R. H., Beeson, K. W., Eisenstein, L., Frauenfelder, H. & Gunsalus, I. C. Dynamics of ligand binding to myoglobin. *Biochemistry* **14**, 5355–5373 (1975).
15. Rabi, I. I., Zacharias, J. R., Millman, S. & Kusch, P. A New Method of Measuring Nuclear Magnetic Moment. *Phys. Rev.* **53**, 318–318 (1938).
16. Bloch, F. Nuclear Induction. *Phys. Rev.* **70**, 460–474 (1946).
17. Purcell, E. M., Torrey, H. C. & Pound, R. V. Resonance Absorption by Nuclear Magnetic Moments in a Solid. *Phys. Rev.* **69**, 37–38 (1946).
18. Wüthrich, K. *NMR of proteins and nucleic acids*. (Wiley, 1986).
19. Wuthrich, K. *NMR In Structural Biology: A Collection Of Papers By Kurt Wuthrich*. (World Scientific, 1995).
20. Riek, R. *et al.* NMR structure of the mouse prion protein domain PrP(121–231). *Nature* **382**, 180–182 (1996).
21. Wüthrich, K. Protein structure determination in solution by NMR spectroscopy. *J. Biol. Chem.* **265**, 22059–22062 (1990).
22. Eaton, G. R., Eaton, S. S. & Salikhov, K. M. *Foundations of modern EPR*. (World Scientific, 1998).

23. Commoner, B., Townsend, J. & Pake, G. E. Free Radicals in Biological Materials. *Nature* **174**, 689–691 (1954).

24. Stone, T. J., Buckman, T., Nordio, P. L. & McConnell, H. M. Spin-labeled biomolecules. *Proc. Natl. Acad. Sci.* **54**, 1010–1017 (1965).

25. Todd, A. P., Cong, J., Levinthal, F., Levinthal, C. & Hubell, W. L. Site-directed mutagenesis of colicin E1 provides specific attachment sites for spin labels whose spectra are sensitive to local conformation. *Proteins Struct. Funct. Bioinforma.* **6**, 294–305 (1989).

26. Hutchison, C. A. *et al.* Mutagenesis at a specific position in a DNA sequence. *J. Biol. Chem.* **253**, 6551–6560 (1978).

27. McConnell, H. M. & Hubbell, W. L. Molecular motion in spin-labeled phospholipids and membranes. *J. Am. Chem. Soc.* **93**, 314–326 (1971).

28. McConnell, H. M. & McFarland, B. G. Physics and chemistry of spin labels. *Q. Rev. Biophys.* **3**, 91–136 (1970).

29. Bordignon, E. Site-Directed Spin Labeling of Membrane Proteins. in *EPR Spectroscopy: Applications in Chemistry and Biology* (eds. Drescher, M. & Jeschke, G.) 121–157 (Springer, 2012).

30. Drescher, M. EPR in Protein Science. in *EPR Spectroscopy: Applications in Chemistry and Biology* (eds. Drescher, M. & Jeschke, G.) 91–119 (Springer, 2012).

31. Klare, J. P. & Steinhoff, H.-J. Spin labeling EPR. *Photosynth. Res.* **102**, 377–390 (2009).

32. Fanucci, G. E. & Cafiso, D. S. Recent advances and applications of site-directed spin labeling. *Curr. Opin. Struct. Biol.* **16**, 644–653 (2006).

33. Mchaourab, H. S., Steed, P. R. & Kazmier, K. Toward the Fourth Dimension of Membrane Protein Structure: Insight into Dynamics from Spin-Labeling EPR Spectroscopy. *Structure* **19**, 1549–1561 (2011).
34. Marsh, D. *Spin-label electron paramagnetic resonance spectroscopy*. (CRC Press/Taylor & Francis Group, 2020).
35. Poole, C. P. *Electron spin resonance: a comprehensive treatise on experimental techniques*. (Dover Publications, 1996).
36. Carrington, A. & McLachlan, A. D. *Introduction to magnetic resonance: with applications to chemistry and chem. physics*. (Chapman and Hall, 1979).
37. *Spin labeling: theory and applications*. (Academic Press, 1976).
38. *Spin labeling II: theory and applications*. (Academic Press, 1979).
39. Guo, Z. Correlation of spin label side-chain dynamics with protein structure: Studies of T4 lysozyme with site-directed mutagenesis and x-ray crystallography. (University of California, Los Angeles).
40. Fleissner, M. R. X-ray structures of nitroxide side chains in proteins: A basis for interpreting distance measurements and dynamic studies by electron paramagnetic resonance. (University of California, Los Angeles).
41. Columbus, L. M. Investigating backbone and side chain dynamics of α-helices in the nanosecond regime with site -directed spin labeling. (University of California, Los Angeles).
42. Warshaviak, D. T. Modeling the structure and dynamics of biological molecules. Part A: Quantum mechanical and experimental studies of nitroxide side chains in proteins. Part B: Molecular modeling of actin and its interactions with cofilin. (University of California, Los Angeles).

43. Lerch, M. Touring the Conformational Landscape of Proteins with High-Pressure SDSL EPR Spectroscopy. (University of California, Los Angeles).
44. McCoy, J. J. High Pressure EPR of Spin Labeled Proteins. (University of California, Los Angeles).
45. Lopez, C. J. Mapping molecular flexibility of spin labeled proteins on the nanosecond and longer time scales via CW lineshape analysis and osmolyte-perturbation EPR. (University of California, Los Angeles).
46. Bridges, M. D. Resolving Rotameric and Conformational Exchange in Spin Labeled Proteins at Biologically-Relevant Temperatures by Saturation Recovery Electron Paramagnetic Resonance. (University of California, Los Angeles).
47. Hubbell, W. L., López, C. J., Altenbach, C. & Yang, Z. Technological advances in site-directed spin labeling of proteins. *Curr. Opin. Struct. Biol.* **23**, 725–733 (2013).
48. Humphries, G. M. K. & McConnell, H. M. 2. Nitroxide Spin Labels. in *Methods in Experimental Physics* (eds. Ehrenstein, G. & Lecar, H.) vol. 20 53–122 (Academic Press, 1982).
49. Fundamentals of Magnetism. in *Nitroxides* 1–45 (John Wiley & Sons, Ltd, 2008).
50. Fermi, E. Über die magnetischen Momente der Atomkerne. *Z. Für Phys.* **60**, 320–333 (1930).
51. Griffith, O. H., Cornell, D. W. & McConnell, H. M. Nitrogen Hyperfine Tensor and g Tensor of Nitroxide Radicals. *J. Chem. Phys.* **43**, 2909–2910 (1965).
52. Ondar, M. A., Grinberg, O. Y., Dubinskii, A. A., Shestakov, A. F. & Lebedev, Y. S. ESR spectroscopy in the two millimeter band and magnetic resonance parameters. *Sov J Chem Phys* **2**, 83–92 (1985).

53. Ondar, M. A., Grinberg, O. Y., Dubinskii, A. A. & Lebedev, Y. S. Study of the effect of the medium on the magnetic-resonance parameters of nitroxyl radicals by high-resolution EPR spectroscopy. *Sov J Chem Phys* **3**, 781–792 (1985).

54. Earle, K. A., Moscicki, J. K., Ge, M., Budil, D. E. & Freed, J. H. 250-GHz electron spin resonance studies of polarity gradients along the aliphatic chains in phospholipid membranes. *Biophys. J.* **66**, 1213–1221 (1994).

55. Krinichnyi, V. I., Grinberg, O. Y., Bogatyrenko, V. R., Likhtenshtein, G. I. & Lebedev, Y. S. Study of the influence of the microsurroundings on magneto-resonance parameters of spin-labelled human serum albumin in the 2 mm e.s.r. range. *Biophys. Russ. Fed.* **30**, 233–237 (1985).

56. Griffith, O. H., Dehlinger, P. J. & Van, S. P. Shape of the hydrophobic barrier of phospholipid bilayers (Evidence for water penetration in biological membranes). *J. Membr. Biol.* **15**, 159–192 (1974).

57. Kawamura, T., Matsunami, S. & Yonezawa, T. Solvent Effects on the g-Value of Di-t-butyl Nitric Oxide. *Bull. Chem. Soc. Jpn.* **40**, 1111–1115 (1967).

58. Marsh, D. Polarity Contributions to Hyperfine Splittings of Hydrogen-Bonded Nitroxides—The Microenvironment of Spin Labels. *J. Magn. Reson.* **157**, 114–118 (2002).

59. Marsh, D. Membrane water-penetration profiles from spin labels. *Eur. Biophys. J.* **31**, 559–562 (2002).

60. Marsh, D. Reaction fields and solvent dependence of the EPR parameters of nitroxides: The microenvironment of spin labels. *J. Magn. Reson.* **190**, 60–67 (2008).

61. Plato, M. *et al.* Molecular orbital study of polarity and hydrogen bonding effects on the g and hyperfine tensors of site directed NO spin labelled bacteriorhodopsin. *Mol. Phys.* **100**, 3711–3721 (2002).

62. Steinhoff, H.-J. *et al.* High-field EPR studies of the structure and conformational changes of site-directed spin labeled bacteriorhodopsin. *Biochim. Biophys. Acta BBA - Bioenerg.* **1457**, 253–262 (2000).

63. Owenius, R., Engström, M., Lindgren, M. & Huber, M. Influence of Solvent Polarity and Hydrogen Bonding on the EPR Parameters of a Nitroxide Spin Label Studied by 9-GHz and 95-GHz EPR Spectroscopy and DFT Calculations. *J. Phys. Chem. A* **105**, 10967–10977 (2001).

64. Krinichnyĭ, V. I., Grinberg, O. I., Iudanova, E. I., Liubashevskaia, E. V. & Antsiferova, L. I. Study of lysozyme by a spin-label method in the 2-mm range. *Biofizika* **32**, 215–220 (1987).

65. Möbius, K., Savitsky, A., Schnegg, A., Plato, M. & Fuchs, M. High-field EPR spectroscopy applied to biological systems: characterization of molecular switches for electron and ion transfer. *Phys. Chem. Chem. Phys.* **7**, 19–42 (2005).

66. Erilov, D. A. *et al.* Water Concentration Profiles in Membranes Measured by ESEEM of Spin-Labeled Lipids. *J. Phys. Chem. B* **109**, 12003–12013 (2005).

67. Wegener, C., Savitsky, A., Pfeiffer, M., Möbius, K. & Steinhoff, H. J. High-field EPR-detected shifts of magnetic tensor components of spin label side chains reveal protein conformational changes: The proton entrance channel of bacteriorhodopsin. *Appl. Magn. Reson.* **21**, 441–452 (2001).

68. Gast, P. *et al.* Hydrogen bonding of nitroxide spin labels in membrane proteins. *Phys. Chem. Chem. Phys.* **16**, 15910–15916 (2014).

69. Robinson, B. H., Mailer, C. & Reese, A. W. Linewidth Analysis of Spin Labels in Liquids: I. Theory and Data Analysis. *J. Magn. Reson.* **138**, 199–209 (1999).

70. Hyde, J. S. & Subczynski, W. K. Simulation of ESR spectra of the oxygen-sensitive spin-label probe CTPO. *J. Magn. Reson. 1969* **56**, 125–130 (1984).

71. Schweiger, A. & Jeschke, G. *Principles of pulse electron paramagnetic resonance*. (Oxford University Press, 2001).

72. Eaton, S. S., Eaton, G. R. & Berliner, L. J. *Biomedical EPR - Part B: Methodology, Instrumentation, and Dynamics*. (Springer Science & Business Media, 2004).

73. Hyde, J. S. & Froncisz, W. Loop gap resonators. *Adv. EPR Appl. Biol. Biochem.* 277–306 (1989).

74. Mett, R. R., Sidabras, J. W., Golovina, I. S. & Hyde, J. S. Dielectric microwave resonators in TE011 cavities for electron paramagnetic resonance spectroscopy. *Rev. Sci. Instrum.* **79**, 094702 (2008).

75. Hubbell, W. L., Froncisz, W. & Hyde, J. S. Continuous and stopped flow EPR spectrometer based on a loop gap resonator. *Rev. Sci. Instrum.* **58**, 1879–1886 (1987).

76. Thomas, D. D., Wendt, C. H., Francisz, W. & Hyde, J. S. Saturation transfer EPR spectroscopy on spin-labeled muscle fibers using a loop-gap resonator. *Biophys. J.* **43**, 131–135 (1983).

77. Carboni, C., Mackenzie, I. S. & McCausland, M. A. H. Nuclear magnetic resonance at microwave frequencies. *Hyperfine Interact.* **51**, 1139–1144 (1989).

Chapter 3: Study Protein Dynamics *via* Electron Paramagnetic Resonance

3.1 Introduction

The electron spin Hamiltonian and resonance condition explicitly define the EPR spectrum of a single spin system in terms of 'delta-function' (i.e., infinitely narrow and sharp) resonant transitions. Such transitions depend on the intrinsic chemical properties and angular anisotropies of the spin. In practical experiments performed on macroscopic samples, the ensemble of unpaired electron spins is measured in the spectrometer. For the total number of spins, N, in the applied static magnetic field, the population ratio of two quantized states (α and β) at thermal equilibrium is described by Boltzmann's law:

$$\frac{N_\beta}{N_\alpha} = e^{-\frac{\Delta E}{kT}} = e^{\frac{-g\beta_e B_0}{kT}} \tag{3.1}$$

where k is Boltzmann's constant, and T is the absolute temperature.

In EPR, the measured signal is dependent on the 'net magnetization', the sum total of all electron magnetic moments in the applied field. Approximately half of all of the spins are magnetically oriented opposite the other half, meaning that the total magnetic moment is not simply proportional to the total number of spins present. For a solution of nitroxide molecules placed in a field of roughly 3300G (corresponding to X-band frequency) at room temperature, the population ratio is approximately 1.001474, meaning that for a total of 10^6 spins there are 782 more spins in the β state than in the α state; this determines the sensitivity of the EPR technique to microwave absorption.

The spin populations are dynamically modulated *via* two types of transitions that are dependent on the interactions with the surroundings. These include spontaneous transitions, in which random spins 'flip' between two states, and stimulated transitions where the application of

an oscillating magnetic field induces the spins to flip.

To explain how such transitions relate to the EPR response, time-dependent perturbation theory and the Bloch equations are used. Because magnetic resonance measurements report the bulk spin magnetization rather than individual spins, Felix Bloch[1] derived a phenomenological depiction of the system with a set of equations that classically describe a single, evolving net magnetization vector. In time-dependent perturbation theory, the main goal is to determine the time-evolution of a perturbed quantum system, with particular emphasis on calculating transition probabilities and modeling the irreversible decay of probability from a small quantum system coupled to a very large quantum system, which in our case, is the individual electron spin Hamiltonian. Both the Bloch equation and perturbation theory have been rigorously discussed in publications. In this chapter, key conclusions are presented to provide a fundamental description of EPR lineshapes and intrinsic timescales.

As manifested in spectral lineshapes, the outstanding sensitivity to molecular motion of EPR spectroscopy makes it an unmatched technique for studying biological systems. At the end of this chapter, a particularly powerful EPR method will be discussed that exclusively detects motion in the μs-ms time range: Saturation Transfer EPR, which serves as the most important method for results presented in this dissertation.

3.2 Spin relaxation

3.2.1 Transition probabilities

The rate at which the microwave magnetic field can induce transitions[2] between the β and α states, $W_{\alpha,\beta}$, depends on the square of the matrix element ⟨β|V|α⟩ for the interaction that

connects them:

$$W_{\alpha,\beta} = 2\pi\gamma_e^2|\langle\beta|V|\alpha\rangle|^2\delta(E_\beta - E_\alpha - h\nu) \quad (3.2)$$

where V represents the time-dependent perturbation (e.g., the radiation field B_1), and the Dirac delta function that imposes the requirement that the transition energy provided needs to match the resonance condition.

It needs to be noted that interaction with the radiation field induces transitions in both directions to occur at the same rate. In the conventional EPR scheme (see Chapter 2), a static field $\mathbf{B}_0$ is applied in the z-direction and the linearly polarized oscillatory field, $\mathbf{B}_1$, which is a component of the applied microwave radiation, is applied perpendicular to the static field. For a single unpaired electron spin, the rate then becomes:

$$W = W_{\alpha,\beta} = W_{\beta,\alpha} = \frac{\pi\gamma_e^2}{2} B_{1,x}^2 \cdot g(\omega_0 - \omega) \quad (3.3)$$

$$B_{1,x} = 2B_1 \cos\omega t \quad (3.4)$$

which shows that the transition rate is proportional to the square of $B_{1,x}$, i.e., to the microwave power. Therefore, the absorption EPR signal intensity is directly proportional to the square root of the microwave power. Here the Dirac delta function is replaced with the envelope function, $g(\omega_0 - \omega)$, as in practice there is no infinitely sharp absorption linewidth.

The rate equation for the instantaneous population in state α (or β) can be derived:

$$\frac{dn}{dt} = W(1 - n) - W(1 + n) = -2Wn \quad (3.5)$$

$$n(t) = n(0) \cdot \exp(-2Wt) \quad (3.6)$$

where n represents the instantaneous difference between the populations of the two states, thus $n(0)$ is the population difference at t = 0 (equilibrium distribution, no applied radiation).

The rate of energy absorption from the radiation can be written as:

$$\frac{dE}{dt} = nW\Delta E = nW \times \hbar\omega_0 \tag{3.7}$$

3.2.2 The Bloch equations

Through the classical lens, for an ensemble of spins (such as electrons) in a magnetic field, a torque is exerted of which the moment is summed to yield the net magnetization **M**:

$$\frac{d\boldsymbol{M}}{dt} = \gamma_e \cdot \boldsymbol{M} \times \boldsymbol{B} = \boldsymbol{M} \times \boldsymbol{\omega} \tag{3.8}$$

When placed in a static field $\mathbf{B}_0$ (which defines the z-direction), the electrons precess about the z-axis at the Larmor frequency (ω_0), but a component of their magnetization vector exists somewhere in the xy plane, randomly such that the sum-total Cartesian x,y-magnetic ('transverse') components are zero (M_x and $M_y = 0$) at thermal equilibrium. The net magnetization $\boldsymbol{M} = \sum \boldsymbol{\mu_e}$ (the sum of all electron magnetic moments) along the z-direction can be expressed then as:

$$M_z = n \cdot \gamma_e \hbar = \chi \cdot B \tag{3.9}$$

Furthermore, the time dependence of **M,** describing its spontaneous return to thermal equilibrium (explained in the next section) can be written for each directional component[3]:

$$\frac{dM_z}{dt} = -\frac{(M_z - M_{z,0})}{T_1},\ \frac{dM_y}{dt} = -\frac{(M_y - M_{y,0})}{T_2},\ \frac{dM_x}{dt} = -\frac{(M_x - M_{x,0})}{T_2} = -\frac{dM_y}{dt} \tag{3.10}$$

where $M_{i,0}$ is the magnetization of a given component at thermal equilibrium (note that $M_{x,0} = M_{y,0} = 0$, and that $M_{z,0}$ = 'M_0' is proportional to the magnetic susceptibility χ of the sum of spins).

Combining equations (3.6) - (3.8) yields the Bloch Equation describing the time dependence of the bulk magnetization in the *laboratory frame* of reference, a stationary coordinate system:

$$\frac{d\boldsymbol{M}}{dt} = \gamma_e \cdot \boldsymbol{M} \times \boldsymbol{B} - \frac{(M_z - M_0)}{T_1}\boldsymbol{k} - \frac{M_y}{T_2}\boldsymbol{j} - \frac{M_x}{T_2}\boldsymbol{i} \tag{3.11}$$

where **i**, **j**, and **k** are unit vectors in the x, y, and z directions, respectively. It should be noted that the Bloch equations are usually solved under the *rotating frame*. The transformations and derivations of the Bloch equations in the rotating frame can be found elsewhere[2,4] and will not be discussed in detail here. Briefly, the oscillatory field $\mathbf{B_1}$ is applied perpendicular to the static field $\mathbf{B}_0$, precessing also at a Larmor frequency (ω_1). In the rotating frame, **i'** is the unit vector that lies along the direction of $\mathbf{B_1}$, and **j'** is perpendicular to **i'**. By performing such a substitution, the unit vectors are considered to be rotating at the angular velocity of the circularly polarized radiation, and change with time. Equation 3.9 becomes:

$$\frac{dM_z}{dt} = -\gamma_e B_1 v - \frac{(M_z - M_0)}{T_1} \tag{3.12a}$$

$$\frac{dv}{dt} = -(\omega_0 - \omega_1)u + \gamma_e B_1 M_z - \frac{v}{T_2} \tag{3.12b}$$

$$\frac{du}{dt} = (\omega_0 - \omega_1)v - \frac{u}{T_2} \tag{3.12c}$$

Going back to the *laboratory frame*, the magnetization in the x-axis (the direction of the applied oscillatory field $\mathbf{B}_1$) can thus be written as:

$$M_x = u\cos\omega_1 t + v\sin\omega_1 t = 2B_1\chi(\omega_1)e^{-i\omega_1 t}$$
$$= 2B_1\chi'(\omega_1)\cos\omega_1 t + 2B_1\chi''(\omega_1)\sin\omega_1 t \tag{3.13}$$

where Bloch introduced here the susceptibility as a complex parameter to describe the magnetization, including its phase relations of components.

The solution to the Bloch equations in the steady state (where derivatives = 0, not necessarily at thermal equilibrium) yields a mathematical description of the EPR signal. For most commercial EPR spectrometers, the recorded steady-state signal is from the absorption mode of the instrument, detecting the change in the resonator Q value (see Chapter 2) that directly results from microwave energy absorption. The average power absorbed per unit volume is given by:

$$\frac{dE}{dt} = \omega_1|M_z| = \omega_1 \mathrm{B_1 v} = B_1^2 M_0 \omega_1 \frac{T_2}{1+T_2^2(\omega_0-\omega_1)^2+\gamma_e^2 B_1^2 T_1 T_2} = 2B_1^2 \omega_1 \chi''(\omega_1) \quad (3.14a)$$

which uses the fact that the solution to 3.12b is:

$$\mathrm{v} = \mathrm{M_0} \frac{\gamma_e \mathrm{B_1 T_2}}{1+\mathrm{T_2^2}(\omega_0-\omega_1)^2+\gamma_e^2 \mathrm{B_1^2 T_1 T_2}} \quad (3.15)$$

Recall that M_0 is proportional to the magnetic susceptibility χ of the sum of spins, and so Equation 3.14a can also be written as:

$$\frac{dE}{dt} = (\chi_0 \mathrm{B_1^2} \omega_0)\omega_1 \frac{\mathrm{T_2}}{1+\mathrm{T_2^2}(\omega_0-\omega_1)^2+\gamma_e^2 \mathrm{B_1^2 T_1 T_2}} \quad (3.14b)$$

Therefore, the absorption signal corresponds to the out-of-phase (relative to the radiation B_1) component v, i.e., the imaginary part of the magnetic susceptibility χ''. The signal reaches a maximum at resonance when $\omega_1 = \omega_0$. With an appropriate instrumental setup, the frequency change can also be detected in 'dispersion mode', directly measuring the real part of the magnetic susceptibility χ'. Note that for pulsed experiments, the above Bloch equation derivations are not relevant beyond the discussion of spin populations. Theoretical details of pulsed EPR experiments are beyond the scope of this dissertation, but can be found in other references[5].

3.2.3 Spin-lattice relaxation (T_1) and saturation

As a magnetic spin system is not thermodynamically isolated in practice, spontaneous transitions occur and constantly drive the spin system to reacquire a state of thermal equilibrium. The spin system is coupled to the so-called lattice, the surrounding environment, which serves as a thermal sink for the microwave energy absorbed in the EPR experiment. This coupling provides the system a pathway to return to its equilibrium population ratio (i.e., the Boltzmann distribution). The corresponding spin transitions involving energy release to the lattice are known

as longitudinal or spin-lattice relaxation (T_1 relaxation).

Modifying equation 3.5 above to include directions of spin transition, the rate equation describing the population difference between two states, considering spin-lattice relaxation can be written as:

$$\frac{dn}{dt} = W_{\beta\to\alpha}(1+n) - W_{\alpha\to\beta}(1-n) \tag{3.16}$$

When the system reaches thermal equilibrium (i.e., following T_1 relaxation), $\frac{dn}{dt} = 0$, and so the equation can be rewritten as:

$$\frac{dn}{dt} = \frac{n_o - n}{T_1} = (W_{\alpha\to\beta} + W_{\beta\to\alpha})(n_o - n) \tag{3.17}$$

where $n_o = (W_{\alpha\to\beta} - W_{\beta\to\alpha})/(W_{\alpha\to\beta} + W_{\beta\to\alpha})$, which is also the equilibrium value of population difference. At time t after the spin system is perturbed, the population difference modulated by the T_1 relaxation can be expressed as:

$$n(t) = n_o[1 - \exp(-t/T_1)] \tag{3.18}$$

One can see that the characteristic time parameter here, T_1, is equivalent to that in the Bloch equations 3.10 and 3.12. Now, by combining equations 3.5 and 3.17, the overall rate equation describes the population difference when microwave radiation is applied:

$$\frac{dn}{dt} = \frac{n_o - n}{T_1} - 2Wn \tag{3.19}$$

When the system reaches a steady state in the radiation field, $\frac{dn}{dt} = 0$, the equation can be rewritten as:

$$n = \frac{n_0}{1+2WT_1} \tag{3.20}$$

Combining equations 3.3 and 3.17, we see a new form for equation 3.7:

$$\frac{dE}{dt} = n_0 \Delta E \frac{W}{1+2WT_1} = n_0 \Delta E \frac{\frac{\pi\gamma_e^2}{2} B_1^2 \cdot g(\omega_0 - \omega)}{1+\pi\gamma_e^2 B_1^2 \cdot g(\omega_0-\omega)T_1} \tag{3.21}$$

which is of the same form as equation 3.14, but here it is quantized.

The amplitude of the absorption signal is modulated by two competing processes: T_1 relaxation and radiation. It should be emphasized that the radiative transitions occur at the same rate from state α to β and *vice versa*, but it is obvious that the relaxation transition from the upper (α) to the lower (β) energy level induced by spin-lattice interactions must occur at a faster rate than the reversed transition, otherwise the spin population difference could not return to the equilibrium value defined by Boltzmann distribution.

From equation 3.20, when $2W \ll T_1$, spin-lattice relaxation dominates and the system is kept stable at thermal equilibrium, where the spin population difference remains at the value n_0. However, when $T_1 \ll 2W$ (i.e., in situations of high power of the oscillatory field B_1), simulated transitions overcome the spin-lattice relaxation, resulting in deviation of the population difference from its equilibrium value. The absorption signal vanishes if the spin population difference can be driven to zero, due to constant stimulated transitions. Such a phenomenon is called saturation.

In conventional CW-EPR experiments, the microwave source is operated at low power or attenuated to avoid saturation of the spin system. When the system is not saturated, equation 3.14 can be simplified (by eliminating the term $\gamma_e^2 B_1^2 T_1 T_2$) as follows:

$$A(\omega_1) = \frac{T_2}{\pi[1+T_2^2(\omega_0-\omega_1)^2]} \tag{3.22a}$$

And in terms of magnetic field:

$$A(B) = \frac{\gamma_e[T_2^2\gamma_e^2(B_0-B)^2]}{\pi T_2[1+T_2^2\gamma_e^2(B_0-B)^2]} \tag{3.22b}$$

which is a Lorentzian lineshape. Note that in this equation B_0 is the field at which the resonance condition is satisfied, not necessarily the static field strength (which corresponds to the B now, as the instrument sweeps field).

The theory describing the origins of spin-lattice relaxation for spin labels in solution is complicated and beyond the scope of this dissertation, but some insightful articles are available[6–8]. In brief, spin-lattice relaxation is dependent on the magnitude of local field fluctuations and on their proximity to the paramagnetic center, which in this case is the nitroxide spin label. Eaton et al.[6] proposed four contributing processes responsible for spin-lattice relaxation effects between 100 and 325 K, two of which depend on the nitroxide rotational correlation time. This motional dependence has enabled the development of a method[9] using T_1 measurements to detect the conformational exchange of spin-labeled proteins, *via* the pulsed technique of saturation recovery (SR) EPR.

In a pulsed SR-EPR experiment, in addition to the static field B_0 and weak radiation B_1, an intense microwave pulse is applied at the frequency of the nitroxide central resonance line (the $m_I = 0$ manifold), which serves to saturate the spin system. The return from saturation to Boltzmann thermal equilibrium is then monitored with a weak observing microwave radiation field, observed as an exponential 'recovery' signal with the characteristic time constant T_1.

In situations where two relaxation pathways or protein states (and thus two rates) exist, the return to equilibrium is in general bi-exponential in form, and the relaxation rate constants are functions of the intrinsic T_1 values and exchange rates for the two components. In the case where extremely slow or no exchange occurs between the two protein states, the observed relaxation rates simply reflect those of the two states; for extremely fast exchange, only a single, averaged relaxation rate is observed. When the exchange lifetime between the two states is similar to the

T_1 values of the two states, the so-called "intermediate exchange regime", two relaxation time constants are observed, however, they are complicated functions of the intrinsic T_1 values, exchange rate, and relative populations. In Bridges, et al.[9], it was reported that most rotameric exchange of the spin label side chain on proteins occurs so quickly as to produce a mono-exponential SR curve. However, for protein conformational exchange, as it is typically at least one order of magnitude slower than the rotameric exchange, intermediate and slow exchange processes were both observed for various spin-labeled sites, thus enabling the use of T_1 measurements to differentiate these two processes.

The value of T_1 is fundamentally important for many SDSL-EPR methods, particularly non-linear EPR techniques (see section 3.4) as it determines the overall amplitude of the absorption signal. At solvent-exposed sites in a protein (MW≦50kDa), the most commonly used nitroxide side chain R1/MTSSL typically has a value of $T_1 \approx$ 1-2 μs[10,11]. Incorporating molecular structures that can restrict internal flexibility has been proven effective for increasing the intrinsic T_1 of spin label side chains, and can potentially advance the application of saturation transfer EPR and power saturation experiments by extending their detection limits in time or distance measurements. Real examples of this will be presented in Chapters 6 and 7.

3.2.4 Spin-spin relaxation (T_2) and homogeneous linewidths

According to the Heisenberg uncertainty relation, the spin-lattice relaxation that limits the lifetime of spins in the upper/excited state brings in broadening to the spectral linewidth. However, in conventional (i.e., non-saturation) CW-EPR experiments, this so-called 'lifetime broadening' is not the dominant contributor to spectral linewidths, particularly for nitroxide spins measured at ambient conditions (where $T_1 \gg T_2$)[6,8,12–14]. Instead, spectral lineshapes are largely

modulated by another time-dependent process, which is known as the transverse or spin-spin relaxation (T_2 relaxation).

It is apparent that this characteristic time is the same T_2 mentioned in the Bloch equations 3.10 and 3.12, which describe the time evolution of transverse spin magnetization components (M_x and M_y). While T_1 relaxation drives the reacquisition of the thermal equilibrium population distribution along the z-axis (M_z), a return of M_x and M_y to their equilibrium (random) distribution of zero happens concurrently. The spin-spin relaxation phenomenon occurs because variation and fluctuations in fields local to each spin cause random changes in the precession of each individual spin, resulting in a loss of spin coherence in the xy-plane (dephasing) of the ensemble. Any magnetic interaction that influences the local field experienced by the spin ensemble can result in T_2 relaxation, and this process induces changes in relative spin-state energies, thus broadening the spectral linewidths. Equation 3.22 shows the strong dependence of conventional CW-EPR lineshapes to T_2, from which can be derived the spectral absorption line half-width at half-height:

$$\Delta B_{1/2} = \frac{1}{\gamma_e T_2} \tag{3.23a}$$

For CW spectra, which is detected as a first derivative spectrum (see Chapter 2), the peak-to-peak linewidth is instead considered:

$$\Delta B_{pp} = \frac{2}{\sqrt{3}} \frac{1}{\gamma_e T_2} \tag{3.23b}$$

T_2-dependent line-broadening in magnetic resonance is often called Lorentzian broadening or homogeneous broadening. In solution, motional contributions originating from molecular tumbling dominate T_2 relaxation, which will be discussed further in Section 3.3. T_2 relaxation also occurs from magnetic interactions between two separate spins, which mainly includes two

mechanisms: the direct spin-spin interactions via collisional Heisenberg exchange, and through-space dipolar interactions.

3.2.5 Spin-spin interactions

3.2.5.1 Dipolar interactions and Heisenberg exchange

As briefly mentioned in Chapter 2, dissolved oxygen in the aqueous solution is sufficient to broaden the EPR linewidth noticeably, such that detailed hyperfine structure and inhomogeneous linewidths are difficult to resolve in most nitroxide spectra. This is essentially a result of the Heisenberg exchange mechanism, which is a quantum mechanical electrostatic interaction arising from collisions of two paramagnetic species that depends on electron orbital overlap during the collision and the collision frequency (and thus relative concentrations and translational diffusion rates). The collision between a nitroxide and a fast-relaxing paramagnetic species (such as O_2) results in a decrease in the T_1 and T_2 values for the nitroxide. Therefore, in some EPR experiments, deoxygenation of samples is necessary to eliminate this effect and properly achieve saturation. Whereas, this mechanism might also be enhanced on purpose to acquire certain information. An extended introduction can be found in chapter 4.

Another type of spin-magnetic interaction that is relevant to SDSL-EPR is the dipolar interaction[15,16], due to interactions between the dipole moments of two or more localized spins. The dipolar interaction is dependent on the distance between the spins (with a $1/r^3$ proportionality), and so this phenomenon is widely employed for the determination of interspin distance measurements. The Hamiltonian for the Heisenberg exchange and dipole-dipole interactions can be generally written as[5]:

$$\widehat{H}_{12} = \widehat{H}_{HE} + \widehat{H}_{DD} = \boldsymbol{J_{12} s_1 \cdot s_2} + \frac{\mu_0 g^2 {\beta_e}^2}{4\pi r_{12}^3}[\boldsymbol{s_1 \cdot s_2} - 3(\boldsymbol{s_1 \cdot r_{12}})(\boldsymbol{s_2 \cdot r_{12}})] \quad (3.24)$$

where J_{12} is the exchange constant, μ_0 is the vacuum permeability, r_{12} is the distance between the two spins, $\mathbf{r_{12}}$ is the interspin vector in the static magnetic field axis system, and $\mathbf{s_1}$ and $\mathbf{s_2}$ are the spin angular momenta vector operators.

It is clear from the form of the above equation that the Heisenberg exchange is isotropic, while the dipole-dipole interaction is orientation-dependent. In the high field limit (where the electron Zeeman interaction is much larger than the dipole-dipole coupling), if two spins are aligned parallel to the magnetic field and are thus parallel to each other, the dipole-dipole Hamiltonian can be simplified by dropping non-secular contributors to get:

$$\widehat{H}_{DD} = \frac{\mu_0 g^2 {\beta_e}^2}{4\pi r_{12}^3}(3\cos^2\theta - 1)\hat{S}_{1,z}\hat{S}_{2,z} = \omega_{12}\hat{S}_{1,z}\hat{S}_{2,z} \quad (3.25)$$

where θ is the angle between the external static magnetic field $\mathbf{B_0}$ and the interspin vector, and ω_{12} is defined as the dipolar coupling frequency.

3.2.5.2 Double Electron Electron Resonance (DEER)

The introduction of a second spin label into protein enables one to obtain distance-related information between spins by measurement of the dipolar interaction. While the use of homogeneous T_2 broadening in CW-EPR can determine interspin distances under 30Å[17,18], pulse techniques make possible the population-weighted distance measurements in the range of *ca*. 20-80 Å. Currently one of the most popular EPR techniques, the double electron-electron resonance experiment, DEER, has the exclusive advantage of being able to measure not only protein-scale distances but also reveal the structural heterogeneity of the conformational ensemble. A brief overview of the basic principles of DEER is provided below, while detailed descriptions of the

theory and applications are available elsewhere[19–25].

Various pulse sequences exist for different types of DEER experiments, including a 3-pulse[20], 4-pulse[24], and 5-pulse[26] sequence. For the DEER data reported in this dissertation, only the 4-pulse experiment, shown in Figure 3.1, was employed.

In 4-pulse DEER, a particular subset of the total spins from the ensemble (observe spins or A spins) is first populated by a $\pi/2$ (90º) pulse in the 'observe sequence', causing the net magnetization to realign along the negative y-axis. Due to local field inhomogeneities in the sample, dephasing[27] occurs in the xy-plane as each individual spin precesses about the z-axis. After a fixed time interval τ_1, a subsequent π (180º) pulse in the observe sequence then inverts the precession direction, causing the previously-dephasing magnetization to refocus in the xy-plane at a later time (τ_1 after the π pulse), forming the primary echo. After another fixed time interval τ_2, a second π pulse in the observe sequence inverts the precession direction again, resulting in a secondary (i.e., refocused) echo at a time τ_2 after the second π pulse. The intensity of this secondary echo, V, is the signal collected in the DEER experiment.

Between application of the first and second observe π pulses, the magnetization of another subset of spins (pump spins or B spins) is inverted through excitation with a π pulse at a resonance frequency different from that used for the observe spins (i.e., at the pump frequency). By varying the time at which this pump pulse occurs (t_p), an oscillatory signal is obtained, the so-called 'dipolar evolution signal'. A varying phase gain of $\omega_{12} \cdot t_p$ (see equation 3.25) is introduced to the observe spins as the pump pulse changes the transient local field experienced by them, which eventually modulates the signal V at the frequency equal to ω_{12}.

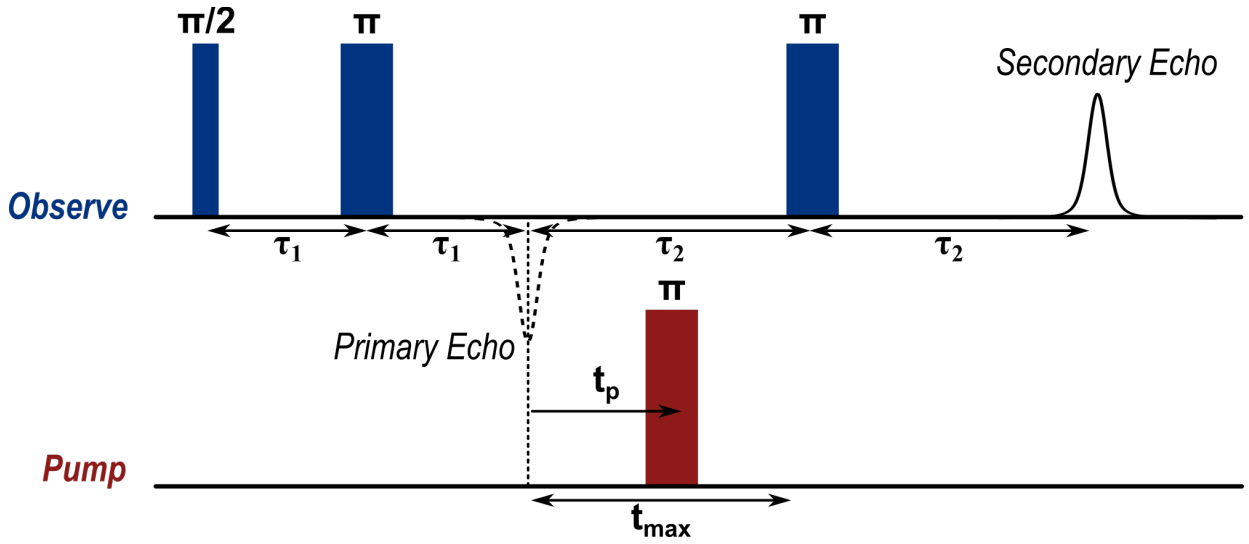

Figure 3.1 The four-pulse DEER sequence described in the text employs pulses of microwave radiation at two different frequencies (blue and red) to induce transitions in two different populations of spins.

The time domain over which this signal is measured must be sufficiently long such that clear features of a full oscillation period (or more) are collected. Depending on the collected time range, empirical expressions for the maximum reliable distance and the maximum distance for which the width of the distribution is reliable were determined[22], respectively:

$$r_{max,\langle r\rangle} = 5\sqrt[3]{t_{max}/2\mu s} \quad (3.26a)$$

$$r_{max,\langle \sigma\rangle} = 4\sqrt[3]{t_{max}/2\mu s} \quad (3.26b)$$

However, recalling that the spin-spin relaxation always acts to dephase spins in the xy-plane (back to zero xy-magnetization), even in the absence of the pump pulse, the echo intensity V decays exponentially as a function of the pulse separation times τ_1 and τ_2. The pulse separation time $\tau_1+\tau_2$ thus sets the maximum t_p for which data can be collected, i.e., the t_{max} in equation 3.26. For this reason, it is typically necessary to freeze nitroxide samples to cryogenic temperatures (~50 K) to maximize T_2[28], since for nitroxides T_2 is ~10-30 ns at room temperature, prohibitively short for DEER measurements. Deuteration of the protein or surrounding solvent

can also help to extend the value of T_2 and thus allow the detection of longer distances.

In randomly oriented samples, such as flash-frozen solutions often used in DEER experiments, the relative population for θ (equation 3.25) is weighted by a factor of sin(θ) and, as such, perpendicular orientations are weighted more heavily than parallel orientations. Typically, although the distribution of θ leads also to a distribution of dipolar frequencies for a specific pair of spins, the pulse radiation is sufficiently wide (but not too wide) to equally excite all resonances at each orientation. On the other hand, for highly rigid samples with well-separated spectral lines and where very narrow pulses are used, specific orientations or narrow ranges of θ can be selectively excited[22,29]. But in the standard DEER experiment, the signal is considered an integration over all possible angles for two spins with a certain distance, and representative of the entire ensemble[30].

In practice, one observes a distribution of distances (due to the intrinsic flexibility proteins and spin label side chains), requiring a summation over all interspin distances weighted by their probabilities to deconvolute the signal. To solve for the distance distribution function, the time-domain dipolar evolution data (after proper background subtraction) is discretized and converted:

$$\mathbf{F}(t_p) = \mathbf{K}(r, t_p) \cdot \mathbf{P}(r) \tag{3.27}$$

where **F** is a vector containing the background-corrected data, **P** is the probability distribution, and **K** is a kernel function containing representative dipolar evolutions for a range of distances. For a given **P**, a kernel function may be readily constructed to solve for **F**. Tikhonov regularization is the most commonly employed method for solving this equation and has been implemented in analysis software. In this dissertation, all DEER data were analyzed using the program LongDistances written by Dr. Christian Altenbach, which employs a modified

regression analysis involving a non-negative model-free analysis. Experimental DEER results will be shown in Chapter 7.

3.3 The effects of rotational dynamics on EPR lineshapes

The remarkable sensitivity of SDSL-EPR to the dynamics of molecules is one of its most important advantages. When the characteristic time scale of molecular rotation matches the inverse of the resonance frequency, it is possible then to resolve the effects of motion on the spectral lineshape[31–33]. Conventional CW-EPR lineshapes exhibit distinct and well-understood responses to rotational motions with correlation times ranging from *ca.* 10^{-11}s to 10^{-7}s by remarkably exploiting the spectral anisotropy of nitroxide spin labels to molecular orientations and surroundings. The detectable motional time range of spectral lineshapes can even be further extended to as long as milliseconds in combination with other techniques such as the saturation transfer EPR, as will be discussed in Section 3.4).

Changes in lineshape manifest due to the relationship between the frequency of detection and the rotational motion (or any spectral exchange process) connecting two orientational, structural, or dynamic states, which each have their own resonance positions in SDSL-EPR. As it is the orientation of the spin (relative to the applied field) that defines the resonance position, it is not only the rate of motion (characterized by the correlation time τ_R) but also the angular amplitude of motion that is crucial for the motional contributions to the spectra. For nitroxide spin labels, rotational motion is most likely to be restricted about the z-axis with a slight tilt angle, which defines the order parameter S (discussed below in Section 3.3.2) in corresponding motional models.

In a theoretical sense, molecular motion affects lineshapes as it modulates T_1 and T_2

relaxation by generating transiently fluctuating fields on top of the oscillatory radiation (B_1) field. Redfield relaxation theory[34,35] describes the dependence of T_1 and T_2 on isotropic rotational correlation time, but it is only valid in the fast motional limit ($\tau_R < 10^{-9}$ sec). For motions slower than 1 ns, different theoretical treatments and experimental models have been presented[14,36–39], some of which will be discussed below.

3.3.1 Effects of the rate of motions on CW-EPR spectra

Recalling that the A- and g- anisotropies define the resonance positions of the powder spectrum[40–43] (i.e., where no motion exists) and based on the timescale required to average out these anisotropies, three motional regimes in EPR spectroscopy have been defined for nitroxides based on the correlation time of isotropic rotational diffusion: the fast/motional narrowing regime ($\tau_R \approx 0.1$ ns ~ 2 ns), the intermediate regime ($\tau_R \approx 2$ ns ~ 100 ns), and the slow/rigid limit regime ($\tau_R > 100$ ns); see Figure 3.2(A).

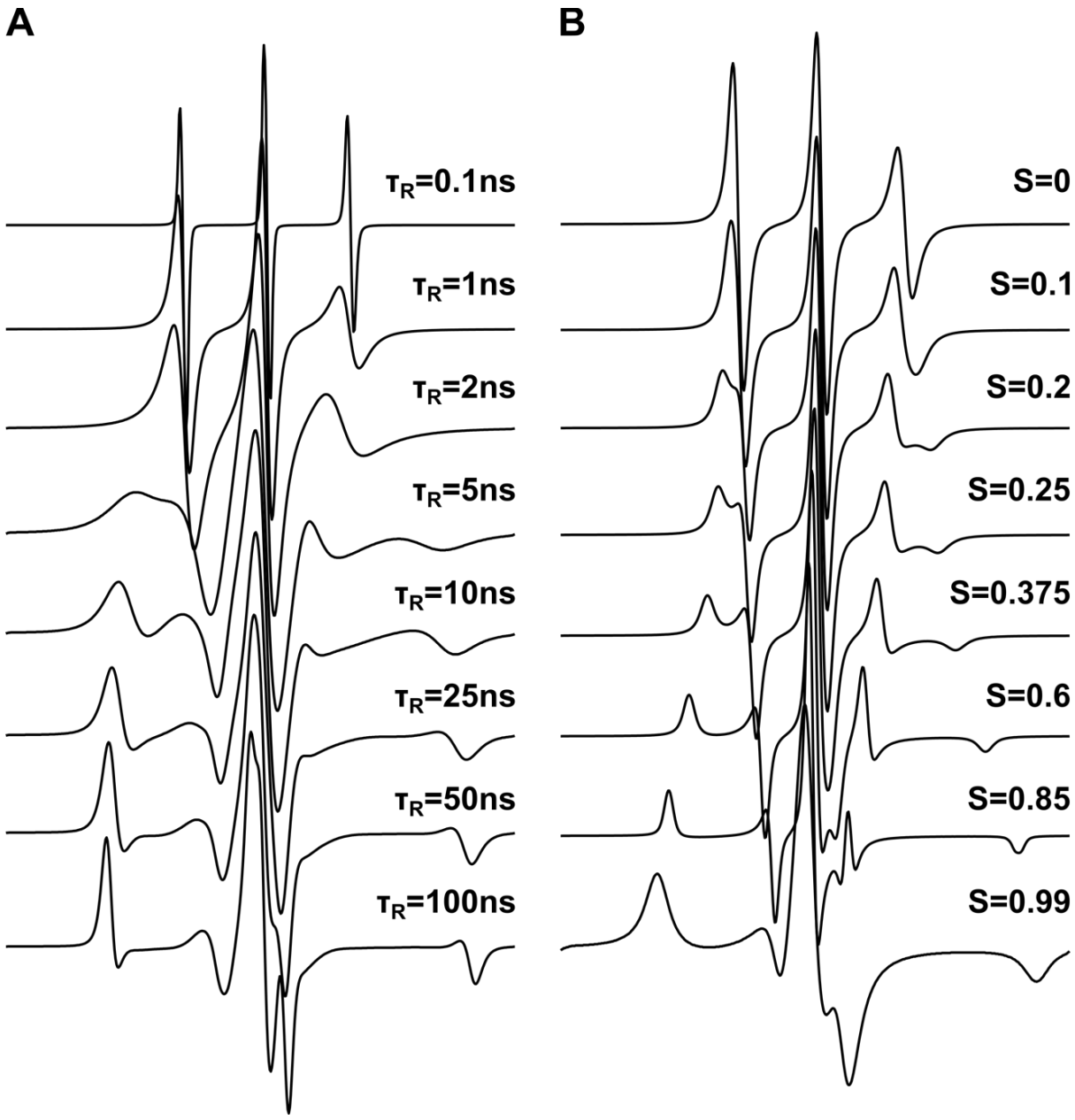

Figure 3.2 (A) X-band CW-EPR spectra of nitroxide spin labels for varying rates of isotropic rotation. From top to bottom, rotational correlation times τ_R (ns) increase. Spectra simulated using the stochastic Liouville equation (see section 3.3.3). (B) X-band CW-EPR spectra of nitroxide spin labels for the restricted angular amplitude of motion. Rotation is about a single axis with the nitroxide z-axis inclined at a fixed tilt angle. From top to bottom, order parameter S increases. Spectra simulated using stochastic Liouville equation with correlation time τ_R = 0.5 ns.

While in X-band, the hyperfine splittings dominate over the effect of the g-tensor, and thus

the timescale of rotational sensitivity is determined by the anisotropy of A-tensors. Increasing in motional rate from the rigid limit, where the spectrum strongly resembles the powder pattern, the discrete resonance lines are first seen broadening as the correlation time decreases, and the effective hyperfine splitting of the outer spectral extrema ($2A_{zz'}$) decreases. Notice that the three hyperfine manifolds broaden differentially due to anisotropy, with the high-field line ($m_I = -1$) broadening more dramatically than the other two.

In this slow motional regime, Freed[14] derived empirical calibrations of spectra to estimate τ_R assuming isotropic rotational motion:

$$\tau_R = a(1 - \frac{A_{zz\prime}}{A_{zz'}(0)})^b \tag{3.28a}$$

$$\tau_R = a'(\frac{\Delta_{m_I}}{\Delta_{m_I}(0)} - 1)^{-b\prime} \tag{3.28b}$$

where a, b, a', and b' are empirical fitting parameters, $A_{zz'}(0)$ represents the rigid limit value for the hyperfine extrema, $\Delta_{m_I}(0)$ represents the rigid limit value for the linewidth (manifold-specific). It should be emphasized that these empirical equations are only valid for isotropic motions. Also, care should be taken for the choice of rigid limit values, as the above calculations can be significantly influenced by the specific conditions of the 'rigid limit'. This will be revisited with real examples in Chapters 5 and 6.

With further increasing the rotational rate, resolved resonance lines within a given manifold eventually begin to move together and eventually collapse to a single broad resonance if:

$$\tau_R = \frac{1}{\gamma_e(A_{zz} - A_{xx})} \approx 2ns \tag{3.29}$$

The collapse of the spectral anisotropy in the low-field hyperfine manifold normally occurs between τ_R = 5~7 ns, whereas that in the high-field manifold it occurs between τ_R = 3~5 ns. All spectral anisotropy effects are negated by the time a correlation time τ_R = 2 ns is reached, where

the sample enters the fast/motional narrowing regime.

In the fast motional regime, the spectra consist of three sharp, well-resolved absorption lines centered at the resonance positions corresponding to the ^{14}N-hyperfine interactions. The width of each line progressively narrows with increasing τ_R, hence the alternate name the 'motional narrowing' regime.

3.3.2 The effects of motional amplitude on CW-EPR spectra

In most cases using spin labels, a nitroxide does not experience unrestricted rotational motion to an angular extent. This means that not all orientations are accessible dynamically, and the motion may not be rapid enough to produce an isotropic average. If the motion is indeed restricted only to certain orientations on the timescale of the experiment, then the spectral anisotropy cannot be completely averaged out, no matter the rate of rotation. Only the magnitude of spectral anisotropy is reduced, depending on the angular amplitude of motion.

A common description for the anisotropic motion of spin labels is as follows: the nitroxide z-axis (nitrogen $2p_z$-orbital) is tilted at an angle to a fixed axis about which the spin label rotates rapidly. The correlation time for rotation about this axis is short, but the rotation of the axis itself is relatively long enough such that the spectral anisotropy is not motionally averaged. Seemingly similar to the spectral rate effects described in the previous section but actually different, as the tilt angle increases (Figure 3.2 (B)), the outer hyperfine peaks (corresponding to $A_{\parallel}$) move inwards while the inner peaks (corresponding to $A_{\perp}$) move outwards. Eventually, the outer and inner hyperfine peaks merge when the tilt angle = 54.74° for nitroxides. An order parameter is defined as:

$$S \equiv \frac{1}{2}(3\langle\cos^2\theta\rangle - 1) = \frac{A_{\parallel} - A_{\perp}}{\Delta A} \tag{3.30}$$

where $\Delta A = A_{zz} - \frac{1}{2}(A_{xx} + A_{yy})$, and the angular brackets represent an average over the ensemble of all accessible orientations.

In practical systems, a complex situation where the rate of motion also contributes enough to modulate the lineshapes on this time scale will be discussed in section 3.3.3. Also, Freed's empirical theorem fails for motions with restricted amplitude as the rotation is no longer isotropic. Instead, it is useful to use an effective Hamiltonian model for evaluating the motional modes represented in the spectra. Further discussions are shown with real experimental data in Chapters 5 and 6.

3.3.3 CW-EPR spectral simulation using the Stochastic Liouville Equation (SLE) and microscopic order macroscopic disorder model (MOMD)

Extending the Classical Bloch equations to simulate lineshapes in the varied-motion situations described above requires significant theoretical modifications: the fast motional regime would employ perturbation theory[44–46], while the slow motional regime requires a 'jump' model[47]. Alternatively, rotational diffusion can be described quantum mechanically by using the density matrix, which leads to the use of the stochastic Liouville equation (SLE) for spin dynamics, which is valid for all motional regimes and takes into consideration distributions of both rate and amplitude of motions.

As the dynamics reported by spin labels in CW-EPR can cover the time range from ps to 100ns, spectral lineshape simulation using SLE has been proven to be an indispensable analytical tool in SDSL-EPR-related studies. Freed and coworkers developed computer programs[14,48] to

calculate the solution to the SLE for different dynamical models of intermediate motions. One motional model that has been proven very useful in modeling the dynamics of nitroxide side chains is the microscopic order macroscopic disorder (MOMD) model.

In the MOMD model, three coordinate frames are employed as illustrated in Figure 3.3. Recall in Figure 2.5 that the principal axis system for a nitroxide is the molecule-fixed magnetic tensor frame (x_M, y_M, z_M), where the z-axis lies along the nitrogen 2p atomic orbital and the x-axis lies along the N–O bond. A second coordinate frame introduced is the principal frame for the rotational diffusion tensor (x_R, y_R, z_R). The relationship between the diffusion and magnetic frames is specified by the diffusion tilt angles (α_D, β_D, γ_D), defined as the Euler angles required for the rotation of the magnetic frame into the diffusion frame.

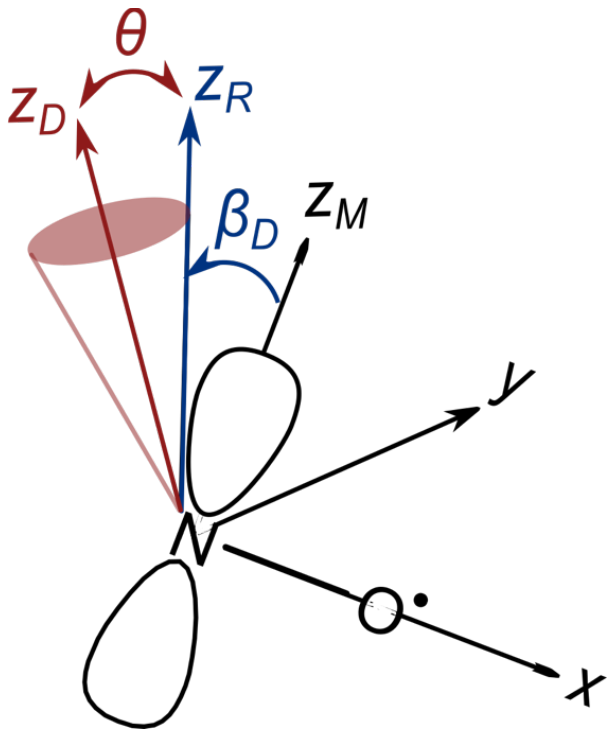

Figure 3.3 The MOMD model. A diagram showing the relationship between the nitroxide magnetic frame (x_M, y_M, z_M), the z-axis of the diffusion tensor (z_R), and the protein fixed director (z_D). The angles β_D and θ are defined as illustrated. Over time, z_R moves within a space defined by the ordering potential.

To describe the anisotropic motion, a restoring (ordering) potential (U) that constrains the spatial extent of the motion of z_R is introduced in MOMD. The ordering potential is expanded as a series of spherical harmonics:

$$U(\Omega) = -\sum_{L,K} c_{L,K} D^{L}_{0K}(\Omega) \tag{3.31}$$

where Ω is a vector representing the diffusion tilt angles, and $c_{L,K}$ are the coefficients of the potential, which are expressed in units of k_BT. Only five possible terms of the potential are typically, namely c_2^0, c_2^2, c_4^0, c_4^2, and c_4^4, and often use of only the term c_2^0 is sufficient for the simulation of the majority of lineshapes.

Using a first-order expansion, the amplitude of motion can be described by:

$$U(\theta) = -\frac{1}{2} k_B T c_{20} (3\cos^2\theta - 1) \tag{3.32}$$

where θ is the (instantaneous) angle between z_R and the symmetry axis of the potential. The symmetry axis z_D of the potential defines the z-axis of the third and final coordinate frame, the director frame. From this, the order parameter S_{20} can be written as:

$$S_{20} = \frac{1}{2}(3\langle\cos^2\theta\rangle - 1) \tag{3.33}$$

where again the angular brackets indicate the spatial average.

For the commonly used disulfide-linked nitroxide spin label side chains attached to the protein, the director frame is uniaxial and fixed in the protein, resulting in an anisotropic motion and can be characterized by a such order parameter. For the individual protein molecule, z_D could form a distribution of angle ψ with respect to the external magnetic field. To obtain the final spectrum corresponding to an isotropic distribution of protein orientations, it is necessary for the spectrum to be summed over all angles ψ.

In the actual simulation program, rates of motion are expressed as a Cartesian rotational diffusion tensor (R_{xx}, R_{yy}, R_{zz}) of logarithms of the rotational correlation rate, given here in a

modified spherical form:

$$\langle R \rangle = \sqrt[3]{R_{xx}R_{yy}R_{zz}} \tag{3.34}$$

$$\tau_R = 1/6 \times 10^{\langle R \rangle} \tag{3.35}$$

In spectral simulations of nitroxide EPR spectra, c_2^0 and $\langle R \rangle$, and the principal values of A- and g-tensors are by far the most important parameters. Other parameters can also dramatically affect the simulated lineshapes and are listed here: the Euler tilt angles (α_D, β_D, γ_D), Lorentzian homogeneous (w_{xx}, w_{yy}, w_{zz}) broadenings, and the Gaussian inhomogeneous broadenings ($gib_0/\Delta^{(0)}$, $gib_2/\Delta^{(2)}$).

It is important to note that, in the MOMD model, strong correlations exist between certain fitting parameters (e.g., β_D and c_2^0), which creates the potential for multiple different yet equally-suitable simulations of experimental spectra. In this dissertation, the program MultiComponent (as implemented by Christian Altenbach (https://sites.google.com/site/altenbach/labview-programs/epr-programs)) is used, which can produce non-unique spectral fits due to these parametric correlations. As such, it is critical to test models that can reasonably describe the physical system studied, and to not rely on results from lineshape simulation alone as 'proof' of theorized structural or dynamic mechanisms.

3.4 Saturation Transfer EPR

Saturation transfer EPR (ST-EPR) is a highly sophisticated method aimed at detecting dynamics in the μs-ms time domain. Many theoretical articles and reviews can be found[5,49–53]. This section serves only as a brief introduction to the method for readers to better understand the results presented in Chapters 5-7 of this dissertation.

3.4.1 Background theory

As discussed above, the powder pattern represents the 'rigid motional limit' of conventional CW-EPR, and is essentially determined by the anisotropy of the spin label used. Motional effects that are slower than 100ns (for nitroxides) can no longer be sensitively resolved by the CW-EPR lineshapes. However, because many functionally important biological processes occur in the time domain of μs-ms, it is important to extend the sensitivity of SDSL-EPR into this crucial time range. For this reason, Hyde and Dalton[54] introduced saturation transfer EPR (ST-EPR) in 1972, a technique that is optimally sensitive to motions in the microsecond region.

Recall that T_1 for nitroxides in solution is much greater than T_2 (e.g., ~1μs vs. ~10ns); as such, any nitroxide EPR method becomes virtually more sensitive to microsecond motion when a saturation condition is created. As aforementioned, conventional CW-EPR is performed at low microwave power to avoid saturation, in the region of so-called 'linear' EPR. By increasing power, the spin system can be partially or fully saturated such that the amplitude of the EPR signal is no longer linearly proportional to the field strength of B_1, (i.e., to the square root of the microwave power), producing a 'nonlinear' response condition. Such nonlinear EPR methods include progressive power saturation CW-EPR and saturation transfer EPR.

Similar to the discussions involving dynamics in the ps-ns time domain, when molecular rotations in the slow regime (μs-ms) can sufficiently influence the resonance absorption (or dispersion, which only differs in terms of detection scheme), for example in ST-EPR, it is then possible to resolve the effects of motion from the spectra. As demonstrated in Chapter 2, the anisotropy of spin labels determines that a very narrow distribution of orientations is excited at each spectral position, i.e., the absorption spectrum possesses highly resolved orientational

resolution. The sensitivity of the spectral position to the orientation (i.e., the change of resonance upon angular changes, $dH_{res}/d\theta$) also varies throughout the spectrum and has a maximum value of about 35 Gauss/rad = 0.61Gauss/°. The change in angle that is sufficient to reduce the resonance (i.e., excitation probability) by a factor of 2 can thus be calculated using the Lorentzian linewidth:

$$\theta_T = \left(\frac{1}{\gamma_e T_2}\right) \times \left(\frac{dH_{res}}{d\theta}\right)^{-1} \tag{3.36}$$

which is approximately 4° for nitroxide spin labels. This orientational-dependent and rotation-modulated absorption of spins is the basis of motional, as well as orientational sensitivity for both conventional CW-EPR and ST-EPR.

When the spin system is only saturated partially, only a subset of spins are at resonance (i.e., excited) and are therefore subjected to saturating radiation. The amount of saturation depends on the competition between the rates of excitation and relaxation back to the ground spin state. Therefore, both the intrinsic spin-lattice relaxation time T_1 and the radiation field strength B_1 are fundamental parameters to consider in such experiments. The characteristic time of any such process must be smaller or comparable to the relaxation time for the process to be detected, otherwise, the spin systems have already returned to the thermal equilibrium.

Different from T_1 and B_1 which globally influence the saturation-relaxation process, when rotational motions occur, the rate of relaxation will increase by causing spins 'transfer' between excited and unexcited angular ranges of the spectrum. Due to the varying sensitivity of the spectral position to the orientation, saturation is also transferred differentially. It is depleted (or augmented if transferred in) preferentially in those parts where the resonance position depends most strongly on the orientation of the nitroxide to the static B_0 field direction, i.e., where the θ_T has a minimum value, while in other parts the transfer of saturation is accordingly less efficient.

Therefore, when the B_0 field scans through the entire resonance range (i.e., all orientations), effects from the orientation-dependent rotation can be resolved from lineshapes.

The sensitivity of the spectrum to rotational motion is minimal at what are referred to as 'turning points' (designated L, C, H in the ST-EPR spectra in the chapters to follow), where the angle θ relative to the magnetic field is 0° or 90°, while maximal sensitivity is found at intermediate spectral positions (designated L'', C', H''). As long as the rotational transfer time τ_T (the time required for rotational motion through the minimum angle $\geqq \theta_T$), is less than or equal to T_1 (that is $\tau_T \leqq T_1$), a change in saturation caused by the motion-induced transfer can be observed. According to the definition of the rotational correlation time (the average time to rotate through one radian), $\tau_R \approx \tau_T / 0.007$ for nitroxide EPR lineshapes (where the minimum θ_T which is 4°). Therefore, saturation transfer can be detected whenever the rotational correlation time, $\tau_R \leqq T_1/0.007$. For nitroxide spin labels, this means that ST-EPR lineshapes are temporally sensitive to dynamics for as long as milliseconds. This allows us to study much slower motions that are inaccessible from linewidths and lineshapes of unsaturated nitroxide EPR spectra.

3.4.2 Experimental approaches

The development of ST-EPR methodology has involved a search for an EPR experimental scheme that is optimally sensitive to saturation, while exploiting the available instrumentation technology, in a time well prior to the development of pulse techniques. The most important ST-EPR methods are the second-harmonic absorption spectrum (detected 90° out of phase, V_2'), the first-harmonic dispersion spectrum (detected 90° out of phase, U_1'[54]), and the first-harmonic absorption spectrum (detected 90° out of phase (V_1'[55]). The conventional unsaturated CW-EPR first-harmonic absorption spectrum detected in-phase is designated as the V_1 spectrum

accordingly. Only V_1 and V_2' spectra are reported and analyzed in this dissertation.

V_2' spectra are the classical form of the ST-EPR display, whose lineshapes are exquisitely sensitive to very slow rotational motion. The terms 'out-of-phase' or 'in-phase' describe the signal phase with respect to the field modulation, rather than of the bridge (which instead provides control of the absorption/dispersion modes). The frequency of modulation is typically set at 50 kHz and of the phase-sensitive detector at 100 kHz. A significant response of the second harmonic to changes in modulation is obtained, which has been shown in practical experiments to possess higher sensitivity to motion in this time domain.

The overall intensity of the nonlinear signal increases with increasing spin-lattice relaxation time. The longer the T_1 and the stronger the B_1, the more efficient saturation is, and theoretically the optimal signal intensity can be expected. One should note, however, that the spin systems cannot be completely saturated (i.e., across the entire spectrum), otherwise, there would be no measurable transfer of saturation. It is thus crucial to calibrate the value of B_1 in the resonator as it helps determine the extent of partial saturation.

When the field strength B_1 is high enough to induce partial saturation, when the modulation frequency is fast compared to the rate of T_1 relaxation (as long as 30μs), instead of the signal being effectively modulated, it lags behind the modulation and a signal can be observed not only in-phase but also even when the reference phase on the phase-sensitive detector is set 90°-out-of-phase. The advantage of using the out-of-phase signal is that it is present only when saturation exists and thus it is selectively sensitive to saturation transfer which can decrease the spectral intensity. As such, the contribution of saturation transfer is more prominent in an out-of-phase signal than in an in-phase signal, as the latter is present regardless of saturation and more sensitive to faster motions (ps-ns).

In brief, the out-of-phase lineshapes depend on rotational motions that take place on the timescale of spin-lattice relaxation. There is not an observable out-of-phase signal if the rotational motion is too fast, or if the spin-lattice relaxation is too fast. While the latter case is straightforward to understand, in the former case, the fast rotational motion is completely averaged out from the whole spectrum, which cannot be effectively resolved as a 'transfer' between resonance positions in lineshapes. However, as a 'path' that alleviates the saturation, its effects can still be distinguished from the spectral integral (i.e., signal intensity) and the center field region. In particular, the lineshapes in the low and high field manifolds are insensitive to motions of fast rate and small amplitude, as both manifolds (m_I = +1 and -1) have wider angular dispersion.

From the discussion above, it is self-evident that the accurate setting of the modulation phase is also crucial for ST-EPR experiments. The same instrumental setup (saturating microwave power, high modulation amplitude, out-of-phase detection) that makes V_2' more sensitive to slow rotational motion also makes it more sensitive to changes in other physical and instrumental variables. A strategy that employs much more precise phase control is necessary. Generally, the phase must be set to an accuracy within 0.3 degrees to avoid misinterpretation of correlation times. Due to the poorly-understood relationship between rotational dynamics and the resulting spectral lineshapes, ST-EPR spectra are usually analyzed by comparing them with reference spectra obtained either from experiments on model systems or from theoretical computer simulations. In this dissertation, published[51,53] experimental settings and reference curves are used. A concise review of nitroxide spin labels used for ST-EPR can be found in Chapter 6, and some further discussions of ST-EPR can be found in Chapters 5 and 6.

3.5 References

1. Bloch, F. Nuclear Induction. *Phys. Rev.* **70**, 460–474 (1946).
2. Carrington, A. & McLachlan, A. D. *Introduction to magnetic resonance: with applications to chemistry and chem. physics*. (Chapman and Hall, 1979).
3. Slichter, C. P. *Principles of magnetic resonance*. (Springer-Verlag GbmH, 2010).
4. Humphries, G. M. K. & McConnell, H. M. 2. Nitroxide Spin Labels. in *Methods in Experimental Physics* (eds. Ehrenstein, G. & Lecar, H.) vol. 20 53–122 (Academic Press, 1982).
5. Marsh, D. *Spin-label electron paramagnetic resonance spectroscopy*. (CRC Press/Taylor & Francis Group, 2020).
6. Sato, H. *et al.* Electron spin–lattice relaxation of nitroxyl radicals in temperature ranges that span glassy solutions to low-viscosity liquids. *J. Magn. Reson.* **191**, 66–77 (2008).
7. Owenius, R., Terry, G. E., Williams, M. J., Eaton, S. S. & Eaton, G. R. Frequency Dependence of Electron Spin Relaxation of Nitroxyl Radicals in Fluid Solution. *J. Phys. Chem. B* **108**, 9475–9481 (2004).
8. Robinson, B., Haas, D. & Mailer, C. Molecular dynamics in liquids: spin-lattice relaxation of nitroxide spin labels. *Science* **263**, 490–493 (1994).
9. Bridges, M. D., Hideg, K. & Hubbell, W. L. Resolving Conformational and Rotameric Exchange in Spin-Labeled Proteins Using Saturation Recovery EPR. *Appl. Magn. Reson.* **37**, 363–390 (2010).
10. Altenbach, C., Froncisz, W., Hyde, J. S. & Hubbell, W. L. Conformation of spin-labeled melittin at membrane surfaces investigated by pulse saturation recovery and continuous wave power saturation electron paramagnetic resonance. *Biophys. J.* **56**, 1183–1191 (1989).

11. Bridges, M. D. Resolving Rotameric and Conformational Exchange in Spin Labeled Proteins at Biologically-Relevant Temperatures by Saturation Recovery Electron Paramagnetic Resonance. (University of California, Los Angeles).
12. Millhauser, G. L. & Freed, J. H. Two-dimensional electron spin echo spectroscopy and slow motions. *J. Chem. Phys.* **81**, 37–48 (1984).
13. Stillman, A. E., Schwartz, L. J. & Freed, J. H. Direct determination of rotational correlation time by electron-spin echoes. *J. Chem. Phys.* **73**, 3502–3503 (1980).
14. Freed, J. H. 3 - Theory of Slow Tumbling ESR Spectra for Nitroxides. in *Spin Labeling* (ed. Berliner, L. J.) 53–132 (Academic Press, 1976).
15. Eaton, G. R. & Eaton, S. S. Resolved Electron-Electron Spin-Spin Splittings in EPR Spectra. in *Spin Labeling: Theory and Applications* (eds. Berliner, L. J. & Reuben, J.) 339–397 (Springer US, 1989).
16. Atkins, P. W. & Kivelson, D. ESR Linewidths in Solution. II. Analysis of Spin—Rotational Relaxation Data. *J. Chem. Phys.* **44**, 169–174 (1966).
17. Altenbach, C., Oh, K.-J., Trabanino, R. J., Hideg, K. & Hubbell, W. L. Estimation of Inter-Residue Distances in Spin Labeled Proteins at Physiological Temperatures: Experimental Strategies and Practical Limitations. *Biochemistry* **40**, 15471–15482 (2001).
18. Kittell, A. W., Hustedt, E. J. & Hyde, J. S. Inter-spin distance determination using L-band (1–2GHz) non-adiabatic rapid sweep electron paramagnetic resonance (NARS EPR). *J. Magn. Reson.* **221**, 51–56 (2012).
19. Jeschke, G., Panek, G., Godt, A., Bender, A. & Paulsen, H. Data analysis procedures for pulse ELDOR measurements of broad distance distributions. *Appl. Magn. Reson.* **26**, 223 (2004).

20. Milov, A. D., Ponomarev, A. B. & Tsvetkov, Yu. D. Electron-electron double resonance in electron spin echo: Model biradical systems and the sensitized photolysis of decalin. *Chem. Phys. Lett.* **110**, 67–72 (1984).
21. Salikhov, K. M., Dzuba, S. A. & Raitsimring, A. M. The theory of electron spin-echo signal decay resulting from dipole-dipole interactions between paramagnetic centers in solids. *J. Magn. Reson. 1969* **42**, 255–276 (1981).
22. Jeschke, G. DEER Distance Measurements on Proteins. *Annu. Rev. Phys. Chem.* **63**, 419–446 (2012).
23. Jeschke, G. & Polyhach, Y. Distance measurements on spin-labelled biomacromolecules by pulsed electron paramagnetic resonance. *Phys. Chem. Chem. Phys.* **9**, 1895–1910 (2007).
24. Pannier, M., Veit, S., Godt, A., Jeschke, G. & Spiess, H. W. Dead-time free measurement of dipole–dipole interactions between electron spins. *J. Magn. Reson.* **213**, 316–325 (2011).
25. Jeschke, G. Distance Measurements in the Nanometer Range by Pulse EPR. *ChemPhysChem* **3**, 927–932 (2002).
26. Borbat, P. P., Georgieva, E. R. & Freed, J. H. Improved Sensitivity for Long-Distance Measurements in Biomolecules: Five-Pulse Double Electron–Electron Resonance. *J. Phys. Chem. Lett.* **4**, 170–175 (2013).
27. Griffiths, D. J. *Introduction to quantum mechanics*. (Prentice Hall, 1995).
28. Jeschke, G., Bender, A., Paulsen, H., Zimmermann, H. & Godt, A. Sensitivity enhancement in pulse EPR distance measurements. *J. Magn. Reson.* **169**, 1–12 (2004).
29. Endeward, B., Butterwick, J. A., MacKinnon, R. & Prisner, T. F. Pulsed Electron−Electron Double-Resonance Determination of Spin-Label Distances and Orientations on the Tetrameric Potassium Ion Channel KcsA. *J. Am. Chem. Soc.* **131**, 15246–15250 (2009).

30. Bode, B. E. *et al.* Counting the Monomers in Nanometer-Sized Oligomers by Pulsed Electron−Electron Double Resonance. *J. Am. Chem. Soc.* **129**, 6736–6745 (2007).
31. Marsh, D. Experimental Methods in Spin-Label Spectral Analysis. in *Spin Labeling* (eds. Berliner, L. J. & Reuben, J.) vol. 8 255–303 (Springer US, 1989).
32. Abergel, D. & Palmer, A. G. Approximate Solutions of the Bloch–McConnell Equations for Two-Site Chemical Exchange. *ChemPhysChem* **5**, 787–793 (2004).
33. McConnell, H. M. Reaction Rates by Nuclear Magnetic Resonance. *J. Chem. Phys.* **28**, 430–431 (1958).
34. Redfield, A. G. The Theory of Relaxation Processes* *This work was started while the author was at Harvard University, and was then partially supported by Joint Services Contract N5ori-76, Project Order I. in *Advances in Magnetic and Optical Resonance* (ed. Waugh, J. S.) vol. 1 1–32 (Academic Press, 1965).
35. Redfield, A. G. On the Theory of Relaxation Processes. *IBM J. Res. Dev.* **1**, 19–31 (1957).
36. Goldman, S. A., Bruno, G. V. & Freed, J. H. Estimating slow-motional rotational correlation times for nitroxides by electron spin resonance. *J. Phys. Chem.* **76**, 1858–1860 (1972).
37. Mason, R. P. & Freed, J. H. Estimating microsecond rotational correlation times from lifetime broadening of nitroxide electron spin resonance spectra near the rigid limit. *J. Phys. Chem.* **78**, 1321–1323 (1974).
38. *Spin labeling II: theory and applications*. (Academic Press, 1979).
39. *Spin labeling: theory and applications*. (Academic Press, 1976).
40. Breit, G. & Rabi, I. I. Measurement of Nuclear Spin. *Phys. Rev.* **38**, 2082–2083 (1931).
41. Weil, J. A. The analysis of large hyperfine splitting in paramagnetic resonance spectroscopy. *J. Magn. Reson. 1969* **4**, 394–399 (1971).

42. Stoll, S. Chapter Six - CW-EPR Spectral Simulations: Solid State. in *Methods in Enzymology* (eds. Qin, P. Z. & Warncke, K.) vol. 563 121–142 (Academic Press, 2015).
43. Stoll, S. & Schweiger, A. EasySpin, a comprehensive software package for spectral simulation and analysis in EPR. *J. Magn. Reson.* **178**, 42–55 (2006).
44. Knowles, P. F., Marsh, D., Rattle, H. W., Knowles, P. F. & Rattle, H. W. E. *Magnetic resonance of biomolecules: an introduction to the theory and practice of NMR and ESR in biological systems*. (Wiley, 1976).
45. Schreier, S., Polnaszek, C. F. & Smith, I. C. P. Spin labels in membranes problems in practice. *Biochim. Biophys. Acta BBA - Rev. Biomembr.* **515**, 395–436 (1978).
46. Kivelson, D. Theory of ESR Linewidths of Free Radicals. *J. Chem. Phys.* **33**, 1094–1106 (1960).
47. Livshits, V. A. Slow anisotropic tumbling in ESR spectra of nitroxyl radicals. *J. Magn. Reson. 1969* **24**, 307–313 (1976).
48. Budil, D. E., Lee, S., Saxena, S. & Freed, J. H. Nonlinear-Least-Squares Analysis of Slow-Motion EPR Spectra in One and Two Dimensions Using a Modified Levenberg–Marquardt Algorithm. *J. Magn. Reson. A* **120**, 155–189 (1996).
49. Thompson, A. R., Binder, B. P., McCaffrey, J. E., Svensson, B. & Thomas, D. D. Chapter Four - Bifunctional Spin Labeling of Muscle Proteins: Accurate Rotational Dynamics, Orientation, and Distance by EPR. in *Methods in Enzymology* (eds. Qin, P. Z. & Warncke, K.) vol. 564 101–123 (Academic Press, 2015).
50. Thomas, D. D. Rotational diffusion of membrane proteins. in *Techniques for the Analysis of Membrane Proteins* (eds. Ragan, C. I. & Cherry, R. J.) 377–431 (Springer Netherlands, 1986).

51. Squier, T. C. & Thomas, D. D. Methodology for increased precision in saturation transfer electron paramagnetic resonance studies of rotational dynamics. *Biophys. J.* **49**, 921–935 (1986).
52. Hyde, J. S. & Thomas, D. D. New Epr Methods for the Study of Very Slow Motion: Application to Spin-Labeled Hemoglobin. *Ann. N. Y. Acad. Sci.* **222**, 680–692 (1973).
53. Thomas, D. D., Dalton, L. R. & Hyde, J. S. Rotational diffusion studied by passage saturation transfer electron paramagnetic resonance. *J. Chem. Phys.* **65**, 3006–3024 (1976).
54. Hyde, J. S. & Dalton, L. Very slowly tumbling spin labels: adiabatic rapid passage. *Chem. Phys. Lett.* **16**, 568–572 (1972).
55. Livshits, V. A. & Marsh, D. Application of the out-of-phase absorption mode to separating overlapping EPR signals with different T1 values. *J. Magn. Reson.* **175**, 317–329 (2005).

Chapter 4: Site-Directed Spin Labeling (SDSL) and Spin labels in Biological Studies

4.1 Introduction to site-directed spin labeling technique and nitroxide spin labels

EPR spectroscopy has long been applied for studying biological molecules ever since the 1950's[1]. However, due to the relative rareness of proteins containing unpaired electrons, it has been largely limited to the area of metalloproteins. The general concept of introducing a specific 'reporter' group that can target and covalently attach to a specific protein residue *via* a 'positioning' group was brought up by Burr and Koshland in 1964[2]. With a qualified reporter of which the position can be precisely controlled, it should be sensitive enough to monitor changes, at the same time gentle enough to introduce minimal perturbance to the natural environment. Thus, the site-specific structure and dynamic information of attached proteins can be obtained by modulating and measuring the behavior of the reporter.

This concept was introduced to electron paramagnetic resonance (EPR) methodology later by McConnell[3]. In a method termed 'spin labeling', where stable free radicals are incorporated into originally 'EPR-silent' protein to serve as the reporter group, the capacity of using EPR for biological studies is greatly extended. By far, the most widely used radicals are nitroxide derivatives[4–7], of which an unpaired electron locates at the $2p_Z$ orbital of the nitrogen atom. In order to limit the internal motion of nitroxide moiety, the nitroxide group is incorporated into a ring structure (six-membered piperidine, five-membered pyrrolidine, or five-membered pyrrole). Regardless of the fact that the N-O moiety is potentially susceptible to reduction[8], which largely limits its usage in live cells, nitroxide-containing spin labels are known to be kinetically stable over a pH range of 3-10 and temperatures up to 80°C[9] due to the existence of quaternary carbons at the neighboring bonds[10], thus suitable for measurements under a large number of biological

conditions.

Other stable radicals such as the triarylmethyl (TAM) radicals[11,12] have also been developed and applied as EPR probes in specific studies. However, nitroxide radicals are not only inherently stable but also can participate in versatile kinds of chemistry, which contributes greatly to their values as exogenous labels. In this dissertation, only nitroxide spin label side chains are used and discussed.

Native residues can be used as the spin label attachment position *via* functional groups with specific reactivity for a particular amino acid side chain, such as lysines, cysteines, etc. However, the inability to selectively label one site from among all reactive residues, as well as the inflexibility to only label their naturally distributed regions on protein both set significant limitations to early applications of spin labeling EPR methods. A groundbreaking advancement was enabled in the late 1980s on the basis of the development of site-directed mutagenesis and recombinant protein expression and purification techniques. Pioneered by Hubbell[13], a technique known as site-directed spin labeling (SDSL) is developed, wherein spin labels could be introduced site-specifically into any position on a recombinant protein that is genetically mutated to the reactive amino acid (usually cysteine). This is shown schematically in Figure 4.1, where a native residue is mutated and then reacted with a nitroxide derivative to generate a nitroxide side chain. Several aspects will be discussed in the next sections, focusing on the variety, structure, and dynamic of nitroxide spin labels.

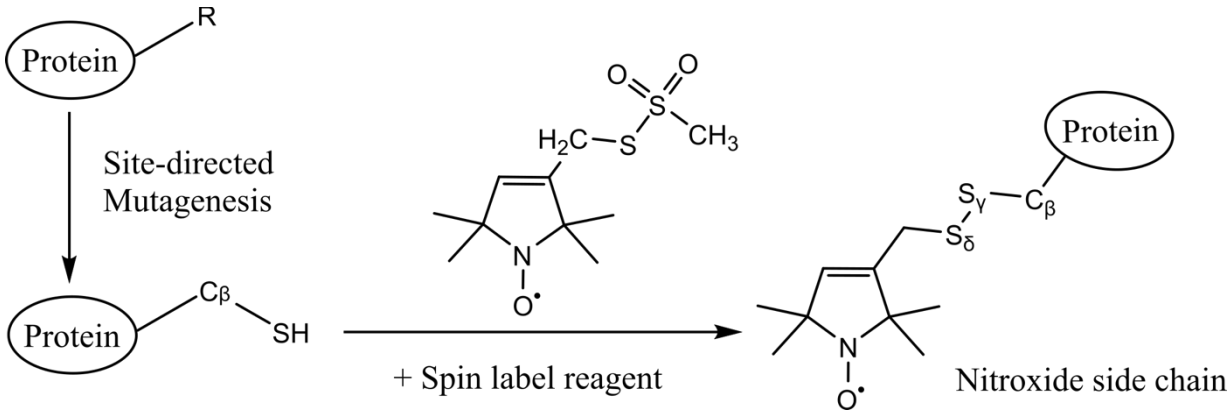

Figure 4.1 Site-directed spin labeling. A selected native residue in the protein is mutated to cysteine *via* site-directed mutagenesis, and the cysteine-containing protein is expressed and purified, and reacted with the cysteine-specific methanethiosulfonate derivative to generate a nitroxide spin label side chain. In the figure, the most widely used methanethiosulfonate reagent MTSSL, and the corresponding spin label side chain after labeling, R1, are shown.

4.2 Development of site-directed nitroxide spin labels

A variety of spin labeling reagents have been developed for the incorporation of a spin label into proteins. The 'positioning' group of reagents determines the chemical specificity to react with which specific kind of residues on the protein. For instance, at neutral pH, the commonly used functional groups, and methanethiosulfonate all react with cysteine residues, while hydroxylsuccinimide reacts with lysines. In order to maximize the success of labeling strategies under diverse experimental conditions, spin label side chains with a variety of chemical structures, linkages, and targeting strategies have been designed, customized, examined, and applied in specific studies, which will be introduced below.

4.2.1 Disulfide-linked spin label side chains: R1 and its derivatives

Due to their high reactivity and specificity, methanethiosulfonate nitroxides (MTS) have

been considered the most popular and most utilized reagents among all candidates, namely the MTSSL (2,2,5,5-tetramethyl-pyrroline-1-oxyl methanethiosulfonate) reagent which results in a disulfide-linked nitroxide side chain designated R1 (Figure 4.2 (A)). *Via* the reaction of which mechanism similar to an S_N2 reaction, protein sulfhydryl anions, including cysteine residues at both solvent-exposed sites and fully buried sites, could be readily labeled.

Over the past years, extensive studies[4,7,14,15] have been done focusing on characterizing this spin label and evaluating its performance in applications. As with any mutation, the possible perturbance of introducing the spin label to the native protein structure was examined. By determining the activity and thermodynamic stability[4] and resolving crystal structures for several R1 spin-labeled T4 lysozyme (T4L) mutants, it was found that the altered activity and stability of the mutants were energetically similar to substitution with other natural amino acids at those sites. The main chain root means square (RMS) deviation < 0.5 Å was also obtained when comparing several R1-labeled T4L structures to the wild-type one[15]. Conclusively, the effect of R1 on protein native backbone fold and thermodynamic stability is proved to be minimal, particularly for solvent-exposed surface sites which are mostly used in this dissertation.

As a probe for detecting protein structure and dynamics, R1 has numerous advantages, including its relatively small size, with a molecular volume comparable to native tryptophan residue, and its relatively flexible linker (5 single bonds). However, such characteristics that make it useful to map local interactions and backbone dynamics on the ns time scale also limit its use in many other aspects. The internal flexibility (see the following section 4.3) leads to both the motional averaging effect when monitoring slow protein internal motions (μs-ms), and the uncertainty in the nitroxide location when determining interspin distance distributions.

To expand the application of methanethiosulfonate nitroxide reagents, a large library of R1

derivatives has been designed and synthesized by the research group of Hideg. Figure 4.2 shows the chemical structures of these resulting spin label side chains upon reaction with cysteine.

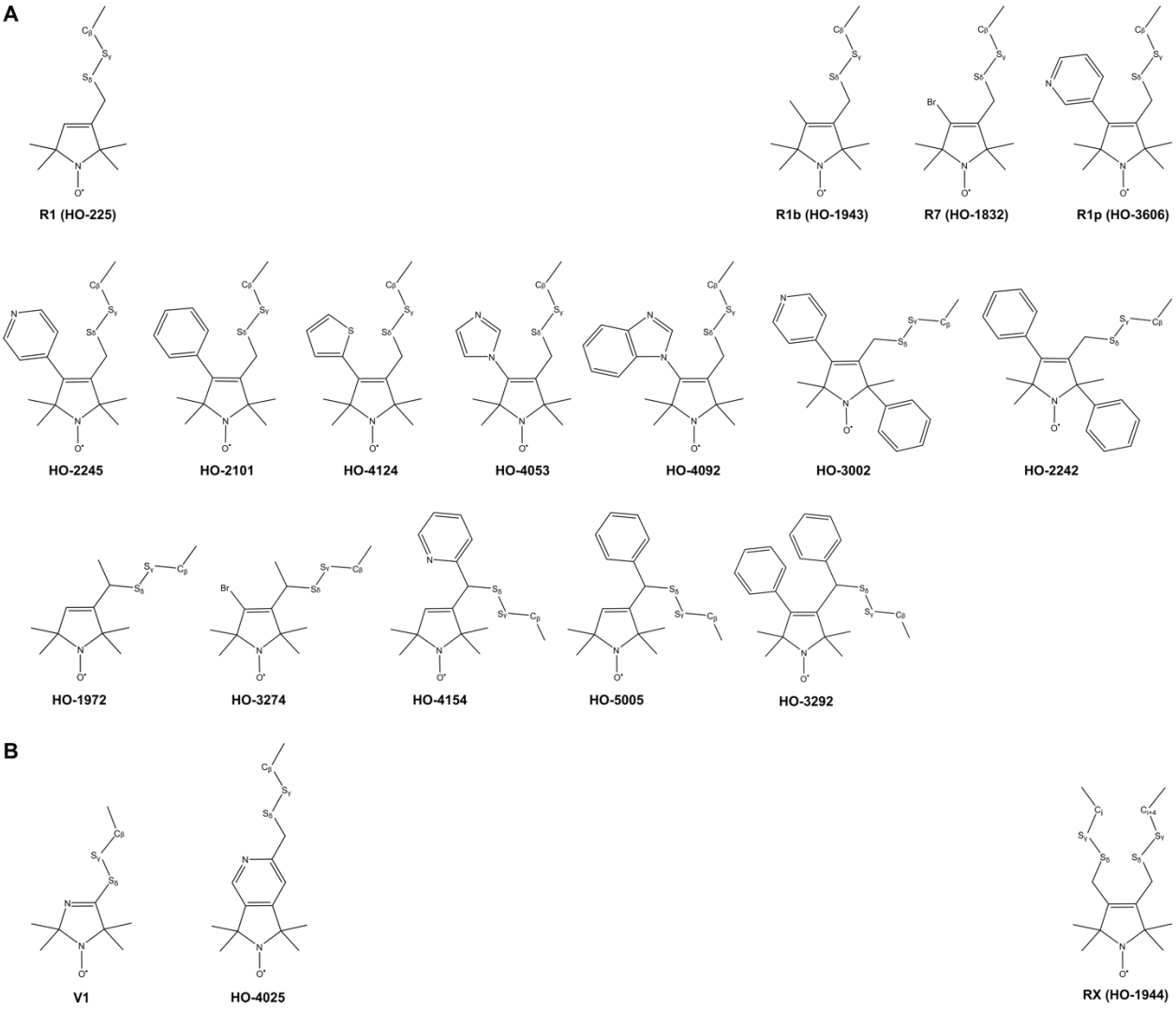

Figure 4.2 Disulfide-linked nitroxide spin labels used in this dissertation. Each unique spin label side chain is designated as indicated. The Hideg HO-codes in parentheses indicate the chemical reagent code for each raw label. (A) R1 and other side chains with bulky substituents in the structure; (B) RX and side chains involving more attractive interactions with the protein backbone.

One general idea to restrict the internal motion is to introduce bulky substituents (Figure 4.2 (A)) to the structure, such as methyl groups or aromatic rings. The substituent can be introduced to the 4-carbon position of the nitroxide ring (HO-2101, etc.), or to replace one of the methyl

groups (HO-2242) on the ring, or to the α-carbon position of the side chain (HO-1972, etc.). This strategy has been shown to effectively restrict the rotation around terminal bonds *via* the steric interaction between the substituent and the disulfide bond, and thus to limit the internal motion of side chains (see R1b (PDB code 1ZWN), R7[16], R1p[17] in previous publications). Even though the hydrophobicity of the bulky substituents may cast a shadow on whether the introduction of such side chains would perturb the native structure of the protein, the fact that they are generally smaller and polar than most widely used fluorescent labels has consolidated the applicability of these derivatives in biological studies.

Another strategy is to enable more attractive interaction within the side chain structure to restrain its mobility. Successfully applied in many studies, particularly ones involving distance measurements with dipolar spectroscopy, the side chain designed V1[18] (Figure 4.2 (B)) that has a shorter linker and an imidazoline nitroxide has been considered as a more rigid probe than R1. Its highly restricted motion is the result of its fewer freely rotating bonds (4 rather than 5) and its unique intra-side chain interaction $N\cdots S_{\gamma}$, which both minimize the relative movement between the nitroxide and the disulfide. To achieve comparable internal rigidity, the reagent HO-4025 was also designed, of which the geometry should allow a similar $N\cdots S_{\delta}$ interaction.

While there have been many monofunctional R1 derivatives proven useful and utilized successfully, HO-1944, a bifunctional nitroxide reagent that cross-links pairs of geometrically fit cysteine residues in α-helices and β-sheets, has been widely accepted as the reference of spin label rigidity in recent years[19]. With a second covalent bond attaching it to protein, the side chain designated RX has shown to be nearly immobilized on the ns time scale, and to adopt a single rotamer on the helix surface site. Although likely, the formation of the cross-link would potentially modify the local structure and conformational equilibria, such strong ordering and

localization make RX an unmatched candidate in distance measurements and slow (μs-ms) motion detection. One aim of this dissertation is to obtain a further characterization of RX in the μs-ms time scale, which will be shown in detail in the next chapter.

Over years, several R1 derivatives have been carefully examined by X-ray crystallography, CW-EPR, and pulsed EPR techniques. Their general properties and applications will be described in the following section 4.3 and discussed in other chapters. In the results that will be presented firstly in this dissertation, some labels have been further examined to complement and extend established knowledge, and some new disulfide-linked spin labels have been characterized to satisfy corresponding applications.

4.2.2 Thioether-linked spin label side chains

In addition to the advantages of disulfide-linked side chains, they have some features that could cause issues in certain experiments. Thiosulfonates are essentially reversible thiol reagents, which could be a rather convenient feature for some experiment designs. However, the fact that the reactive disulfide is susceptible to reducing agents leads to sometimes spontaneous cleavage in aqueous solution for some labels, such as V1, thus introducing additional perturbance in spectral analysis and leading to limitations to its applicable environments.

Over the development of spin labels, there have been other kinds that also react with cysteines but utilize different chemistry to form different linkages. Among them, the two most used traditional nitroxide labels are iodoacetamide-functionalized derivatives and maleimide-functionalized derivatives (Figure 4.3). Both reagents would react with thiols in an irreversible manner and form a product with a more stable and permanent thioether linkage that is not cleavable by the usual reducing reagents.

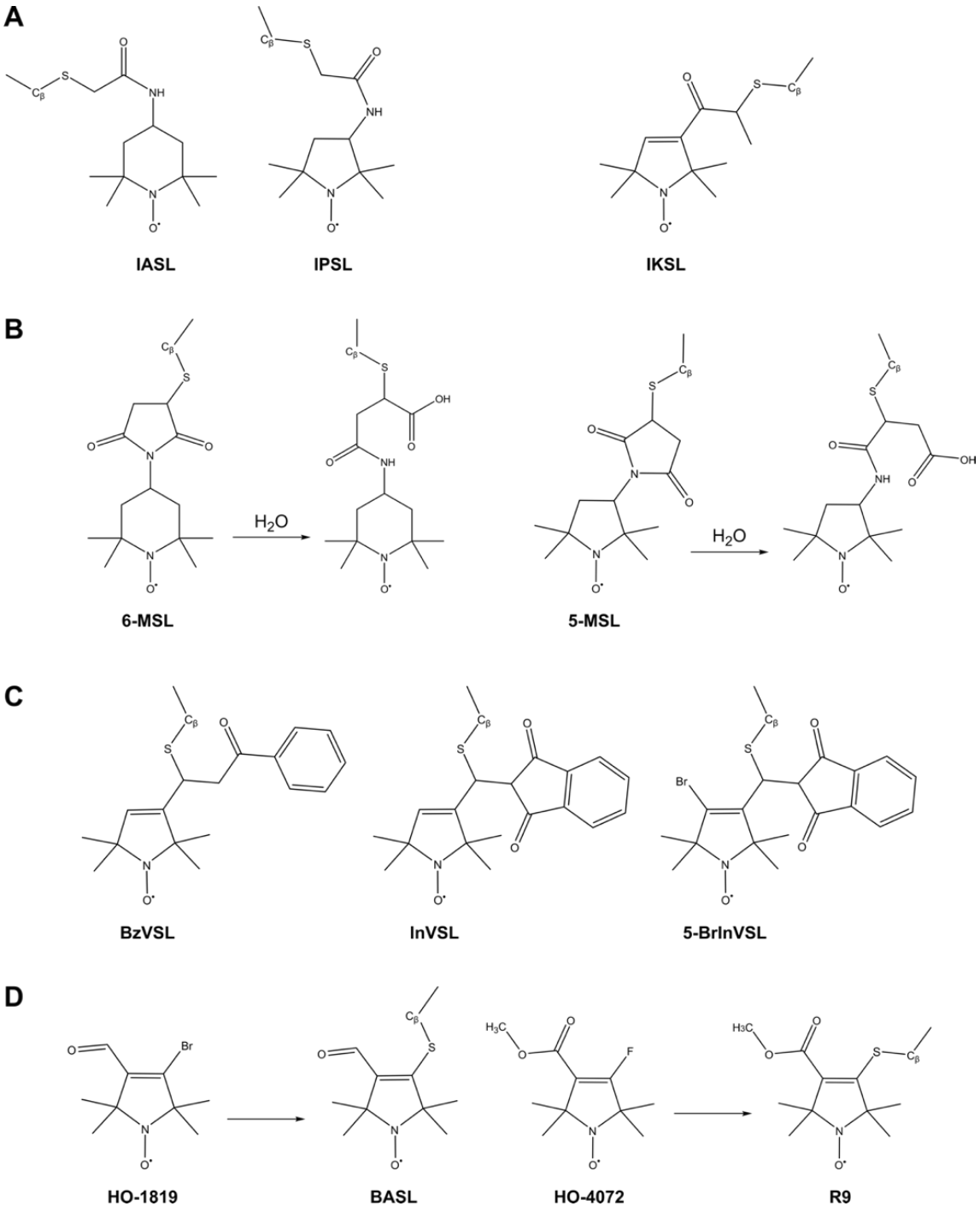

Figure 4.3 Thioether-linked nitroxide spin labels. Each unique spin label side chain is designated as indicated. (A) Spin label side chains that are generated *via* sulfhydryl-iodoacetamide reaction; (B) Spin label side chains that are generated *via* sulfhydryl-maleimide reaction, and their irreversibly hydrolyzed products; (C) Spin label side chains that are generated *via* reaction between the sulfhydryl groups with β-substituted vinyl aryl ketone reagents; (D) Spin

label side chains with shorter linkage that are generated *via* a bromoacrylaldehyde reagent or a fluoro reagent HO-4072.

Reacting with nucleophiles *via* an S_N2 reaction mechanism, iodoacetamide nitroxide spin label (Figure 4.3(A)) is usually found as a piperidine (IASL[20]) or pyrrolidine (IPSL[21]) iodoacetamide and has been used extensively in early works with spin-label methods[22]. However, its applicability suffers slightly from the fact that the reaction conditions can be relatively harsh (>10-fold excess, several hours) for the aim protein. Moreover, while these reagents are usually most reactive with thiol groups, both ε-amino groups in Lys and thioether groups in Met could be partially modified under conditions of many folds' excesses, leading to a variety of labeled residues. Based on studies using iodoacetamide nitroxide spin labels, the iodoketo spin label (IKSL[23]) was designed in order to achieve a higher reactivity and more restricted internal motion, making it more appropriate for slow motion detection.

Due to the limitation of iodoacetamide/iodoketo labels, over many years, the maleimide piperidine (or pyrrolidine) nitroxide (MSL[20]) was rather the more popular choice of spin labels and employed in over half of all spin-label studies. The basis of many methodologies has been developed with a model system utilizing the maleimide spin label, such as the saturation transfer EPR (ST-EPR) technique[22,24,25]. Through the Michael addition, it has been shown that maleimide derivatives are highly specific for thiols between pH 6.5 and 7.5, while the major competing groups, ε-amino groups in Lys, react 1000 times slower than at pH<7.5.

However, there are also drawbacks[26] for maleimide spin labels. While its specificity to cysteines is essentially dependent on the pH value, the pK_a of thiol groups under various local environments can shift dramatically from one to another. Moreover, although the thioether linkage from Michael addition is usually considered stable, the thiosuccinimide product is rather

hydrolytically unstable and susceptible to slow thiol exchange *via* a retro-Michael reaction which ends up releasing the spin label side chain. The addition of thiol to the maleimide will introduce a new chiral center to the side chain, leaving potentially a mixture of two epimers. Upon irreversible hydrolysis, a chemically stable succinamide acid form of the side chain will be generated (Figure 4.3(B)), further complicating the composition of EPR signaling species.

While maleimide labels were proven useful for detecting motions in the wide time range from ps to ms, there have always been efforts to design new spin labels with higher reactivity and less mobility. As well as utilizing the Michael addition reaction, several β-substituted vinyl aryl ketone derivatives[21,27–30] (Figure 4.3(C)) were found to be highly sulfhydryl-reactive due to the strong electron withdrawing groups in their structures, and strongly immobilized relative to the protein molecule benefiting from the steric bulk of those aryl groups. Among them, an indane dione nitroxide spin label (InVSL) has been reported as sufficiently immobilized and generally applicable for ST-EPR measurements in many systems, such as Na^+/K^+-ATPase[29], Ca^{2+}-ATPase[31], rhodopsin[32], myosin[21], etc.

As compared to MTS derivative reagents, both MSL and InVSL are sterically more demanding, leading to not only an impediment of their reactivity but also the concern of whether their introduction to the structure will perturb the conformational equilibria of protein. In recent years, new reagents to generate thioether-linked spin label side chains with smaller sizes and polar structures have emerged (Figure 4.3(D)), such as the bromoacrylaldehyde spin label (BASL[33]). BASL was found to be selective for surface residues, suggesting a potential application for samples with multiple buried cysteines. While its short thioether linkage with only three bonds is likely to minimize possible structural perturbance, the presence of the reactive aldehyde group in its structure could instead lead to unfavored bonding or extra

modification, depending on specific chemical conditions. In chapter 7 of this dissertation, a similar but improved fluoro spin label reagent (HO-4072) that has been fully characterized to show several advantages in distance measurement and motion detection will be discussed carefully.

In conclusion, with a long history of being used as the EPR probe, both the advantages and disadvantages of thioether-linked spin labels are obvious. While its linkage is more permanent and less susceptible to reduction, its chemistry can be less specific and complicated under conditions. As the alternative to disulfide-linked spin labels which are also generally commercially available, they are still playing unique and important roles in SDSL-EPR related studies.

4.2.3 Non-cysteine targeted spin labels

Only proteins carrying native or mutated cysteines will be used in this dissertation. However, there have constantly been developments of SDSL techniques to expand its application for all kinds of biological systems, including peptides[34], lipids[35], nucleotides[36], etc.

Even for proteins, although cysteines are usually preferred as the targeting residues due to their facile reactivity and the more scarcely distributed abundance among natural amino acids, labeling strategies based on targeting different residues would undoubtedly allow enhanced versatility concerning the incorporation of spin labels. Disulfide bonds are widely found inside proteins and have been proven necessary for maintaining the function and stability of some proteins in many cases. Due to the great flexibility of R1 that enables labeling to even fully buried sites, it is inevitable to eliminate any undesired native cysteines through mutagenesis, which could lead to unpredicted change or loss of protein functions. Moreover, accompanied by

an increasing interest in distance measurement using EPR techniques, as well as other needs of introducing distinguishably different probes to multiple targeting sites, a variety of reagents that react with non-cysteine targets have been designed and characterized.

Nitroxide spin labels with the hydroxysuccinimide functional group (Figure 4.4 (A)) were designed for targeting lysine residues, which offers an alternative way to introduce spin labels on protein. However, since lysines are typically much more abundant than cysteines, the specificity of labeling is likely to be sacrificed with the utilization of these labels, thus making this strategy less favorable. Reagents with designed linkers that can site-specific attach the spin label to other natural amino acids are also available, including serine[37], arginine[38], tyrosine[39], etc.

Among all strategies, one way that can truly achieve a bio-orthogonal reactivity to all natural amino acids is the use of unnatural amino acid (UAA) spin labels (Figure 4.4 (B)). In response to the nonsense amber codon, genetically encoded unnatural amino acid can be site-specifically incorporated into recombinant proteins expressed in Escherichia coli[40], Saccharomyces cerevisiae[41], and mammalian cells[42], which theoretically makes SDSL methodology amenable to any protein regardless of the sequence.

Via the reaction between p-acetyl-L-phenylalanine (p-AcF) and a hydroxylamine nitroxide reagent, the nitroxide side chain K1[43] can be generated under a relatively harsh condition (at pH 4, 37℃ for several hours). Instead, the reaction between p-azido-L-phenylalanine (p-AzF) and a cyclo-octyne nitroxide reagent can generate a triazole-linked nitroxide side chain T1[5,44] under pH neutral environment, as an application of copper-free click chemistry techniques. Although a sophisticated characterization of all the fundamental properties of K1 was published, further exploration and development are still needed to fully uncover the potential of using UAA methodology with SDSL-EPR.

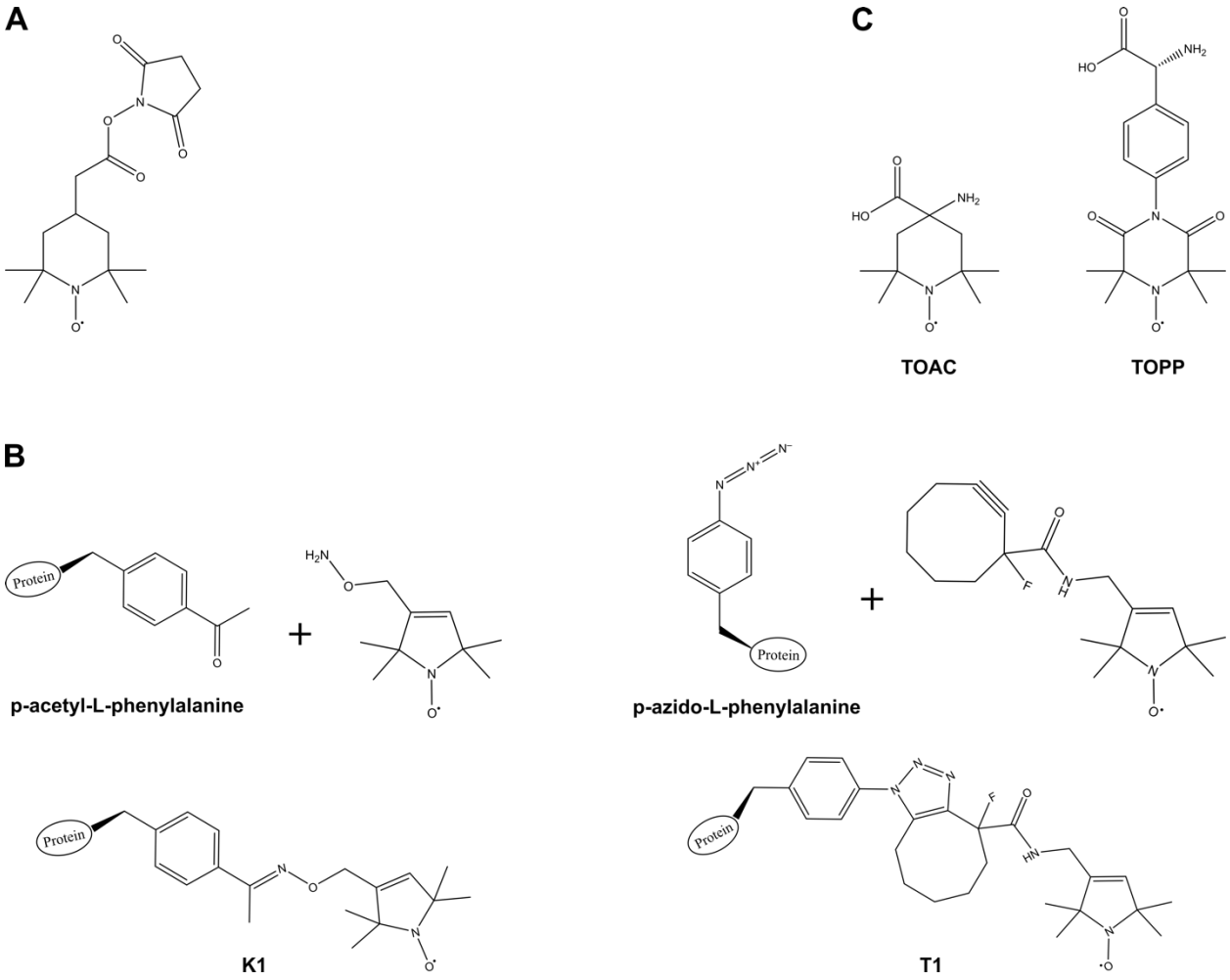

Figure 4.4 Non-cysteine targeted spin label reagents and side chains. Each unique spin label side chain is designated as indicated. (A) Hydroxysuccinimide nitroxide reagent; (B) Unnatural amino acid spin label reagents, and corresponding side chains K1 and T1; (C) TOAC and TOPP side chains.

Last but not least, benefiting from the application of solid-phase synthesis in the chemical biology area, non-native amino acid spin labels that can be directly incorporated into peptides have also been developed (Figure 4.4 (C)), such as 2,2,6,6-tetramethyl-piperidine-1-oxyl-4-amino-4-carboxylic acid (TOAC[45]) or its pyrrolidine derivative (POAC[46]). The fixed position of such a side chain in the peptide backbone makes it unique for slow motion detection and measurement of orientations. However, the relatively poor yield of peptide coupling reaction has thus limited its usage to only small peptides and proteins in which the side chain can be

incorporated *via* total synthesis instead. Moreover, the incorporation of such a sterically hindered structure leads to a very limited range of dihedral angles, thus introducing a significant backbone distortion to which the side chain attaches. Though other structures allowing greater flexibility are designed to overcome this problem, such as the TOPP[47], in general, it is still practically difficult for these labels to be widely applied in biological systems.

4.3 Internal structure and dynamics of nitroxide spin labels and applications of SDSL

As discussed in previous publications and this dissertation, there are three major contributors (their motions and chemical properties) to consider when analyzing results (of either the dynamics or structures) obtained using SDSL-EPR: the macromolecule as a whole (protein molecules in this dissertation), the local structure to which the probe is tethered (e.g., an α-helix or β-sheet), and the spin label side chain itself. While the nature of the systems studied dictates what characteristics or behaviors should be expected, the capacity and applicability of each specific SDSL-EPR technique are largely influenced by the choice of spin labels. In this section, the already established fundamental structural and dynamic properties of R1 and other derivative spin labels will be reviewed, and appropriate experimental applications based on the properties of various labels will be discussed.

4.3.1 Crystal structures of disulfide-linked spin labels

For the broad library of spin labels used in SDSL-EPR, there are three different types of the parent nitroxide ring structures: six-membered rings (piperidines[48]), five-membered rings (pyrrolidines, pyrrolines[49–51], and imidazolines[52]), and fused aromatic rings (isoindolines[53,54]).

From a chemical synthesis perspective, the piperidine nitroxide that can be easily derivatized and further functionalized makes it a versatile and accessible candidate. However, the fact that this hexagonal ring structure is sensitive to chemically reducing conditions[55,56] and it is internally less rigid than 5-membered pyrrole rings have made it an economic but less favored choice for protein studies.

While isoindoline and imidazoline spin labels have their own unique benefits in protein labeling studies, such as utility as fluorescence-enhanced or pH-sensitive probes, currently pyrroline nitroxides are the most widely used type of spin labels, largely due to the ubiquitous popularity of R1. The planarity of the pyrroline ring provides both adequate structural rigidity of the label and minimal perturbation of protein structures. In this dissertation, only pyrroline nitroxides are discussed.

4.3.1.1 Preferred rotamers and the χ_4/χ_5 model of R1

The atomic-level structures of several pyrroline nitroxide compounds have been determined by X-ray crystallography[57], confirming the planarity of the ring structure at 100 K. Measurements from these structures give an average N-O bond length (~1.28 Å) that is consistent with a three-electron bond structure[58], suggesting the predominant localization of the unpaired electron to the N-O bond as well as the likelihood of structural resonance.

When attached to macromolecules, in most cases the planarity and the structural anisotropy of the nitroxide are retained. However, a different configuration may be adopted depending on both internal flexibility and interactions with nearby moieties. Note that the EPR spectral lineshape encodes structural and dynamic information not only on the backbone to which the label is introduced and neighboring residues, but also on the tertiary structure in the vicinity of

the nitroxide. To truly understand and interpret the behavior of spin label side chains on protein molecules, atomic-resolution structural information is needed. From this, one can identify and characterize the populated side chain rotamer(s), and the nearest-neighbor interactions that are responsible for stabilizing such configuration(s).

Efforts have been made to establish the structural basis for understanding spin-label motions by obtaining high-resolution crystallographic data. A number of different structures[16,43,59] have been collected from studies of R1 introduced to non-interacting solvent-exposed surface sites on helices and loops. Considering all five bonds comprising the disulfide linkage between the protein and the spin label, in theory, segmental motion by rotational isomerism about the single bond can occur for four of the five, where the disulfide bond itself is excluded as it is known to have a relatively high rotational energy barrier and thus slow isomerization on the CW-EPR time scale[14,60].

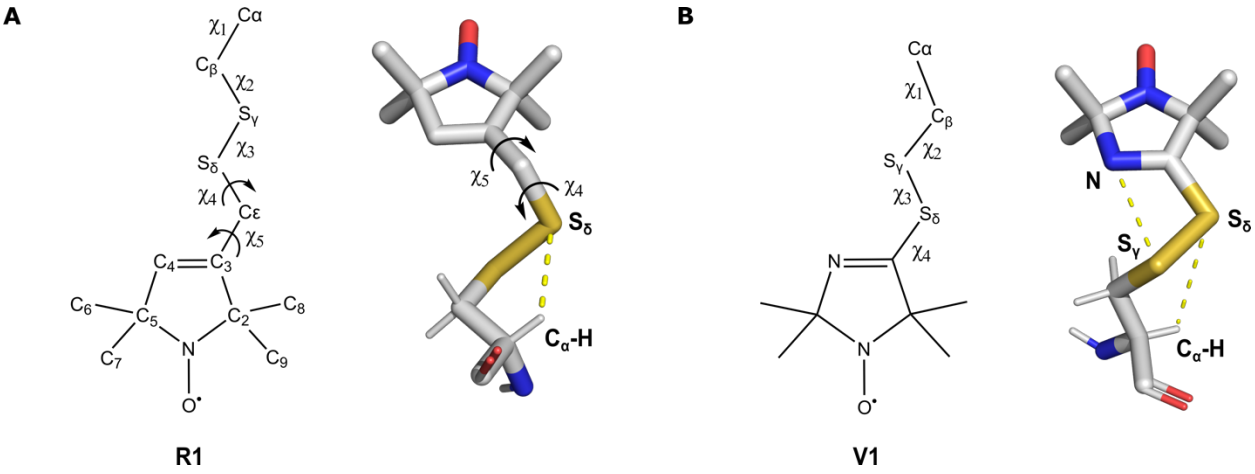

Figure 4.5 (A) The R1 side chain with designations of atoms and dihedral angles used in the text, and the molecular model (from PDB code 2CUU). The C_α-H···S_δ interaction that restricts the motion of the disulfide linkage is shown. (B) The V1 side chain with designations of atoms and dihedral angles that are used in the text, and the molecular model (from PDB code 3K2R). The C_α-H···S_δ interaction, and the N···S_γ interaction are shown.

However, it has been shown[16,43,59] that at surface sites on T4 lysozyme and other proteins,

including a membrane protein, there exists a ubiquitous intra-residue hydrogen-bonding interaction between the S_δ and C_α-H (Figure 4.5 (A)). The same interaction between the disulfide sulfur and the backbone has also been identified for RX[19], R1b[61], R7[16], and V1[18] side chains from their crystal structures, serving as an effective restrictor to rotational motion about the first two bonds of the linkage.

The existence of this interaction defines a limited rotamer library for disulfide-linked spin label side chains on helical sites. Among the various R1-labeled protein structures determined to date, the $\{\chi_1, \chi_2\}$ set of rotamers is predominantly populated by only three permutations, namely the {m, m}, {t, m}, and {t, p} dihedral combinations (nominal values[62] of t, p, m are ±180°, +60° and -60°, respectively, but variations of ±20° are commonly observed in experiments), in that order of frequency. Combined with the restriction in χ_3 (which usually only adopts +90° or -90°) due to the barrier to rotation of disulfide bonds, all give rise to an anisotropic motion on the ns time scale described by torsional oscillations about the χ_4/χ_5 dihedral angles only; this is known as the 'χ_4/χ_5 model'[7].

The χ_4/χ_5 model was originally proposed based on lineshape simulation and mutational analysis for EPR measurements of T4 lysozyme using R1 derivatives with various 4-substituents and a different parent ring structure (the pyrrolidine). X-ray diffraction results[15,16,59,61,63,64] indicated that the electron density was only well-resolved for the atom group C_α-C_β-S_γ-S_δ of R1 side chains, supporting the conclusions of the χ_4/χ_5 model. While χ_1, χ_2, and χ_3 have restricted motions, the behavior of disulfide-linked spin labels is essentially determined by the terminal S_δ-C_ε-C_3 single bonds, the nitroxide ring, and any accessible interactions. This is further supported by the effectiveness of introducing bulky substituents or moieties favoring further interaction with the peptide backbone to constrain the internal motion of the whole side chain.

However, regardless of the importance of crystal structures, it should be noted that the nitroxide side chain might adopt another configuration or exhibit complex dynamics in ambient/physiological conditions (aqueous solution, non-cryogenic temperatures). As previously discussed, the protein crystallization process preferentially selects the most energetically favored conformational structure in the crystal environment, which is a static description of protein conformational equilibrium without contributions from dynamics. Moreover, both the cryogenic temperatures typically used for X-ray diffraction and the extremely dehydrating conditions required for protein crystallization could both severely modulate the rotameric equilibria, possibly introducing new steric contacts between the nitroxide and symmetry-related molecules in the crystal lattice, which could lead to conformational deviations between crystal and solution structures.

In the crystal structure of T4L115R1[16] measured at 100K, only the {m, m} rotamer is observed, while two spectral components by CW-EPR suggest two populations of R1-rotamers at room temperature. Another crystal structure was obtained at 298K, a rare and difficult feat, revealing the coexistence of two rotamers: {m, m} and {t, m}, an observation consistent with the CW-EPR spectral lineshape. Therefore, spectroscopic measurements and computational approaches are still needed, serving a complementary role to crystal structures, to fully understand the structure-function paradigm of spin-label side chains, which will be further discussed below.

4.3.1.2 Structural modeling and rotamer libraries

With a growing number of applications for DEER and other SDSL-EPR methods, predicting the conformational state of a spin label introduced at a target site in a protein is of considerable

interest. Many efforts have been made to properly correlate the internal flexibility of spin labels to the interpretation of distance measurements. The fact that electron densities of terminal nitroxide atoms have yet to be resolved in the crystal structures obtained for R1 at non-interacting helical sites makes it problematic to model the conformational distribution of the label itself and to translate the inter-spin distances obtained in DEER, for example, into structural constraints of macromolecules. On the other hand, for situations where the spin label experiences highly restricted internal motion, such as for R1 on buried sites or rigid spin labels, such as R1f, V1, and RX, nearly all atoms after the C_α-C_β-S_γ-S_δ can be resolved.

For the double mutant T4L65V1/76V1[18], a unique intra-side chain interaction N$\cdots$$S_\gamma$ was identified that effectively eliminates the internal motion of the side chain by restricting χ_4 (Figure 4.5 (B)). In another 6 structures[65] of V1-labeled T4L, χ_4 was found to be 0°±20°, suggesting that this internal strain is independent of attached sites. This fact makes V1 a good candidate for distance measurements, as the location of the nitroxide can be better predicted when χ_4 is so limited.

In the case of T4L115RX119, a high-resolution crystal structure (1.0 Å) was obtained[66], showing *via* electron density of the nitroxide ring a bent, rather than planar, nitroxide ring. This finding is important for quantum-chemical calculation and simulation analysis, for which the accurate orientations of the electron g-tensors and A-tensors with respect to the molecule are needed. Still, more crystal structures of RX are needed to explore how much the potential distortion/perturbation of the protein might be induced by this side chain.

Besides the continuing efforts on designing new probes and obtaining structures of higher resolution, results obtained *via* computational methods also play an important role in understanding and thus predicting spin label behaviors. Density functional theory calculations[14]

have been employed to estimate a detailed energy profile of a spin-labeled protein structure, with particular emphasis placed on the rotameric interactions with the surroundings, including both the protein backbone and solvent molecules. At reasonable computational cost, the relative gas phase energies of these rotamers in a defined structural element (e.g., a single amino acid or a ten residue α-helix) can be computed, revealing the structural determinants of stability for each.

In the initial design of DEER experiments, often preparing a representation of possible spin label rotamers on the target protein structure is sufficient, which will be followed by the comparison with acquired DEER data. Based on our fundamental knowledge of rotamer populations as identified by crystallography, rotamer libraries have been constructed and used in molecular modeling toolboxes such as MMM[67,68] (Multiscale Modeling of Macromolecules) *via* molecular dynamics (MD) simulation.

Using the information presented above, potential perturbation of native protein structure induced by mutation and spin labeling at particular sites can be visualized, examined, and modulated ahead of time, while possible experimental difficulties can be avoided. For example, particular molecules may be hard to crystallize, or transient structural states may not be stable and thus might not be amenable to structural characterization. Along with the continued advancement of computational methods in recent years, it can be expected that simulation and computation will play increasingly important roles in SDSL-EPR research in the future.

4.3.2 Detection of dynamics using R1 and its derivatives

As explained above, the anisotropic motion of the spin label side chain preferentially averages the magnetic tensor parameters of the nitroxide, such that the EPR spectral lineshapes are sensitive to modulation by the motions of the protein and local interactions with the protein.

The relaxation pathway also serves as another principal basis for evaluating the applicability and sensitivity of SDSL-EPR techniques methods in protein science. The intrinsic T_1 and T_2 of a sample define the time domain of detectable dynamics, while their apparent values can be analyzed to resolve the changes in dynamics, structure, or polarity at a spin-labeled site. Applications for the detection of motion will be introduced in this and the next sections.

4.3.2.1 Determining backbone flexibility and scanning local secondary structure

The conventional X-band CW-EPR lineshape is exquisitely sensitive to motions occurring in the time domain of τ_R = 0.1 ns-100 ns, which can directly contribute to T_2 relaxation broadening and anisotropic averaging for nitroxide spin labels (Chapter 3). While the relative spectral impacts from hyperfine and the g-anisotropies are dependent on the microwave frequency, the time window for motional sensitivity of the lineshape can also be adjusted to some extent by acquiring EPR spectra at different frequencies. In this dissertation, X-band EPR is mostly reported.

Benefiting from high sample sensitivity at relatively low concentrations and the capacity to acquire data under multiple environments, SDSL-EPR is suitable for monitoring the response to changes in various conditions, including pH, temperature, viscosity, chemical denaturation, light, and pressure. Through rigorous lineshape analysis, quantitative information about the rate and angular amplitude (order) of nitroxide motion can be obtained.

As aforementioned, the lineshape encodes three major contributions in this time scale: the Brownian rotational diffusion of the protein molecule, local backbone fluctuations, and internal motion of the spin label side chain. In sample preparation or spectral analysis, if one can eliminate or isolate the motional contributions of protein tumbling and side chain rotation, it

becomes possible to extract information on protein dynamics.

In the time scale of X-band CW-EPR, for membrane proteins and soluble proteins with molecular weights greater than ~50 kDa, the contribution from protein rotational diffusion is negligible. For small soluble proteins, rotational diffusion can be minimized by either increasing the effective viscosity of the solution or attaching the protein to solid supports, such as the affinity resin. Lopez et al.[69] carefully examined and characterized the effects on EPR measurements brought by using a viscogen (sucrose and Ficoll 70) or by immobilizing the protein molecules to stationary phase[70], proving that both methods are sufficient in practice for restricting the rotational diffusion of protein.

As previously introduced, considerable effort has been put forth in recent years to characterize the internal motions of the nitroxide side chain, such that now the internal motion of the R1 side chain on non-interacting solvent-exposed sites is well understood. To summarize what is known, for sites where there is no additional tertiary interaction imposed on the R1 side chain, through lineshape analysis (spectral simulation, or qualitative parameters, etc.) based on the χ_4/χ_5 model, variations in order parameter (S) and correlation time (τ) are assumed to reflect contributions from local backbone fluctuations of each site[71].

The validity of such analysis has been supported by studies of multiple proteins. Comparing EPR data to a result measured by NMR ^{15}N relaxation experiments[72], Columbus et al.[73] studied the site-dependent variation by introducing the R1 side chains along the basic leucine zipper (bZip) motif of the yeast transcription factor GCN4. A linear gradient of backbone motions on the nanosecond to picosecond time scale was identified *via* CW-EPR spectral analysis, which mirrors the result observed by NMR measurements. A more complete work was reported by Lopez et al.[74] where R1 side chains were placed at 39 solvent-exposed sites of sperm whale

myoglobin and the sequence-dependent mobility of each was analyzed. With a large series of spectra that exhibited a broad range of R1 mobility, data presented in this study support the interpretation that differences in both rate and amplitude of motion of R1 at non-interacting surface sites indeed reflect relative differences in the backbone fluctuations on the ps-ns time scale.

For sites potentially involving interaction between the nitroxide and neighboring atoms, the sensitivity of nitroxide side chains to the surrounding environment provides a way to probe the local secondary and tertiary fold using SDSL-EPR. In a properly folded protein, the mobility of the spin label side chain located at completely buried sites or partially hindered sites is expected to be highly restricted due to steric repulsion and hydrophobic packing with nearby groups, while at surface or loop sites the side chain is more flexible exhibiting shorter correlation times and/or smaller amplitudes. Such variation can be directly inferred from their spectral lineshapes.

By sequential replacement of native side chains with a single spin label along segments with well-defined secondary structure (i.e., α-helices and β-sheets), a periodic pattern of rate and order with respect to sequence position is observed *via* lineshape analysis. The efficacy of this 'nitroxide scanning' method was demonstrated in studies done in T4L by Mchaourab et al.[4], and in cellular retinol-binding protein by Lietzow et al.[75] *Via* a semi-quantitative measure of mobility (the central linewidth of CW-EPR spectra) in α-helices R1 reports periods of mobility of ~3.6, while the periodicity for β-sheets is 2, clearly indicating that the regularity of R1 mobility with sequence position can serve as an effective way to identify topographically different structural elements of proteins. Besides the central linewidth, the second moment of the complete absorption lineshape can also be used as a valid parameter. Although it should be noted that for more complicated spectra with multiple components and/or strongly anisotropic motions, it is

necessary to perform further analysis other than measurement of semi-quantitative parameters to obtain accurate mobility information, e.g., spectral lineshape simulation.

Although our fundamental understanding of several R1 derivatives on non-interacting solvent-exposed helical sites has been established from studies that involve crystal structures and lineshape analysis of CW-EPR spectra, they have not yet been applied in a large number of systems. These R1 derivatives include the 4-substituent-modified side chains: R1b, R7, R1p, the cross-linking side chain RX, and the imidazoline side chain V1. As compared to R1, the functional uniqueness of each structure reveals that these side chains can detect and report dynamics and interactions in different fashions than R1 itself. Moreover, it is also evident that the potential for introducing structural perturbation in proteins varies widely for these side chains, e.g., RX which has a second covalent bond with the protein may be more perturbative than R1, R1b, or R1f.

As mentioned above, most of these labels are designed to have less internal mobility and exhibit fewer rotamers, especially in the ps-ns time range, which fundamentally simplifies dynamics analysis of EPR spectra by eliminating the motional contribution from the side chain itself, and therefore revealing more details about local interactions and protein backbone dynamics. However, the pronounced immobility leads to lower sensitivity (compared to R1) to nanosecond backbone fluctuations of relatively small angular amplitude. Crystal structures of R1f, V1, and RX all confirm that there is only a single rotamer populated on α-helical sites. With minimized motional averaging, the magnetic anisotropies are better resolved in their spectra, suggesting that an ideal application of these labels will be monitoring slower motions that involve larger angular movements. More studies are still needed in order to accumulate an adequate knowledge basis of these labels such that their potential can be fully revealed.

4.3.2.2 Identification of conformational exchange

Regardless of its incomparable sensitivity to motions in the ps-ns time domain, there are several bottleneck difficulties when using the conventional CW-EPR method to detect dynamics beyond its rigid limit (>100ns with nitroxide spin labels). However, due to the great significance of the sub-millisecond time domain in which many functionally important biological processes occur, efforts have been made to extend the applicability of conventional CW-EPR methods to this time range in order to benefit from its technical simplicity and equipment accessibility.

The theoretical basis of using conventional CW-EPR lineshapes for slow motion detection is: 1. The insensitivity of anisotropic averaging and linewidth broadening that is dependent on the T_2 relaxation (for nitroxide spin labels, usually T_2 = 15-30 ns) to slow exchange between conformational substates, of which the lifetime is usually >100 ns; 2. The sensitivity of nitroxide to distinct interactions with the local environments in each substate. As a result, spectra often consist of two (or more) separately resolved components that may arise from the two (or more) substates in slow exchange[76].

Approaches are designed to overcome the two major obstacles of this method: first, as mentioned, the CW-EPR spectrum encodes contributions from other fast motions, which will lead to linewidth broadening and thus dominating the spectral lineshapes. To uncover the hidden influence of slow dynamics, stationary-phase SDSL-EPR strategies or the use of viscogen are required for small proteins. Moreover, evidence from X-crystallography structures has shown that complex spectra with multiple components can also arise from the existence of multiple rotamers of the spin label side chain at a given site, which requires additional experimental strategies to distinguish the conformational equilibria from rotameric equilibria.

Lopez et al.[69] examined the method of using osmolyte perturbation to identify the origin of multiple components. Due to the difference in solvent-accessible surface area between various conformational substates, it is expected to observe apparent lineshape changes that reflect the response of the system to solvent perturbation with stabilizing osmolytes such as sucrose. On the contrary, there is no significant variation in solvent-accessible surface area between molecules with different side chain rotamers, therefore no significant lineshape change should be detected. Similarly, the method of using hydrostatic pressure[77] to probe conformational substates has also been developed, which is based on the different responses to high pressure between conformations of different hydrophobic molecular volumes.

As introduced in previous chapters, few spectroscopic techniques can offer dynamic information about biological systems in the time domain of μs-ms. While the versatility of applicable systems (such as membrane proteins) makes SDSL-EPR a particularly attractive tool, the limitation of conventional CW-EPR makes it fundamentally inappropriate for this timescale. Although the simplicity of the perturbation method makes it suitable for facile screening of proteins to reveal possible conformational substates, it evaluates slow protein dynamics in a rather indirect way and is still largely hindered by its sensitivity to fast (ps-ns) motions. However, neither the effectiveness of stationary-phase strategies nor known spin labels with restricted motions have yet been truly examined in the time domain of μs-ms.

In recent years, methods using pulsed-EPR techniques, such as electron-electron double resonance (ELDOR[19]) and saturation recovery EPR (SR-EPR[78]), have been described to measure μs-ms rotational diffusion. Essentially, both methods are designed to probe and evaluate changes dependent on the T_1 relaxation (1-10 μs with nitroxide spin labels) which can be modulated by slow conformational dynamics. By using the highly constrained cross-linked side chain, RX, in

the pulsed ELDOR experiment, Fleissner et al. were able to observe slow motions involving helix B of T4L and give a characteristic correlation time $\tau_R \sim 6$ μs, which preliminarily showed the effectiveness of RX as a sensor for slow motion detection. This will be further explored and results will be shown in this dissertation.

Nevertheless, not to mention the high hardware requirement for setting up pulse experiments, the sensitivity to the motions of these approaches is limited to a rather narrow window. In order to truly expand the time scale over which SDSL-EPR can be used, approaches based on another continuous-wave methodology, the ST-EPR, will be carefully examined in this dissertation. Detailed discussions will be found in the following chapters.

4.3.3 Mapping protein topography and the application of paramagnetic species

While the capacity for dynamics detection is one of the most important advantages of SDSL-EPR, it can offer other information about protein three-dimensional structure. Due to the collisions occurring *via* Heisenberg exchange, the intrinsic relaxation of nitroxide can be modulated by the second paramagnetic species in the environment, which can be a second, bound nitroxide spin label or transition metal molecules, or O_2 dissolved in solution, thus making the EPR spectra of spin-labeled proteins sensitive to their presence. This mechanism is concentration-dependent and distance-dependent, enabling a method of using SDSL-EPR to determine such properties of the system.

Since the relaxation (T_1 and T_2) and spectral anisotropy (dominated by the nitroxide hyperfine splitting in X-band and Q-band) are determinants for measurable EPR response, methods are developed accordingly to exploit the relation between these properties and elements from targeted systems. As the main focus of this dissertation is on dynamic detection, the

detailed introduction and discussion will not be included, which can be found in other references.

As introduced in previous chapters, the dipolar structure in which the unpaired electron located on the nitrogen atom of nitroxide spin labels is favored by polar environments, so that the hyperfine splitting value of EPR spectra can be directly used as a semi-quantitative parameter to evaluate the polarity of environments. It is widely known that the folded globular proteins usually have a well-packed hydrophobic core, therefore, a change in polarity can be used to monitor the global/local unfolding process. When the nitroxide is placed in a rather hydrophobic environment compared to solvent-exposed locations, the apparent hyperfine splitting is decreased, which could indicate that the spin label side chain is buried inside the protein or an interior cavity. This parameter has also been extensively used in studies involving phospholipid bilayers to report a gradient of polarity[79,80].

It needs to be aware that the intrinsic properties, particularly the chemical structure, of spin labels bring in unignorable effects to the value of hyperfine splitting, such as the intramolecular resonance which will influence the electron density distribution. Hence, a comparison between results obtained by different labels has to be carefully examined before being utilized in practical analysis.

With more versatile approaches to acquisition, solvent accessibility is also a valuable parameter that can be determined in EPR experiments, which is directly related to the Heisenberg exchange process. The measurement of solvent accessibility can reveal important topographical and structural information, such as the immersion depth of local structural elements in the membrane. The periodic accessibility can also be used as the reporting parameter for nitroxide scanning experiments to distinguish secondary structural elements[81].

Collisions between the nitroxide and the second fast-relaxing paramagnetic species will

result in a decrease in both values of T_1 and T_2, particularly the T_1, therefore providing the feasibility of using methods that directly measure T_1 or parameters modulated by T_1 and T_2 relaxation to determine the solvent accessibility. The experimental strategies normally involve the addition of a fast-relaxing paramagnetic agent to the solution containing the nitroxide-labeled protein and measuring the corresponding effects. Such experiments are generally called relaxation enhancement SDSL-EPR, which can be implemented either directly by measuring changes in T_1 with pulsed SR-EPR, or by continuous-wave power saturation[82].

While the pulsed SR-EPR method[83] is rather straightforward, a brief elucidation of the latter method is presented here. As learned in chapter 3, the amplitude of absorption signals increases linearly with radiation power, i.e., the oscillatory field strength, until the thermal equilibrium distribution is perturbed, leading to a decrease in signal amplitude and eventually saturation. With the addition of fast-relaxing agents, a higher power is required to achieve the saturation of the signal, as the spin now recovers back at a faster rate (shorter T_1) to thermal equilibrium. By fitting the power dependence of the amplitude of whole spectra or the central line-height (the most intense feature), the parameter $P_{1/2}$, which is the power required to reduce the amplitude to one-half its value in the absence of saturation, can be obtained. The difference in the values of $P_{1/2}$ with or without the fast-relaxing agents serves as a metric of the accessibility of nitroxide spin labels to agents in solution, which is directly proportional to relaxant concentration.

Conventionally, O_2 and nickel-complexes (Ni (II) ethylene-diamine diacetate, NiEDDA, or Ni (II) bis(acetylacetonate), $Ni(acac)_2$, etc.) are ideal candidates as the relaxants in accessibility studies considering their water-solubility and neutral nature. As O_2 is smaller in molecular size and less polar than NiEDDA, both the interior of protein as well as phospholipid bilayers are accessible to O_2 but not NiEDDA. Some analysis methodologies are designed on the basis of

such variation in accessibility between relaxants, of which the ratio can be used to estimate immersion depth in the membrane[84], or to identify structural elements from the topological map depicted according to the distribution of accessibility[85–87].

An extension of the power saturation relaxation enhancement experiment is to determine the intermolecular distance at ambient temperatures between the nitroxide spin label and the added paramagnetic species, by making use of the distance dependence[88] of the relaxation enhancement. In order to measure long-range distances (20−60 Å) near physiological temperatures, both paramagnetic species with relaxation time on the nanosecond time scale (e.g., Cu^{2+}) and spin labels with long T_1 are needed. The binding of paramagnetic species is required[89–92] to correlate the inter-spin distance to structural information of proteins, which can be achieved *via* high affinity Cu^{2+} binding pentapeptide (-GGGHG-) inserted in computationally optimized loop sequences[12]. It is reported that with a TAM radical and bound Cu^{2+}, the upper limit of the accessible distance could be extended to ≈ 50 Å[11].

Regardless of the great potential of relaxation enhancement methods, nowadays, distance measurement using DEER is still the most popular strategy to obtain structural information with SDSL-EPR. Even though its applicability has been more or less limited by the fact that DEER experiments are required to be carried out at cryogenic temperatures (50−80 K), its incomparable ability to be able to measure long-range distances (20 Å to 80 Å and possibly 100 Å) and to provide probability distributions with high sensitivity in a variety of environments makes this technique an exceptional tool for exploring protein topography and structural heterogeneity. Huge numbers of reviews[93–99] can be found in the literature, with its fundamental theories introduced in chapter 3 and some actual results presented in the following chapters of this dissertation.

4.4 References

1. Commoner, B., Townsend, J. & Pake, G. E. Free Radicals in Biological Materials. *Nature* **174**, 689–691 (1954).
2. Burr, M. & Koshland, D. E. Use of 'reporter groups' in structure-function studies of proteins. *Proc. Natl. Acad. Sci.* **52**, 1017–1024 (1964).
3. Stone, T. J., Buckman, T., Nordio, P. L. & McConnell, H. M. Spin-labeled biomolecules. *Proc. Natl. Acad. Sci.* **54**, 1010–1017 (1965).
4. Mchaourab, H. S., Lietzow, M. A., Hideg, K. & Hubbell, W. L. Motion of Spin-Labeled Side Chains in T4 Lysozyme. Correlation with Protein Structure and Dynamics. *Biochemistry* **35**, 7692–7704 (1996).
5. Hubbell, W. L., López, C. J., Altenbach, C. & Yang, Z. Technological advances in site-directed spin labeling of proteins. *Curr. Opin. Struct. Biol.* **23**, 725–733 (2013).
6. Mchaourab, H. S., Kálai, T., Hideg, K. & Hubbell, W. L. Motion of Spin-Labeled Side Chains in T4 Lysozyme: Effect of Side Chain Structure. *Biochemistry* **38**, 2947–2955 (1999).
7. Columbus, L., Kálai, T., Jekö, J., Hideg, K. & Hubbell, W. L. Molecular Motion of Spin Labeled Side Chains in α-Helices: Analysis by Variation of Side Chain Structure. *Biochemistry* **40**, 3828–3846 (2001).
8. Getz, E. B., Xiao, M., Chakrabarty, T., Cooke, R. & Selvin, P. R. A Comparison between the Sulfhydryl Reductants Tris(2-carboxyethyl)phosphine and Dithiothreitol for Use in Protein Biochemistry. *Anal. Biochem.* **273**, 73–80 (1999).

9. Campbell, I. D. & Dwek, R. A. *Biological spectroscopy*. (Benjamin/Cummings Pub. Co, 1984).
10. Dupeyre, R.-M. & Rassa, A. Nitroxides. XIX. Norpseudopelletierine-N-oxyl, a New, Stable, Unhindered Free Radical. *J. Am. Chem. Soc.* **88**, 3180–3181 (1966).
11. Yang, Z. *et al.* A triarylmethyl spin label for long-range distance measurement at physiological temperatures using T1 relaxation enhancement. *J. Magn. Reson.* **269**, 50–54 (2016).
12. Yang, Z. *et al.* Long-Range Distance Measurements in Proteins at Physiological Temperatures Using Saturation Recovery EPR Spectroscopy. *J. Am. Chem. Soc.* **136**, 15356–15365 (2014).
13. Todd, A. P., Cong, J., Levinthal, F., Levinthal, C. & Hubell, W. L. Site-directed mutagenesis of colicin E1 provides specific attachment sites for spin labels whose spectra are sensitive to local conformation. *Proteins Struct. Funct. Bioinforma.* **6**, 294–305 (1989).
14. Warshaviak, D. T., Serbulea, L., Houk, K. N. & Hubbell, W. L. Conformational Analysis of a Nitroxide Side Chain in an α-Helix with Density Functional Theory. *J. Phys. Chem. B* **115**, 397–405 (2011).
15. Fleissner, M. R., Cascio, D. & Hubbell, W. L. Structural origin of weakly ordered nitroxide motion in spin-labeled proteins. *Protein Sci.* **18**, 893–908 (2009).
16. Guo, Z., Cascio, D., Hideg, K., Kálái, T. & Hubbell, W. L. Structural determinants of nitroxide motion in spin-labeled proteins: Tertiary contact and solvent-inaccessible sites in helix G of T4 lysozyme. *Protein Sci.* **16**, 1069–1086 (2007).
17. Fawzi, N. L. *et al.* A rigid disulfide-linked nitroxide side chain simplifies the quantitative analysis of PRE data. *J. Biomol. NMR* **51**, 105 (2011).

18. Toledo Warshaviak, D., Khramtsov, V. V., Cascio, D., Altenbach, C. & Hubbell, W. L. Structure and dynamics of an imidazoline nitroxide side chain with strongly hindered internal motion in proteins. *J. Magn. Reson.* **232**, 53–61 (2013).
19. Fleissner, M. R. *et al.* Structure and dynamics of a conformationally constrained nitroxide side chain and applications in EPR spectroscopy. *Proc. Natl. Acad. Sci.* **108**, 16241–16246 (2011).
20. Berliner, L. J. The Spin-Label Approach to Labeling Membrane Protein Sulfhydryl Groups*. *Ann. N. Y. Acad. Sci.* **414**, 153–161 (1983).
21. Roopnarine, O., Hideg, K. & Thomas, D. D. Saturation transfer electron parametric resonance of an indane-dione spin-label. Calibration with hemoglobin and application to myosin rotational dynamics. *Biophys. J.* **64**, 1896–1907 (1993).
22. Thomas, D. D., Seidel, J. C., Hyde, J. S. & Gergely, J. Motion of subfragment-1 in myosin and its supramolecular complexes: saturation transfer electron paramagnetic resonance. *Proc. Natl. Acad. Sci.* **72**, 1729–1733 (1975).
23. Raucher, D., Sar, C. P., Hideg, K. & Fajer, P. G. Myosin Catalytic Domain Flexibility in MgADP. *Biochemistry* **33**, 14317–14323 (1994).
24. Squier, T. C. & Thomas, D. D. Methodology for increased precision in saturation transfer electron paramagnetic resonance studies of rotational dynamics. *Biophys. J.* **49**, 921–935 (1986).
25. Thomas, D. D., Dalton, L. R. & Hyde, J. S. Rotational diffusion studied by passage saturation transfer electron paramagnetic resonance. *J. Chem. Phys.* **65**, 3006–3024 (1976).
26. Renault, K., Fredy, J. W., Renard, P.-Y. & Sabot, C. Covalent Modification of Biomolecules through Maleimide-Based Labeling Strategies. *Bioconjug. Chem.* **29**, 2497–2513 (2018).

27. Esmann, M., Sar, P. C., Hideg, K. & Marsh, D. Maleimide, Iodoacetamide, Indanedione, and Chloromercuric Spin Label Reagents with Derivatized Nitroxide Rings as ESR Reporter Groups for Protein Conformation and Dynamics. *Anal. Biochem.* **213**, 336–348 (1993).
28. Esmann, M., Hankovszky, H. O., Hideg, K. & Marsh, D. A novel spin-label for study of membrane protein rotational diffusion using saturation transfer electron spin resonance. Application to selectively labelled Class I and Class II -SH groups of the shark rectal gland Na+/K+-ATPase. *Biochim. Biophys. Acta BBA - Biomembr.* **978**, 209–215 (1989).
29. Esmann, M., Hankovszky, H. O., Hideg, K., Pedersen, J. A. & Marsh, D. Vinyl ketone reagents for covalent protein modification. Nitroxide derivatives suited to rotational diffusion studies by saturation transfer electron spin resonance, using membrane-bound Na,K-ATPase as an example. *Anal. Biochem.* **189**, 274–282 (1990).
30. Esmann, M., Hideg, K. & Marsh, D. Conventional and saturation transfer EPR spectroscopy of Na+/K+-ATPase modified with different maleimide-nitroxide derivatives. *Biochim. Biophys. Acta BBA - Protein Struct. Mol. Enzymol.* **1159**, 51–59 (1992).
31. Horváth, L. I., Dux, L., Hankovszky, H. O., Hideg, K. & Marsh, D. Saturation transfer electron spin resonance of Ca2(+)-ATPase covalently spin-labeled with beta-substituted vinyl ketone- and maleimide-nitroxide derivatives. Effects of segmental motion and labeling levels. *Biophys. J.* **58**, 231–241 (1990).
32. Ryba, N. J. P. *et al.* Rhodopsin mobility, structure, and lipid-protein interaction in squid photoreceptor membranes. *Biochemistry* **32**, 3298–3305 (1993).
33. Heaven, G., Hollas, M. A., Tabernero, L. & Fielding, A. J. Spin Labeling of Surface Cysteines Using a Bromoacrylaldehyde Spin Label. *Appl. Magn. Reson.* **52**, 959–970 (2021).

34. Fajer, P. G. Electron Spin Resonance Spectroscopy Labeling in Peptide and Protein Analysis. in *Encyclopedia of Analytical Chemistry* (John Wiley & Sons, Ltd, 2006).
35. *Spin labeling: theory and applications*. (Academic Press, 1976).
36. Reginsson, G. W. & Schiemann, O. Spin Labeling of DNA and RNA. in *Encyclopedia of Biophysics* (ed. Roberts, G. C. K.) 2429–2431 (Springer, 2013).
37. Berliner, L. J. & McConnell, H. M. A spin-labeled substrate for alpha-chymotrypsin. *Proc. Natl. Acad. Sci.* **55**, 708–712 (1966).
38. Hankovszky, O. H. *et al.* New nitroxide reagents for the selective spin-labelling at the guanidino moiety of arginine residues in peptides and proteins. *Biochim. Biophys. Acta BBA - Protein Struct. Mol. Enzymol.* **916**, 152–155 (1987).
39. Adackaparayil, M. & Smith, J. H. Preparation and reactivity of a new spin label reagent. *J. Org. Chem.* **42**, 1655–1656 (1977).
40. Wang, L., Zhang, Z., Brock, A. & Schultz, P. G. Addition of the keto functional group to the genetic code of Escherichia coli. *Proc. Natl. Acad. Sci.* **100**, 56–61 (2003).
41. Chin, J. W. *et al.* An Expanded Eukaryotic Genetic Code. *Science* **301**, 964–967 (2003).
42. Liu, W., Brock, A., Chen, S., Chen, S. & Schultz, P. G. Genetic incorporation of unnatural amino acids into proteins in mammalian cells. *Nat. Methods* **4**, 239–244 (2007).
43. Fleissner, M. R. *et al.* Site-directed spin labeling of a genetically encoded unnatural amino acid. *Proc. Natl. Acad. Sci.* **106**, 21637–21642 (2009).
44. Kálai, T., Fleissner, M. R., Jekő, J., Hubbell, W. L. & Hideg, K. Synthesis of new spin labels for Cu-free click conjugation. *Tetrahedron Lett.* **52**, 2747–2749 (2011).

45. Schreier, S., Bozelli, J. C., Marín, N., Vieira, R. F. F. & Nakaie, C. R. The spin label amino acid TOAC and its uses in studies of peptides: chemical, physicochemical, spectroscopic, and conformational aspects. *Biophys. Rev.* **4**, 45–66 (2012).

46. Tominaga, M. *et al.* Fmoc-POAC: [(9-Fluorenylmethyloxycarbonyl)-2, 2, 5, 5-tetramethylpyrrolidine-N-oxyl-3-amino-4-carboxylic Acid]: A Novel Protected Spin Labeled β-Amino Acid for Peptide and Protein Chemistry. *Chem. Pharm. Bull. (Tokyo)* **49**, 1027–1029 (2001).

47. Stoller, S., Sicoli, G., Baranova, T. Y., Bennati, M. & Diederichsen, U. TOPP: A Novel Nitroxide-Labeled Amino Acid for EPR Distance Measurements. *Angew. Chem. Int. Ed.* **50**, 9743–9746 (2011).

48. Pauly, H. & Rossbach, J. Ueber die Bildung von Pyrrolin- und Pyrrolidin-Derivaten aus Triacetonamin. *Berichte Dtsch. Chem. Ges.* **32**, 2000–2014 (1899).

49. Sosnovsky, G. & Cai, Z. A Study of the Favorskii Rearrangement with 3-Bromo-4-oxo-2,2,6,6-tetramethylpiperidine-1-oxyl. *J. Org. Chem.* **60**, 3414–3418 (1995).

50. Zhdanov, R. I. Nitroxyl Radicals and Non-Radical Reactions of Free Radicals. in *Bioactive Spin Labels* (ed. Zhdanov, R. I.) 23–82 (Springer, 1992).

51. Hideg, K., Kálai, T. & Sár, C. P. Recent results in chemistry and biology of nitroxides. *J. Heterocycl. Chem.* **42**, 437–450 (2005).

52. Khramtsov, V. V. Functional EPR Spectroscopy and Imaging of Nitroxides. in *Supramolecular Structure and Function 9* (ed. Pifat-Mrzljak, G.) 181–208 (Springer Netherlands, 2007).

53. Blinco, J. P., McMurtrie, J. C. & Bottle, S. E. The First Example of an Azaphenalene Profluorescent Nitroxide. *Eur. J. Org. Chem.* **2007**, 4638–4641 (2007).

54. Bottle, S. E., Chand, U. & Micallef, A. S. Hydrogen Abstraction From Unactivated Hydrocarbons Using a Photochemically Excited Isoindoline Nitroxide. *Chem. Lett.* **26**, 857–858 (1997).

55. Couet, W. R. *et al.* Influerce of chemical structure of nitroxyl spin labels on their reduction by ascorbic acid. *Tetrahedron* **41**, 1165–1172 (1985).

56. Morris, S. *et al.* Chemical and Electrochemical Reduction Rates of Cyclic Nitroxides (Nitroxyls). *J. Pharm. Sci.* **80**, 149–152 (1991).

57. Turley, J. W. & Boer, F. P. The crystal structure of the nitroxide free radical 2,2,5,5-tetramethyl-3-carbamidopyrroline-1-oxyl. *Acta Crystallogr. B* **28**, 1641–1644 (1972).

58. Lajzerowicz-bonneteau, J. 6 - Molecular Structures of Nitroxides. in *Spin Labeling* (ed. Berliner, L. J.) 239–249 (Academic Press, 1976).

59. Langen, R., Oh, K. J., Cascio, D. & Hubbell, W. L. Crystal Structures of Spin Labeled T4 Lysozyme Mutants: Implications for the Interpretation of EPR Spectra in Terms of Structure. *Biochemistry* **39**, 8396–8405 (2000).

60. Jiao, D., Barfield, M., Combariza, J. E. & Hruby, V. J. Ab initio molecular orbital studies of the rotational barriers and the sulfur-33 and carbon-13 chemical shieldings for dimethyl disulfide. *J. Am. Chem. Soc.* **114**, 3639–3643 (1992).

61. Fleissner, M. R. X-ray structures of nitroxide side chains in proteins: A basis for interpreting distance measurements and dynamic studies by electron paramagnetic resonance. (University of California, Los Angeles).

62. Lovell, S. C., Word, J. M., Richardson, J. S. & Richardson, D. C. The penultimate rotamer library. *Proteins Struct. Funct. Bioinforma.* **40**, 389–408 (2000).

63. Guo, Z. Correlation of spin label side-chain dynamics with protein structure: Studies of T4 lysozyme with site-directed mutagenesis and x-ray crystallography. (University of California, Los Angeles).

64. Guo, Z., Cascio, D., Hideg, K. & Hubbell, W. L. Structural determinants of nitroxide motion in spin-labeled proteins: Solvent-exposed sites in helix B of T4 lysozyme. *Protein Sci.* **17**, 228–239 (2008).

65. Balo, A. R., Feyrer, H. & Ernst, O. P. Toward Precise Interpretation of DEER-Based Distance Distributions: Insights from Structural Characterization of V1 Spin-Labeled Side Chains. *Biochemistry* **55**, 5256–5263 (2016).

66. Consentius, P. *et al.* Internal Dynamics of the 3-Pyrroline-N-Oxide Ring in Spin-Labeled Proteins. *J. Phys. Chem. Lett.* **8**, 1113–1117 (2017).

67. Jeschke, G. MMM: A toolbox for integrative structure modeling. *Protein Sci.* **27**, 76–85 (2018).

68. Jeschke, G. MMM: Integrative ensemble modeling and ensemble analysis. *Protein Sci.* **30**, 125–135 (2021).

69. López, C. J., Fleissner, M. R., Guo, Z., Kusnetzow, A. K. & Hubbell, W. L. Osmolyte perturbation reveals conformational equilibria in spin-labeled proteins. *Protein Sci.* **18**, 1637–1652 (2009).

70. López, C. J., Fleissner, M. R., Brooks, E. K. & Hubbell, W. L. Stationary-Phase EPR for Exploring Protein Structure, Conformation, and Dynamics in Spin-Labeled Proteins. *Biochemistry* **53**, 7067–7075 (2014).

71. Columbus, L. & Hubbell, W. L. A new spin on protein dynamics. *Trends Biochem. Sci.* **27**, 288–295 (2002).

72. Bracken, C., Carr, P. A., Cavanagh, J. & Palmer, A. G. Temperature dependence of intramolecular dynamics of the basic leucine zipper of GCN4: implications for the entropy of association with DNA11Edited by P. E. Wright. *J. Mol. Biol.* **285**, 2133–2146 (1999).

73. Columbus, L. & Hubbell, W. L. Mapping Backbone Dynamics in Solution with Site-Directed Spin Labeling: GCN4−58 bZip Free and Bound to DNA. *Biochemistry* **43**, 7273–7287 (2004).

74. López, C. J., Oga, S. & Hubbell, W. L. Mapping Molecular Flexibility of Proteins with Site-Directed Spin Labeling: A Case Study of Myoglobin. *Biochemistry* **51**, 6568–6583 (2012).

75. Lietzow, M. A. & Hubbell, W. L. Motion of Spin Label Side Chains in Cellular Retinol-Binding Protein: Correlation with Structure and Nearest-Neighbor Interactions in an Antiparallel β-Sheet. *Biochemistry* **43**, 3137–3151 (2004).

76. López, C. J., Yang, Z., Altenbach, C. & Hubbell, W. L. Conformational selection and adaptation to ligand binding in T4 lysozyme cavity mutants. *Proc. Natl. Acad. Sci.* **110**, E4306–E4315 (2013).

77. McCoy, J. & Hubbell, W. L. High-pressure EPR reveals conformational equilibria and volumetric properties of spin-labeled proteins. *Proc. Natl. Acad. Sci.* **108**, 1331–1336 (2011).

78. Bridges, M. D., Hideg, K. & Hubbell, W. L. Resolving Conformational and Rotameric Exchange in Spin-Labeled Proteins Using Saturation Recovery EPR. *Appl. Magn. Reson.* **37**, 363–390 (2010).

79. Griffith, O. H., Dehlinger, P. J. & Van, S. P. Shape of the hydrophobic barrier of phospholipid bilayers (Evidence for water penetration in biological membranes). *J. Membr. Biol.* **15**, 159–192 (1974).

80. Gross, A., Columbus, L., Hideg, K., Altenbach, C. & Hubbell, W. L. Structure of the KcsA Potassium Channel from Streptomyces lividans: A Site-Directed Spin Labeling Study of the Second Transmembrane Segment. *Biochemistry* **38**, 10324–10335 (1999).

81. Hubbell, W. L., Mchaourab, H. S., Altenbach, C. & Lietzow, M. A. Watching proteins move using site-directed spin labeling. *Structure* **4**, 779–783 (1996).

82. Altenbach, C., Froncisz, W., Hemker, R., Mchaourab, H. & Hubbell, W. L. Accessibility of Nitroxide Side Chains: Absolute Heisenberg Exchange Rates from Power Saturation EPR. *Biophys. J.* **89**, 2103–2112 (2005).

83. Pyka, J., Ilnicki, J., Altenbach, C., Hubbell, W. L. & Froncisz, W. Accessibility and Dynamics of Nitroxide Side Chains in T4 Lysozyme Measured by Saturation Recovery EPR. *Biophys. J.* **89**, 2059–2068 (2005).

84. Oh, K. J. *et al.* Organization of Diphtheria Toxin T Domain in Bilayers: A Site-Directed Spin Labeling Study. *Science* **273**, 810–812 (1996).

85. Altenbach, C., Greenhalgh, D. A., Khorana, H. G. & Hubbell, W. L. A collision gradient method to determine the immersion depth of nitroxides in lipid bilayers: application to spin-labeled mutants of bacteriorhodopsin. *Proc. Natl. Acad. Sci.* **91**, 1667–1671 (1994).

86. Salwiński, Ł. & Hubbell, W. L. Structure in the channel forming domain of colicin E1 bound to membranes: The 402–424 sequence. *Protein Sci.* **8**, 562–572 (1999).

87. Vogelsang, M. S. Site-directed spin labeling of colicin E1: pH effects on solution and membrane-bound structures. (University of California, Los Angeles).

88. Leigh, J. S. ESR Rigid-Lattice Line Shape in a System of Two Interacting Spins. *J. Chem. Phys.* **52**, 2608–2612 (1970).

89. Jung, K., Voss, J., He, M., Hubbell, W. L. & Kaback, H. R. Engineering a Metal Binding Site within a Polytopic Membrane Protein, the Lactose Permease of Escherichia coli. *Biochemistry* **34**, 6272–6277 (1995).

90. Voss, J., Salwiński, L., Kaback, H. R. & Hubbell, W. L. A method for distance determination in proteins using a designed metal ion binding site and site-directed spin labeling: evaluation with T4 lysozyme. *Proc. Natl. Acad. Sci.* **92**, 12295–12299 (1995).

91. Voss, J., Hubbell, W. L. & Kaback, H. R. Distance determination in proteins using designed metal ion binding sites and site-directed spin labeling: application to the lactose permease of Escherichia coli. *Proc. Natl. Acad. Sci.* **92**, 12300–12303 (1995).

92. Voss, J., Hubbell, W. L. & Kaback, H. R. Helix Packing in the Lactose Permease Determined by Metal−Nitroxide Interaction. *Biochemistry* **37**, 211–216 (1998).

93. Jeschke, G. DEER Distance Measurements on Proteins. *Annu. Rev. Phys. Chem.* **63**, 419–446 (2012).

94. Elgeti, M. & Hubbell, W. L. DEER Analysis of GPCR Conformational Heterogeneity. *Biomolecules* **11**, 778 (2021).

95. Borbat, P. P. & Freed, J. H. [3] - Measuring Distances by Pulsed Dipolar ESR Spectroscopy: Spin-Labeled Histidine Kinases. in *Methods in Enzymology* (eds. Simon, M. I., Crane, B. R. & Crane, A.) vol. 423 52–116 (Academic Press, 2007).

96. Jeschke, G. & Polyhach, Y. Distance measurements on spin-labelled biomacromolecules by pulsed electron paramagnetic resonance. *Phys. Chem. Chem. Phys.* **9**, 1895–1910 (2007).

97. Borbat, P. P., Davis, J. H., Butcher, S. E. & Freed, J. H. Measurement of Large Distances in Biomolecules Using Double-Quantum Filtered Refocused Electron Spin−Echoes. *J. Am. Chem. Soc.* **126**, 7746–7747 (2004).

98. Pannier, M., Veit, S., Godt, A., Jeschke, G. & Spiess, H. W. Dead-time free measurement of dipole–dipole interactions between electron spins. *J. Magn. Reson.* **213**, 316–325 (2011).
99. Jeschke, G. Distance Measurements in the Nanometer Range by Pulse EPR. *ChemPhysChem* **3**, 927–932 (2002).

Chapter 5: Saturation Transfer EPR reveals dynamics in the μs-ms time range using a conformationally constrained bifunctional spin label (RX)

5.1 Introduction

It is clear that both the capability of resolving dynamics over a wide range of timescales and the versatility of applications make SDSL-EPR a uniquely powerful tool for exploring protein internal dynamics. However, lineshapes of conventional CW-EPR are insensitive to motions with correlation times longer than 10^{-7}s, which is therefore called the 'rigid limit'. While the importance of detecting slow structural and dynamic information of protein under physiological conditions has now been widely acknowledged, there are very few techniques that can directly monitor protein internal dynamics in the time domain of μs-ms.

Accompanying the development of pulsed-EPR techniques, methods utilizing pulsed-ELDOR[1] and pulsed SR-EPR[2] have been developed for measuring μs-ms rotational diffusion events. Yet, their sensitivity to motions is limited to a rather narrow window (see Figure 2.1), which makes them less ideal choices especially when the hardware requirements for setting up pulse experiments are considered. In the toolbox of SDSL-EPR methods, Saturation Transfer EPR (ST-EPR) is particularly attractive, as it extends the timescale of motions which can be studied using nitroxide spin labels to as long as 10^{-3} s, and requires little to no additional hardware compared to CW-EPR spectrometers.

Ever since its early application[3] in studies of muscle proteins[4] and membrane transporters[5], ST-EPR was specifically designed for studying very slow rotational diffusion (slower than the rigid limit of conventional CW-EPR), making it one of the most valuable SDSL-EPR methods. With the fact that conventional CW-EPR and ST-EPR can be measured in concert using the same

equipment by only modifying necessary parameters, there are few, if any, biophysics methods that compete effectively with the method in this incomparable wide detection range of timescales.

Generally speaking (see detailed theoretical backgrounds in chapter 3), ST-EPR is sensitive to any process that can alleviate the saturation during the time course of T_1 relaxation[6–11]. However, regardless of its unique capacity and potential for probing the conformational changes of proteins, it has not been applied widely to small (≤ 50kDa), soluble proteins under physiological conditions such as a hydrated environment at room temperature. As introduced in chapter 4, all EPR spectra inevitably encode three contributions in the fast time domain (ps-ns) from such systems: the rotational diffusion of the protein molecule, local backbone fluctuations, and internal motion of the spin label side chain. Any of these contributors of motion introduce additional energy dissipation pathways, therefore largely interfering with or even eliminating the signal response to slower dynamics.

Up to now, most ST-EPR practices were employed for systems that either have considerable molecular weights, or have native environments, such as in membranes or lipids, that can naturally restrict the Brownian rotation of protein. The majority of these ST-EPR studies focused on monitoring the overall motion of protein as a macromolecule[12,13], which can be used as an indicator of polymerization, intermolecular interaction, or change of environment (e.g., phase transition of lipids). There have been only a few studies discussing ST-EPR application to the protein internal dynamics[14], such as movements involving a whole secondary element or the entire subdomain, etc.

However, considerable effort has been spent on finding spin probes for slow motion detection, most of which have already been introduced in chapter 4. Among them, thioether-

linked labels 5- or 6-MSL[4] and InVSL[15–18], the non-native amino acid label TOAC[19], and the bifunctionally attached label RX[20–23], are intuitive candidates when designing an experiment to obtain ST-EPR spectra.

Benefiting from its doubly covalent disulfide linkages, the internal motion of RX is highly restricted, thus allowing for direct measurement of microsecond dynamics, precise distance, and even orientation measurements. Thompson[20] et al. first used the RX side chain for ST-EPR measurements in the study of actomyosin complex, successfully demonstrating its value for probing slow protein dynamics. The thorough characterization by Fleissner[1] et al. has established a solid foundation for extending its further applications. It has so far been widely accepted as a standard of maximized rigidity for spin label side chains, i.e., it is expected to bring in minimal influence from its internal mobility, leaving the foreground to protein dynamics, thus making it the ideal selection of label when exploring a new experimental methodology.

Another study exploring new monofunctionally attached labels with the effectively restricted motion for ST-EPR measurements will be shown in the next chapter, in which a more detailed discussion about choosing spin labels can be found. In this chapter, experiments using spin-labeled mutants of the sperm whale myoglobin and bacteriophage protein T4 Lysozyme will be presented, to examine the feasibility of a methodology that integrates both the stationary-phase techniques (see chapter 1 and below) and the utilization of rigid spin label (RX) to isolate and monitor slow protein motions. Results presented here demonstrate that the applicability of SDSL ST-EPR can be generally extended to ordinary protein objects to directly monitor protein internal dynamics in the μs-ms time range. The effectiveness of this methodology facilitates the further development of new experimental tools and strategies, which can substantially help to advance the understanding of molecular mechanisms of protein function.

5.1.1 Stationary-Phase SDSL-EPR

A primary motivation for the development of ST-EPR was the need for probing the slow rotational motions in biological assemblies, such as integral membrane proteins, which reside in a high effective viscosity medium, or muscle proteins, which are attached to muscle filaments/fibrils. As compared to small, globular proteins in aqueous solutions that experience rapid tumbling with a correlation time in the ns range, these molecules are by nature nearly or completely immobilized. In order to directly observe internal motions occurring in the time domain of μs-ms, the Brownian rotation needs to be sufficiently slow to not abate the sensitivity of ST-EPR.

To properly interpret ST-EPR results, a reference is required, which corresponds to the slowest motion that ST-EPR spectra are still sensitive to. To determine this "rigid limit of ST-EPR", several methods of immobilization have been employed: samples are measured under lower temperatures or completely frozen in liquid nitrogen[24,25], or crosslinked by chemical reagents such as glutaraldehyde[12], or precipitated in saturated ammonium sulfate solution[26], or lyophilized[26]. Each of these methods has its own advantages, however, none is suitable for probing protein dynamics under physiological conditions. Either temperature adjustment or solidification treatment (freezing/precipitation/lyophilization) might considerably perturb the thermodynamic energy landscape and hydration/solvation status, thus modifying the conformational equilibrium and internal dynamics.

Thomas et. al[27] attached isolated myosin heads covalently to controlled pore glass beads (CPG, 5-10 μm particle size, 550Å pore size) that were coated and activated with cyanogen bromide (CNBr). The spectra of tethered samples were intrinsically similar to that of precipitated

Hemoglobin (a rigid limit standard for ST-EPR methodological experiments) and myofibrils, suggesting millisecond motions. This result suggests that the attachment of proteins to modified matrices may be an effective method of immobilization at room temperature.

In recent years, a large variety of stationary-phase strategies[28–32] have emerged along with rapidly evolving chemical biology techniques, greatly expanding the toolkit for protein modification and immobilization. A wide range of hybrid immobilization constructs can be achieved by assembling different supporting materials, linkage chemistry, targeting groups, and even the spacer between protein and matrix, so that for each specific application a variety of parameters can be optimized.

The fact that SDSL-EPR is selectively sensitive to only spin-labeled species and does not rely on optical properties for detection makes it advantageous over many biophysical methods for studies involving immobilized proteins. Lopez[33] et. al have thoroughly discussed the effectiveness of several attachment methods for restricting the rotational diffusion in the CW-EPR time domain (ps-ns), and evaluated how non-specific and site-specific methods influence the protein conformational equilibria, of which the results are summarized as the "stationary-phase SDSL-EPR" methodology.

In this work (stationary-phase SDSL-EPR), three different linkage chemistries commonly used in biophysical and biochemical studies were applied in the four strategies included: 1. CNBr that binds primary amine groups from native lysines; 2. Dibenzyl cyclooctyne (DBCO) that binds azido groups from unnatural amino acids (UAA); 3. Streptavidin that couples to biotin from biotinylated proteins. The utilization of all strategies achieved high effective concentrations (≥300μM) without aggregation, which is conducive to providing high signal-to-noise data in measurements.

The published results have revealed that each strategy is sufficient to suppress the rotational motion of the attached protein to a level beyond the rigid limit of CW-EPR at room temperature. Meanwhile, by comparing both CW-EPR lineshapes and DEER distance distributions, it can be concluded that the native secondary structure, tertiary fold, and backbone dynamics of labeled proteins attached to solid supports are largely retained as those in solution.

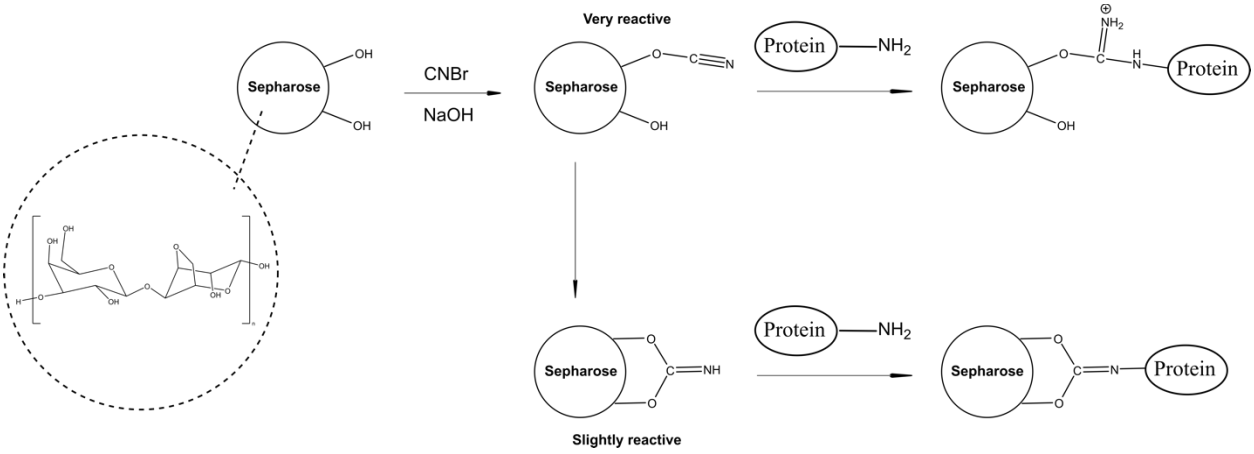

Figure 5.1 Immobilization strategy using CNBr-activated Sepharose. Cyanogen bromide (CNBr) in base (NaOH) solution reacts with hydroxyl groups on Sepharose (crosslinked, beaded-form agarose) to form cyanate esters or imidocarbonates, which reacts with the primary amine from lysines.

This work laid a concrete foundation for integrating the immobilization methods into any SDSL-EPR based methodology. Despite enduring discussions about whether the heterogeneous multiple-point attachment and nonspecific orientation of proteins on the solid surface will lead to potential loss of activity[34,35], attachment methods using native residues effortlessly have broad applicability since they do not require additional modification to the native protein. Due to its obvious convenience and high binding capacity, the covalent attachment to CNBr-activated Sepharose (Figure 5.1) is chosen as the initial method of immobilization (this method and the matrix will be abbreviated as 'CNBr' in the following contents). For further development of the methodology, some other attachment schemes are also examined, and results will be discussed in

the next chapter.

5.1.2 “α-Helical proteins”: Holo-myoglobin and T4 lysozyme

Over the past 50 years, the major application of ST-EPR has been in the study of muscle proteins (myosin, actin, etc.), and membrane-bound proteins, including Na^+/K^+-ATPase[36], Ca^{2+}-ATPase, rhodopsin[37], cytochrome oxidase[38], etc. Many of these systems carry several native cysteines that are solvent exposed, and the spin labels were naturally attached to those sites. While such locations of probes are satisfactory for studies focused on the mobility of protein as a whole, it is not ideal for understanding protein internal dynamics that are more localized and site-dependent. In order to examine the ST-EPR methodology aiming at extending the applicability to ordinary protein systems in the aqueous solution, a well-characterized experimental protein that is structurally stable to site-directed mutagenesis is required as a model system. Both myoglobin (Mb) and T4 Lysozyme (T4L) are ideal systems for such an aim.

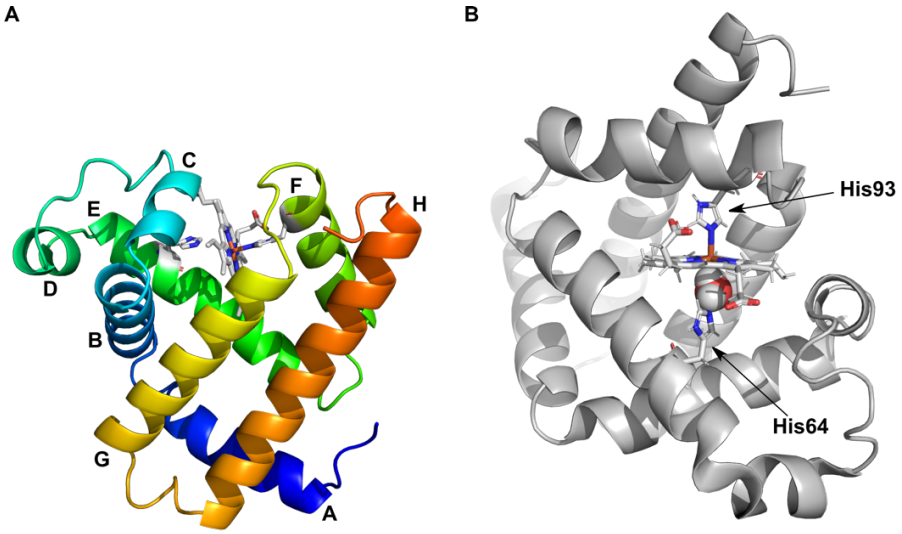

Figure 5.2 Structure of sperm whale myoglobin. (A) Ribbon model of myoglobin (PDB: 2MBW) showing the location of A-H helices. (B) Heme-binding pocket, showing the heme, the proximal and distal histidines, and the ligand (water) (PDB:1CQ2).

Myoglobin, whose primary function is to store oxygen in cardiac and skeletal muscles and is capable to bind other gas molecules, was the first protein of which the crystal structure to be obtained at atomic resolution by the groundbreaking work of Kendrew[39] and colleagues. Sperm whale myoglobin[40–42] (Figure 5.2 (A)), the specific type used in this dissertation, is a monomer consisting of 153 amino acids (18.0 kDa) and a heme group in its center. It is an oblate spheroid of ~3 nm diameter, and roughly 70% of its chain is folded into 8 α-helices (denoted A-H), while the rest form interhelical turns connecting structural elements.

Heme is a coordination complex consisting of an iron ion coordinated to a porphyrin acting as a tetradentate ligand. In sperm whale myoglobin, the protein is covalently bonded to the porphyrin ring via a histidine-iron bond (from His93) at the fifth coordination position of the metal center (Figure 5.2 (B)), and to a distal histidine (His64) near the opposite side of the ring. The distal imidazole is not bonded to the iron but is available to interact with the substrate O_2. It is also known that myoglobin can bind carbon monoxide (CO), of which the affinity is 60 times greater than O_2.

It is often referred to as Holomyoglobin (HoloMb) when the heme group is bound, and Apomyoglobin (ApoMb) when not. The prosthetic group in myoglobin is responsible for its functionality, in which the iron center in heme can exist in either ferrous (Fe^{2+}) or ferric (Fe^{3+}) oxidation states, but only the ferrous (Fe^{2+}) state is capable of binding oxygen. Oxidation of the iron from ferrous state to ferric state yields metmyoglobin (met-Mb), turning the protein into a physiologically inactive form with water as the primary ligand in the distal site instead of O_2.

The prosthetic group also gives rise to the characteristic absorbance spectra of HoloMb,

which have been extensively described and are highly informative concerning the state of both heme and protein[43–50]. The narrow, intense band in the ultraviolet region (at approximately 409-410 nm for sperm whale HoloMb) is characteristic of all heme proteins and is commonly referred to as the Soret band. Arising from a $\pi \rightarrow \pi^*$ transition of the porphyrin ring, the position, intensity, and shape of the Soret band all strongly depend on the oxidation state of the heme iron, making it extremely sensitive and useful for revealing the identities of ligands bound to the heme, but also for detecting the structural integrity of the protein.

Myoglobin has long been studied by the biophysical and protein science community, accumulating a wealth of results from multiple techniques leveraging its structural simplicity (almost completely α-helical), high expression yields and simple purification strategy, its tolerance to mutagenesis, and high stability. While there is no observable pathway from the well-packed, high-resolution crystal structure for ligand entrance and migration to the binding center, the results of multiple experiments revealed that the existence of internal fluctuation between conformational and statistical substates resembles a prerequisite for ligand binding.

Lopez[51] et al. placed R1 side chains at 39 solvent-exposed sites of sperm whale myoglobin and analyzed its sequence-dependent mobility on the ps-ns time scale by SDSL CW-EPR. As judged by A_{409}/A_{280} ratio, the spin-labeled HoloMb could be fully reconstituted with heme, confirming that it was unlikely that the mutations of the selected residues impaired the function and structural integrity of the protein. Spectra obtained in this study reflect relatively low amplitude backbone fluctuations of each helix in the fast time domain (ps-ns), showing that HoloMb is well-ordered with limited conformational flexibility in discrete regions of the molecule. Such characteristics promise HoloMb as a suitable model system for examining the functionality of a methodology aiming at detecting slower motions.

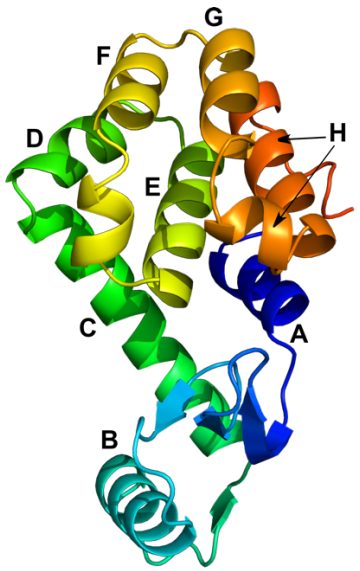

Figure 5.3 Structure of pseudo wild-type T4L. Ribbon model of C54T/C97A T4L (PDB: 1L63) showing the location of A-H helices.

T4L[52] (Figure 5.3) consists of 164 residues (18.6 kDa), folded into also 8 α-helices (denoted A-H) and a small antiparallel β-sheet between helix A and B. It is a globular protein of ellipsoidal shape, roughly divided into two domains connected by the long helix C. T4L is known for its extremely high tolerance to amino acid substitutions. The pseudo wild-type (pWT) T4L[53] used in this dissertation has two natural cysteine groups (Cys54 and Cys97) of the original wild-type replaced with Threonine and Alanine for subsequent SDSL applications. The thermostability of pWT is almost identical to that of the WT.

Similar to myoglobin, the general paradigm between the structure, dynamics, and function of T4L is experimentally well understood through vast amounts of studies[54–58]. Particularly, its superior stability has enabled it one of the most ideal platforms by which to explore the feasibility and functionality of methods and techniques. A significant number of single or multiple cysteine mutants engineered for EPR studies have been reported by the Hubbell research group over the last 20 years[59–64], building up an exclusively EPR-based archive for this

protein of its structure and dynamics.

Both the analysis of thermal factors from crystal structures and spectroscopic measurements in solution revealed that there exist both highly-ordered regions (minimal backbone fluctuations) and several dynamic regions to allow substrate binding. The “hinge-bending” motion has been proposed to occur in solution to open and close the active site cleft located between the N-terminal and the C-terminal domains[65]. While there is no structural unfolding involved in this process, certain degrees of conformational fluctuations were detected from changes of interspin distances in a previous publication[65].

In summary, both HoloMb and pWT-T4L are thoroughly characterized model proteins possessing well-ordered structures and limited internal flexibility, from which sites with a minimum of mobility in the fast time domain could be selected. As such, the efficacy of the methodology for revealing slow dynamics can be demonstrated with less ambiguity.

5.2 Results

5.2.1 The internal dynamics of RX

This section serves as a supplement to the characterization work of RX by Fleissner et al., aiming at obtaining an extended understanding of its internal dynamic mode. Site 72 in T4L, in the center of the long rigid helix C, has long been used as a reference site[33,66,67] for R1 and other spin labels, where little contribution is expected from local backbone fluctuations to the motion detected by the nitroxide, so that the internal dynamics of the side chain is isolated. As verified in previous studies, the side chain is fully solvent exposed and does not contact other amino acid residues from the protein. The mutant 68C/72C is used accordingly in order to introduce the RX

side chain, of which site 68 is also confirmed to be fully solvent exposed by the spectrum of 68R1.

As introduced in chapters 2 and 3, both the effective hyperfine splitting ($2A_{zz'}$) and linewidth (estimated from the low field peak FWHM) are sensitive spectral parameters that can be used as indicators reflecting changes in local environments, as well as nitroxide intrinsic dynamics. In the following sections, both parameters will be used for estimating the nitroxide rigidity due to their directness. Whereas, it is essential to perform spectral simulations to analyze the dynamic mode of the spin label side chain, and to truly reveal the origin of its mobility.

5.2.1.1 T4L68RX72 attached to Sepharose in frozen solution

In order to examine the effects originating from intrinsic chemical properties of spin labels and environmental polarity, obtaining spectra corresponding to no motion is necessary, which can be achieved by recording EPR spectra at cryogenic temperatures. Fleissner et al. determined the frozen spectrum of T4L5RX9 on CNBr at -50℃ (~223K). However, because the hydration shell surrounding the protein and spin label side chains is still present at 223K and the spectral parameters were shown to be dependent on it[24,25], 80K (in liquid nitrogen) is used as the rigid limit temperature in this work, at which any motional mode from either proteins or labels is completely frozen out. Moreover, at these low temperatures, the hydrogen-bond equilibrium is completely stabilized to avoid additional effects on hyperfine splittings and linewidths.

An effective hyperfine splitting $2A_{zz'}(0)$ = 73.356 G was obtained for T4L68RX72 on CNBr in the frozen H_2O-based solution, and a $2A_{zz'}(0)$ =74.177 G was obtained for T4L72R1 on CNBr which is just subtly different from RX due to their similar nitroxide ring structures (Figure 5.4). Corresponding to the completely immobilized status of nitroxide, the $2A_{zz'}(0)$ value will be used

as the intrinsic $2A_{zz}$ tensor value for each spin label in the spectral simulation as it represents the contribution from the electronic structure of each respective label. The spectra under ambient conditions were also obtained (Figure 5.4A). The difference $\Delta 2A_{zz'} = 2A_{zz'}(0) - 2A_{zz'}$ is a metric that can be used to compare the relative mobilities of the different labels (see chapter 3). As the reference of maximum rigidity, RX has a $\Delta 2A_{zz'}$ of only 2.9 G, while R1 has a $\Delta 2A_{zz'}$ of 20.8 G, reflecting a high degree of side chain flexibility.

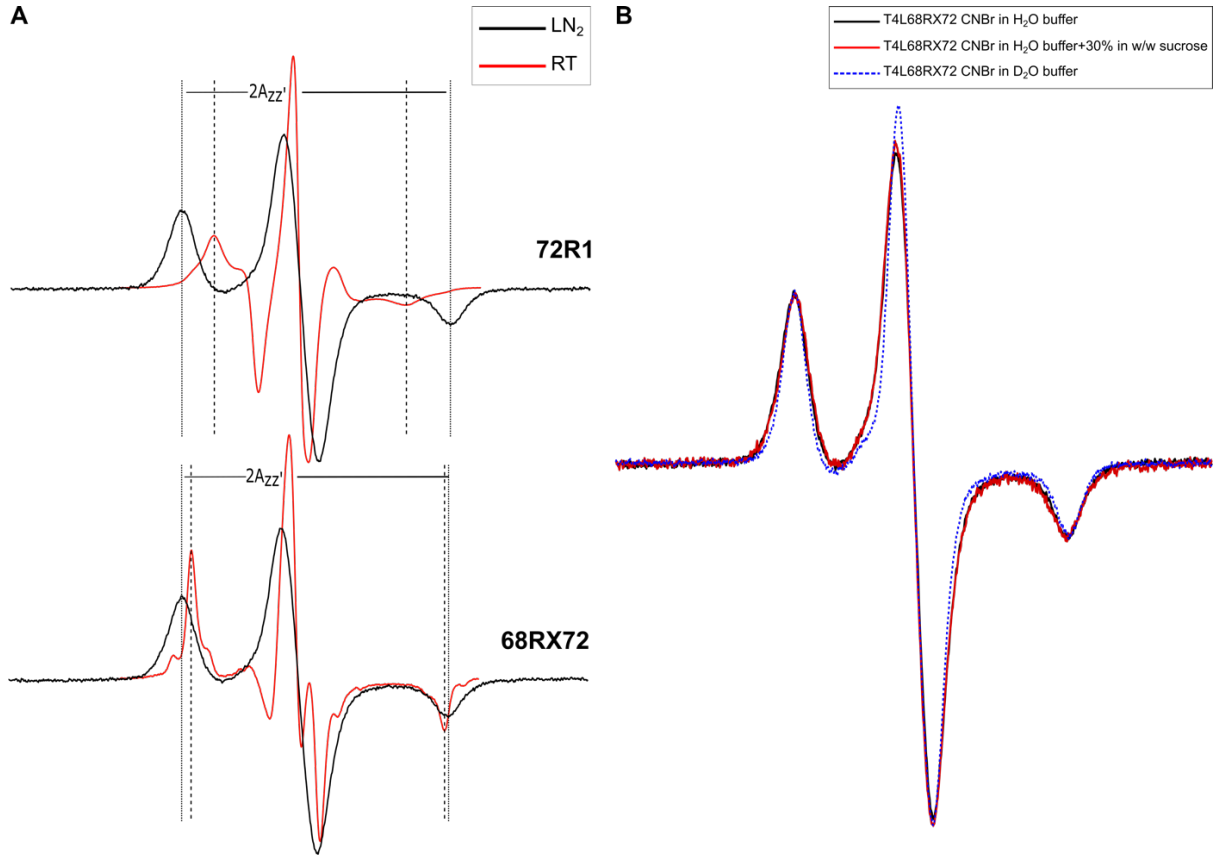

Figure 5.4 (A) CW-EPR spectra (frozen in liquid nitrogen (LN_2): black curves; at room temperature (RT): red curves) of R1 and RX on T4L attached to CNBr-activated Sepharose. The magnetic field scan width is 100 G for RT spectra and 160 G for frozen spectra. The vertical lines are drawn as references for comparing effective $2A_{zz'}$. (B) Frozen CW-EPR spectra of T4L68RX72 on CNBr under various solution conditions.

As mentioned in chapter 2, extremely broad lines with inhomogeneously broadened lineshapes of Gaussian character are widely observed for nitroxide spin labels at low

temperatures, which is related to the heterogeneity of microenvironment in the vicinity of nitroxide[68,69]. Such heterogeneity can originate from the conformational equilibrium of local structures or the network of hydrogen bonds. As shown in Figure 5.4 (B), the exchange from the H_2O-based buffer to the D_2O-based buffer leads to the narrowing of the linewidths (most obvious in the center peak), supporting the notion that it is the surrounding rather than conformational exchange as the origin of the broad lines.

It should be noted that $2A_{zz'}$ values are also dependent on the polarity. In some subsequent experiments, sucrose (30% in w/w) is added to the solution to modulate the viscosity. To distinguish whether the accompanying changes in the $2A_{zz'}$ values correspond to changes in polarity or mobility, the frozen spectrum of T4L68RX72 on CNBr in solution added the sucrose (30% in w/w) was also obtained. The identical lineshapes with and without sucrose, further support that changes in polarity can be excluded as the origin of changes in the $2A_{zz'}$ value.

5.2.1.2 Viscosity and temperature dependence for T4L68RX72

Timofeev described an analysis method to sequester the contribution purely from the internal motion of the spin label side chain: $2A_{zz'}$ values of the same sample are measured in a series of solutions with increasing viscosity and plotted as a function of viscosity[70]. Since only the rotational diffusion of macromolecules (proteins) can be effectively suppressed by increased viscosity, the extrapolated y-intercept (infinite viscosity) reflects mostly the residual motion of the spin label, and small contributions from the protein backbone.

When the label is attached to a site such as 72C, the extrapolated $2A_{zz'}$ (inf) can serve as an independent indicator of side chain mobility. A value of $2A_{zz'}$ (inf) = 71.515 G was obtained for T4L68RX72 (slightly higher than the value of 70.8 G measured by Fleissner et al. for

T4L5RX9), and a value of $2A_{zz'}$ (inf) = 58.741 G was obtained for T4L72R1 (Figure 5.5), which clearly shows the much higher mobility of R1 side chain and the effectiveness of bifunctional attachment for restricting internal motions. The proximity of the $2A_{zz'}$ value of RX (70.493G) to its $2A_{zz'}$ (inf) value is remarkable, as it confirms the value of using solid supports to eliminate rotational diffusion of proteins at ambient temperature.

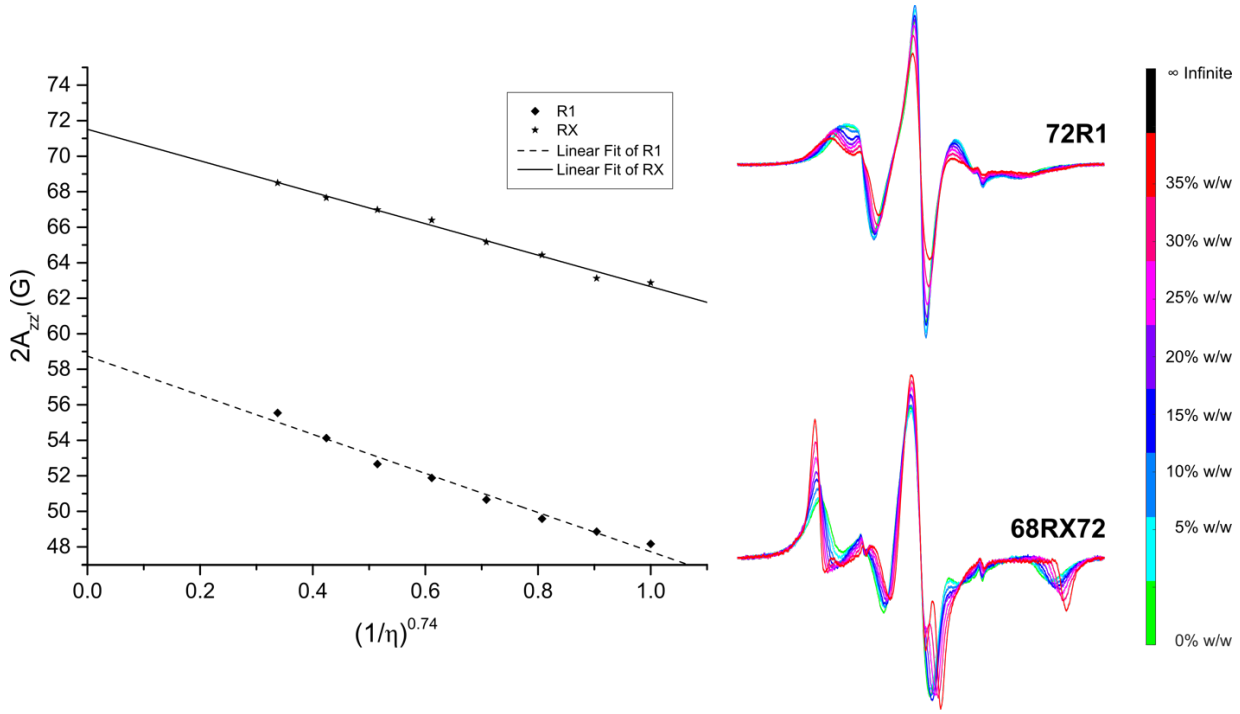

Figure 5.5 The viscosity dependence of CW-EPR spectra (normalized to the spin count calculated by double integration) and values of $2A_{zz'}$ for T4L72R1 and T4L68RX72 in sucrose solution (concentrations ranging from 0 to 35% w/w in buffer). Viscosities of the sucrose solutions were taken from the CRC Handbook of Chemistry and Physics[71]. At each concentration, $2A_{zz'}$ is determined and plotted vs. the function of viscosity as indicated. Linear extrapolation of the plot to infinite viscosity yields $2A_{zz'}$ in the limit of zero rotational diffusion of the protein.

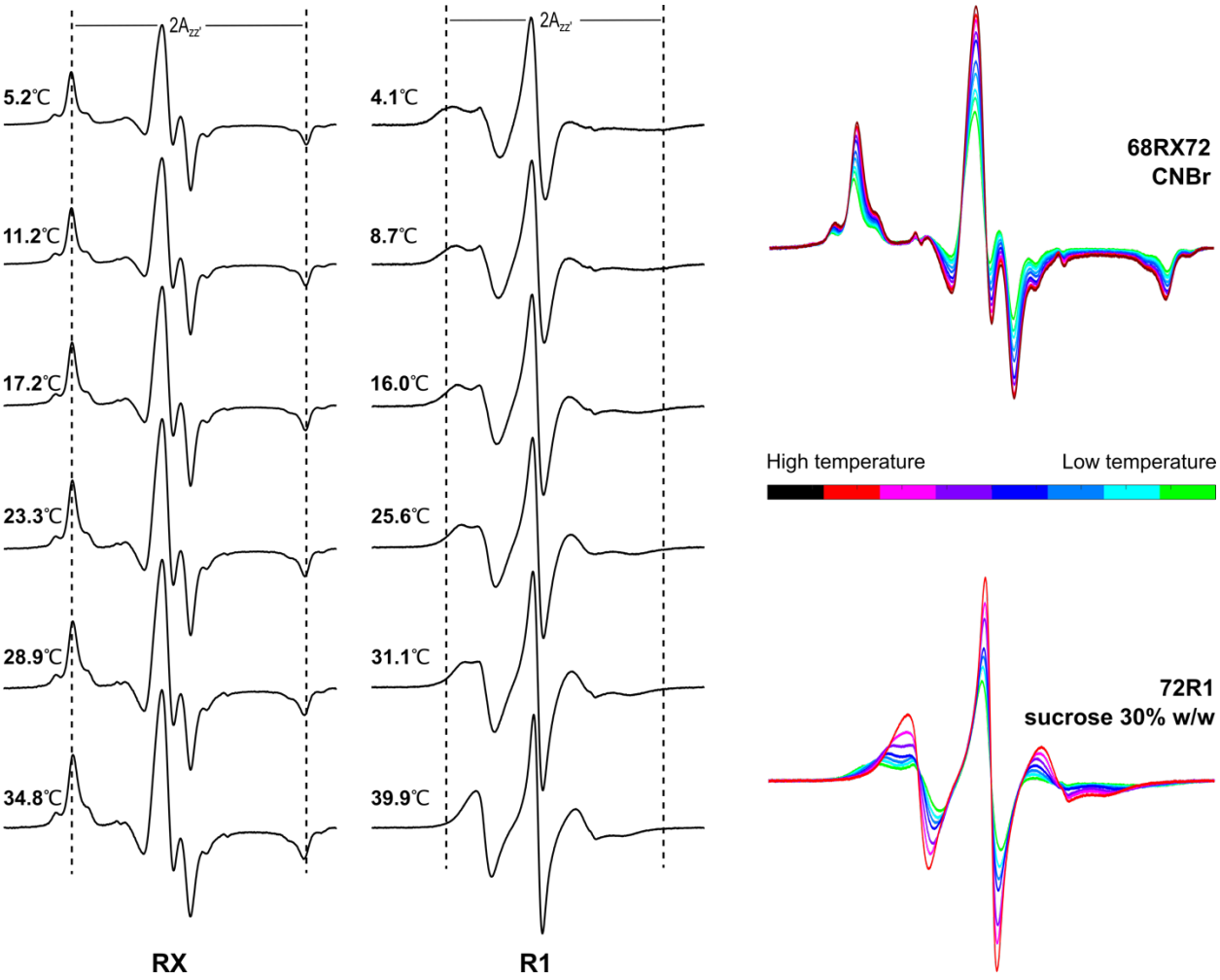

Figure 5.6 Normalized CW-EPR spectra of: T4L72R1 in sucrose (30% w/w) at temperatures ranging from 4°C to 40°C (published results[72]); T4L68RX72 on CNBr at temperatures ranging from 5°C to 35°C. The vertical lines are drawn as references for comparing effective $2A_{zz'}$ values.

The small difference between the $2A_{zz'}$ (inf) of RX with its rigid limit value $2A_{zz'}$(0) originates most likely from residual backbone fluctuations, since polarity changes due to the addition of sucrose in this concentration range were excluded (0% w/w vs. 30% w/w, see Figure 5.4 (B)). This result, that the same parameter measured for the 68RX72 mutant is higher in value than the 5RX9 mutant, is also consistent with helix C being more rigid than the N-terminus. Also, it is reasonable to assume that residual dynamics of the RX side chain exist, despite it being strongly immobilized compared to other side chains.

Another common way to analyze side chain dynamics is to approximate the activation energy with Arrhenius law by varying the temperature. As temperature increases, new modes of motion will be excited if the activation energy between modes is overcome. The higher activation energy is required, the stronger the restriction is in mobility in the current dynamic mode, and other modes will be less likely populated.

The temperature dependence of the T4L68RX72 (on CNBr) CW-EPR spectra (Figure 5.6) was investigated in the range of 5-35°C. Neither the aqueous solution freezes nor the agarose structure is disrupted within this temperature range. As compared to published results[72] for R1 in viscous medium (30% sucrose w/w), the spectral changes over the whole detection range were so small that no significant changes of the fitting parameters were detected in the lineshape simulation (results not shown). The decrease in $2A_{zz'}$ values was less than 1 G as the temperature increased from 5°C to 35°C, while the linewidths remained constant over the whole temperature range.

In CW-EPR spectra, any motions slower than the CW-EPR rigid limit (<100 ns) are essentially indistinguishable. Even at 35°C, the spectrum of T4L68RX72 on CNBr still approaches the rigid limit of CW-EPR, showing a “pseudo powder pattern”, demonstrating the strong immobilization of this spin label side chain. The insensitivity of lineshapes to temperature, as observed for T4L68RX72 on CNBr, further suggests that activation energies for motional modes of both side chains and protein backbone are too high to be thermally activated in this temperature range, at least in the nanosecond time scale. It implies that slower (microsecond), collective motions dominate the resonant energy distribution (spectrum) of labeled proteins, showing characteristically rigid limit lineshapes in CW-EPR.

5.2.1.3 Global fits to both the X-band spectrum and the Q-band spectrum of T4L68RX72 attached to Sepharose

Conventionally, when the spectrum falls in the category of "intermediate immobilization", values of the hyperfine splitting, as well as linewidths, can be used to estimate the rate of motion based on their monofunctional dependence to the correlation times, τ_R (see chapter 3). However, the simplified methods have an important failing in that they are not applicable to spectra arising from highly anisotropic motion.

Freed's theorem[73–76] indicates that when the correlation time is longer than the order of nanoseconds, both the unresolved inhomogeneous components and the excess motional width contribute to the linewidth for Lorentzian lineshapes. This implies that a certain degree of broadening is supposed to retain even when there is no motional averaging, which has indeed been observed in the frozen spectra (Figure 5.2) or the spectrum of spin labels attached to buried sites (see next chapter for examples). However, almost all spectra of RX-labeled protein samples exhibit extremely narrow linewidths, implying the existence of strong anisotropy rather than slow tumbling. When the motion of the nitroxide, explicitly the angular amplitude, is highly restricted, the magnitude of relaxation effects is accordingly suppressed, which mainly involves the T_2 relaxation on the time scale of CW-EPR. Consequently, the T_2-dependent Lorentzian linewidth is effectively narrowed.

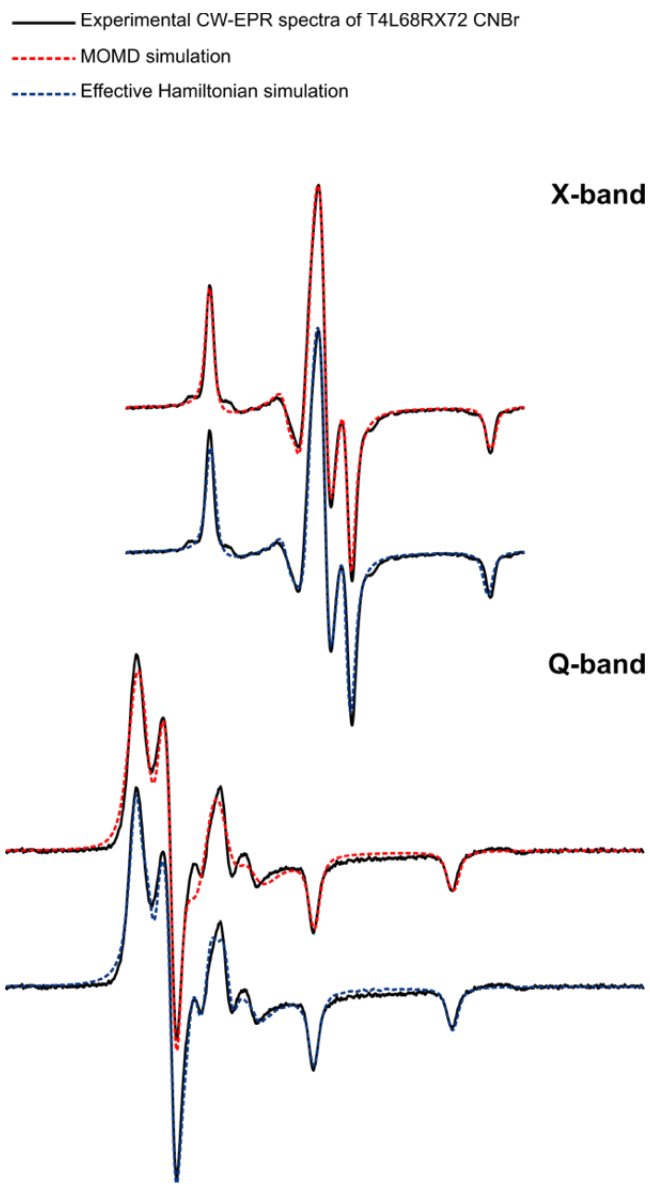

Figure 5.7 The X-band (100 Gauss field width) and Q-band (160 Gauss field width) experimental CW-EPR spectra of T4L68RX72 on CNBr (black, solid lines) superposed with simulated spectra (dashed lines) according to the MOMD model (red lines), and the time-independent effective Hamiltonian model (blue lines).

It is noteworthy that the sample is not aligned in a specific orientation, thus the anisotropy is likely to originate from the spin label. The mechanism of RX rigidity can be truly revealed from the quantitative assessment of the amplitude and rate of its internal motions *via* spectral simulations. Indeed, the MOMD (microscopic order macroscopic disorder) simulation of

T4L5RX9 on CNBr in Fleissner et al. indicated a single anisotropic motional component with an order parameter as high as S = 0.9 and a correlation time as short as τ_R = 2 ns.

To further confirm the generality of using this motional model to account for the internal dynamics of RX on solvent-exposed helical sites, MOMD spectral simulations using also a single anisotropic motional component were performed for the spectrum of T4L68RX72 on CNBr, with the only important difference in the value of principal hyperfine splitting, A_{zz}. The 37.5 G determined at -50°C was substituted by the 36.7 G measured in liquid nitrogen. The best fit (Figure 5.7, red curves, and Table 5.1) requires a fast internal motion with a correlation time $\tau_R \approx 3.0$ ns, and an extremely high degree of order (S = 0.93) that can be described as motion confined within a cone of half-angle ≈ 12.5° (for 72R1 the half-angle ≈ 37°). This finding was in accordance with the results described for T4L5RX9 on CNBr.

The MOMD model[77] allows for the anisotropic motion of a nitroxide due to a restoring potential determined by the properties of the side chain (microscopic order), but with a random distribution of the protein with respect to the external field (macroscopic disorder), thus providing an order parameter and the rate of the motion. Within the context of this motional model (rapid anisotropic rotation), it has been pointed out by Hubbell and McConnell[78,79] that the spectrum of a spin label experiencing such motion can be approximated using a time-independent effective Hamiltonian. Within this model, the motion is assumed to be sufficiently rapid to average the magnetic parameters of the nitroxide over the space of the restricted motion. At X-band frequency, the hyperfine interactions dominate, thus the value of A-tensors, particularly $2A_{zz'}$, should be "effectively" averaged in the absence of motion ($\tau_R \gg 10$ ns).

In fact, taking $2A_{zz'}$ = 69.5 G and assuming an axially symmetric motion in a cone ($A_{zz'} \gg A_{xx'} \approx A_{yy'}$), a reasonably good fit can be achieved for the experimental spectrum of T4L68RX72

on CNBr (Figure 5.7, blue curves, and Table 5.1). This result compellingly supports the "fast rate, high order" motional model for the internal dynamics of RX.

Table 5.1 Parameters for simulations

	$<R>/s^{-1}$	τ_R/ns	S	c_0^2	α_D/°	β_D/°	γ_D/°
MOMD-X band	7.75	2.96	0.930	14.33	0	0	0
MOMD-Q band	7.99	1.71	0.907	11.02	0	1.15	0
H_{eff}-X band	n.a.	∞	n.a.	n.a.	6.79	6.96	24.90
H_{eff}-Q band	n.a.	∞	n.a.	n.a.	0	10.79	0

For the MOMD model at both X- and Q-band, the magnetic parameters used for simulations are as follows: $A_{xx} = 6.31G, A_{yy} = 5.37G, A_{zz} = 36.74G;\ g_{xx} = 2.00800 \pm 0.00015, g_{yy} = 2.00586 \pm 0.00015, g_{zz} = 2.00199 \pm 0.00005$; For effective Hamiltonian (H_{eff}) model at both X- and Q-band, the magnetic parameters used for simulations are as follows: $A_{xx} = 7.17G \pm 0.5G, A_{yy} = 5.29 \pm 0.5G, A_{zz} = 34.77 \pm 0.05G;\ g_{xx} = 2.00829 \pm 0.00025, g_{yy} = 2.00573 \pm 0.00025, g_{zz} = 2.00251 \pm 0.00001$.

In the MOMD model, a restoring (ordering) potential that constrains the spatial extent of the motion is introduced to the simulation of anisotropic motions. $< R >= \sqrt[3]{R_{xx}R_{yy}R_{zz}}$ is log10 of the average rotational diffusion tensor; τ_R is the rotational correlation time; $S = -\frac{1}{2} < (3\cos^2\theta - 1) >$ is the order parameter; c_0^2 is a scaling coefficient for the potential; θ is the instantaneous angle between the z-axis of the diffusion tensor and the symmetry axis of the potential; the diffusion tilt angles α_D, β_D, γ_D between the rotational diffusion and magnetic frames are defined as the Euler angles which are required for rotation of the magnetic frame into the diffusion frame.

It is known that the EPR spectra obtained at different microwave frequencies have a varying degree of sensitivity to motions at different time scales[80]. At high frequencies, the slower motion may show as just a dynamically frozen snapshot and thus the rate remains undetermined, but the faster motions can be better captured and are fully resolved in the lineshapes than at lower frequencies where they are averaged out. The EPR spectra recorded at different frequencies can be fit simultaneously with a common set of magnetic parameters. This way, the variation identified by comparing the spectra recorded at more than one frequency facilitates the resolution

of motional modes on different timescales.

Q-band (34GHz) CW-EPR spectra were measured for the same sample (T4L68RX72 on CNBr) as used in X-band experiments. Moreover, both MOMD and effective Hamiltonian models were tested for the spectral simulation. The results (Figure 5.7 and Table 5.1) show that an adequately good fit can be obtained for both Q-band and X-band spectra using the same set of parameters with reasonable differentiation (mainly the g-tensors which are poorly resolved in X-band spectra). Furthermore, the slight decrease in the τ_R value obtained from the Q-band MOMD fit substantiates that Q-band spectra are endowed with enhanced sensitivity for faster dynamics.

The multifrequency global fits support the earlier finding of RX exhibiting a highly anisotropic internal dynamic mode of strongly restricted amplitude, which confirms its application as the reference spin label of maximum rigidity, and thus one of the most promising probes in slow motion detection or distance measurements.

5.2.2 Probing dynamics in the μs-ms time range with RX on solvent-exposed α-helical sites

The aim is to prove the effectiveness of the proposed methodology for revealing dynamics in the time range of μs-ms, therefore, well-behaved sites that were extensively studied in previous work were selected for the experiments in this section. No fast or largescale backbone motions were expected for the regions at which the chosen sites locate, minimizing contributions from relative movements between spin labels and the protein body. Moreover, all chosen sites (except 27C and 31C of HoloMb) reflect a single dynamic state in CW-EPR lineshape simulation of their corresponding R1-labeled samples, suggesting no existence of conformational exchanges.

Due to the complexity of the ST-EPR mechanism and instrument setup, empirical parameters from spectra are used to determine values of correlation times (τ_R) by calibration

curves developed from standards possessing isotropic rotational motions of known τ_R. Conventionally used parameters include line-height ratios at different spectral positions[81] (as noted in the following figures), and the integrated spectral intensity[82] (I_{ST}).

As introduced in chapter 3, ST-EPR is sensitive to any process that influences the saturation during the time course of T_1 relaxation, directly or indirectly. Both experiments and simulations have shown that under the V_2' measurement scheme, spectral ratios retain the sensitivity to the orientational dependence and anisotropy of the detected slow motions, while the integral is more sensitive to changes in T_1 and B_1 (effective field strength).

In this work, the apparent correlation times are mainly derived by line-height ratios and should be considered as a qualitative and relative estimation of the **time range** of motions, not as accurate absolute values. Some further discussions can be found in the following sections. Theoretically and practically, each spin label and/or protein has its uniqueness that leads to discrepancies in τ_R obtained from different parameters. Structurally, the geometry influences the polarity of different side chains, which affects saturation-relaxation properties such as the intrinsic T_1 relaxation times. Dynamically, either the anisotropy of motions or multiple dynamic substates[83] can lead to deviation from values calibrated from the isotropic rotation model.

It is less reliable to determine accurate values of τ_R from I_{ST} in which more uncertainties accumulate. The intensity parameter reports an overall response and possesses a higher sensitivity to changes in physical parameters which can be easily differentiated by different instruments, resonators, sample specifications, etc. Instead, line-height ratios in three different regions of the magnetic field have varying sensitivities to orientations and amplitudes of motions. The center-field ratio (C'/C) is more dependent on faster motions (10^{-7}s~10^{-5}s) and local interactions around the spin. Rather, low- and high-field ratios (H''/H and L''/L) show

greater sensitivity in the time range of 10^{-5}s~10^{-3}s. The actual application of these different parameters will demonstrate the aspects and usefulness of the different ratios.

5.2.2.1 ST-EPR at ambient conditions

Sites have been picked from solvent-exposed sites of well-packed helix B, helix E, helix G, and helix H with low B-factors in the crystal structure of HoloMb (Figure 5.8 (A)). In solution, all helices exhibit low backbone mobility as shown by both NMR and CW-EPR. Helix G and H are known to retain folded even in myoglobin's low pH molten globule state as one of the core helices (A-G-H). For T4L (Figure 5.8 (B)), both helix C and helix H are stable structures and have been extensively studied in previous work.

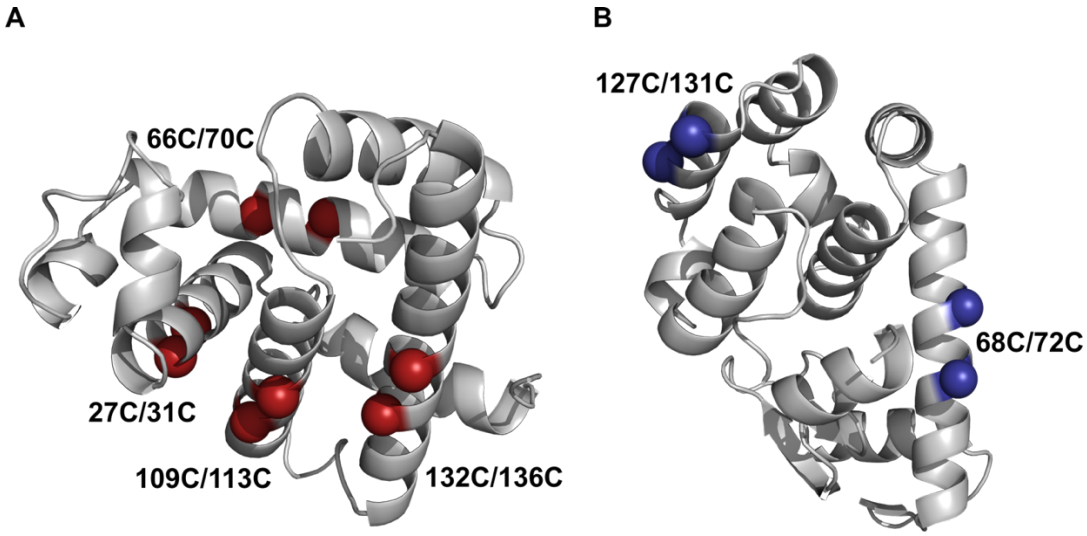

Figure 5.8 (A) Ribbon diagram of HoloMb (PDB code 2MBW) showing the solvent-exposed sites used in this study. The red spheres at the Cα indicate cysteine residues where spin labels are introduced; (B) Ribbon diagram of pseudo-WT T4L (PDB code 3LZM) showing the solvent-exposed sites used in this study. The blue spheres at the Cα indicate cysteine residues where spin labels are introduced.

Figure 5.9 shows the CW-EPR and ST-EPR spectra measured for corresponding mutants at room temperature. All samples were covalently attached to CNBr-Sepharose to remove rotational

diffusion. The ambient conditions in this dissertation refer to an environment where the attached proteins are placed in aqueous solutions at room temperature. The CW-EPR spectra at all sites show prominent features as the powder pattern (large $2A_{zz'}$, narrow linewidth, well-resolved lineshapes) and are hardly distinguishable from each other. Slight variations were only observed in the central field and a relatively decreased value of $2A_{zz'}$ for 132RX136, which will be revisited. It is obvious that the dominant dynamics of these mutants were not detectable within the ps-ns motional regime, leading to the insensitivity of CW-EPR spectral lineshapes. Both the strong immobilization of RX and rigid attachment to solid supports appear to be effective in restricting the nanosecond motions of all mutants studied.

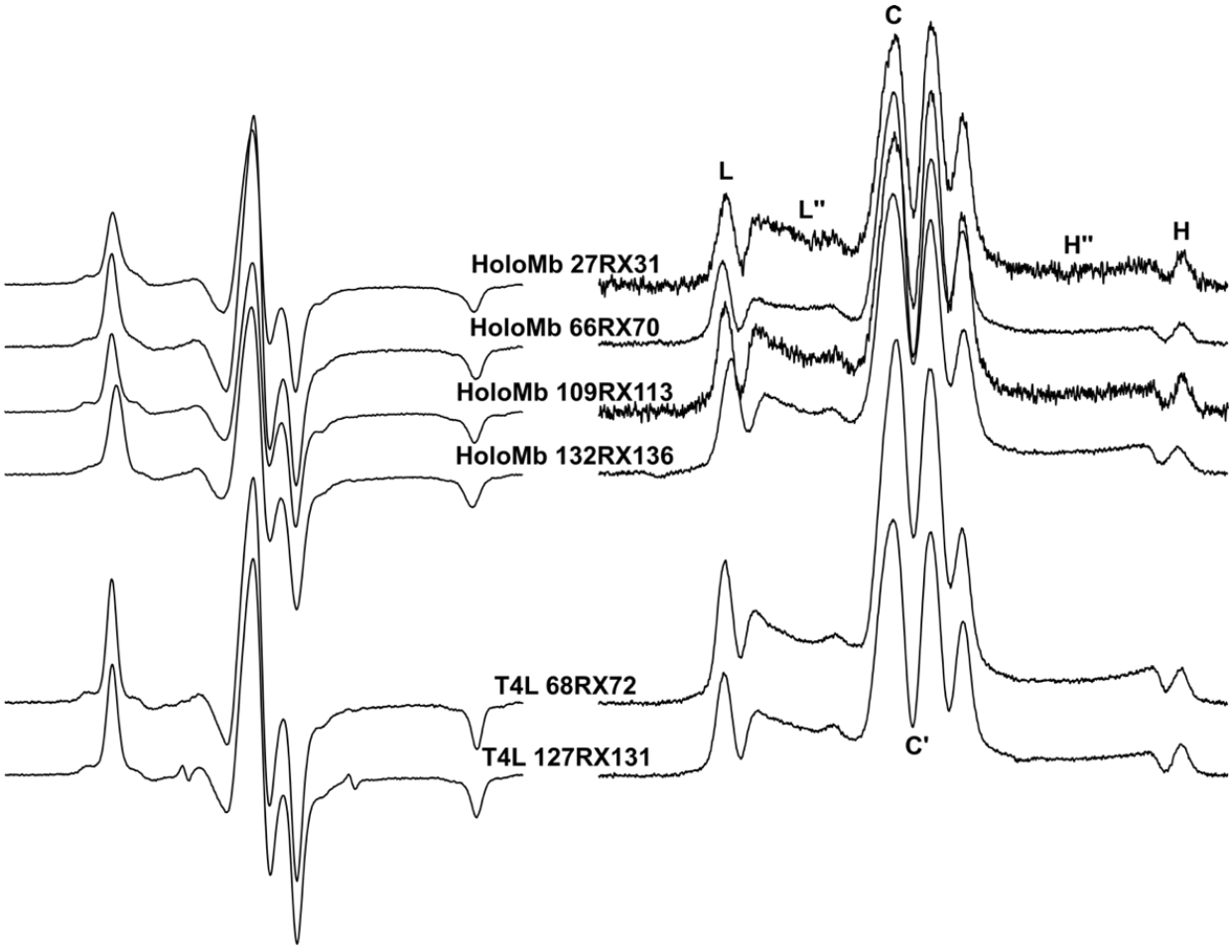

Figure 5.9 CW-EPR and ST-EPR spectra of RX-labeled HoloMb and T4L mutants at room temperature. All mutants were attached to CNBr-activated Sepharose. The magnetic field scan width is 100 G. Line heights used to calculate parameters are defined as shown, with the following explanations: All line heights are measured with respect to the baseline. L is the resolved peak in the low field. L" is defined as the line height at the field position 10 Gauss to the right of L. Similarly, H is the resolved peak in the high field, and H" is 15 Gauss to the left. The C and C' are the first peak and trough in the center.

In contrast, more spectral details are resolved in the ST-EPR lineshapes (see section 5.3 for complete data of parameters). While the overall lineshapes of examined sites are qualitatively similar, the anisotropic nature of detected dynamics is obvious from the discrepancies between parameters, which could originate from either the motional mode of protein, or the highly ordered RX. The H''/H parameter is more dependent on anisotropic features and amplitude of motions[84], due to the higher intrinsic sensitivity to angular changes of the corresponding manifold ($m_I = -1$), reporting dynamics with correlation times around >50μs. Instead, from the L''/L parameters, the motion with correlation time around 20~30μs was generally observed for all mutants in which the solvent-accessible helical sites were labeled.

The qualitatively similar lineshapes suggest that a certain type of motional mode in the microsecond time range is generally detected on helical sites of two globular proteins, of which the apparent correlation times are all in the same order of gratitude. Some basic conclusions could be drawn by comparing the results of T4L68RX72 and T4L127RX131. First, close values of both L''/L and H''/H parameters indicate that the microsecond dynamics of both mutants are substantially the same, which is reasonably expected for sites from topographically same regions under highly similar environments. Complementarily, the variations coherently observed in I_{ST} and C'/C parameters reveal the existence of differentiated backbone fluctuations on a relatively fast time scale, considering that these parameters are more sensitive to sub-microsecond

dynamics and local interactions.

Indeed, previous studies[62,72] using R1 suggested that the helix H possessed a higher degree of mobility, judging from the lower order parameter of 131R1 to 72R1 obtained in spectral simulation. However, as all motions are coupled to the internal motion of the R1 side chain, there is no direct evidence in the ps-ns time range confirming this structural origin of high mobility. Due to the strong immobilization of RX, unlike 72R1 and 131R1, the CW-EPR spectra of 68RX72 and 127RX131 are essentially identical (with negligible amounts of free spins), clearly excluding the possible contribution from side chain rotameric exchange.

Moreover, the results imply that the characteristic time scale of the higher backbone mobility of helix H detected by ST-EPR is most probable to fall in the range of < 10μs, as it seems not sensible to L''/L parameters. It is unlikely that the difference in the H''/H parameter originates from the backbone fluctuation of relatively small amplitude, which instead might be the consequence of more complicated motional mode and/or interactions.

Among the four HoloMb mutants, the value of the H''/H parameter of 132RX136 was exceptionally large, with its L''/L parameter also reporting the longest correlation time. Either additional interactions or backbone rigidity could lead to a slow effective correlation time. In the CW-EPR study of HoloMb by Lopez et al., the spectrum of 132R1 was fitted with a very high order parameter for R1 (0.68), suggesting the possibility of steric interactions between the nitroxide ring and its surroundings. This section of helix H was also reported to exhibit low B-factor values and minimal local fluctuations.

It needs to be pointed out that the CW-EPR of 132RX136 exhibited a smaller $2A_{zz'}$ value, implying that the nitroxide could be residing in a more hydrophobic environment. It has also been suspected that the formation of crosslink when generating the RX side chain could distort

the local geometry to enforce the extension of helicity to the i+4 position. Thus, it appears conceivable, that the attachment of RX to 132C and 136C induced a change in the tilt angle of the helix, causing certain degrees of hindrances to the nitroxide. More experiments are needed to distinguish whether such a distortion could be the structural origin of the long apparent correlation time.

In conclusion, using the immobilized side chain RX and stationary phase attachment has been proven practical for detecting slow dynamics of spin labels on solvent-exposed helix sites. On solid supports, protein dynamics with correlation times up to ~150 μs can be resolved from high-field ratios of RX-labeled samples. It is the first time that motional modes of helical sites whose lifetimes are in the range of sub-milliseconds have been directly described using standard CW-EPR equipment at ambient conditions.

5.2.2.2 ST-EPR in rigid limit

To confirm that the detectable time range of slow motions can reach the previously published rigid limit for ST-EPR spectra ($>10^{-3}$ s) using the currently applied apparatus, precipitated hemoglobin labeled with 6-MSL[26,85] was prepared. Hemoglobin is a model system for studying isotropic Brownian rotational diffusion and has been commonly used to determine the reference curves of correlation times for ST-EPR. For comparison, we also prepared precipitated, RX-labeled T4L mutants.

While there exist differences mainly in the center field, two ST-EPR lineshapes (Figure 5.10 (A)) are highly similar even though completely different spin labels and proteins were measured, providing a reliable estimate of the rigid limit. From the H''/H parameters, the motion with correlation time >1 ms was observed for both samples, indicating that there is very little, if any,

residual segmental flexibility, which is consistent with previously published results for precipitated proteins. Judging from the variations reflected in CW-EPR spectra, the differences in center peaks are unlikely to arise from motional effects in the millisecond range. Here, this result validates the equivalence and effectiveness of the current experiment for detecting slow motions as long as in the millisecond time range.

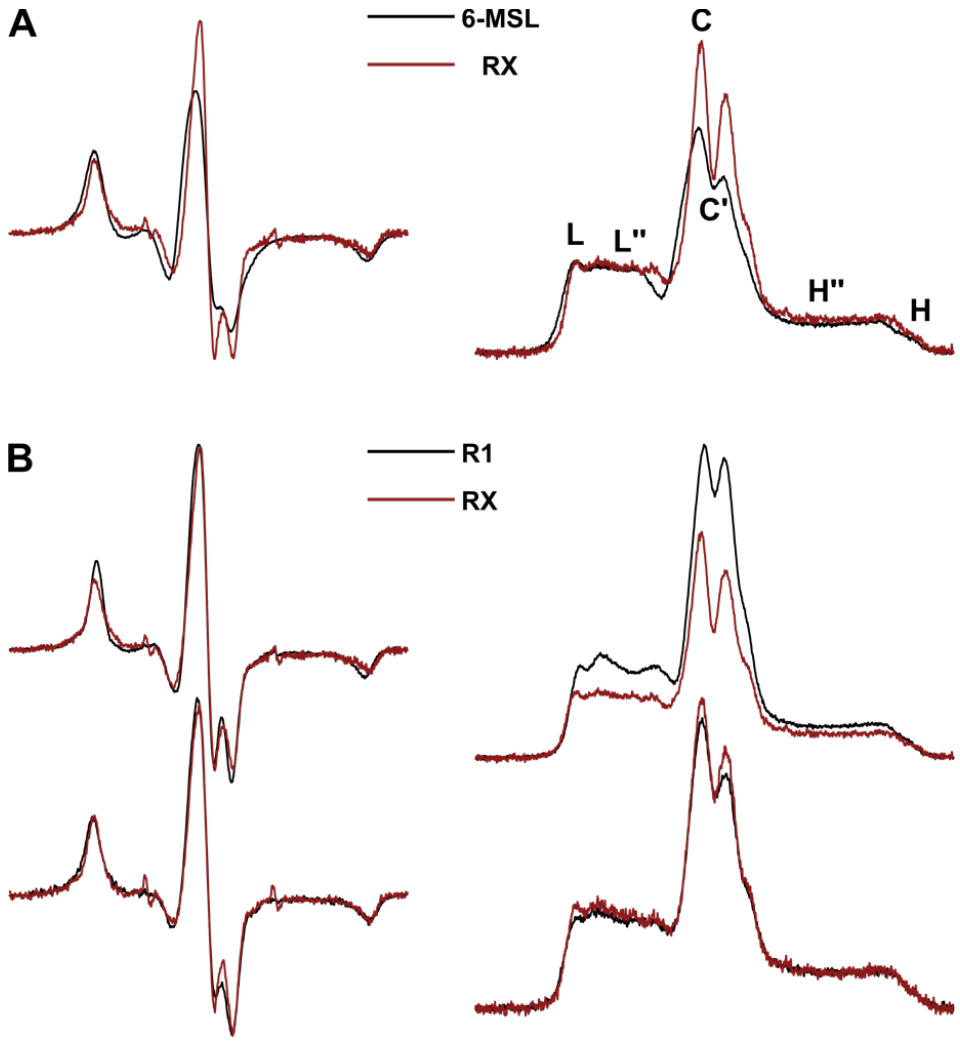

Figure 5.10 CW-EPR and ST-EPR spectra of precipitated proteins: (A) Hemoglobin labeled with 6-MSL and T4L68RX72; (B) upper: T4L68RX72 and T4L72R1; lower: T4L127RX131, T4L131R1. The magnetic field scan width is 100 G. Both CW-EPR and ST-EPR spectra were normalized to the spin count calculated by double integration of V_1 spectra (CW-EPR at non-saturating low power, see chapters 3 and 8).

In the precipitated state, the microenvironment surrounding the nitroxide is rather complicated. To better understand this immobilization state, effects from the labeling sites and spin label side chains to the lineshapes were explored with the maximized rigid side chain RX and the more mobile R1 (Figure 5.10 (B)). Results showed that the L''/L parameters of all four mutants were almost identical (see section 5.3). All H''/H parameters reported on motions with correlation times >1.5 ms, which confirms that neither the backbone fluctuation nor the side chain flexibility is sufficient to influence the ST-EPR lineshape of precipitated samples.

The elimination of contribution from its internal mobility of R1 could arise from a complete immobilization of the side chain. The I_{ST} of 72R1 is particularly large, suggesting a longer T_1 which is also observed when the side chain is less solvent accessible (see chapter 4), e.g., when buried in the hydrophobic interior. Indeed, the relatively broad linewidths (as compared to the linewidths from spectra of labeled proteins attached to solid supports) in CW-EPR spectra imply the existence of heterogeneity of the environment, which could be associated with more direct contact to the nitroxide within the micro 'crystal lattice' of precipitated proteins. Further discussion can be found in the following section.

5.2.2.3 Exploring the μs-ms dynamics of immobilized proteins under various conditions

To better understand the nature of the microsecond dynamics observed from attached proteins in ST-EPR spectra, labeled mutants were immobilized under various conditions and ST-EPR spectra were measured (Figure 5.11). To obtain the reference corresponding to the slowest motion of labeled proteins, samples were immobilized by two different preparation methods. A portion was precipitated in a saturated ammonium sulfate solution. Another portion was firstly tethered to the CNBr-activated Sepharose, then crosslinked by a sufficient amount of

glutaraldehyde. A Schiff base is formed between ε-amino groups of lysine and aldehyde functions on monomeric and polymeric forms of glutaraldehyde. As lysine normally distributes across the whole protein, this strategy can 'lock' the protein internally *via* covalent bonds between structural elements where the lysine locates.

Both precipitation and crosslinking are widely used (e.g., in solid-state NMR[86–90]) to immobilize proteins in order to make the slow internal motions of proteins accessible to spectroscopic detection. Resembling a polycrystalline status[91–93], it is likely that there are direct protein-protein contacts in the precipitated proteins. Any large-scale motions, both global and segmental, could be restricted by either confine of the lattice or protein interactions. Though there is no atomic-level structure, the capacity of precipitated proteins exhibiting nicely resolved solid-state NMR signals has reflected the existence of only a considerably small amount of residual fluctuations but the protein is mostly immobilized.

As a comparison, glutaraldehyde crosslinking should quench global motions by the formed matrix without affecting internal dynamics, as this matrix is 'softer' than the micro-lattices in precipitation. For proteins that are already tethered to the solid support, extensive crosslinking should reinforce the elimination of any residual global rotational and translational motion. Most of the large-scale segmental motions of which correlation times are longer than 10μs should still be retained, at least not as much diminished as in the precipitation. This has been implied by both results from solid-state NMR studies[86,88,89] and early ST-EPR studies of skeletal proteins[94]. Hence, the glutaraldehyde preparation serves as a reference showing how slow is the protein when there are only 'pure' internal motions, while the precipitated preparation stands for the slowest dynamics for a hydrated protein (compared to lyophilization).

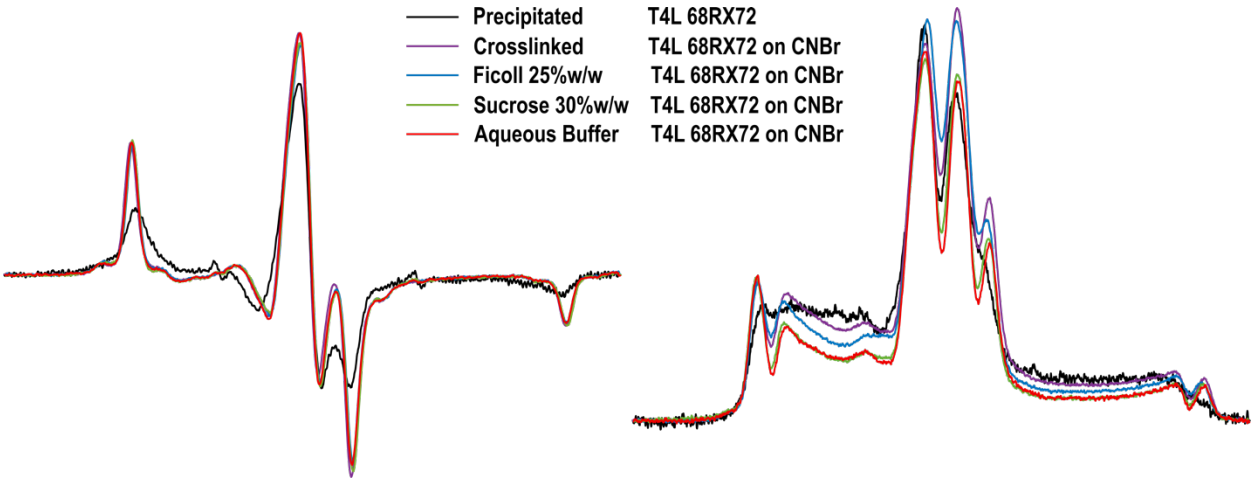

Figure 5.11 ST-EPR and CW-EPR spectra of T4L68RX72 under different conditions. All ST-EPR lineshapes are scaled by the height of the low-field peak for a better comparison. All CW-EPR spectra are normalized to the spin count calculated by double integration.

Measuring ST-EPR showed that on the same site, the precipitated protein exhibited dynamics >1ms, while the crosslinked protein exhibited dynamics ~200 μs (see next section for parameters). Instead, proteins on the CNBr-activated Sepharose reported dynamics ~80 μs. The close order of gratitude in the time scale (around 100 μs) again manifests the validity that it is mainly the internal dynamics of proteins detected by ST-EPR. There are faster motional modes existing in the non-crosslinked attached sample, leading to a smaller apparent correlation time. The origin of it could be residual global motions relative to the solid support, or it could be some internal fluctuations being suppressed more or less by the matrix formed in crosslinked samples. Considering the heterogeneity of protein dynamics, it is reasonable to speculate that some motions carried out by highly flexible structural elements (e.g., loops) could still be restricted by the soft yet extensive crosslinking.

One approach that may shed light on this is to measure the response of attached proteins to solvent perturbation by sucrose and Ficoll[95–99]. It was shown in previous work that sucrose, as a stabilizing osmolyte, can both slow down the rotational diffusion of the whole protein by its

micro-viscosity, and shift the conformational equilibria by osmolarity to identify conformational exchange between substates. While Ficoll is known as a crowding agent favoring the state of a protein with the smaller excluded volume, it can also slow down the rotational diffusion as a macromolecule. Both reagents have been used in SDSL-EPR studies to restrict the rotational diffusion of small proteins in solution.

To distinguish the possible origin of motions, sucrose (30% in w/w) or Ficoll (25% in w/w) was added to protein samples that were already attached to CNBr-activated Sepharose. CW-EPR spectra show no noticeable change upon the addition of sucrose or Ficoll, confirming that there is no fast motion being induced by either the osmolarity or crowding effects, and the time scales of residual dynamics are likely in the μs-ms range.

From ST-EPR spectra, there is a discrepancy between two empirical parameters reporting on correlation time, the spectral height ratios and the integral. ST-EPR spectra of sucrose-added samples have highly similar lineshapes to tethered samples in just aqueous buffer but possess a higher value of intensity integral. It can be inferred that the addition of 30% w/w sucrose has no effect on the motions of tethered proteins but possibly on the relaxation (other pathways of relaxation rather than the rotational motions of proteins and/or spin labels). More experiments are needed to elucidate the complicated mechanism of how relaxation may be influenced by sucrose. One reasonable explanation is that sucrose slows down the translational diffusion of dissolved oxygen, which lowers the collision rate and thus the relaxation rate of nitroxides. It has been shown in other studies[6,7,100–102] that the integral of ST-EPR does respond to changes in oxygen percentages in the sample, while the lineshapes stay the same. The fact that lineshapes of sucrose-added samples showed no significant change implies that the additional mobility in the non-crosslinked, attached sample is not residual global motions in the macroscopic level such as

the rotation relative to the solid supports, which would show response to changes in viscosity.

For the Ficoll-added samples, both the lineshapes and the integral differ from tethered samples in the buffer. The determined parameters revealed slower motion, but it seems more likely that the detected dynamics are due to crowding effects. Independent evidence from different studies suggests contrasting effects of crowding[97,99]: Crowding effects on proteins are commonly considered from two perspectives, the entropic contributions arising from the macromolecular nature of crowders, and the enthalpic contribution arising from chemical interactions between crowders and proteins. Considering that the difference is observed between Ficoll and its monomer, sucrose, it is highly possible that in our case the modulation of motions is driven mainly by entropy. Otherwise, sucrose-added samples should show similar responses but in different magnitudes due to the chemical similarity between sucrose and Ficoll.

Ficoll-added samples exhibited dynamics ~150 μs, which is intermediate between values of crosslinked and non-crosslinked. It is hard to tell so far whether the crosslinking and the crowding restrict the protein in a similar way but to a different extent, or they restrict different types of motional modes. To be able to tell this, measurements on different sites probing the response of different regions, and/or using different spin label side chains (see chapter 6) are necessary. In fact, similar effects upon the addition of sucrose and/or Ficoll were observed from ST-EPR spectra of HoloMb mutants that were also attached to CNBr-Sepharose (Figure 5.12). Both Ficoll-added mutants reported slower dynamics, while lineshapes of sucrose-added samples had no significant change, yet the integrals were higher.

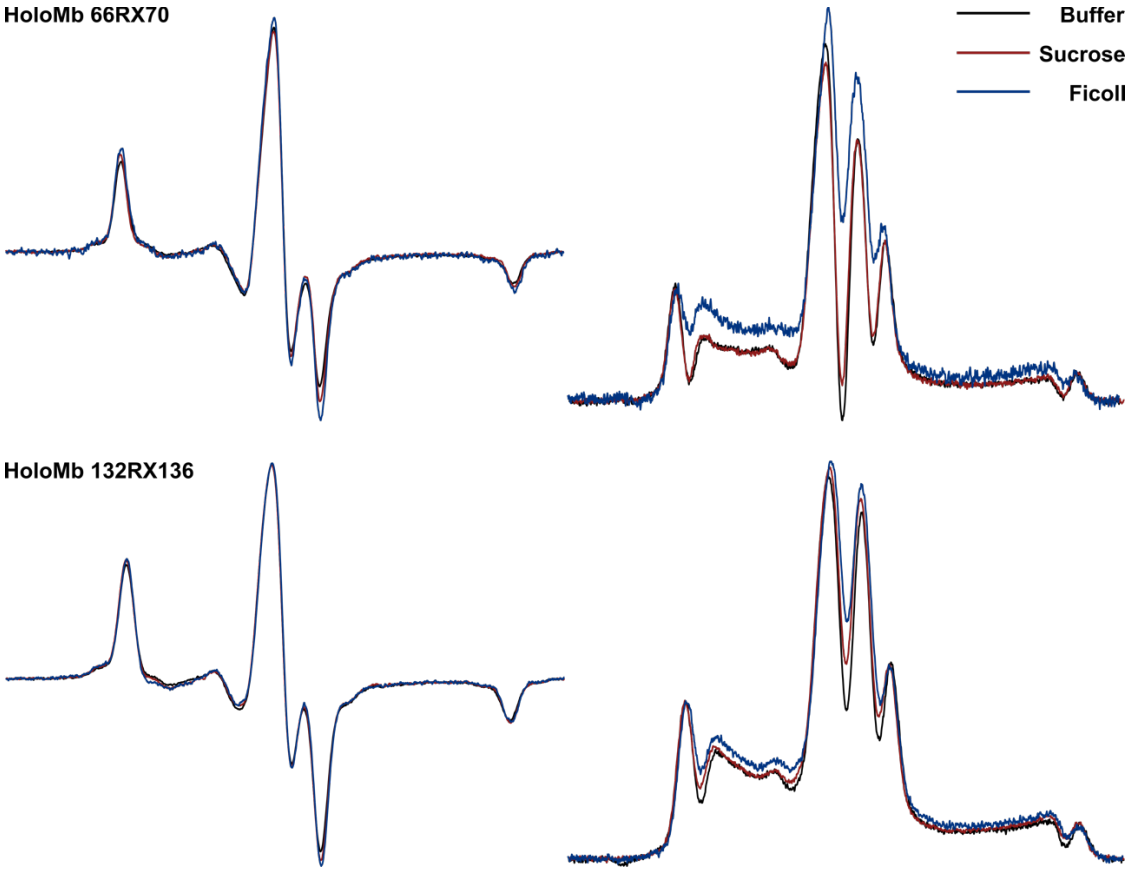

Figure 5.12 ST-EPR and CW-EPR spectra of HoloMb66RX70 and HoloMb132RX136 on CNBr-activated Sepharose, in buffer, in sucrose 30% w/w, in Ficoll 25% w/w.

One possibility is that the Ficoll restricts segmental movements by directly contacting proteins like in the precipitation. The other possibility is that the protein adopts a different conformation with a smaller excluded volume and less mobility, which means a higher energy barrier for the internal motions of the protein. Indistinguishable CW-EPR lineshapes indicate that the local environment experienced by the spin label is largely retained, suggesting a collective motion concerning the coherent movement of multiple side chains.

Also, the insensitivity of ST-EPR lineshapes to osmolarity suggests that there is no distinct difference in solvation surface area during the occurrence of this motion. One possibility is that one or a few helices either rotate as a whole about its longitudinal axis, or twist on the solvent-

exposing surface, leading to a different packing of side chains or a rearrangement of bound water molecules in the interior. Either model can introduce higher internal friction of proteins in the thermodynamic equilibrium, hence slowing down its internal dynamics.

Though there are still gaps between these qualitative descriptions of dynamics and a complete motional model, these results demonstrate the versatility and sensitivity of ST-EPR in the μs-ms time domain. The intricate hierarchy of protein internal dynamic modes has been dissected under several different conditions: rigidly confining environment (precipitation/crystal lattice), soft gel/matrix (chemical crosslinking), crowded media (Ficoll), and the aqueous solution of different viscosities (sucrose). It was demonstrated that the methodology integrating both the stationary-phase techniques and a highly restricted spin label side chain is capable to extend the applicability of ST-EPR for slow motion detection to small protein systems at ambient conditions. Some extended discussions will be shown in the next chapter, where other stationary-phase schemes and spin labels are examined.

5.3 Tabulated ST-EPR empirical parameters and correlation times

All empirical parameters and correlation times measured from ST-EPR spectra of HoloMb and T4L mutants that were labeled by RX are tabulated on the following pages, including the precipitated 72R1 and 131R1 (and R1f, RY which will be introduced in chapter 6). The signal-to-noise was estimated from the baseline and peak intensity of each spectrum and also included as the +/- deviation for values of L"/L and H"/H, and propagated to the corresponding correlation times ($\tau_{R,\,L"/L}$ and $\tau_{R,\,H"/H}$).

1. RX on different helical sites (HoloMb&T4L) in buffer

	L''/L	τ_R/sec	C'/C	τ_R/sec	H''/H	τ_R/sec	Integral
HoloMb 27RX31 CNBr	0.57	2.9×10^{-5}	0.27	1.2×10^{-5}	0.52	5.0×10^{-5}	
HoloMb 66RX70 CNBr	0.46	1.7×10^{-5}	-0.05	4.8×10^{-6}	0.61	7.2×10^{-5}	0.2138
HoloMb 109RX113 CNBr	0.51	2.2×10^{-5}	0.38	1.8×10^{-5}	0.43	3.2×10^{-5}	
HoloMb 132RX136 CNBr	0.57	2.9×10^{-5}	0.39	1.8×10^{-5}	0.81	1.5×10^{-4}	0.3308
T4LpWT-68RX72 CNBr	0.48	1.9×10^{-5}	0.46	2.3×10^{-5}	0.65	8.4×10^{-5}	0.4707
T4LpWT-127RX131 CNBr	0.52	2.3×10^{-5}	0.19	9.8×10^{-6}	0.57	6.1×10^{-5}	0.3216

2. Precipitation in $(NH_4)_2SO_4$

	L''/L	τ_R/sec	C'/C	τ_R/sec	H''/H	τ_R/sec	Integral
T4LpWT-72R1	0.92	1.0×10^{-4}	0.83	2.8×10^{-4}	1.80	4.1×10^{-3}	0.9750
T4LpWT-68RX72	0.93	1.0×10^{-4}	0.56	3.4×10^{-5}	1.57	1.6×10^{-3}	0.6698
T4LpWT-72R1f	0.94	1.0×10^{-4}	0.78	1.4×10^{-4}	2.44	∞	1.2407
T4LpWT-72RY	1.08	1.6×10^{-4}	0.88	7.0×10^{-4}	2.80	∞	1.5959
T4LpWT-131R1	0.95	1.1×10^{-4}	0.73	9.0×10^{-5}	1.88	6.4×10^{-3}	0.7355
T4LpWT-127RX131	0.89	9.0×10^{-5}	0.67	6.1×10^{-5}	1.64	2.1×10^{-3}	0.7670
T4LpWT-131R1f	0.98	1.2×10^{-4}	0.79	1.6×10^{-4}	1.99	1.4×10^{-2}	1.1161
T4LpWT-131RY	1.04	1.4×10^{-4}	0.84	3.0×10^{-4}	2.17	2.1×10^{-1}	1.5866

3. T4LpWT68RX72 in various conditions

	L''/L	τ_R/sec	C'/C	τ_R/sec	H''/H	τ_R/sec	Integral
T4LpWT-68RX72 precipitation	0.93	1.0×10^{-4}	0.56	3.4×10^{-5}	1.57	1.6×10^{-3}	0.6698
T4LpWT-68RX72 CNBr-glutaraldehyde	0.74	5.5×10^{-5}	0.65	5.6×10^{-5}	0.88	1.9×10^{-4}	0.6960
T4LpWT-68RX72 CNBr-Ficoll	0.61	3.4×10^{-5}	0.70	7.3×10^{-5}	0.80	1.4×10^{-4}	0.8277
T4LpWT-68RX72 CNBr-Sucrose	0.48	2.0×10^{-5}	0.52	3.0×10^{-5}	0.63	7.9×10^{-5}	0.6546
T4LpWT-68RX72 CNBr-Buffer	0.48	1.9×10^{-5}	0.46	2.3×10^{-5}	0.65	8.4×10^{-5}	0.4707

4. Sucrose/Ficoll effects

	L''/L	τ_R/sec	C'/C	τ_R/sec	H''/H	τ_R/sec	Integral
HoloMb 66RX70 CNBr-Buffer	0.46	1.7×10^{-5}	-0.05	4.8×10^{-6}	0.61	7.2×10^{-5}	0.2138
HoloMb 66RX70 CNBr-Sucrose	0.46	1.7×10^{-5}	-0.04	6.4×10^{-6}	0.58	6.4×10^{-5}	0.3221
HoloMb 66RX70 CNBr-Ficoll	0.63	3.8×10^{-5}	0.46	2.3×10^{-5}	0.88	1.9×10^{-4}	0.5888
HoloMb 109RX113 CNBr-Buffer	0.51	2.2×10^{-5}	0.38	1.8×10^{-5}	0.43	3.2×10^{-5}	
HoloMb 109RX113 CNBr-Sucrose	0.46	1.8×10^{-5}	0.48	2.6×10^{-5}	0.34	1.9×10^{-5}	
HoloMb 132RX136 CNBr-Buffer	0.57	2.9×10^{-5}	0.39	1.8×10^{-5}	0.81	1.5×10^{-4}	0.3308
HoloMb 132RX136 CNBr-Sucrose	0.57	3.0×10^{-5}	0.50	2.7×10^{-5}	0.85	1.7×10^{-4}	0.5181
HoloMb 132RX136 CNBr-Ficoll	0.63	3.7×10^{-5}	0.60	4.2×10^{-5}	1.02	2.9×10^{-4}	0.6422
T4LpWT-68RX72 CNBr-Buffer	0.48	1.9×10^{-5}	0.46	2.3×10^{-5}	0.65	8.4×10^{-5}	0.4707
T4LpWT-68RX72 CNBr-Sucrose	0.48	2.0×10^{-5}	0.52	3.0×10^{-5}	0.63	7.9×10^{-5}	0.6546
T4LpWT-68RX72 CNBr-Ficoll	0.61	3.4×10^{-5}	0.70	7.3×10^{-5}	0.80	1.4×10^{-4}	0.8277

5. Signal noises

	L''/L±Noise	τ_R±Noise/sec	H''/H±Noise	τ_R±Noise/sec
T4LpWT-68RX72 precipitation	0.93±0.03	$1.0 \pm 0.1 \times 10^{-4}$	1.57±0.14	$1.6 \pm 0.6 \times 10^{-3}$
T4LpWT-68RX72 CNBr-glutaraldehyde	0.74±0.01	$5.5 \pm 0.1 \times 10^{-5}$	0.88±0.01	$1.9 \pm 0.1 \times 10^{-4}$
T4LpWT-68RX72 CNBr-Ficoll	0.61±0.01	$3.4 \pm 0.1 \times 10^{-5}$	0.80±0.02	$1.4 \pm 0.1 \times 10^{-4}$
T4LpWT-68RX72 CNBr-Sucrose	0.48±<0.01	$2.0 \pm 0.1 \times 10^{-5}$	0.63±0.01	$7.9 \pm 0.5 \times 10^{-5}$
T4LpWT-68RX72 CNBr-Buffer	0.48±0.01	$1.9 \pm 0.05 \times 10^{-5}$	0.65±0.03	$8.4 \pm 0.8 \times 10^{-5}$
T4LpWT-127RX131 CNBr-Buffer	0.52±0.01	$2.3 \pm 0.1 \times 10^{-5}$	0.57±0.02	$6.1 \pm 0.6 \times 10^{-5}$
HoloMb 27RX31 CNBr-Buffer	0.57±0.04	$2.9 \pm 0.4 \times 10^{-5}$	0.52±0.09	$5.0 \pm 1.9 \times 10^{-5}$
HoloMb 66RX70 CNBr-Buffer	0.46±0.02	$1.7 \pm 0.1 \times 10^{-5}$	0.61±0.05	$7.2 \pm 1.3 \times 10^{-5}$
HoloMb 109RX113 CNBr-Buffer	0.51±0.03	$2.2 \pm 0.3 \times 10^{-5}$	0.43±0.08	$3.2 \pm 1.2 \times 10^{-5}$
HoloMb 132RX136 CNBr-Buffer	0.57±0.01	$2.9 \pm 0.1 \times 10^{-5}$	0.81±0.04	$1.5 \pm 0.2 \times 10^{-4}$

5.4 References

1. Fleissner, M. R. *et al.* Structure and dynamics of a conformationally constrained nitroxide side chain and applications in EPR spectroscopy. *Proc. Natl. Acad. Sci.* **108**, 16241–16246 (2011).
2. Bridges, M. D., Hideg, K. & Hubbell, W. L. Resolving Conformational and Rotameric Exchange in Spin-Labeled Proteins Using Saturation Recovery EPR. *Appl. Magn. Reson.* **37**, 363–390 (2010).

3. Hyde, J. S. & Thomas, D. D. New Epr Methods for the Study of Very Slow Motion: Application to Spin-Labeled Hemoglobin. *Ann. N. Y. Acad. Sci.* **222**, 680–692 (1973).
4. Thomas, D. D., Seidel, J. C., Hyde, J. S. & Gergely, J. Motion of subfragment-1 in myosin and its supramolecular complexes: saturation transfer electron paramagnetic resonance. *Proc. Natl. Acad. Sci.* **72**, 1729–1733 (1975).
5. Hidalgo, C., Thomas, D. D. & Ikemoto, N. Effect of the lipid environment on protein motion and enzymatic activity of sarcoplasmic reticulum calcium ATPase. *J. Biol. Chem.* **253**, 6879–6887 (1978).
6. Marsh, D. & Horváth, L. Influence of Heisenberg spin exchange on conventional and phase-quadrature EPR lineshapes and intensities under saturation. *J. Magn. Reson. 1969* **97**, 13–26 (1992).
7. Delmelle, M. Saturation transfer electron paramagnetic resonance. Influence of some experimental parameters on the spectra. *J. Magn. Reson. 1969* **51**, 245–251 (1983).
8. Páli, T., Livshits, V. A. & Marsh, D. Dependence of Saturation-Transfer EPR Intensities on Spin–Lattice Relaxation. *J. Magn. Reson. B* **113**, 151–159 (1996).
9. Livshits, V. A. & Marsh, D. Application of the out-of-phase absorption mode to separating overlapping EPR signals with different T1 values. *J. Magn. Reson.* **175**, 317–329 (2005).
10. Esmann, M. & Marsh, D. Local translational diffusion rates of membranous Na+,K(+)-ATPase measured by saturation transfer ESR spectroscopy. *Proc. Natl. Acad. Sci.* **89**, 7606–7609 (1992).
11. van den Dries, I. J., de Jager, P. A. & Hemminga, M. A. Sensitivity of Saturation Transfer Electron Spin Resonance Extended to Extremely Slow Mobility in Glassy Materials. *J. Magn. Reson.* **131**, 241–247 (1998).

12. Thomas, D. D. & Hidalgo, C. Rotational motion of the sarcoplasmic reticulum Ca2+-ATPase. *Proc. Natl. Acad. Sci.* **75**, 5488–5492 (1978).
13. Marsh, D. Molecular motion in phospholipid bilayers in the gel phase: long axis rotation. *Biochemistry* **19**, 1632–1637 (1980).
14. Fung, L. W.-M. & Johnson, M. E. Multiple motions of the spectrin-actin complex in the saturation transfer EPR time domain. *J. Magn. Reson. 1969* **51**, 233–244 (1983).
15. Horváth, L. I., Dux, L., Hankovszky, H. O., Hideg, K. & Marsh, D. Saturation transfer electron spin resonance of Ca2(+)-ATPase covalently spin-labeled with beta-substituted vinyl ketone- and maleimide-nitroxide derivatives. Effects of segmental motion and labeling levels. *Biophys. J.* **58**, 231–241 (1990).
16. Esmann, M., Sar, P. C., Hideg, K. & Marsh, D. Maleimide, Iodoacetamide, Indanedione, and Chloromercuric Spin Label Reagents with Derivatized Nitroxide Rings as ESR Reporter Groups for Protein Conformation and Dynamics. *Anal. Biochem.* **213**, 336–348 (1993).
17. Esmann, M., Hankovszky, H. O., Hideg, K., Pedersen, J. A. & Marsh, D. Vinyl ketone reagents for covalent protein modification. Nitroxide derivatives suited to rotational diffusion studies by saturation transfer electron spin resonance, using membrane-bound Na,K-ATPase as an example. *Anal. Biochem.* **189**, 274–282 (1990).
18. Esmann, M., Hankovszky, H. O., Hideg, K. & Marsh, D. A novel spin-label for study of membrane protein rotational diffusion using saturation transfer electron spin resonance. Application to selectively labelled Class I and Class II -SH groups of the shark rectal gland Na+/K+-ATPase. *Biochim. Biophys. Acta BBA - Biomembr.* **978**, 209–215 (1989).

19. James, Z. M., McCaffrey, J. E., Torgersen, K. D., Karim, C. B. & Thomas, D. D. Protein-Protein Interactions in Calcium Transport Regulation Probed by Saturation Transfer Electron Paramagnetic Resonance. *Biophys. J.* **103**, 1370–1378 (2012).
20. Thompson, A. R., Naber, N., Wilson, C., Cooke, R. & Thomas, D. D. Structural Dynamics of the Actomyosin Complex Probed by a Bifunctional Spin Label that Cross-Links SH1 and SH2. *Biophys. J.* **95**, 5238–5246 (2008).
21. Mello, R. N. & Thomas, D. D. Three Distinct Actin-Attached Structural States of Myosin in Muscle Fibers. *Biophys. J.* **102**, 1088–1096 (2012).
22. Thompson, A. R., Binder, B. P., McCaffrey, J. E., Svensson, B. & Thomas, D. D. Chapter Four - Bifunctional Spin Labeling of Muscle Proteins: Accurate Rotational Dynamics, Orientation, and Distance by EPR. in *Methods in Enzymology* (eds. Qin, P. Z. & Warncke, K.) vol. 564 101–123 (Academic Press, 2015).
23. Kuo, Y.-H. & Chiang, Y.-W. Slow Dynamics around a Protein and Its Coupling to Solvent. *ACS Cent. Sci.* **4**, 645–655 (2018).
24. Johnson, M. E. Apparent hydrogen bonding by strongly immobilized spin-labels. *Biochemistry* **20**, 3319–3328 (1981).
25. Johnson, M. E. Librational motion of an 'immobilized' spin label: hemoglobin spin labeled by a maleimide derivative. *Biochemistry* **17**, 1223–1228 (1978).
26. Thomas, D. D., Dalton, L. R. & Hyde, J. S. Rotational diffusion studied by passage saturation transfer electron paramagnetic resonance. *J. Chem. Phys.* **65**, 3006–3024 (1976).
27. Thomas, D. D., Ishiwata, S., Seidel, J. C. & Gergely, J. Submillisecond rotational dynamics of spin-labeled myosin heads in myofibrils. *Biophys. J.* **32**, 873–889 (1980).

28. Zucca, P., Fernandez-Lafuente, R. & Sanjust, E. Agarose and Its Derivatives as Supports for Enzyme Immobilization. *Molecules* **21**, 1577 (2016).

29. Mohamad, N. R., Marzuki, N. H. C., Buang, N. A., Huyop, F. & Wahab, R. A. An overview of technologies for immobilization of enzymes and surface analysis techniques for immobilized enzymes. *Biotechnol. Biotechnol. Equip.* **29**, 205–220 (2015).

30. Santos, J. C. S. dos *et al.* Importance of the Support Properties for Immobilization or Purification of Enzymes. *ChemCatChem* **7**, 2413–2432 (2015).

31. Rusmini, F., Zhong, Z. & Feijen, J. Protein Immobilization Strategies for Protein Biochips. *Biomacromolecules* **8**, 1775–1789 (2007).

32. Rosen, C. B. & Francis, M. B. Targeting the N terminus for site-selective protein modification. *Nat. Chem. Biol.* **13**, 697–705 (2017).

33. López, C. J., Fleissner, M. R., Brooks, E. K. & Hubbell, W. L. Stationary-Phase EPR for Exploring Protein Structure, Conformation, and Dynamics in Spin-Labeled Proteins. *Biochemistry* **53**, 7067–7075 (2014).

34. Butler, J. E. *et al.* The immunochemistry of sandwich elisas—VI. Greater than 90% of monoclonal and 75% of polyclonal anti-fluorescyl capture antibodies (CAbs) are denatured by passive adsorption. *Mol. Immunol.* **30**, 1165–1175 (1993).

35. Lu, J. R. *et al.* The Denaturation of Lysozyme Layers Adsorbed at the Hydrophobic Solid/Liquid Surface Studied by Neutron Reflection. *J. Colloid Interface Sci.* **206**, 212–223 (1998).

36. Esmann, M., Horvath, L. I. & Marsh, D. Saturation-transfer electron spin resonance studies on the mobility of spin-labeled sodium and potassium ion activated adenosine triphosphatase in membranes from Squalus acanthias. *Biochemistry* **26**, 8675–8683 (1987).

37. Ryba, N. J. P. *et al.* Rhodopsin mobility, structure, and lipid-protein interaction in squid photoreceptor membranes. *Biochemistry* **32**, 3298–3305 (1993).

38. Páli, T., Kleinschmidt, J. H., Powell, G. L. & Marsh, D. Nonlinear Electron Paramagnetic Resonance Studies of the Interaction of Cytochrome c Oxidase with Spin-Labeled Lipids in Gel-Phase Membranes. *Biochemistry* **39**, 2355–2361 (2000).

39. Kendrew, J. C. *et al.* Structure of Myoglobin: A Three-Dimensional Fourier Synthesis at 2 Å. Resolution. *Nature* **185**, 422–427 (1960).

40. Frauenfelder, Hans. *et al.* Proteins and pressure. *J. Phys. Chem.* **94**, 1024–1037 (1990).

41. Frauenfelder, H., McMahon, B. H. & Fenimore, P. W. Myoglobin: The hydrogen atom of biology and a paradigm of complexity. *Proc. Natl. Acad. Sci.* **100**, 8615–8617 (2003).

42. Springer, B. A. & Sligar, S. G. High-level expression of sperm whale myoglobin in Escherichia coli. *Proc. Natl. Acad. Sci.* **84**, 8961–8965 (1987).

43. Antonini, E. & Brunori, M. *Hemoglobin and myoglobin in their reactions with ligands*. (North-Holland Publishing Company, 1971).

44. Weiss, C., Kobayashi, H. & Gouterman, M. Spectra of porphyrins: Part III. Self-consistent molecular orbital calculations of porphyrin and related ring systems. *J. Mol. Spectrosc.* **16**, 415–450 (1965).

45. Kampen, E. J. van & Zijlstra, W. G. Determination of Hemoglobin and Its Derivatives. in *Advances in Clinical Chemistry* (eds. Sobotka, H. & Stewart, C. P.) vol. 8 141–187 (Elsevier, 1966).

46. van Kampen, E. J. & Zijlstra, W. G. Spectrophotometry of Hemoglobin and Hemoglobin Derivatives. in *Advances in Clinical Chemistry* (eds. Latner, A. L. & Schwartz, M. K.) vol. 23 199–257 (Elsevier, 1983).

47. Schechter, A. N. & Epstein, C. J. Spectral studies on the denaturation of myoglobin. *J. Mol. Biol.* **35**, 567–589 (1968).

48. Eaton, W. A. & Hochstrasser, R. M. Single-Crystal Spectra of Ferrimyoglobin Complexes in Polarized Light. *J. Chem. Phys.* **49**, 985–995 (1968).

49. Anderson, A. B. & Robertson, C. R. Absorption spectra indicate conformational alteration of myoglobin adsorbed on polydimethylsiloxane. *Biophys. J.* **68**, 2091–2097 (1995).

50. Engler, N. *et al.* Protein Dynamics in an Intermediate State of Myoglobin: Optical Absorption, Resonance Raman Spectroscopy, and X-Ray Structure Analysis. *Biophys. J.* **78**, 2081–2092 (2000).

51. López, C. J., Oga, S. & Hubbell, W. L. Mapping Molecular Flexibility of Proteins with Site-Directed Spin Labeling: A Case Study of Myoglobin. *Biochemistry* **51**, 6568–6583 (2012).

52. Matthews, B. W. Studies on Protein Stability With T4 Lysozyme. in *Advances in Protein Chemistry* (eds. Anfinsen, C. B., Richards, F. M., Edsall, J. T. & Eisenberg, D. S.) vol. 46 249–278 (Academic Press, 1995).

53. Matsumura, M. & Matthews, B. W. Control of Enzyme Activity by an Engineered Disulfide Bond. *Science* **243**, 792–794 (1989).

54. Chen, B. L., Baase, W. A., Nicholson, H. & Schellman, J. A. Folding kinetics of T4 lysozyme and nine mutants at 12 .degree.C. *Biochemistry* **31**, 1464–1476 (1992).

55. Chen, B. L., Baase, W. A. & Schellman, J. A. Low-temperature unfolding of a mutant of phage T4 lysozyme. 2. Kinetic investigations. *Biochemistry* **28**, 691–699 (1989).

56. Chen, B. L. & Schellman, J. A. Low-temperature unfolding of a mutant of phage T4 lysozyme. 1. Equilibrium studies. *Biochemistry* **28**, 685–691 (1989).

57. Harris, D. L. & Hudson, B. S. Photophysics of tryptophan in bacteriophage T4 lysozymes. *Biochemistry* **29**, 5276–5285 (1990).
58. Van Gilst, M. & Hudson, B. S. Histidine-tryptophan interactions in T4 lysozyme: 'Anomalous' pH dependence of fluorescence. *Biophys. Chem.* **63**, 17–25 (1996).
59. Lopez, C. J. Mapping molecular flexibility of spin labeled proteins on the nanosecond and longer time scales via CW lineshape analysis and osmolyte-perturbation EPR. (University of California, Los Angeles).
60. Bridges, M. D. Resolving Rotameric and Conformational Exchange in Spin Labeled Proteins at Biologically-Relevant Temperatures by Saturation Recovery Electron Paramagnetic Resonance. (University of California, Los Angeles).
61. Lerch, M. Touring the Conformational Landscape of Proteins with High-Pressure SDSL EPR Spectroscopy. (University of California, Los Angeles).
62. Columbus, L. M. Investigating backbone and side chain dynamics of α-helices in the nanosecond regime with site -directed spin labeling. (University of California, Los Angeles).
63. Guo, Z. Correlation of spin label side-chain dynamics with protein structure: Studies of T4 lysozyme with site-directed mutagenesis and x-ray crystallography. (University of California, Los Angeles).
64. Fleissner, M. R. X-ray structures of nitroxide side chains in proteins: A basis for interpreting distance measurements and dynamic studies by electron paramagnetic resonance. (University of California, Los Angeles).
65. Mchaourab, H. S., Oh, K. J., Fang, C. J. & Hubbell, W. L. Conformation of T4 Lysozyme in Solution. Hinge-Bending Motion and the Substrate-Induced Conformational Transition Studied by Site-Directed Spin Labeling. *Biochemistry* **36**, 307–316 (1997).

66. Mchaourab, H. S., Lietzow, M. A., Hideg, K. & Hubbell, W. L. Motion of Spin-Labeled Side Chains in T4 Lysozyme. Correlation with Protein Structure and Dynamics. *Biochemistry* **35**, 7692–7704 (1996).

67. López, C. J., Fleissner, M. R., Guo, Z., Kusnetzow, A. K. & Hubbell, W. L. Osmolyte perturbation reveals conformational equilibria in spin-labeled proteins. *Protein Sci.* **18**, 1637–1652 (2009).

68. Erilov, D. A. *et al.* Water Concentration Profiles in Membranes Measured by ESEEM of Spin-Labeled Lipids. *J. Phys. Chem. B* **109**, 12003–12013 (2005).

69. Guzzi, R., Bartucci, R., Sportelli, L., Esmann, M. & Marsh, D. Conformational Heterogeneity and Spin-Labeled −SH Groups: Pulsed EPR of Na,K-ATPase. *Biochemistry* **48**, 8343–8354 (2009).

70. Timofeev, V. P. & Tsetlin, V. I. Analysis of mobility of protein side chains by spin label technique. *Biophys. Struct. Mech.* **10**, 93–108 (1983).

71. Lide, D. R. *CRC Handbook of Chemistry and Physics, 85th Edition*. (CRC Press, 2004).

72. Columbus, L., Kálai, T., Jekö, J., Hideg, K. & Hubbell, W. L. Molecular Motion of Spin Labeled Side Chains in α-Helices: Analysis by Variation of Side Chain Structure. *Biochemistry* **40**, 3828–3846 (2001).

73. Robinson, B. H., Mailer, C. & Reese, A. W. Linewidth Analysis of Spin Labels in Liquids: I. Theory and Data Analysis. *J. Magn. Reson.* **138**, 199–209 (1999).

74. Goldman, S. A., Bruno, G. V. & Freed, J. H. Estimating slow-motional rotational correlation times for nitroxides by electron spin resonance. *J. Phys. Chem.* **76**, 1858–1860 (1972).

75. Mason, R. P. & Freed, J. H. Estimating microsecond rotational correlation times from lifetime broadening of nitroxide electron spin resonance spectra near the rigid limit. *J. Phys. Chem.* **78**, 1321–1323 (1974).

76. Freed, J. H. 3 - Theory of Slow Tumbling ESR Spectra for Nitroxides. in *Spin Labeling* (ed. Berliner, L. J.) 53–132 (Academic Press, 1976).

77. Budil, D. E., Lee, S., Saxena, S. & Freed, J. H. Nonlinear-Least-Squares Analysis of Slow-Motion EPR Spectra in One and Two Dimensions Using a Modified Levenberg–Marquardt Algorithm. *J. Magn. Reson. A* **120**, 155–189 (1996).

78. Hubbell, W. L. & McConnell, H. M. Motion of steroid spin labels in membranes*. *Proc. Natl. Acad. Sci.* **63**, 16–22 (1969).

79. Hubbell, W. L. & McConnell, H. M. Orientation and motion of amphiphilic spin labels in membranes*. *Proc. Natl. Acad. Sci.* **64**, 20–27 (1969).

80. Zhang, Z. *et al.* Multifrequency Electron Spin Resonance Study of the Dynamics of Spin Labeled T4 Lysozyme. *J. Phys. Chem. B* **114**, 5503–5521 (2010).

81. Robinson, B. H. & Dalton, L. R. Anisotropic rotational diffusion studied by passage saturation transfer electron paramagnetic resonance. *J. Chem. Phys.* **72**, 1312–1324 (1980).

82. Evans, C. A. Use of the integral of saturation transfer electron paramagnetic resonance spectra to determine molecular rotational correlation times. Slowly tumbling spin labels in the presence of rapidly tumbling spin labels. *J. Magn. Reson. 1969* **44**, 109–116 (1981).

83. Horváth, L. & Marsh, D. Analysis of multicomponent saturation transfer ESR spectra using the integral method: Application to membrane systems. *J. Magn. Reson. 1969* **54**, 363–373 (1983).

84. Howard, E. C., Lindahl, K. M., Polnaszek, C. F. & Thomas, D. D. Simulation of saturation transfer electron paramagnetic resonance spectra for rotational motion with restricted angular amplitude. *Biophys. J.* **64**, 581–593 (1993).

85. Squier, T. C. & Thomas, D. D. Methodology for increased precision in saturation transfer electron paramagnetic resonance studies of rotational dynamics. *Biophys. J.* **49**, 921–935 (1986).

86. Zech, S. G., Wand, A. J. & McDermott, A. E. Protein Structure Determination by High-Resolution Solid-State NMR Spectroscopy: Application to Microcrystalline Ubiquitin. *J. Am. Chem. Soc.* **127**, 8618–8626 (2005).

87. Kaieda, S., S. Plivelic, T. & Halle, B. Structure and kinetics of chemically cross-linked protein gels from small-angle X-ray scattering. *Phys. Chem. Chem. Phys.* **16**, 4002–4011 (2014).

88. Persson, E. & Halle, B. Nanosecond to Microsecond Protein Dynamics Probed by Magnetic Relaxation Dispersion of Buried Water Molecules. *J. Am. Chem. Soc.* **130**, 1774–1787 (2008).

89. Sunde, E. P. & Halle, B. Slow Internal Protein Dynamics from Water 1H Magnetic Relaxation Dispersion. *J. Am. Chem. Soc.* **131**, 18214–18215 (2009).

90. Kaieda, S. & Halle, B. Internal Water and Microsecond Dynamics in Myoglobin. *J. Phys. Chem. B* **117**, 14676–14687 (2013).

91. Timasheff, S. N. & Arakawa, T. Mechanism of protein precipitation and stabilization by co-solvents. *J. Cryst. Growth* **90**, 39–46 (1988).

92. Martin, R. W. & Zilm, K. W. Preparation of protein nanocrystals and their characterization by solid state NMR. *J. Magn. Reson.* **165**, 162–174 (2003).

93. Greene, D. G., Modla, S., Wagner, N. J., Sandler, S. I. & Lenhoff, A. M. Local Crystalline Structure in an Amorphous Protein Dense Phase. *Biophys. J.* **109**, 1716–1723 (2015).

94. Fung, L. W., Kalaw, B. O., Hatfield, R. M. & Dias, M. N. Erythrocyte spectrin maintains its segmental motions on oxidation: a spin-label EPR study. *Biophys. J.* **70**, 841–851 (1996).

95. Biswas, S., Mukherjee, S. K. & Chowdhury, P. K. Crowder-Induced Rigidity in a Multidomain Protein: Insights from Solvation. *J. Phys. Chem. B* **120**, 12501–12510 (2016).

96. Makowski, L. *et al.* Molecular Crowding Inhibits Intramolecular Breathing Motions in Proteins. *J. Mol. Biol.* **375**, 529–546 (2008).

97. Politou, A. & Temussi, P. A. Revisiting a dogma: the effect of volume exclusion in molecular crowding. *Curr. Opin. Struct. Biol.* **30**, 1–6 (2015).

98. Wang, Y., Sarkar, M., Smith, A. E., Krois, A. S. & Pielak, G. J. Macromolecular Crowding and Protein Stability. *J. Am. Chem. Soc.* **134**, 16614–16618 (2012).

99. Senske, M. *et al.* Protein Stabilization by Macromolecular Crowding through Enthalpy Rather Than Entropy. *J. Am. Chem. Soc.* **136**, 9036–9041 (2014).

100. Hikita, H., Asai, S. & Azuma, Y. Solubility and diffusivity of oxygen in aqueous sucrose solutions. *Can. J. Chem. Eng.* **56**, 371–374 (1978).

101. Popp, C. A. & Hyde, J. S. Effects of oxygen on EPR spectra of nitroxide spin-label probes of model membranes. *J. Magn. Reson. 1969* **43**, 249–258 (1981).

102. Subczynski, W. K. & Hyde, J. S. Diffusion of oxygen in water and hydrocarbons using an electron spin resonance spin-label technique. *Biophys. J.* **45**, 743–748 (1984).

Chapter 6: Monofunctional nitroxide spin labels with strongly hindered internal motion

6.1 Introduction

6.1.1 Spin labels for ST-EPR

Like any method involving the utilization of probes, the proper choice of spin labels is one of the key components for a successful SDSL-EPR experiment. Although the criteria for selection will constantly evolve to satisfy various study aims, generally, the specificity, rigidity, as well as balance between reactivity and preservation of function are the essential aspects when evaluating or designing a spin label. In ST-EPR measurement where the internal motion of spin labels strongly interferes with the sensitivity to slower dynamics, the rigidity of the spin label is the most crucial property to consider.

In the initial stage of ST-EPR method development, iodoacetamide derivatives[1] and maleimide derivatives[2] were universally used. While they could detect dynamics in the microsecond time domain, several drawbacks drove the continuous exploration of other labels. Among those was the pronounced pH-dependent specificity of the reaction to cysteines, which consequently compromised the reactivity. It was also observed that the binding of these labels was unstable under various conditions. It is likely that upon ligand binding (nucleotides[3] and vanadate[4] in published studies), the changed conformational flexibility of protein will lead to weakened attachment and increased mobility of spin labels.

Between these two, the internal mobility of iodoacetamide labels is more pronounced, making the maleimide labels (5- and 6-MSL) a better and more common choice. However, as described in chapter 4, the relatively high chemical reactivity of the maleimide group can lead to

a mixture of EPR signaling species and multiple spectral components. Moreover, the contribution from the internal dynamics of MSL is still non-negligible, potentially hindering the detection of slower motional modes. Aiming at introducing a probe with higher reactivity and less mobility, β-substituted vinyl aryl ketone derivatives, particularly the 5-InVSL[5–8], were synthesized and applied in several studies and proven to be an effectively immobilized side chain for probing microsecond dynamics.

However, both MSL and InVSL are sterically demanding, leading to not only the impediment of their reactivity but also the concern of potentially affecting the structure and conformational equilibrium of the target protein. A more general obstacle originates from the chemical properties of their functional groups. Although the thioether linkage generated from Michael addition is usually considered stable and not cleavable (compared to the disulfide linkage), the thiosuccinimide product is hydrolytically unstable and susceptible to slow thiol exchange via a retro-Michael reaction. This leads to cleavage and release of the spin label side chain (see chapter 4).

More recently, benefiting from the application of solid-phase synthesis in the chemical biology area, the spin-labeled amino acid 2,2,6,6-tetramethyl-piperidine-1-oxyl-4-amino-4-carboxyl (TOAC) has been synthesized and applied for ST-EPR experiments[9], which incorporates directly into fixed positions in protein backbones via amide bonds. However, despite its strong immobilization, it requires peptide synthesis to incorporate this label and thus is not compatible with proteins with molecular weight above about 6 kDa. Additionally, the range of adoptable dihedral angles of TOAC is extremely limited, leading to backbone distortions.

Efforts to find better probes for slow motion detection have also been constantly put over the

development of new R1-based spin labels. Despite the many advantages that R1 has, its inherent flexibility is even higher than for IASL or MSL. In chapter 5 (and previous publications), the cross-linked spin label side chain RX was described, which provides high performance in measuring both fast and slow protein dynamics[10,11]. However, applying RX requires the mutagenesis of two residues for each detection, which not only complicates the sample preparation but may also affect the thermal stability or folding of some local structures. To adopt an energetically relaxed conformation of the side chain, the second cysteine usually needs to be located at the i+3 or i+4 position of an α-helix or the i+2 position of a β-strand. The formation of the crosslink is likely to lead to strain in forming a proper helix extending to the i+3 or i+4 position, thereby potentially modifying the local structure and dynamics.

To this end, monofunctionally disulfide-linked spin label side chains with sufficiently restricted internal mobility would be a valuable addition to the SDSL-EPR toolbox. Such spin label side chains not only promise to be a suitable sensor for monitoring protein dynamics in a time domain that is particularly challenging for other methods, but would also be advantageous for distance determination using DEER (see chapter 7). In this work, two rigid, monofunctionally linked R1-derivatized spin labels are thoroughly characterized to examine their applicability, especially emphasizing their comparable efficacy to the bifunctionally linked RX for slow motion detection.

6.1.2 4-Substituted R1-derivatives

4-substituted R1 derivatives have been considered practical contenders in the search for SDSL-EPR probes with more restricted mobility. A whole series of 4-substituted derivatives of increasing size were initially tested by Columbus et al., aiming at using the hydrophobic bulk of

substituents to hinder the rotations about the two terminal bonds.[12] Suggested by CW-EPR spectra and the molecular modeling[12], it was eventually confirmed with the crystal structures[13] that the 4-substituents could efficiently limit the amplitude of rotations about χ_4 and χ_5, mainly the χ_5, by the steric interactions of substituents with the S_δ atom. Consequently, such interactions constrain the internal motions of the whole spin label side chain, enhancing the sensitivity for detecting protein backbone dynamics.

Three 4-substituted derivatives have been successfully incorporated into T4L at a solvent-exposed helical site (site 131), and high-resolution crystal structures were determined. As reported by Fleissner et al., structures of the 4-methyl (R1b[14]) and 4-bromo (R7[15]) derivatives indicate that the strain to rotations arises internally within the side chain, while the structure of the 4-phenyl (R1f[16]) derivative reveals a weak interaction between the phenyl ring and the protein backbone which is presumably responsible for its greater hindered motion comparing to R1b and R7.

Indeed, regardless of the highly ordered dynamic character reflected from the CW-EPR lineshapes of all spin label side chains, only the structure of T4L131R1f reveals a single conformation of the side chain with almost all non-hydrogen atoms resolved. The fact that for R1b and R7 the nitroxide rings are unresolved implies the existence of residual motions about the final two single bonds. Results from the experiment in which the R1f[16] side chain was placed at multiple helical sites in T4L indicate that (at most sites) despite its rigidity is likely to originate from the intermolecular interaction with protein backbones, it appears to be general at solvent-exposed helical sites and therefore promising R1f as a useful alternative to R1 for monitoring dynamics and measuring distances.

Understanding the structural basis of 4-substituent derivatives has allowed us to design new

spin labels more effectively with improved properties. Inspired by the fact that the phenyl ring structure is more effective than the methyl- or bromo- substituents in hindering motions, a second phenyl ring was introduced to the carbon between the S_δ atom and the nitroxide ring, which serves as an α-substituent. Presumably, this phenyl ring can further suppress the configurational space that two terminal single bonds can adopt, thus enabling a spin label with even stronger rigidity than R1f. The reagent HO-3292 has been synthesized accordingly by the Kálai group, generating the side chain RY of which the properties have been carefully investigated for this dissertation. Relevant results and several applications will be shown and discussed in this chapter. Another two R1 derivatives with restricted mobility that were reported in previous publications, the R1p[17] and R2f (also called R8 in some articles), will not be reviewed here, but relevant studies[18–21] can be found.

6.2 Internal dynamics of monofunctional rigid nitroxide spin labels in the ps-ns time range

As both a continuation and extension of the exploration by Fleissner et al.[22], the internal dynamics of R1f, and also of the novel side chain RY, are characterized carefully in the ps-ns time range to evaluate their potential for use as the monitor of slow protein motions. Similarly, as in any spin label characterization study, the labeled protein is either investigated in a high-viscosity medium (sucrose or Ficoll) or attached to a solid support in order to eliminate rotational diffusion and isolate dynamic modes of side chain and protein.

6.2.1 R1f and RY on α-helix surface sites

6.2.1.1 Comparison to R1 and RX side chains in CW-EPR spectra

Both R1f and RY side chains were introduced to representative helical sites (shown in Figure 5.8) of two model proteins, the HoloMb and the pseudo wild-type of T4L, which were covalently attached to CNBr-Sepharose in this experiment. All spin labeling sites are solvent accessible, located in non-terminal regions of well-packed stable helices. The same mutants were also labeled with R1 or corresponding double-cysteine mutants with the RX side chain, serving as a qualitative reference of internal rigidity.

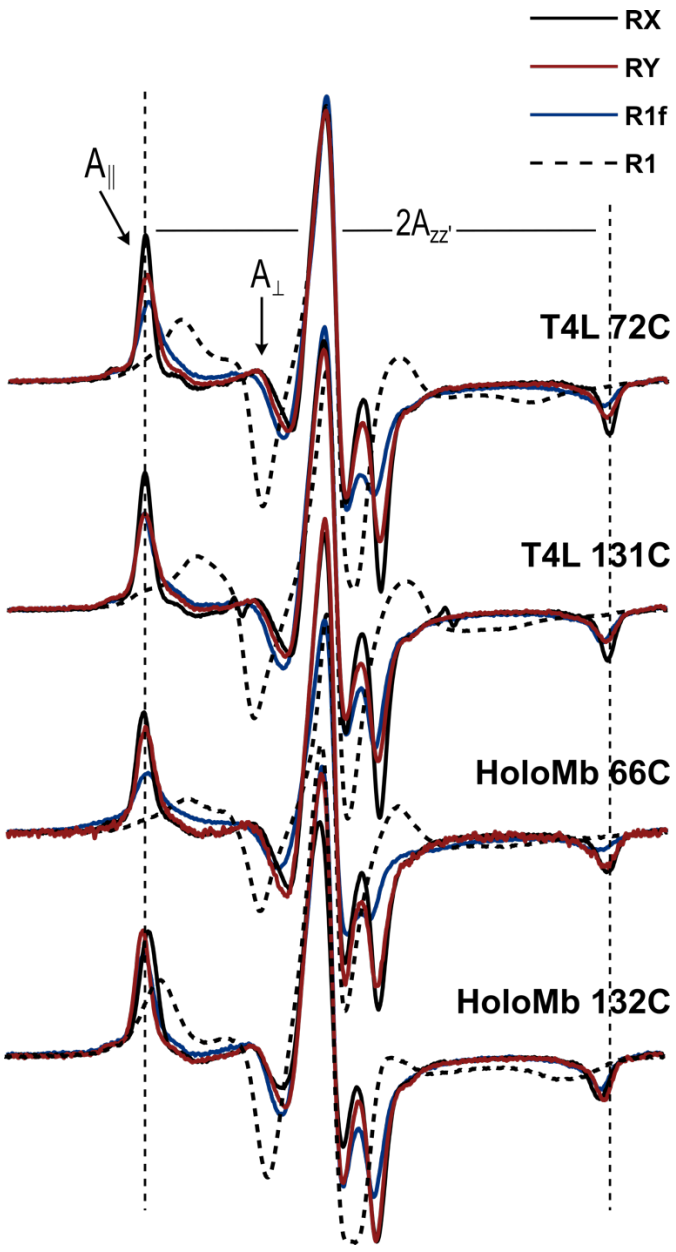

Figure 6.1 CW-EPR spectra (normalized to the spin count calculated by double integration) of RX (black curves), RY (red curves), R1f (blue curves), R1 (dash curves) on proteins at room temperature. All mutants are attached to CNBr-activated Sepharose. The magnetic field scan width is 100G.

CW-EPR spectra (Figure 6.1) of all mutants derivatized with R1f, RY, or RX clearly reflect strong immobilization of the nitroxide compared with the same sample labeled with R1. All sites were readily labeled, and no features relating to the local or global unfolding of structures are observed from spectral lineshapes, i.e., no abnormal broadenings (precipitation) or sharpness (free-tumbling disordered structures), implying negligible perturbation by the introduced labels. In each case, the spectra of R1f and RY labeled samples are indicative of a highly ordered nitroxide motion, as evidenced by the well-resolved parallel ($A_{\parallel}$) and perpendicular ($A_{\perp}$) components of the hyperfine tensor, the large effective hyperfine splitting, $2A_{zz'}$, and the narrow linewidth of the low-field peak. Notably, even though monofunctionally attached, the spectra of RY strongly resemble the lineshape pattern of RX ($2A_{zz'}$, e.g., 70.493G (RX) and 70.005G (RY) at site 72C).

The regular increase in the hyperfine splitting observed for four side chains from RX to R1 is correlated with an increased narrowing of the linewidths, which suggests the decreased mobility of side chains due to a decrease in the amplitude of motions on the ns timescale. Just as for RX, the narrow linewidth strongly implies that both R1f and RY possess a highly anisotropic, i.e., ordered, rapid internal motion with restricted angular amplitudes. While RX is a bifunctionally attached side chain, the increasingly suppressed amplitude of motion from R1 to R1f and to RY is consistent with the increase in the sizes of their bulk moiety. These spectra can theoretically be accounted for reasonably well by a single anisotropic motional component of nitroxide with similar rapid rates and varying degrees of order, i.e., the value of S_{20}. Some simulation results will be shown in the following sections.

6.2.1.2 Effects of nearest neighbor mutations on CW-EPR spectra of R1f and RY side chains

To evaluate the role of nearby residue side chains in the high ordering of R1f or RY, four neighboring residues (N68, Q69, V75, R76 shown in Figure 6.2 (A) and D127, E128, N132, K135 shown in Figure 6.2 (B)) were individually mutated to Alanine on the 72C and 131C background T4L constructs, respectively, which can potentially interact with the spin label side chains at 72C or 131C.

Spectra (Figure 6.2) of all alanine mutants (except for 131RY/128A which proved unstable and was not successfully prepared) were labeled with R1f or RY, respectively, and attached to CNBr-Sepharose. All spectra show high similarities to the spectrum of their corresponding 72C or 131C mutant in pseudo wild-type T4L background. The chosen mutations have been shown by corresponding CW-EPR spectra of R1-labeled samples to have negligent effects on the local structure of helix C or helix H. If at all, the 72R1/75A construct shows a slightly more prominent difference to 72R1 in the lineshapes which is invisible for either 72RY/75A or 72R1f/75A, therefore it is more likely originated from R1-exclusive properties.

As compared with spectra of R1-labeled samples under the same condition, more details in lineshapes were resolved due to the higher order of the immobilized labels. Remarkably, spectra of all RY-labeled mutants are essentially identical to the spectrum of the original construct with highly resolved spectral features, suggesting that specific local residue interactions are not responsible for its surprisingly high rigidity, but inherent properties. Instead, minor differences were observed for 76A/72R1f and 132A/131R1f, which are more likely caused by small local changes brought by the mutation, especially the residue 76 which is originally an arginine, a long and flexible amino acid side chain.

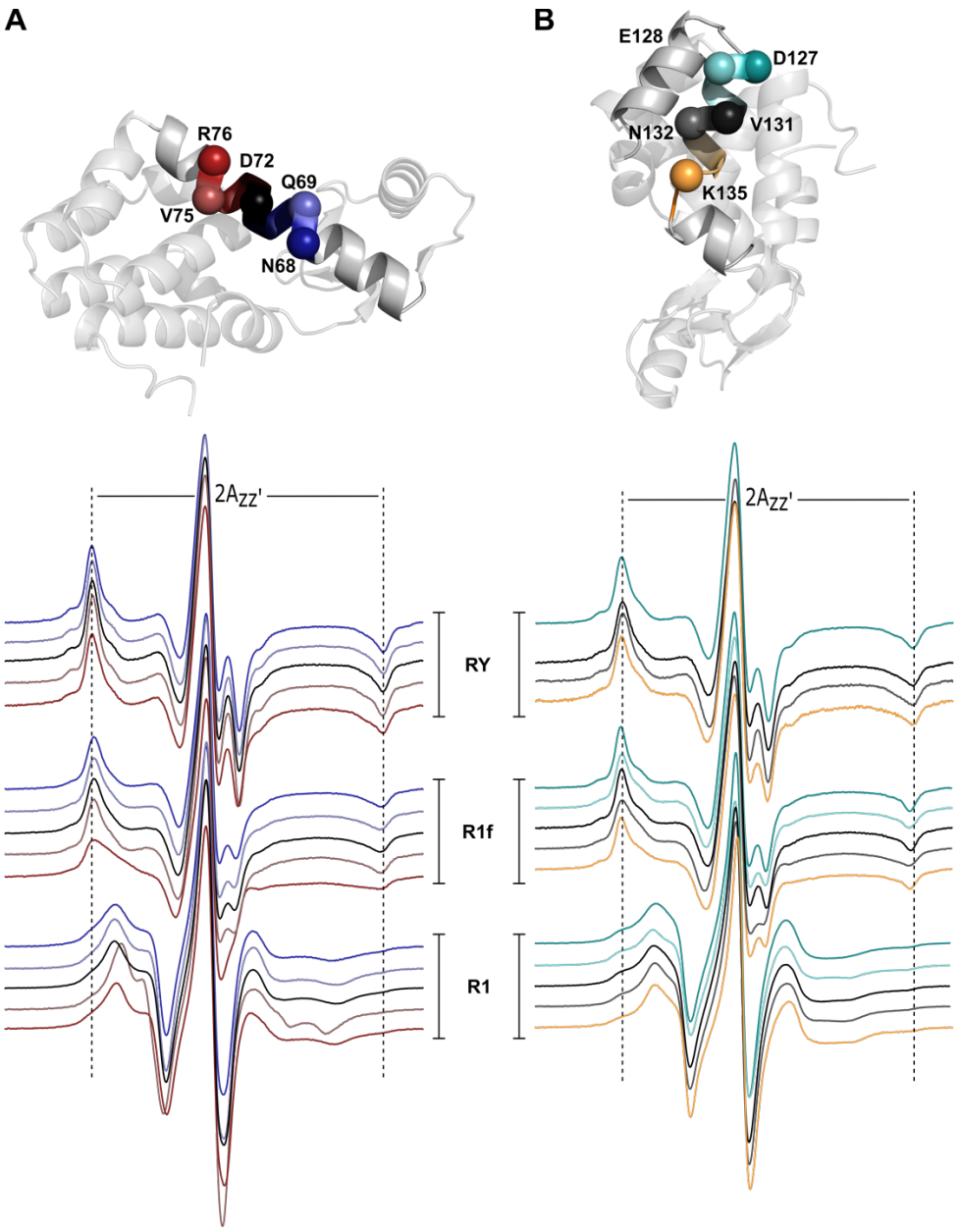

Figure 6.2 Ribbon diagram of T4L (PDB code: 3LZM) showing the residue (A) 72C and (B) 131C where spin labels are introduced, and their neighboring alanine replacements. Each colored sphere at the Cα corresponds to the same-colored spectrum, indicating the alanine mutation site. CW-EPR spectra of RY, R1f, and R1 on proteins are shown with vertical lines as references for comparing effective hyperfine splittings ($2A_{zz'}$). All mutants were attached to CNBr-activated Sepharose and measured at room temperature. The magnetic field scan width is 100G.

In general, the highly constrained mobility of the R1f or RY side chain is consistently retained in the alanine mutants, which supports the assertion that the restricted internal motion of

both labels is not the result of direct interaction with any of these neighboring side chains. Although the crystal structure of 131R1f implies that such rigidity is not originated from internal interactions within the side chain, such results still substantiate the fundamental hypothesis that both side chains can generally exhibit strong immobilization at solvent-exposed sites.

6.2.1.3 Mobility of RY side chains on solvent-accessible sites

In order to explore its labeling compatibility and the performance in reporting nanosecond dynamics in helical proteins, the side chain RY was introduced, one at a time, to solvent-exposed sites in the interior of regular helices of HoloMb (Figure 6.3 (A)) and T4L (Figure 6.3 (B)). EPR spectra of R1 at each of these sites have been previously published and reproduced here for comparison.

Firstly, we found that the RY side chain could be introduced with a good yield at the tested sites, assuring the application of RY for ST-EPR measurements in which a relatively high spin concentration (≥300μM) is necessary for optimal signal intensity. The efficiency of labeling was quantified by comparing the final spin and protein concentrations of the sample, and the high labeling efficiency (>75%) was consistently achieved.

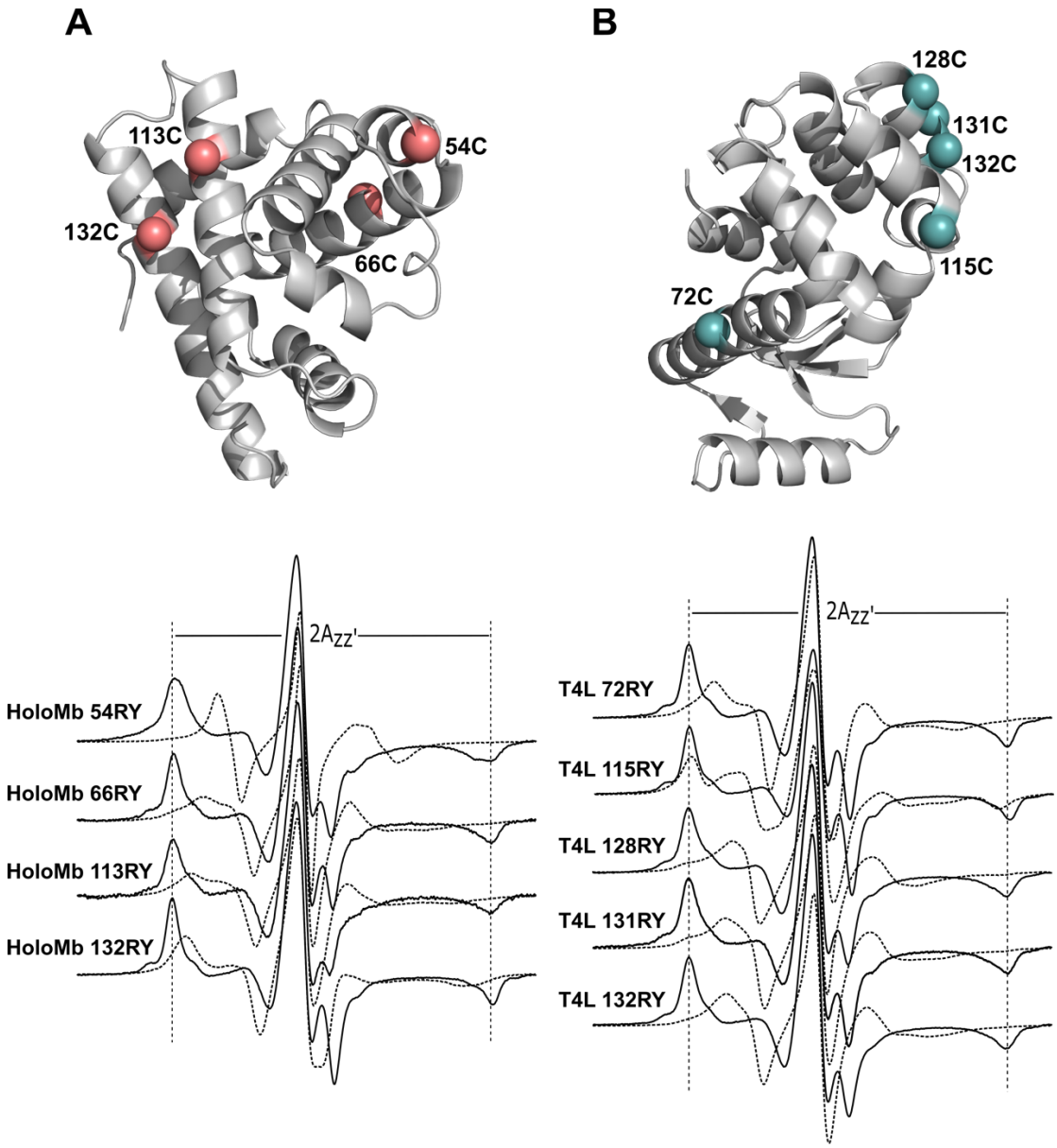

Figure 6.3 Ribbon diagram of (A) HoloMb (PDB code: 2MBW) and (B) T4L (PDB code: 3LZM) showing the residues where RY (solid curves) and R1 (dashed curves) side chains were introduced. Each colored sphere at the Cα indicates a labeling site. CW-EPR spectra are shown with vertical lines as references for comparing effective hyperfine splittings ($2A_{zz'}$). All mutants were attached to CNBr-activated Sepharose, except for 115R1 which is in 30% sucrose w/w and measured at room temperature. The magnetic field scan width is 100G.

It has been well established that the motion of the R1 side chain can be largely modulated by the backbone fluctuations and tertiary interactions, providing its substantial sensitivity to local

environments on the ps-ns time scale. Oppositely, RY appears to be universally immobilized at each site in regular helical structures as revealed by the well-resolved hyperfine extrema and large apparent hyperfine splittings, reflecting virtually no site-specific variation in nanosecond mobility. Although minor differences in linewidth and splitting pattern of $M_I = 0$ (central field) manifold were observed, the CW-EPR lineshapes of RY are essentially as insensitive to fast dynamics similar to RX, which is a prerequisite to resolve μs-ms dynamics.

Furthermore, RY was also tested for the reaction with a membrane protein, the rhodopsin[23–27] (Figure 6.4), which contains a total of nine native cysteines but only two of them are solvent-accessible. In this experiment, the wild-type rhodopsin was placed either in its native bilayer membranes, ROS (rod outer segment disc membranes), or in a micellar solution of detergent (dodecylmaltoside, DM), where all of its three states, 'dark', 'light', 'opsin', were measured accordingly under both environments.

As a chromoprotein, the internally bound ligand of rhodopsin, 11-cis-retinal, will be isomerized to the all-trans-retinal form upon illumination, inducing a conformational change of rhodopsin from its 'dark' inactive state to the 'light' physiologically active state within milliseconds. Moreover, conformational changes following activation have been observed, the 'light-activated' state of rhodopsin decays with the slow dissociation of the chromophore, all-trans-retinal, leading back the protein to the ligand-free 'opsin' form[28].

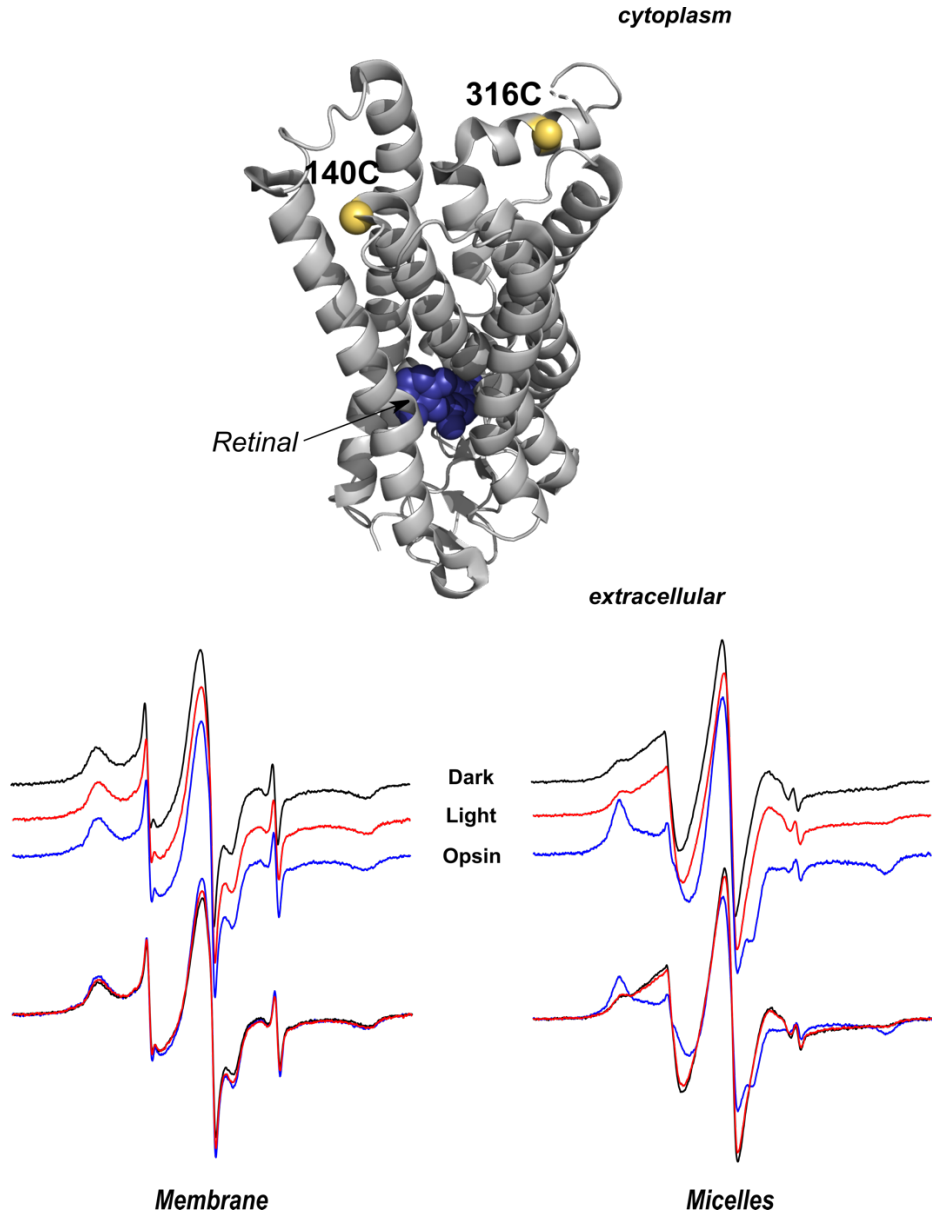

Figure 6.4 Ribbon model of rhodopsin in the 'dark'/inactive state (PDB code: 1GZM), which spans the width of the rod's intradiscal membrane, with the 'cytoplasmic' and the 'extracellular' sides identified in the figure. The CPK form of 11-cis-retinal is shown as blue spheres. Yellow spheres show the Cα atoms corresponding to accessible cysteine residues where the RY side chain is likely to be introduced in the present study. Normalized CW-EPR spectra are displayed staggered and also overlayed for direct comparison. The magnetic field scan width is 100G.

Practical concerns about using bulky spin labels arise mainly from their steric volume and hydrophobicity. The existence of two phenyl rings in the structure of RY could hypothetically

hinder or even block its accessibility to a protein that resides in lipids. As a proof of concept, the reagent HO-3292 was incubated with stoichiometric amounts of wild-type rhodopsin in ROS. After the reaction, the concentrations of rhodopsin molecules and active spins in the mixture were determined. It turned out that the spin counts determined from the CW-EPR spectrum (double integral is converted into the number of spins) were equivalent to a 2-fold of the concentration of rhodopsin determined via optical spectroscopy, implying that there were exactly two cysteines labeled after the reaction. A similar result was also obtained for labeling the rhodopsin eluted in the DM solution, from which the spin count was at roughly 1.6-fold protein concentration.

Corresponded spectra were collected and normalized for comparison. Notably, details about different dynamic modes cannot be fully described with these spectra alone, which are likely reporting on both lipid/detergent and protein dynamics. Results are shown mainly for demonstrating that the RY side chain is still sensitive to the surrounding environment when attached to a membrane protein.

Differences were observed between samples in bilayers and in DM, which is consistent with previous studies using the R1 side chain[27]. On the other hand, there were essentially no significant changes from the lineshapes of dark states and light states on the CW-EPR timescale. Shifts in populations upon activation were generally observed from the spectra of R1 mutants (140C, 227C, 250C, 316C), in which two well-resolved components co-existed.

However, as also indicated in the publication, the two states of R1 could arise from conformational heterogeneity of either R1 or the protein. While the stronger immobility of RY could be masking small local changes, leading to insensitive spectral changes, this minimized internal flexibility is also likely to eliminate the contribution from rotameric equilibria,

monitoring the protein dynamics more directly. The fact that apparent changes could still be detected upon dissociation of retinal (from light to opsin) also suggests that the RY side chain is still 'functional' to structural changes. For WT rhodopsin used in this work, the opsin state has been known extremely unstable in the detergent solution, thus it is likely that the spectrum corresponded to an aggregated form of the protein in micelles. Further analysis is beyond the capacity of current results and more experiments will be designed in the future.

6.2.2 Degree of destabilization to T4L by the substitution for RY side chains

To some extent, it is unavoidable to bring in perturbance to the structure and thermodynamic stability of native protein when applying techniques involving mutagenesis and exogenous labels. Although steric structures are frequently seen in proteins, such as native amino acids (tryptophan and phenylalanine) or fluorescence probes, introducing bulky spin labels to proteins has always been a fundamental concern.

The degree of destabilization caused by the presence of R1 at multiple sites of pseudo wild-type T4L was assessed by monitoring thermal unfolding with circular dichroism[29]. Values of the derived thermodynamic parameters for the unfolding fall within the range of values found for substitutions at these sites by native amino acids. This result indicates that the introduction of R1 can be considered tolerable for globular proteins. It has been widely accepted that R1 introduces minimal disturbance to the conformational equilibrium and functionality of the labeled protein, which is particularly true for a protein such as T4L which is known for its high tolerance towards mutations.

Here, a similar experiment was performed to evaluate the potential degree of destabilization brought by the RY side chain. There are many methods designed for examining the stability of

proteins. Various environmental factors contributing to the stability can be regulated to control the unfolding process, such as the temperature, pH, and ionic strength, while different compatible spectroscopic techniques enable a multi-perspective characterization. However, as the complexity of unfolding has not yet been fully uncovered, the comparison between results acquired using different methods can be greatly influenced by apparatus-specific factors, and thus becomes less reliable.

In this dissertation, a two-state chemical denaturation process for fully-labeled T4L72RY was modulated by urea concentration and monitored by tryptophan fluorescence. Stability analysis using urea denaturation curves[30–34] has long been widely applied due to its relatively simple experimental requirements and nature of reversibility. As compared to another commonly used denaturant GdmCl, the mechanism of urea denaturation is not relevant to the pH or the ionic strength of the solutions, making it a better-controlled system to extract thermodynamic information under equilibrium. The fluorescence of tryptophan is sensitive to the polarity of its local environment. Indicated by a red shift in the steady-state emission spectrum, a transition accompanied by the protein denaturation from the hydrophobic core of protein to the aqueous solution can be sensed by buried tryptophan residues, thus offering a way to monitor protein conformational changes and analyze thermodynamic parameters.

Thermodynamic analysis was performed on the urea-induced change in the center of spectral mass (see chapter 8 for details). The comparative experiments were accordingly made for the unlabeled cysteine mutant sample (72C) and R1-labeled sample (72R1). Change in the center of spectral mass instead of fluorescence intensity at a single wavelength was used because this quantity is recognized as less prone to instrumental noise and other non-specific experimental variations as an integral measurement. It is also a more sensitive value because it reflects

changes involving the entire spectrum, not only the wavelength positions but also the lineshapes. Three tryptophan residues are known to be present in the C-terminal lobe of pseudo wild-type T4L at sites 126, 138, and 158. Plotting of change in intensity did not yield a smooth urea denaturation curve (results not shown), revealing characteristics of the non-simultaneous unfolding of regions in which the three residues locate, while the plots of change in the center spectral mass versus urea concentration exhibit smooth curves reflecting clear features for two-state behaviors.

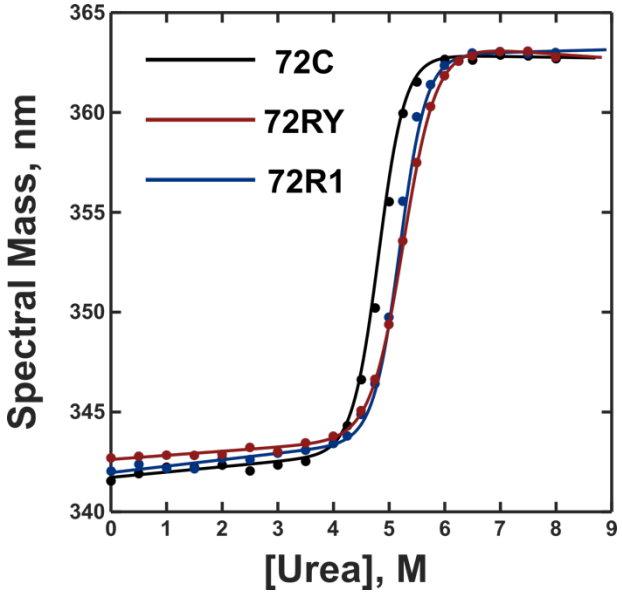

Figure 6.5 Urea denaturation curves of T4L72C, T4L72R1, and T4L72RY based on the center of spectral mass of tryptophan fluorescence emission, fit to the equation describing a two-state, reversible unfolding process at equilibrium (details are described in chapter 8, materials and methods).

Table 6.1 Thermodynamic properties derived from the two-state model fit of urea denaturation curves

	T4L72C	T4L72R1	T4L72RY
ΔG_0 (kcal/mol)	12.0 ± 0.91	11.6 ± 1.6	10.5 ± 0.43
$\Delta\Delta G_0$ (kcal/mol)		-0.4	-1.5
m (kcal·L/mol^2)	2.47 ± 0.19	2.26 ± 0.33	2.00 ± 0.084
$[Urea]_{1/2}$ (mol/L)	4.87	5.13	5.25

All three spin-labeled mutants displayed cooperative transitions under increasing amounts of urea as illustrated by the representative curves (Figure 6.5), which is consistent with observations

made in other denaturation studies[29]. Fits to the two-state (native/folded versus denatured/unfolded) model yield apparent free energies of unfolding in the absence of denaturant, ΔG_0; the slope of the transition of denaturation, m; and the urea concentration at 50% denaturation, i.e., the midpoint of the transition, $[Urea]_{1/2}$, respectively, for T4L72C, T4L72R1, and T4L72RY.

The values of $\Delta\Delta G_0$ for 72R1 and 72RY both fall within the range of values found for substitutions (relative to 72C) by native amino acids[35,36]. All of the derived thermodynamic parameters (Table 6.1) for the unfolding are in the same range as that obtained for the cysteine mutant. A decrease of 1.5kcal/mol in the free energy of unfolding induced by introducing the RY to 72C is comparable to the substitution by R1 at some sites on T4L (e.g., R80C[29]).

This result suggests that the degree of destabilization caused by the presence of RY on the solvent-exposed helix is acceptable. While it is expected for a side chain carrying hydrophobic and steric substituents to introduce a certain degree of destabilization, the actual value of free-energy decrease is rather insignificant considering that typical values for single amino acid substitutions are in the 2-5 kcal/mol range[29,35,36].

Interestingly, an increase in the transition midpoint $[Urea]_{1/2}$ was observed, implying that spin labeling stabilized the native fold over the unfolded state. However, the change in free energy contrarily indicated that the process was rather destabilized. Such effect was essentially due to the shift of the m-value which is believed to be dependent on the difference in solvent accessible surface area (ASA) between the native and denatured states. Nevertheless, these changes in value are still within the typical ranges expected for single amino acid substitutions. Both parameters provide more detailed information on the environment surrounding tryptophan residues, which is beyond the scope of this work.

6.2.3 Characterizing internal dynamic modes of the R1f and RY side chains

Results shown above undoubtedly demonstrate that the internal motions of both R1f and RY side chains at solvent-exposed sites exhibit highly restricted motion on the time scale of CW-EPR, similar to the bifunctional side chain RX, making them alternative spin label candidates for slow motion detection.

To further evaluate and understand their internal dynamics, a series of characterizations were carried out for R1f and RY. The experimental strategies have been thoroughly explained and discussed in either previous publications or chapter 5. To avoid redundancy, the following results will be simply displayed with only sparsely discussed.

6.2.3.1 The $2A_{zz'}(0)$, $2A_{zz'}(inf)$, and $2A_{zz'}$ of T4L72R1f and T4L72RY attached to Sepharose

CW-EPR spectra of T4L72R1f and T4L72RY were measured in a series of sucrose solutions with increasing concentration to obtain their extrapolated values of hyperfine splitting $2A_{zz'}$ (inf). A value of $2A_{zz'}$ (inf) = 71.036G was obtained for T4L72R1f, and a value of $2A_{zz'}$ (inf) = 71.412G for T4L72RY (Figure 6.6, left). Both are close to the reference value of T4L68RX72, with slight differences indicating the further internal immobilization of RY compared to R1f.

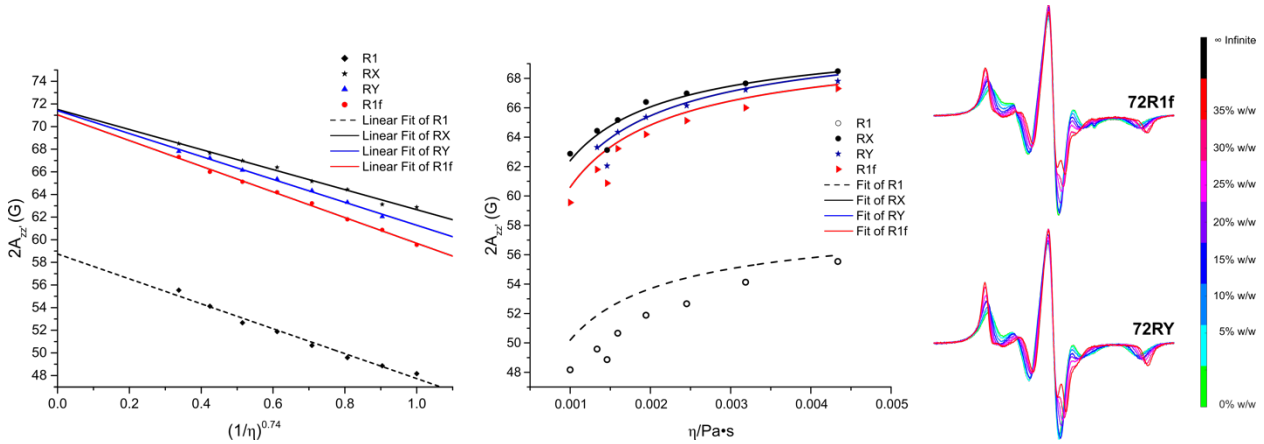

Figure 6.6 The viscosity dependence of CW-EPR spectra (normalized to the spin count calculated by double integration) and values of $2A_{zz'}$ for T4L72R1f and T4L72RY in sucrose solution (concentrations ranging from 0 to 35% w/w in buffer). Viscosities of the sucrose solutions were taken from the CRC handbook (1). At each concentration, $2A_{zz'}$ is determined and plotted vs. the function of viscosity as indicated. Linear extrapolation of the plot to infinite viscosity yields $2A_{zz'}$ in the limit of zero rotational diffusion of the protein.

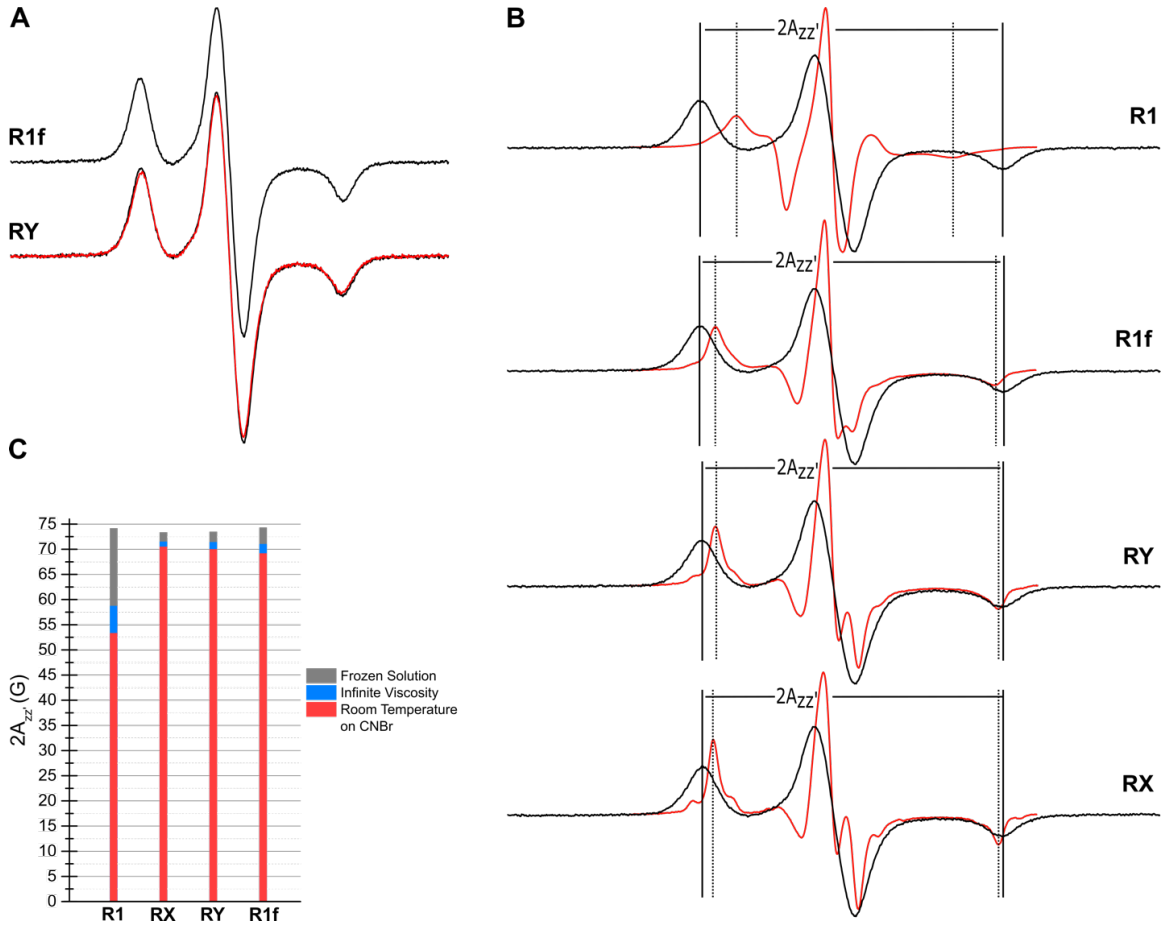

Figure 6.7 (A) Frozen CW-EPR spectra of T4L72R1f and T4L72RY (black: buffer; red: 30% w/w sucrose) on CNBr-activated Sepharose. (B) CW-EPR spectra (frozen in liquid nitrogen: black curves; at room temperature (RT): red curves) of 72R1, 72R1f, 72RY, and 68RX72 on T4L attached to CNBr-activated Sepharose. The magnetic field scan width is 100 G for RT spectra and 160G for frozen spectra. The vertical lines are drawn as references for comparing effective $2A_{zz'}$. (C) $2A_{zz'}$ values of T4L72R1, T4L72R1f, T4L72RY, and T4L68RX72 under three different conditions.

The frozen (in liquid nitrogen) and room temperature spectra of T4L72R1f and T4L72RY attached to CNBr were also determined (Figure 6.7 (A)(B)). Potential effects from sucrose addition were also examined for T4L72RY as for T4L68RX72 and were also excluded (red curve in Figure 6.7 (A)). Compared to the maximum rigidity RX having a $\Delta 2A_{zz'}$ ($2A_{zz'}(0) - 2A_{zz'}$) of 2.9G, R1f has a $\Delta 2A_{zz'}$ of 5.1G, while RY has a $\Delta 2A_{zz'}$ of 3.5G, which again reflects that the internal dynamics of both side chains are effectively restricted but RY possesses the stronger immobility than R1f.

As shown in Figure. 6.7 (C), for rigid labels (RX, RY, R1f), the values of $2A_{zz'}(0)$, $2A_{zz'}$ (inf), and $2A_{zz'}$ under three conditions are substantially similar, which is definitively different from R1. This result undoubtedly demonstrates that: (1) the closeness between values of $2A_{zz'}(0)$ and $2A_{zz'}(\text{inf})$ signifies that both new monofunctional labels have adequately restricted internal motions as comparable as the bifunctional side chain RX; (2) the closeness between values of $2A_{zz'}(\text{inf})$ and $2A_{zz'}$ manifests again the practicability of using solid support attachment. When attached to solid supports, any residual ps-ns motions that are still detectable from CW-EPR lineshapes are originated from the internal motion of spin labels and backbone fluctuations, while the rotational diffusion is virtually eliminated.

Nevertheless, some distinctions are still recognizable between the RX and the relatively more mobile side chain R1f. Qualitatively, the spectra of T4L72R1f all possess broader

linewidths, arising from either additional interaction with surroundings or less restricted amplitude of motion (decreased T_2). In fact, the use of $2A_{zz'}$ in Timofeev analysis method[37] which is derived from Freed's theorem is only valid when the internal motion of the side chain is either adequately slow to approach the 'slow motional regime' of CW-EPR (> 7ns), or so fast but anisotropic in the z-direction that it behaves as effectively frozen out. Otherwise, the effective hyperfine splittings are unevenly averaged by the side chain motion as the viscosity increases, leading to an overestimation of the extrapolated $2A_{zz'}$(inf) value.

A rational examination is to estimate the correlation time of protein (in this case, T4L) by directly fitting the viscosity-dependent values of $2A_{zz'}$ (Figure 6.6, middle). It turns out that both 68RX72 and 72RY could achieve a reasonable fit reporting a correlation time in the same order of magnitude for T4L (6-10 ns). While the fitting for 72R1f actually shows a certain deviation in the high viscosity range between the modeling function and experimental data, the attempt for 72R1 essentially fails to attain a qualified fitting. This test provided mathematical evidence that the R1f side chain behaves subtly differently from RX in terms of internal motional mode, while the RY side chain is more practically similar.

6.2.3.2 Temperature-dependent CW-EPR spectra of T4L72R1f and T4L72RY attached to Sepharose

The temperature dependence of the T4L72R1f and T4L72RY (on CNBr) CW-EPR spectra (Figure 6.8) was also investigated in the range of 5-35°C. The decrease in $2A_{zz'}$ values is less than 1.5G for both R1f and RY as the temperature increases from 5°C to 35°C, as well as the increase in low field linewidth of RY is less than 0.5G.

The fact that CW-EPR lineshapes show marginal dependence on temperature over the

examined range suggests that the existent dynamics for both labels, particularly the RY, are so strongly restricted on the nanosecond time scale that sufficiently high activation energy is to be overcome to excite new spectral component. Similar to RX, the high-ordering motional model could match reasonably well with experimental results obtained for RY. Only the motion of large angular amplitude can effectively change values of the order parameter, S_{20}, which would apparently require high activation energies.

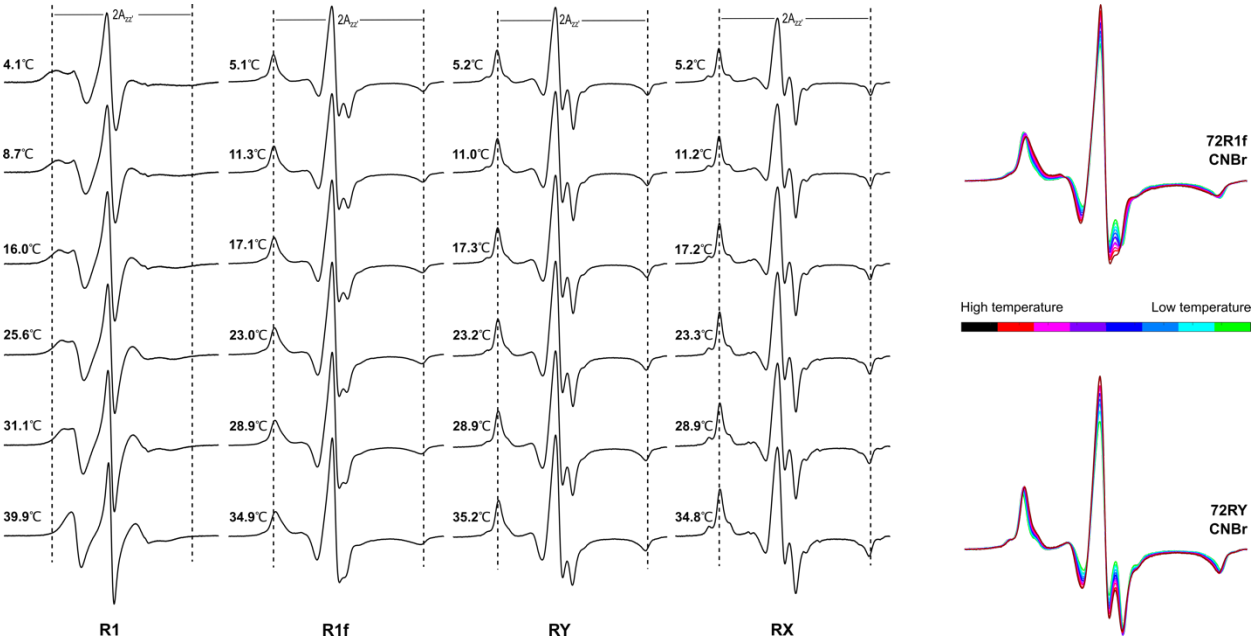

Figure 6.8 Normalized CW-EPR spectra of T472R1f on CNBr and T4L72RY on CNBr at temperatures ranging from 5°C to 35°C. The vertical lines are drawn as references for comparing effective $2A_{zz'}$ values.

In comparison, a relatively more apparent increase in low field linewidth was observed for R1f as 2G, implying the presence of a rather complex dynamic state. In fact, the spectrum of T4L72R1f on CNBr cannot be satisfactorily fit with the single component in lineshape simulation (results not shown) but requires two components with different correlation times and/or order parameters, of which the dominant component corresponds to a fast, highly restricted motion like RX and RY in a cone with angular amplitude of approximately 16.4°.

Heat-induced changes could rather originate from the less dominant component, which is less restricted and thus theoretically has the lower activation energy. While the R1f side chain behaves practically immobilized on protein in the CW-EPR detection range, additional experiments are needed to fully uncover the structural origin for the existence of multi-components.

6.2.3.3 Global fits to both the X-band spectrum and the Q-band spectrum of T4L72RY attached to Sepharose

To confirm that RY possesses also a highly anisotropic internal dynamic mode with a fast rotational rate and strongly restricted angular amplitude, the Q-band CW-EPR spectra were measured for the same sample (T4L72RY on CNBr) under the same conditions used in X-band measurement. Moreover, both MOMD and effective Hamiltonian models were tested for the spectral simulation (Figure 6.9).

The best MOMD fit in X-band (Table 6.2) requires a fast internal motion with a correlation time $\tau_R \approx 3.0$ ns, and with a high degree of order (S = 0.91) that can be described as motion confined within a cone of half-angle ≈ 14.3° (recall that for 68RX72 the half-angle ≈ 12.5°). Resembling the simulation results for RX, the decrease in the τ_R value obtained from the Q-band MOMD fit compellingly implies that its internal dynamics are too fast to be visible in X-band, yet so robustly restricted to exhibit powder pattern spectra.

The global fit results clearly show that an adequately good fit can be obtained for: (1) the experimental Q-band spectrum using the same set of parameters from X-band fits with reasonable differentiation (mainly the g-tensors which are poorly resolved in X-band spectra); and (2) the effective Hamiltonian model in both X- and Q-band. Coherently, the rapid anisotropic

motional mode was verified to be the effective model portraying dynamic characters of the RY side chain on solvent-exposed helix sites.

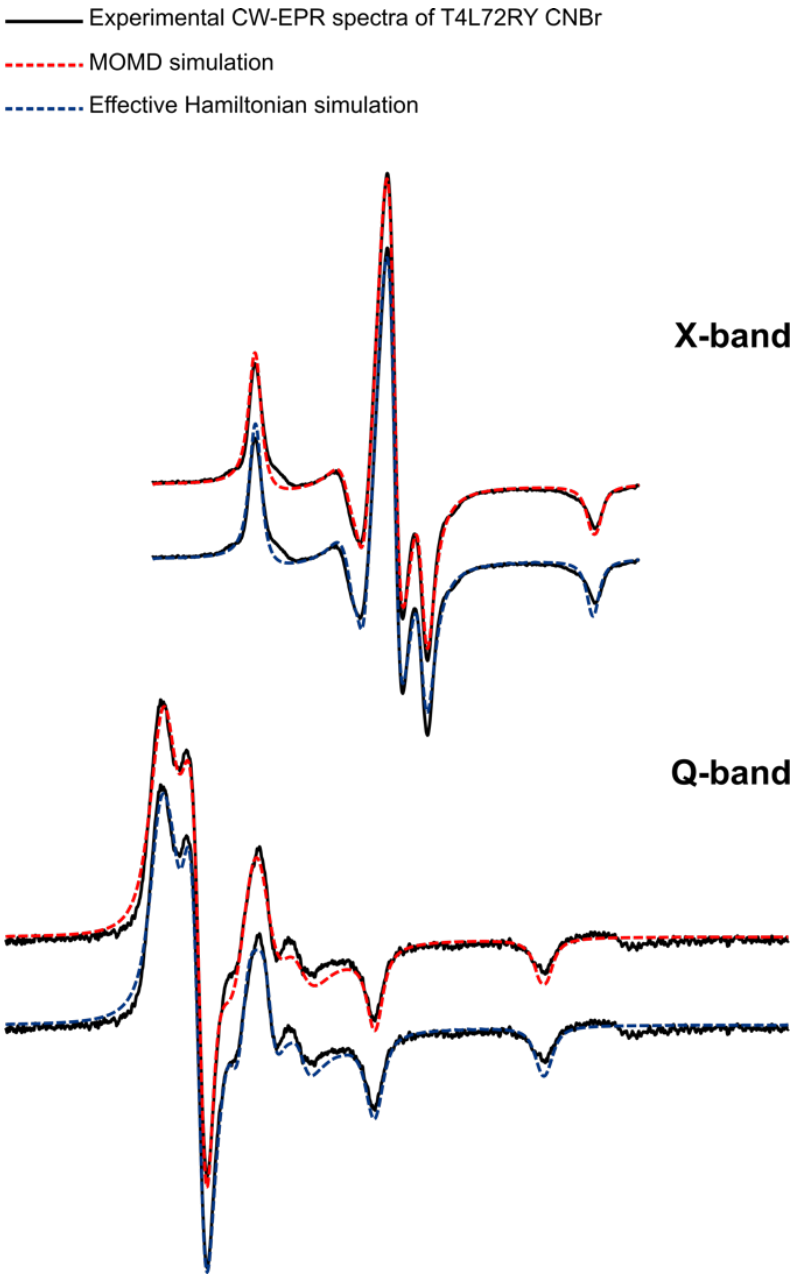

Figure 6.9 The X-band and Q-band experimental CW-EPR spectra of T4L72RY on CNBr (black, solid lines) superposed with simulated spectra (dashed lines) according to the MOMD model (red lines), and the time-independent effective Hamiltonian model (blue lines).

Table 6.2 Parameters for simulations

	$\langle R \rangle / s^{-1}$	τ_R/ns	S	c_0^2	α_D/°	β_D/°	γ_D/°
MOMD-X band	7.75	2.96	0.908	11.16	0	0	0
MOMD-Q band	8.17	1.12	0.891	9.53	0	1.15	0
H_{eff}-X band	n.a.	∞	n.a.	n.a.	9.85	12.85	19.30
H_{eff}-Q band	n.a.	∞	n.a.	n.a.	0	5.42	0

For MOMD model at both X- and Q-band, the magnetic parameters used for simulations are as follows: $A_{xx} = 6.31G, A_{yy} = 5.37G, A_{zz} = 36.74G$; $g_{xx} = 2.00800 \pm 0.00015, g_{yy} = 2.00586 \pm 0.00015, g_{zz} = 2.00199 \pm 0.00005$; For effective Hamiltonian (H_{eff}) model at both X- and Q-band, the magnetic parameters used for simulations are as follows: $A_{xx} = 7.36G, A_{yy} = 6.40G, A_{zz} = 34.66G$; $g_{xx} = 2.00774, g_{yy} = 2.00581, g_{zz} = 2.00236$.

6.3 Measurement of the μs-ms protein dynamics with monofunctional rigid spin labels using ST-EPR on solvent-exposed α-helical sites

Results exhibited above conclusively consolidate the presumption that the monofunctionally attached side chain RY possesses adequately restricted internal motion as comparable to the bifunctional label RX in practical motion detection. Indeed, both R1f and RY have shown to be promising candidates in characterizations performed with CW-EPR, i.e., in the time range of ps-ns. To uncover the real capacity of new labels for monitoring internal dynamics in the μs-ms time domain, ST-EPR spectra of small model proteins labeled with R1f and RY have been recorded. All mutants are attached to CNBr-activated Sepharose (unless specifically specified) so that μs-ms dynamics under physiological conditions can be measured.

6.3.1 ST-EPR under ambient conditions

Sites have been picked from solvent-accessible sites of rigidly packed helices of HoloMb

and T4L. Figure 6.10 shows the CW-EPR and ST-EPR spectra measured for corresponding mutants at room temperature. Apparent features as the powder patten (large $2A_{zz'}$, narrow linewidth, well-resolved lineshapes) are distinguishable from all spectra, among which the relatively broader linewidths of R1f-labeled samples indicate a larger degree of mobility of the side chain than RY, particularly the 66R1f. Spectra of RY-labeled samples are hardly distinguishable from each other, resembling RX. It needs to be noted that, unlike RX, there is no decrease in the values of $2A_{zz'}$ for 132R1f and 132RY, which supports the contention that the attachment of RX might induce local conformational changes that brings in subtle hindrance to the nitroxide.

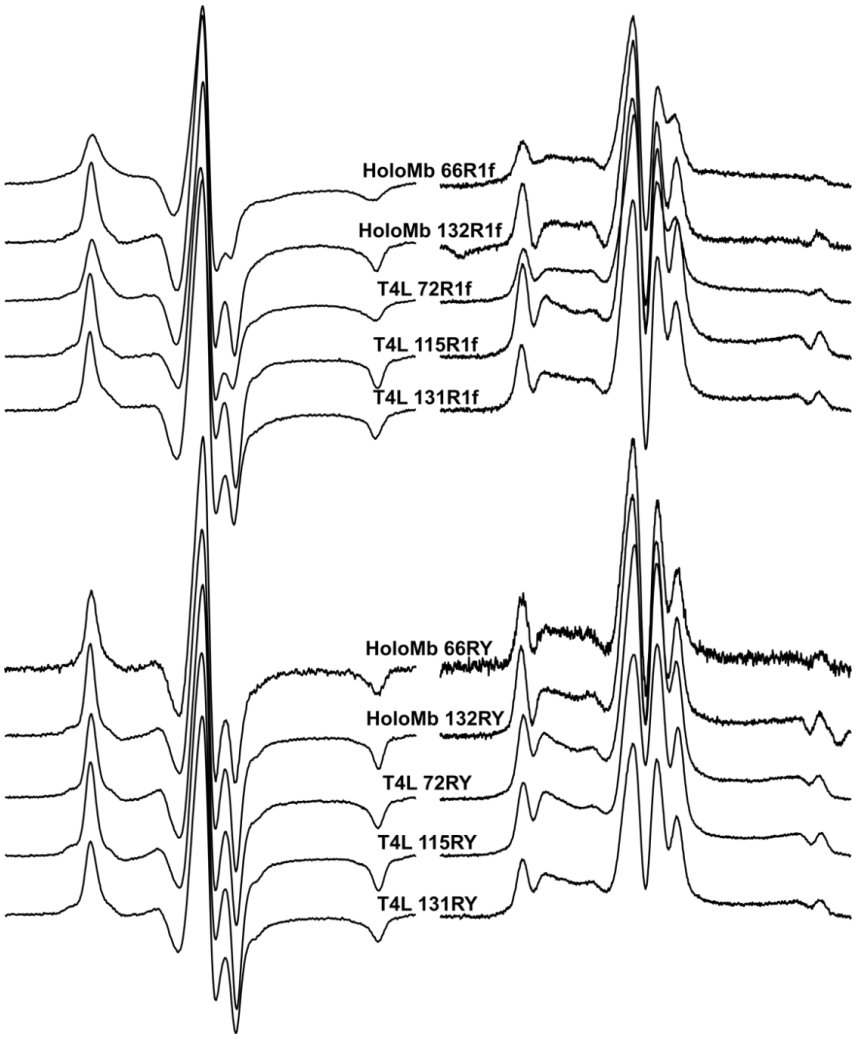

Figure 6.10 CW-EPR and ST-EPR spectra of R1f-labeled and RY-labeled HoloMb and T4L mutants at room temperature. All mutants were attached to CNBr-activated Sepharose. The magnetic field scan width is 100 G.

As expected, ST-EPR spectra exhibit more information in the time range beyond the rigid limit of CW-EPR. Again, the existence of anisotropy is evidently noticeable from the discrepancies between parameters (see section 6.5) for these two highly ordered labels. Most spectra of R1f-labeled mutants have negative values of C''/C parameters and smaller I_{ST}, implying the higher internal flexibility of spin label, yet the L''/L and H''/H parameters[38] detect motions within the same order of gratitude in the time scale as corresponding RX-labeled samples (e.g., 20~30μs from L''/L parameters).

Both the qualitatively similar lineshapes and the close estimation of correlation times unequivocally demonstrate the effectiveness of using these new, monofunctional rigid labels on solid supports for measuring dynamics in this time domain. It can be confirmed that the highly restricted internal motions of these labels are practically as promising as RX beyond the CW-EPR rigid limit. Consistent with the characterization in the ps-ns time range, RY is generally more immobilized than R1f or even RX on some sites, possibly because of its more hydrophobic and steric structure. On solid supports, protein dynamics with correlation times >100μs can be resolved from H''/H parameters of either R1f or RY, revealing the same type of motional mode in the microsecond time range detected on helical sites by RX.

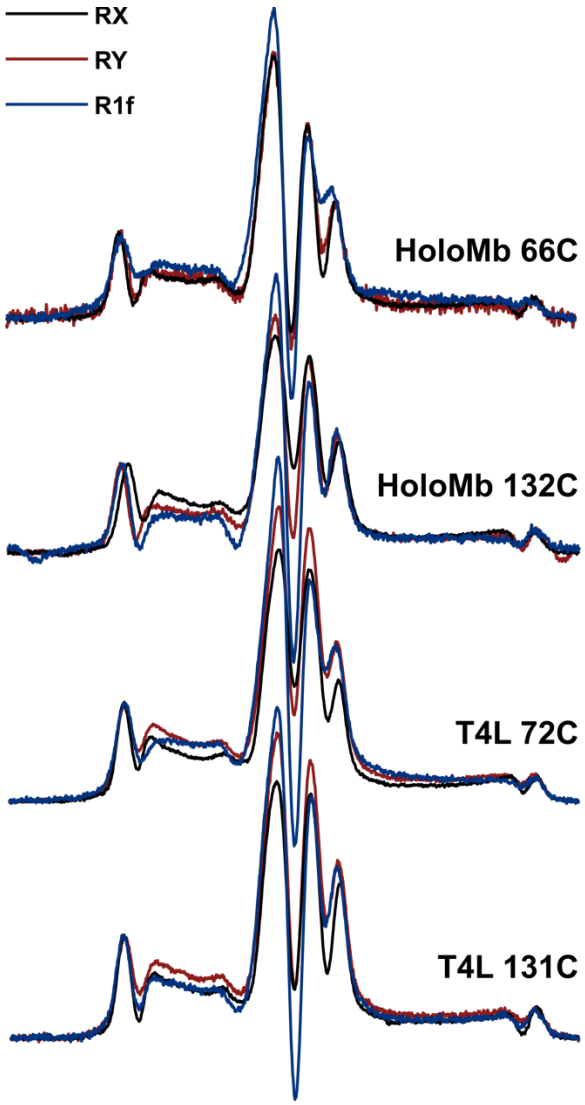

Figure 6.11 Overlaid ST-EPR spectra of RX/RY/R1f on proteins at room temperature. All mutants attached to CNBr-activated Sepharose. The magnetic field scan width is 100 G. Line heights used to calculate parameters are defined as shown. All ST-EPR lineshapes are scaled by the height of the low-field peak for a better comparison.

Characteristics of ST-EPR spectra obtained with spin labels of restricted anisotropic motions are further revealed from the comparison between results of RY (or RX) with R1f, a side chain that still possesses residual mobility in the fast time range. Even though the intrinsic values of T_1 for RX, RY, and R1f measured from SR-EPR experiments are essentially long (personal communications with M. Bridges: 2.9μs for 72R1 on CNBr, 7.7μs for 68RX72 on CNBr, 7.2μs

for 72R1f on CNBr, 6.8μs for 72RY on CNBr, 7.7μs for 131RY on CNBr), it is undeniable that the contribution from this extra flexibility decreases the overall spectral intensity, i.e., the detectable amount of magnetic resonance. Consequently, it is obvious from the spectral lineshape of 66R1f that the high field region is poorly resolved, leading to an overestimated value of apparent correlation time.

On the other hand, it is still sufficient to conclude from the value of the L''/L parameter that the spectrum is able to monitor slow dynamics in the microsecond range. As the amplitude of anisotropic internal motion is highly restricted, the transfer of saturation can only be effectively carried by motions involving a considerable range of angular width in the μs-ms time scale. Therefore, both the L''/L and H''/H parameters of R1f still preserve the sensitivity to slow motions of large amplitude, while the C'/C and integral parameters are more susceptible to fast fluctuations. A further discussion can be found in section 6.6.

6.3.2 Effects of nearest neighbor mutations on ST-EPR spectra of R1f and RY side chains

To explore whether nearby residue side chains might exert an influence on the dynamics in the μs-ms time range detected with ST-EPR spectra, the T4L construct 72C and 131C were subjected to various mutations of residues around the site to alanines, and corresponding mutants were labeled with either R1f or RY to be measured (Figure 6.12).

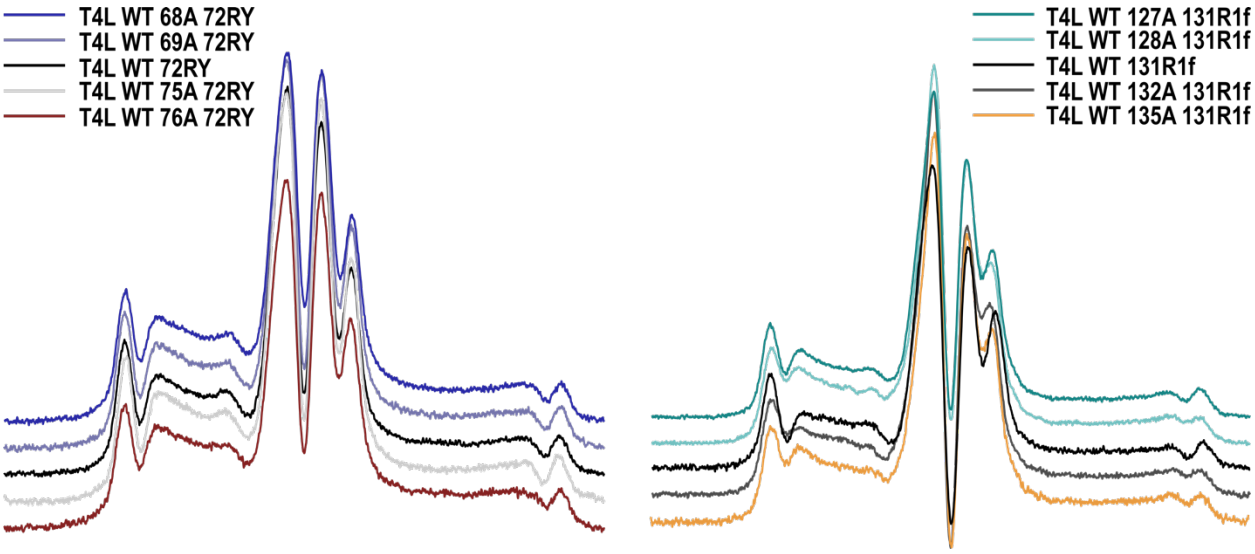

Figure 6.12 ST-EPR spectra of RY and R1f on corresponded alanine-substituted mutants. All mutants are attached to CNBr-activated Sepharose and measured under room temperature. The magnetic field scan width is 100G.

Spectra of four alanine mutants labeled with RY are all principally alike, reporting highly similar correlation times derived from all parameters (except one) as 72RY in the pseudo wild-type T4L background. This result compellingly suggests that the slow motion detected on helical sites from ST-EPR is not relevant to specific local side chain dynamics and/or interactions. While some influences might appear when multiple residues were mutated simultaneously, a single mutation to alanine seems to be not sufficient for modifying the slow motional mode and inducing considerable changes in ST-EPR spectra. Such substitution is supposed to largely retain the backbone configuration. This observation is consistent with the previous inference that only motions involving certain degrees of angular amplitude in the μs-ms time scale could contribute distinguishably to the ST-EPR lineshapes.

In the case of RY, the only noticeable difference is from 72RY/75A and only its H''/H parameter reports a faster motion. Whereas, more variations were shown from the ST-EPR spectra of alanine mutants labeled with R1f, particularly the 128A/131R1f. 127A/131R1f and 128A/131R1f exhibit higher values in both C'/C and integral parameters, suggesting that

fluctuations on a relatively fast time scale might be modified by the alanine substitution. Moreover, values of both L''/L and H''/H parameters from 128A/131R1f are larger than the 131R1f in pseudo wild-type T4L background, indicating that changes occur in the slow-motion time domain.

While the origin of the lower value in the H''/H parameter for 72RY/75A is unclear with current experimental data, as all the rest of the spectral parameters are unaffected, it is unlikely that the dominant motional mode is fundamentally changed. Considering the higher sensitivity of the H''/H parameter to anisotropic features and amplitude of motions, one reasonable hypothesis is that the substitution from hydrophobic valine to alanine leads to changes in the packing of side chains surrounding the nitroxide, which releases a certain degree of flexibility of the RY side chain within a limited range of orientation. A re-orientation of the nitroxide of restricted amplitude could be the cause of the reduced value of the H''/H parameter.

As for the more complicated results of R1f-labeled mutants, at the moment it is only possible to propose speculations based on the previous observation that the crystal structure of 131R1f suggests its rigidity is relevant to interactions with the backbone. A combination of the less rigid side chain and the less stable helix (short and known to possess higher mobility) might be more susceptible to modifications, thus affecting the backbone dynamics, which brings in changes to multiple spectral parameters. It needs to point out that regardless of the origin, this change falls in the sub-microsecond time range, as previous CW-EPR spectra (section 6.2.1.2) did not show significant differences in the fast time scale.

6.3.3 The μs-ms dynamics of immobilized proteins under various conditions

6.3.3.1 ST-EPR in rigid limit

Precipitated T4L mutants labeled with R1f or RY were also prepared and measured accordingly (Figure 6.13). While all spectral lineshapes are qualitatively similar and show clear features as expected for a rigid limit reference, both R1f and RY report extremely slow dynamics with their H''/H parameters and I_{ST}. On the one hand, there should be contributions from their long intrinsic T_1 values. On the other hand, the hydrophobic and steric nature of these two side chains might be playing negligible roles in maximizing the immobilization of nitroxides.

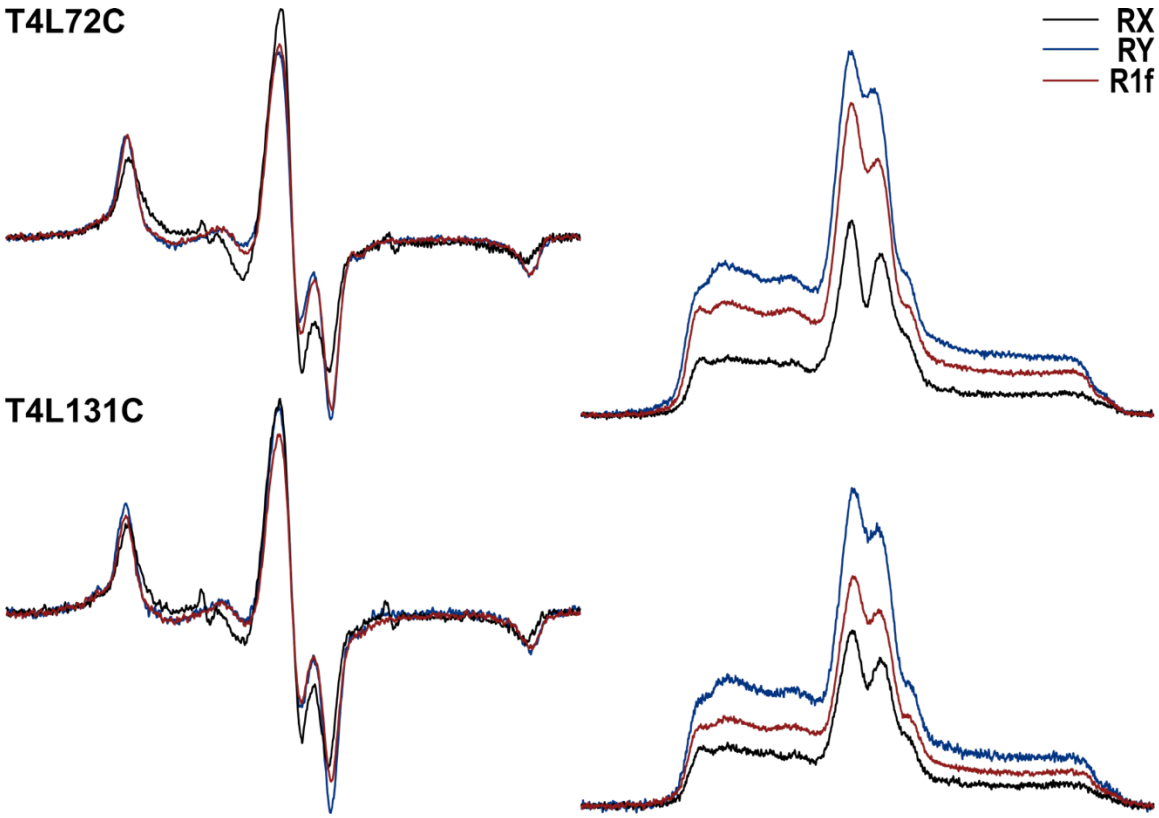

Figure 6.13 CW-EPR and ST-EPR spectra of precipitated proteins. T4L68RX72, T4L72RY, T4LR1f, and T4L127RX131, T4L131RY, T4L131R1f. The magnetic field scan width is 100 G. Both CW-EPR and ST-EPR spectra are normalized to the spin count calculated by double integration of V_1 spectra (CW-EPR at low power, see chapter 8).

Recalling that both R1f and RY side chains exhibit slightly higher degrees of mobility in the ps-ns time scale than RX, thus it is unlikely that the high values of H''/H parameters and I_{ST}

correlate with the internal dynamics of side chains. As confirmed by the similarity between spectra of precipitated R1-labeled and RX-labeled mutants (chapter 5), the side chain flexibility is not sufficient to bring in influences to the ST-EPR lineshapes, especially to the rigid-limit ST-EPR spectra. Instead, within the micro 'crystal lattice' of precipitated proteins, it is more reasonable to presume that the number of direct contacts to the nitroxide is proportional to the steric size of side chains, which leads to further immobilization of the side chain. This conjecture is also consistent with the observation that the bulkier RY side chains exhibit stronger immobility than R1f side chains.

6.3.3.2 Temperature-dependent ST-EPR spectra of T4L72RY attached to Sepharose

The temperature dependence of thermal motions is one of the most valuable thermodynamic parameters characterizing the energy barriers between states encoding structural information. For a strongly immobilized system, such as the T4L68RX72 or T4L72RY on CNBr, the temperature dependence is essentially invisible from CW-EPR spectral lineshapes, which indicates that the lifetime of existent states falls in the time range longer than 100 ns (CW-EPR rigid limit), corresponding to the higher activation energies.

To explore whether there is detectable temperature dependence in the μs-ms time domain, ST-EPR spectra of T4L72RY on CNBr (Figure 6.14) were determined at several temperatures in the range of 5-35°C. When the temperature is increased, all spectral parameters regularly decrease, indicating the increase in mobility on the μs-ms time scale. The H''/H parameter reports the slowest motion at low temperatures with correlation time ~200μs, which is in the same order of gratitude as the motion observed for crosslinked T4L68RX72 on CNBr.

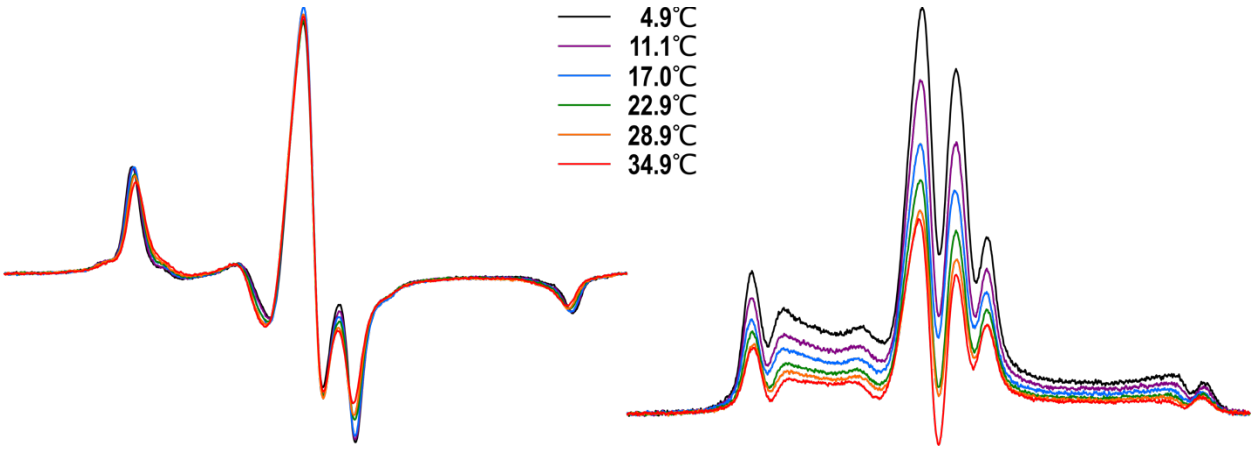

Figure 6.14 Normalized CW-EPR and ST-EPR (based on V_1) spectra of T4L72RY on CNBr at temperatures ranging from 5°C to 35°C

The sensitivity of ST-EPR spectra to temperatures confirms again that the existing motional mode corresponds to high activation energies. It can be inferred that slow, collective motions involving considerable angular movements are necessary to release the restricted nitroxide from high ordering. There is no sufficient evidence to determine the relationship between the crosslinked motional mode and the low-temperature motional mode, but both spectra report probably the slowest protein internal dynamics.

While the characteristics in lineshapes are qualitatively retained over the tempering range, the analysis with different parameters yields different temperature dependence. A non-linear Arrhenius behavior is observed for the lineshape parameters but not the integral parameter, which is clearly reflected by the uneven decrease in values of L''/L and H''/H parameters. The cause of the departure from the ideal relationship between the spectral parameters and temperatures is intriguing but complicated.

Similar results[39–44] have been repeatedly observed for membrane proteins, such as in the studies of Ca^{2+}-ATPase, some of which have demonstrated the phenomenon as an order-to-disorder phase transition of the membrane lipid. However, a variety of alternative explanations

have also been suggested, including a reduction in the anisotropy in lipids, changes in intermolecular interactions, and a reflection of protein conformational change, etc. As the activation energy for lipid "microviscosity" in membranes was determined to be constant in the examined temperature range[45], it is more likely that this is not a property of surrounded lipids but the embedded protein itself. Moreover, similar non-linear behaviors were determined from the Arrhenius plots of Ca^{2+}-ATPase enzymatic activity, suggesting the relation to the functionalization of proteins.

For the model system (T4L72RY) measured in this work, there are essentially fewer relevant variables. Over this temperature range, the probability of phase transition (which would be from water to ice) or change in environmental fluidity is minimal. Squier and Thomas proposed that the presence of small amounts of weakly immobilized probes could result in a similar discrepancy between the temperature dependence of lineshape parameters and the integral intensity. However, there is no evidence from the CW-EPR spectra of T4L72RY on CNBr that certain amounts of weakly immobilized probes are populated upon heating up. Considering the fact that at room temperature, a single anisotropic component is sufficient to satisfactorily fit the spectra of 68RX72 or 72RY, this possible origin could be mostly ruled out for these highly immobilized side chains.

Collectively, it is most likely that this temperature dependence is a direct reflection of protein internal dynamics. As the temperature increases, the amplitude of protein fluctuations also increases, leading to a subsequent re-orientation of the nitroxide probe and eventually overcoming the activation energy barriers. The plateau regions occur between 11.1℃ to 17.0℃, and between 22.9℃ to 28.9℃, which potentially implies the existence of a temperature-dependent equilibrium between multiple conformational substates under those temperatures. This

energetic profile is a theoretically more reasonable description for collective motions involving considerable angular movements, in which concrete stages rather than continuous dynamics are expected.

However, the nature of ST-EPR determines that results solely obtained by this technique are difficult to interpret unambiguously. Furthermore, some irreversible changes were observed to take place in the measurements for temperature-dependent ST-EPR of T4L68RX72 on CNBr (spectra not shown, but spectral parameters can be found in section 6.5). Changes in values of L''/L and H''/H parameters exhibit non-monotonic tendency, where the sample measured under room temperature (22-23°C) reports the fastest dynamics. Measurements using other techniques are necessary to fully reveal the mechanism behind this phenomenon, such as distance mapping via DEER to provide information on the magnitude, while the outstanding advantage of ST-EPR shown here is being able to monitor slow dynamics *in situ*.

6.3.3.3 T4L72RY in various immobilization matrices

As the monofunctionally attached spin label showed comparable rigidity as the bifunctional RX, the characteristics of the RY side chain in slow motion detection were further investigated. Labeled mutants have also been immobilized under various conditions accordingly: precipitation, glutaraldehyde crosslinked, add sucrose, and/or Ficoll (Figure 6.15).

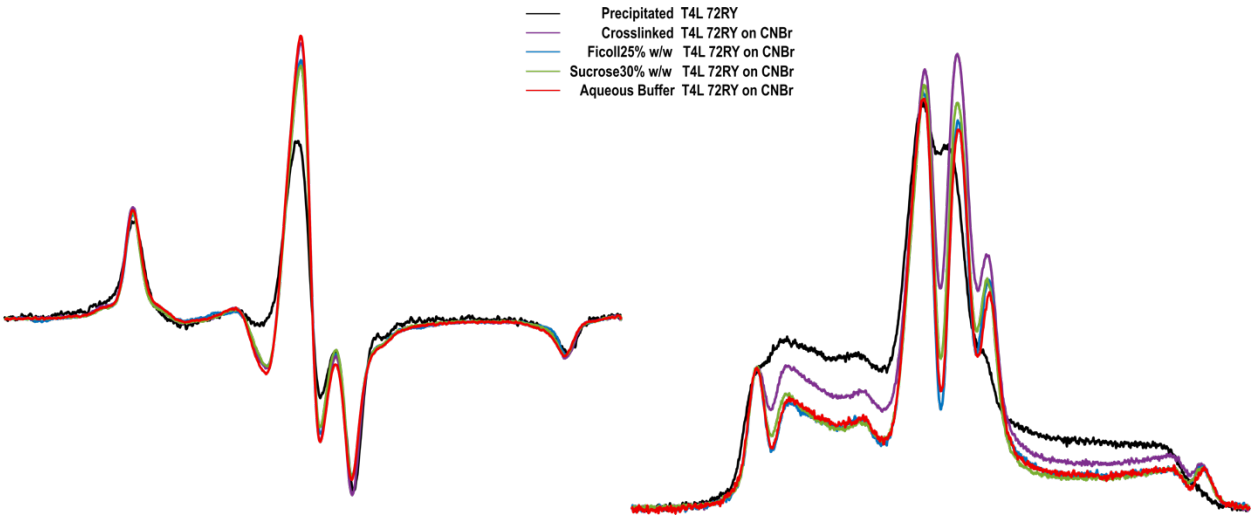

Figure 6.15 ST-EPR and CW-EPR spectra of T4L72RY under different conditions. All ST-EPR lineshapes are scaled by the height of the low-field peak for a better comparison. All CW-EPR spectra are normalized to the spin count calculated by double integration.

While all CW-EPR lineshapes (except for the precipitation possessing heterogeneous and complicated microenvironments) are indistinguishable from each other, ST-EPR spectra sensitively reflect the variations in dynamics under different conditions. The results are largely the same as what has been observed using RX, except for one discrepancy: the addition of Ficoll has no effect on the spectral lineshapes of T4L72RY on CNBr. The ST-EPR spectrum of the Ficoll-added sample has highly similar lineshapes to the sample in just the aqueous buffer but possesses a higher value of intensity integral, which resembles the situation of the sucrose-added sample.

This result could be a discovery of some critically unique characteristics of the RY side chain. Structurally different from the crosslinker RX, the rigidity of RY presumably arises from the non-covalent restriction to bond rotations *via* the two phenyl groups. The hydrophobicity and aromaticity of phenyl groups could significantly modify the behaviors of the side chain. However, in the time domain of ps-ns, the CW-EPR lineshapes are not sensitive enough due to

the practically comparable rigidity of RY to RX.

More features are already resolved from the ST-EPR spectra of solid-attached samples in just the buffer. While the values of C'/C parameters still follow the same relationship of immobility determined in the ps-ns time range, both 72RY and 72R1f actually report motions with longer correlation times from their L''/L and H''/H parameters. This result implies that the RX side chain might be more sensitive to certain motions in the μs-ms time range that are not detected by R1f or RY. In other words, the saturation 'transfer' is more efficient in the RX-labeled sample, thus exhibiting a relatively short correlation time.

Although previous studies[46] indicate that a restriction in the angular amplitude of rotational motion can increase the observed effective rotational correlation time, all characterization results with CW-EPR confirm that the nitroxide is more restricted in the RX side chain, thus excluding this possibility. Moreover, as all mutants are attached to CNBr-Sepharose, although there might be concerns about potential non-specific multiple-point attachments, effects from the solid supports are unlikely to contribute. Discussions involving the attachment schemes will be revisited in the following section, where the other attachment methods are examined and analyzed.

In the experiment measuring the same mutant under various conditions, the loss of sensitivity upon Ficoll addition observed for 72RY might also originate from the different sensitivity of RY side chains to motions, particularly the anisotropic motions. The relative orientation of the spin label axis relative to the protein rotation axis is crucial for the sensitivity of spin labels. Recall that RX is approximately perpendicular to the axis of the helix, if the axis of the RY side chain is rather in parallel to the helix, the additional motion identified by RX could be invisible to RY. In other words, the ST-EPR spectra of T4L72RY report the same

dynamics with or without the Ficoll, of which the $\tau_R \approx 140\mu s$.

Such difference in the intrinsic sensitivity could potentially make the RY side chain a particularly valuable candidate for detecting anisotropic motions. Although more evidence is needed to further consolidate this hypothesis, it needs to be pointed out that the Ficoll-added T4L68RX72 on CNBr reports exactly the same correlation time from its value of the H''/H parameter, where the addition of Ficoll presumably suppresses one particular motion on the μs-ms time scale.

6.4 Probing dynamics in the μs-ms time range using monofunctional side chains

6.4.1 A survey: effects of immobilization on protein internal dynamics in the μs-ms time range

In this section, different strategies for tethering proteins to solid supports are explored with ST-EPR. As mentioned above, a large number of strategies have been developed in recent years for tethering macromolecules to stationary substances in protein studies and biosensor applications. However, the extent to which tethering modifies the energy landscape and therefore function of proteins is often unknown. Few biophysical methods can monitor these heterogeneous systems of diverse physiochemical properties, and explore the conformational ensemble with site-specific resolution. SDSL-EPR, especially ST-EPR, serves as a unique choice for this purpose in a manner inaccessible to other methods.

As both a continuation and extension of the study of stationary-phase EPR[18], two generally used tethering strategies are tested now with the model protein, pseudo wild-type T4L by ST-EPR in addition to attachment using CNBr-activated Sepharose which has been successfully used for ST-EPR measurements: to streptavidin-functionalized resin by biotinylated tags (Figure

6.16); to immobilized metal-ion (Ni and Zn) resin (functionalized by NTA or IDA) by histidine tags (Figure 6.17). Monofunctional spin labels are used to simplify the mutant generation process, and to minimize potential perturbation brought by more mutations.

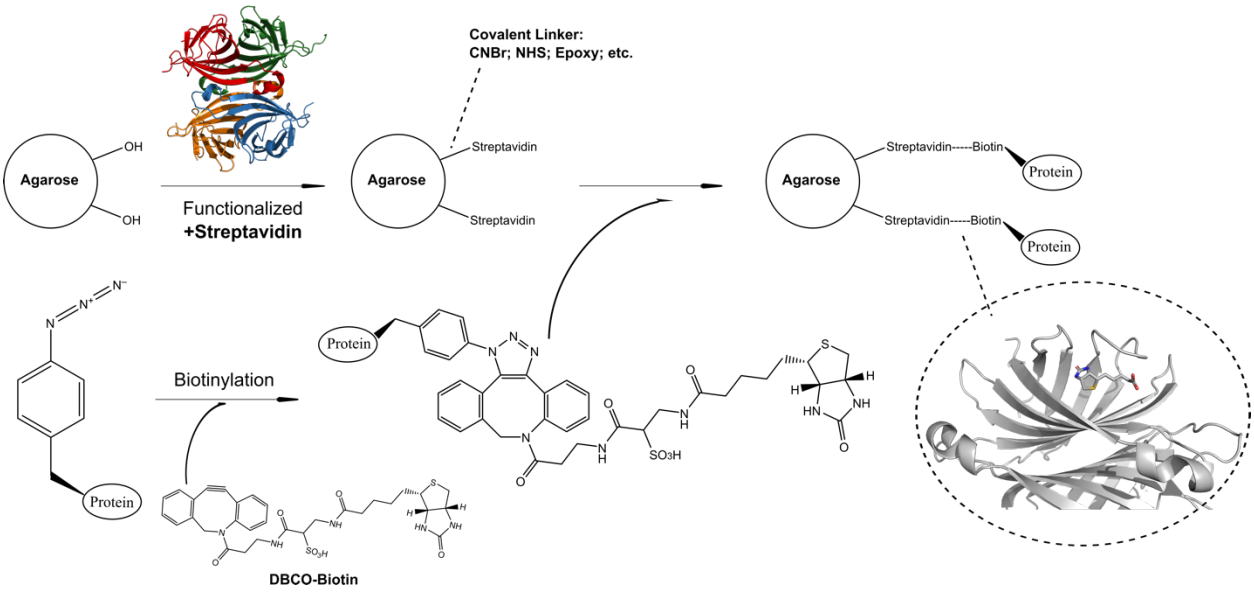

Figure 6.16 Immobilization strategy using unnatural amino acids (p-AzF in this dissertation) and streptavidin-functionalized resin. Insert: the streptavidin-biotin interaction (PDB code: 3RY1). Details can be found in chapter 8.

Both R1f and RY give qualitatively the same results. By comparing the highly similar CW-EPR lineshapes (Figure 6.18) and the apparently different ST-EPR lineshape obtained with different strategies, it can be concluded: (1) All tethering strategies effectively immobilize proteins in the fast time domain (ps-ns) by slowing down the Brownian rotational diffusion to a similar extent, judging from $2A_{zz'}$ values and linewidths of low-field peaks in CW-EPR spectra. (2) In ST-EPR spectra, all constructs report detectable dynamics in the slow time domain (μs-ms). However, their residual motions vary apparently in this domain.

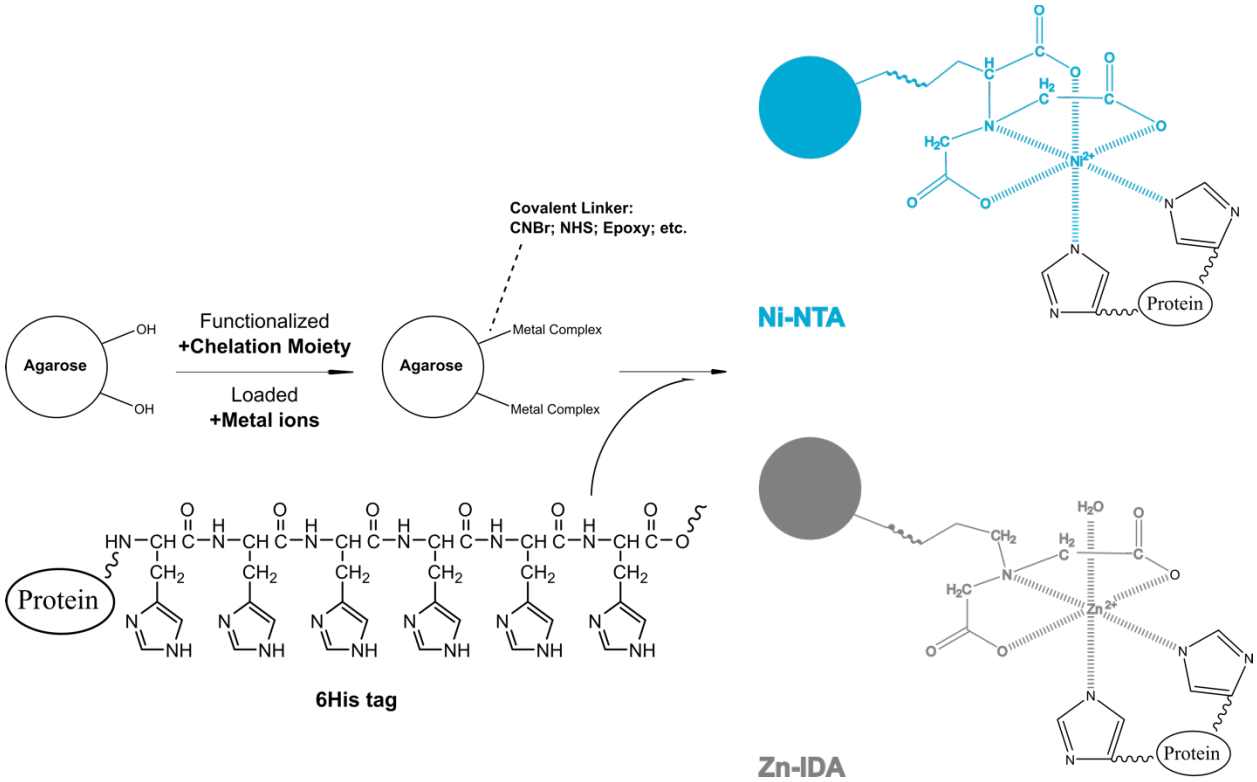

Figure 6.17 Immobilization strategy using histidine tags and IMAC resin (loaded with Ni-NTA/Zn-IDA). Details can be found in chapter 8.

Based on high-field ratios, the attachment *via* CNBr restricts the correlation time of protein dynamics to >100μs, and streptavidin-biotin strategies to ~50μs, while the His-tag-metal-ion to only ~30μs. On the other hand, different strategies all show motions in the time domain of 10^{-5}~10^{-4} s, confirming that what is detected by ST-EPR mostly comes from a common origin. While the specific construct of attachments has effects on the absolute values of correlation times, the dominating dynamics measured by ST-EPR are the internal dynamics of tethered proteins.

Compared to either the crystallization or chemical crosslinking that may hinder the intrinsic dynamics of proteins in the aqueous solution more or less, tethering to solid supports effectively eliminates the contribution from Brownian rotational diffusion while maintaining mostly the

physiological state of proteins. These results demonstrate the feasibility of using SDSL-EPR to study tethering strategies by directly offering dynamics in the difficult μs-ms time range, which may help to modulate the performance of proteins on the functionalized surface in bioanalytical applications.

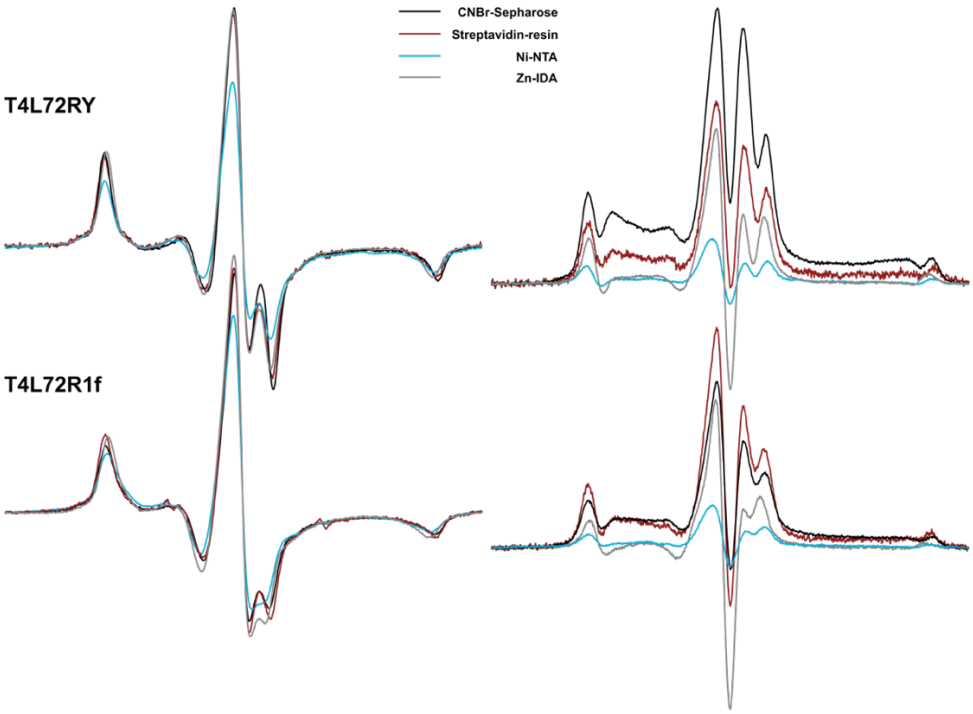

Figure 6.18 CW-EPR and ST-EPR spectra of labeled mutants attached to solid supports by corresponding methods. For comparison, all ST-EPR lineshapes are scaled by the height of the low-field peak, and the vertical lines are drawn in CW-EPR spectra as references for $2A_{zz}$' changes.

The attachment to solid supports also helps to improve the stability of samples in solution. The high effective concentrations (≥300μM) that can be achieved without aggregation provide high signal-to-noise data for ST-EPR measurements. The better quality of data can potentially enable real-time recording of transient changes for measuring the kinetics of conformational exchange.

As summarized, different tethering strategies all effectively eliminate contributions from the Brownian rotational diffusion so that the internal dynamics in the time domain of μs-ms can be

revealed. However, clear variations are identified between different attachment strategies.

It is practically hard to assign specific origins to explain differences in τ_R values between strategies. Each construct consists of different structural elements that are relevant to the specific chemistry utilized for the method, for example, the linkers. Serving as the "hinge" connecting protein molecules and solid supports, its intrinsic length and internal flexibility can surely influence the relative motion between the residue and the attachment point. The histidine tags consist of 6 molecules and are designed to retain internal flexibility to a certain extent, while the covalent bond formed between lysines and CNBr-activated Sepharose is short and rigid.

Moreover, the commercially available beads/resins are functionalized variously, aiming at different purposes including high resistance to flow pressure, or high loading capacity to maximize purification efficiency, etc. Extra covalent linkers are thus added to the matrix (see Figures 6.16 and 6.17) in order to introduce the functional groups. While there are several popular choices of linker utilizing well-examined chemistry, such as the CNBr reaction and NHS reaction, the specific details are often unreleased, such as the length of the linkage, or the strength of interactions forming the linkage, etc.

In the ST-EPR experiments, the results obtained from Zn-IDA resin are very likely to be heavily influenced by the specific functionalization method. While its CW-EPR spectra show sufficient immobilization, the ST-EPR spectra report abnormally fast motions in the microsecond range. Moreover, the values of its integral parameters are too close to the values obtained from Ni-NTA resin. Considering that Ni^{2+} ion is known to be a fast-relaxing agent while Zn^{2+} ion is not, values of the integral parameter that is directly decided by values of T_1 should be apparently larger for mutants attached to Zn-IDA resin, which is not observed. Therefore, it is highly possible that the linker included in Zn-IDA resin is longer and/or more flexible, leading to

additional dynamics in the time range of 100ns-µs.

As previously mentioned, the solvent perturbation experiments using sucrose and Ficoll were also tested with mutants that are site-specifically attached to the streptavidin resin *via* the azido-DBCO-biotin linkage. Both 72RY and 72R1f report slower dynamics upon the addition of Ficoll judging from their ST-EPR spectral lineshapes. However, it needs to be emphasized that the differences between the Ficoll-added 72RY sample and 72RY in only the buffer are obviously small. In fact, both values of their L''/L and H''/H parameters are basically the same, implying that the 'transfer' is largely the same in efficacy between the resonance positions, i.e., relative orientations.

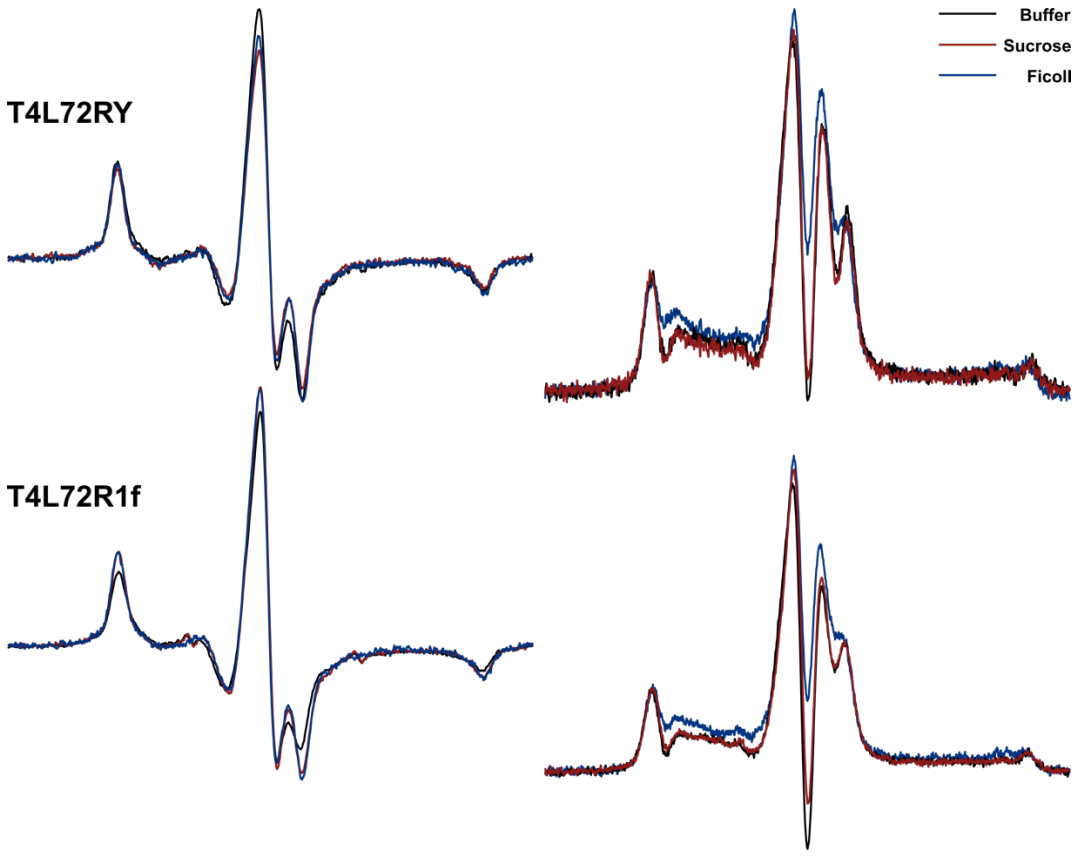

Figure 6.19 ST-EPR spectra of T4L72RY and T4L72R1f on streptavidin-functionalized resin, in buffer, in sucrose 30% w/w, in Ficoll 25% w/w.

This observation suggests that there exist certain amounts of additional microsecond-range

motions in proteins immobilized *via* this scheme relative to the attachment *via* CNBr. The variations are so subtle that it is very likely to be originated from partial changes in the anisotropy of the dynamics. Even though the streptavidin-biotin interaction is recognized as one of the most stable interactions[47,48], the whole linkage is longer and more complicated compared to the CNBr-lysine linkage. Besides, the difference between site-specific attachment and heterogeneous non-specific attachment could also contribute to the variations in lineshapes.

6.4.2 Exploring dynamics in the μs-ms time range of T4L cavity mutant L121A/L131A

To show how might multiple motional modes in exchange be reflected in ST-EPR spectra, the L121A/L133A cavity mutant of T4L is used. Cavities and pockets are generally found in globular proteins, playing a critical role in function execution such as ligand binding. However, there is usually very little difference distinguished in crystal structures between the WT and corresponding cavity mutants, which has made it hard to provide the structural basis and thus the mechanism of how is the cavity related to the function.

In one previous work[49] of the T4L L121A/L133A cavity mutant using SDSL-EPR methods, in solution, additional conformational substates in equilibrium exchange with the WT-like conformation are implied by multiple components in CW-EPR lineshape simulation. The “cavity conformation” exhibits slower rates and higher orders identified on several sites. Thus, it is proposed to adopt an alternative packing structure where the protein fills or partially fills the cavity with side chains. SR-EPR evaluates the timescale of exchange between conformational substates to be >70μs, which is beyond its detection limit of either CW-EPR or SR-EPR. In short, although the existence of conformational exchange can be inferred from a combination of CW-EPR, SR-EPR, and distance measurement results, there is no direct characterization of the

dynamics of the “cavity conformation” that is in exchange with the WT-like conformation on a sub-ms timescale.

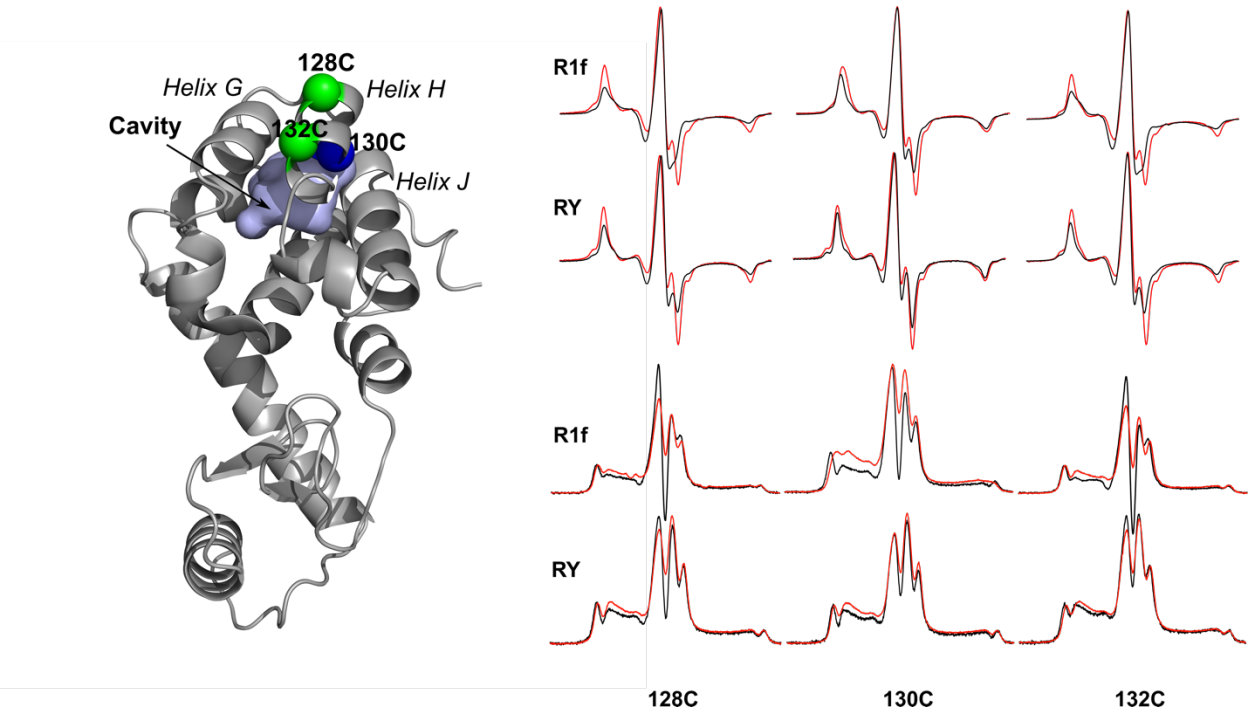

Figure 6.20 Ribbon diagram of T4L L121A/L133A cavity mutant (PDB code 251L) showing the sites used in this study. The surface of the cavity is shown in lightblue. The green and blue spheres at Cα identify the sites where R1f/RY is introduced. Corresponding CW-EPR and ST-EPR spectra of pWT-T4L (black curves) and T4L L121A/L133A cavity mutants (red curves) on CNBr-activated Sepharose are shown.

Sites involved in the exchange (on Helix H, Figure 6.20) are labeled with R1f or RY in both pseudo wild-type T4L and L121A/L133A cavity mutant. Primarily, all CW-EPR spectra exhibit strong immobilization characteristics, particularly the spectra of RY-labeled mutants which are essentially indistinguishable from each other. Yet, clear variations are resolved in ST-EPR spectra. According to L’’/L and H’’/H parameters, all mutants report dynamics with correlation times in the range of 10^{-5}~10^{-4}s, and L121A/L133A cavity mutants exhibit slower dynamics than pWT-T4L.

Among all, labeled L121A/L133A/130R1f shows the longest correlation time as 250μs. In

the previous work, a series of results suggest that the nitroxide of 130R1 is sequestered in the cavity of L121A/L133A.The strongly stabilizing interaction of “buried” 130R1 is presumably due to the complementary size of the R1 side chain to the hydrophobic cavity, as well as the hydrophobic nature of the disulfide linkage and nitroxide ring of R1. Considering that R1f has an adequately larger size and a more hydrophobic structure, it is reasonable to speculate that the side chain is also sequestered tightly in the cavity. In other words, the correlation time measured from the L121A/L133A/130R1f sample corresponds to the least mobility of labeled proteins, representing approximately the complete immobilization of nitroxide relative to the surroundings.

Based on high-field ratios of R1f-labeled samples, two solvent-exposed sites, 128C and 132C both report dynamics ~70μs of pWT-T4L, and dynamics ~120μs of the L121A/L133A cavity mutants. Even though the absolute values of correlation times are slightly different on the two sites, there are clearly two distinguishably different motional modes monitored from the cavity mutant and the WT. Compared with the L121A/L133A/130R1f as a mobility limit, it can be inferred that the dynamics are more restricted in the cavity mutant than in the WT, but there are still motions detectable on the microsecond time scale.

While in the WT, motions reflected from lineshapes are very similar to what is detected from helical sites of HoloMb and pWT-T4L, there are several possible origins of the slower dynamics in the cavity mutant. On the one hand, the cavity conformation is identified as the more immobilized component in the previous work, showing lower mobility than the WT conformation. It could be that the internal dynamics of the cavity conformation possess an apparent correlation time of ~120μs.

On the other hand, as suggested from previous results, the cavity conformation is in

exchange with the WT-like conformation on a sub-ms timescale in the cavity mutant. Therefore, it could also be that it is the overall dynamics from a mix of two co-existing conformations that we are monitoring. The slight difference in the correlation time of 128R1f and 132R1f may either attribute to the difference in their local flexibilities, or the relative populations of the two conformations. Titrations of ligands bound to the cavity are needed to further understand the mechanism.

Located at a contact site between helices H and J, residue 130C has shown its uniqueness in previous studies. SR analysis showed that the two components in its CW-EPR spectrum arise from two conformations rather than two rotamers of R1, revealing inherent flexibility in the helix H even in the WT conformation. However, in the ST-EPR spectrum of 130C in pWT-T4L, both low-field and high-field ratios, and the integrated intensity indicate that this site experiences the same dynamics on the μs timescale as 128C and 132C in pWT-T4L. Only the center-field ratio that is more susceptible to faster and more local motions reports a longer correlation time, possibly corresponding to the more immobilized component in its CW-EPR spectrum.

This result demonstrates again that the local flexibility is not necessarily reflected in ST-EPR lineshapes. Based on just multiple components in CW-EPR spectra, it is hard to distinguish motions with various values of rates and amplitudes when they are all slower than the rigid limit (100ns). On the ST-EPR timescale (μs-ms), only motions with sufficient angular amplitudes can efficiently transfer the saturation of spins, thus leading to adequate changes in spectra. Therefore, it is most likely that microsecond motions that are generally detected on helical sites are collective motions involving multiple structural elements.

RY-labeled samples give a qualitatively same conclusion as R1f that L121A/L133A cavity mutants exhibit slower dynamics than pWT-T4L. However, there are some inconsistencies

between mutants that probably attribute to differences in the structure of RY. Based on high-field ratios, it is the L121A/L133A/132RY rather than L121A/L133A/130RY that shows the longest correlation time of 230μs. One possible model is that due to the larger size of the RY side chain, the nitroxide cannot be sequestered in the hydrophobic cavity of L121A/L133A/130C. Therefore, this sample instead monitors the same motional mode as 128C and 132C.

For the R1f-labeled mutants carrying 130C, the $2A_{zz'}$ in the CW-EPR spectrum of the cavity mutant is actually smaller than the $2A_{zz'}$ of the pWT-T4L mutant, implying that the nitroxide resides in a more hydrophobic environment. However, in the case of RY-labeled samples, the $2A_{zz'}$ of the cavity mutant has not changed significantly, supporting the proposed model that the nitroxide is still exposed to solvent. Also, because of the larger size and the more hydrophobic nature, the side chain of RY on residue 132C may interact with helix G, leading to longer correlation times, while the distance is too far for other spin labels. Although RY is more immobilized than R1f or even RX, which might bring in additional information complicating the results when applied in more practical systems, each of these labels has its own advantages and disadvantages. This will be summarized and discussed further in section 6.6.

6.5 Tabulated ST-EPR empirical parameters and correlation times

By repeatedly taking ST-EPR measurements on a single sample, the standard deviations were estimated for the values of L''/L, $\tau_{R,\,L''/L}$, H''/H, and $\tau_{R,\,H''/H}$ determined from ST-EPR spectra of R1f- and RY-labeled samples, serving as an evaluation of measurement precision. For R1f, the ratio of standard deviation to average for L"/L is 4.76%; $\tau_{R,\,L''/L}$: 11.6%; H"/H: 5.78%; $\tau_{R,\,H''/H}$: 15.1%. For RY, L"/L: 4.63%; $\tau_{R,\,L''/L}$: 11.2%; H"/H: 3.78%; $\tau_{R,\,H''/H}$: 9.3%. The percentage

rather than the absolute value of standard deviation is used considering the relatively wide range for these parameter values.

All empirical parameters and correlation times measured from ST-EPR spectra of HoloMb and T4L mutants that were labeled by either R1f or RY are tabulated on the following pages. The signal noise was estimated from the baseline and peak intensity of each spectrum and also included as the +/- deviation for values of L"/L and H"/H, and propagated to the corresponding correlation times ($\tau_{R,\,L"/L}$ and $\tau_{R,\,H"/H}$).

1. RY on different helical sites (HoloMb&T4L) in buffer

	L”/L	τ_R/sec	C’/C	τ_R/sec	H”/H	τ_R/sec	Integral
HoloMb 66RY CNBr-Buffer	0.50	2.2×10^{-5}	-0.12	4.0×10^{-6}	0.67	9.2×10^{-5}	0.1945
HoloMb 132RY CNBr-Buffer	0.46	1.8×10^{-5}	0.06	6.7×10^{-6}	0.55	5.5×10^{-5}	0.2383
T4LpWT 72RY CNBr-Buffer	0.64	3.9×10^{-5}	0.29	1.3×10^{-5}	0.79	1.4×10^{-4}	0.2538
T4LpWT 115RY CNBr-Buffer	0.73	5.4×10^{-5}	0.45	2.2×10^{-5}	0.76	1.3×10^{-4}	0.4017
T4LpWT 131RY CNBr-Buffer	0.66	4.1×10^{-5}	0.16	9.0×10^{-6}	0.80	1.4×10^{-4}	0.2879
T4LpWT 72RY/68A CNBr-Buffer	0.69	4.7×10^{-5}	0.31	1.4×10^{-5}	0.84	1.6×10^{-4}	0.2658
T4LpWT 72RY/69A CNBr-Buffer	0.64	3.9×10^{-5}	0.20	1.0×10^{-5}	0.76	1.3×10^{-4}	0.2678
T4LpWT 72RY/75A CNBr-Buffer	0.63	3.7×10^{-5}	0.20	9.9×10^{-6}	0.66	8.6×10^{-5}	0.2785
T4LpWT 72RY/76A CNBr-Buffer	0.70	4.9×10^{-5}	0.21	1.0×10^{-5}	0.86	1.7×10^{-4}	0.2588
T4LpWT 128RY CNBr-Buffer	0.69	4.6×10^{-5}	0.20	1×10^{-5}	0.78	1.3×10^{-4}	0.4620*
T4L 121A/133A 128RY CNBr-Buffer	0.86	8.3×10^{-5}	0.60	4.3×10^{-5}	0.84	1.7×10^{-4}	1.2058*
T4LpWT 130RY CNBr-Buffer	0.69	4.7×10^{-5}	0.43	3.5×10^{-5}	0.67	9.2×10^{-5}	0.8153*
T4L 121A/133A 130RY CNBr-Buffer	0.88	8.8×10^{-5}	0.64	5.4×10^{-5}	0.83	1.6×10^{-4}	1.0258*
T4LpWT 132RY CNBr-Buffer	0.80	6.8×10^{-5}	0.44	2.2×10^{-5}	0.81	1.5×10^{-4}	0.4408*
T4L 121A/133A 132RY CNBr-Buffer	0.92	9.9×10^{-5}	0.62	4.6×10^{-5}	0.94	2.3×10^{-4}	1.1250*

*The non-saturating first-derivative in-phase absorption spectra (V_1) used in these measurements are taken under a different value of power/field strength from other data in this work, so these values can only be used for comparison within this dataset but not to others

2. R1f on different helical sites (HoloMb&T4L) in buffer

	L”/L	τ_R/sec	C’/C	τ_R/sec	H”/H	τ_R/sec	Integral
HoloMb-66R1f CNBr-Buffer	0.55	2.7×10^{-5}	-0.35	2.0×10^{-6}	0.86	1.8×10^{-4}	0.1024
HoloMb-113R1f CNBr-Buffer	0.31	5.8×10^{-6}	-0.28	2.5×10^{-6}	0.41	2.8×10^{-5}	0.1128
HoloMb-132R1f CNBr-Buffer	0.38	1.1×10^{-5}	-0.40	1.6×10^{-6}	0.56	5.8×10^{-5}	0.1061
T4LpWT-72R1f CNBr-Buffer	0.59	3.1×10^{-5}	-0.13	3.8×10^{-6}	0.87	1.8×10^{-4}	0.1598
T4LpWT-115R1f CNBr-Buffer	0.54	2.6×10^{-5}	0.20	1.0×10^{-5}	0.68	9.4×10^{-5}	0.2732
T4LpWT-131R1f CNBr-Buffer	0.53	2.5×10^{-5}	-0.18	3.3×10^{-6}	0.66	8.8×10^{-5}	0.1755
T4LpWT-131R1f/127A CNBr-Buffer	0.54	2.6×10^{-5}	0.02	6.0×10^{-6}	0.64	8.2×10^{-5}	0.3006
T4LpWT-131R1f/128A CNBr-Buffer	0.60	3.4×10^{-5}	0.06	6.8×10^{-6}	0.81	1.5×10^{-4}	0.3152
T4LpWT-131R1f/132A CNBr-Buffer	0.60	3.4×10^{-5}	-0.13	3.9×10^{-6}	0.75	1.2×10^{-4}	0.2540
T4LpWT-131R1f/135A CNBr-Buffer	0.61	3.5×10^{-5}	-0.06	4.8×10^{-6}	0.74	1.2×10^{-4}	0.1879
T4LpWT-128R1f CNBr-Buffer	0.56	2.8×10^{-5}	-0.21	3.0×10^{-6}	0.62	7.5×10^{-5}	0.2268
T4L 121A/133A 128R1f CNBr-Buffer	0.69	4.7×10^{-5}	0.40	1.9×10^{-5}	0.79	1.4×10^{-4}	0.4714
T4LpWT-130R1f CNBr-Buffer	0.56	2.8×10^{-5}	0.11	7.7×10^{-6}	0.66	8.7×10^{-5}	0.2340
T4L 121A/133A 130R1f CNBr-Buffer	0.80	6.7×10^{-5}	0.62	4.6×10^{-5}	0.97	2.5×10^{-4}	0.5615
T4LpWT-132R1f CNBr-Buffer	0.45	1.6×10^{-5}	-0.36	1.9×10^{-6}	0.58	6.4×10^{-5}	0.1766
T4L 121A/133A 132R1f CNBr-Buffer	0.66	4.2×10^{-5}	0.29	1.3×10^{-5}	0.72	1.1×10^{-4}	0.3086

3. T4LpWT 72RY, various conditions

	L"/L	τ_R/sec	C'/C	τ_R/sec	H"/H	τ_R/sec	Integral
T4LpWT 72RY precipitation	1.08	1.6×10^{-4}	0.88	7.0×10^{-4}	2.80	∞	1.5959
T4LpWT 72RY CNBr-glutaraldehyde	0.85	8.0×10^{-5}	0.50	2.8×10^{-5}	1.00	2.7×10^{-4}	0.6028
T4LpWT 72RY CNBr-Ficoll	0.61	3.5×10^{-5}	0.24	1.1×10^{-5}	0.77	1.3×10^{-4}	0.3951
T4LpWT 72RY CNBr-sucrose	0.61	3.5×10^{-5}	0.35	1.6×10^{-5}	0.71	1.1×10^{-4}	0.4316
T4LpWT 72RY CNBr-Buffer	0.65	4.0×10^{-5}	0.29	1.3×10^{-5}	0.79	1.4×10^{-4}	0.2538

4. T4LpWT 72R1f, various conditions

	L"/L	τ_R/sec	C'/C	τ_R/sec	H"/H	τ_R/sec	Integral
T4LpWT 72R1f precipitation	0.94	1.0×10^{-4}	0.78	1.4×10^{-4}	2.44	∞	1.2407
T4LpWT 72R1f CNBr-glutaraldehyde	0.72	5.1×10^{-5}	0.02	6.0×10^{-6}	0.92	2.1×10^{-4}	0.2651
T4LpWT 72R1f CNBr-Buffer	0.59	3.1×10^{-5}	-0.13	3.8×10^{-6}	0.87	1.8×10^{-4}	0.1598

5. Sucrose/Ficoll effects

	L”/L	τ_R/sec	C’/C	τ_R/sec	H”/H	τ_R/sec	Integral
HoloMb 132R1f CNBr-Buffer	0.38	1.1×10^{-5}	-0.40	1.6×10^{-6}	0.56	5.8×10^{-5}	0.1061
HoloMb 132R1f CNBr-Sucrose	0.38	1.0×10^{-5}	-0.21	3.0×10^{-6}	0.44	3.4×10^{-5}	0.2116
HoloMb 132R1f CNBr-Ficoll	0.54	2.6×10^{-5}	-0.01	5.5×10^{-6}	0.62	7.5×10^{-5}	0.3229
T4LpWT 72RY CNBr-Buffer	0.65	4.0×10^{-5}	0.29	1.3×10^{-5}	0.79	1.4×10^{-4}	0.2538
T4LpWT 72RY CNBr-Sucrose	0.61	3.5×10^{-5}	0.35	1.6×10^{-5}	0.71	1.1×10^{-4}	0.4316
T4LpWT 72RY CNBr-Ficoll	0.61	3.5×10^{-5}	0.24	1.1×10^{-5}	0.77	1.3×10^{-4}	0.3951

6. T4LpWT 68RX72, T4LpWT 72RY, T4LpWT 72R1f, temperature dependence

	L”/L	τ_R/sec	C’/C	τ_R/sec	H”/H	τ_R/sec	Integral
T4LpWT-68RX72 CNBr-RT	0.48	1.9×10^{-5}	0.46	2.3×10^{-5}	0.65	8.4×10^{-5}	0.4707
T4LpWT-68RX72 CNBr-5.2℃	0.51	2.2×10^{-5}	0.52	3.0×10^{-5}	0.87	1.8×10^{-4}	0.7248
T4LpWT-68RX72 CNBr-34.8℃	0.63	3.8×10^{-5}	0.66	5.7×10^{-5}	0.67	9.0×10^{-5}	0.7620
T4LpWT 72RY CNBr-RT	0.61	3.5×10^{-5}	0.21	1.0×10^{-5}	0.78	1.3×10^{-4}	0.2538
T4LpWT 72RY CNBr-4.9℃	0.60	3.4×10^{-5}	0.39	1.8×10^{-5}	0.94	2.2×10^{-4}	0.4712
T4LpWT 72RY CNBr-11.1℃	0.57	3.0×10^{-5}	0.29	1.3×10^{-5}	0.90	2.0×10^{-4}	0.3693
T4LpWT 72RY CNBr-17.0℃	0.57	3.0×10^{-5}	0.28	1.3×10^{-5}	0.91	2.0×10^{-4}	0.3032
T4LpWT 72RY CNBr-22.9℃	0.51	2.3×10^{-5}	0.11	7.8×10^{-6}	0.75	1.2×10^{-4}	0.2411
T4LpWT 72RY CNBr-28.9℃	0.52	2.3×10^{-5}	0.08	7.1×10^{-6}	0.76	1.3×10^{-4}	0.2051
T4LpWT 72RY CNBr-34.9℃	0.45	1.7×10^{-5}	-0.16	3.5×10^{-6}	0.65	8.4×10^{-5}	0.1755
T4LpWT 72R1f CNBr-RT	0.59	3.1×10^{-5}	-0.13	3.8×10^{-6}	0.87	1.8×10^{-4}	0.1598
T4LpWT 72R1f CNBr-5.1℃	0.58	3.0×10^{-5}	0.06	6.7×10^{-6}	1.21	5.1×10^{-4}	0.2694
T4LpWT 72R1f CNBr-34.8℃	0.52	2.3×10^{-5}	-0.41	1.6×10^{-6}	0.71	1.1×10^{-4}	0.1069

7. Solid-support attachments

	L”/L	τ_R/sec	C’/C	τ_R/sec	H”/H	τ_R/sec	Integral
T4LpWT 72R1f CNBr	0.59	3.1×10^{-5}	-0.13	3.8×10^{-6}	0.87	1.8×10^{-4}	0.1598
T4LpWT 72R1f Biotin-Streptavidin-Buffer	0.43	1.5×10^{-5}	-0.26	2.6×10^{-6}	0.57	6.1×10^{-5}	0.1725
T4LpWT 72R1f Biotin-Streptavidin-sucrose	0.40	1.2×10^{-5}	-0.10	4.2×10^{-6}	0.44	3.3×10^{-5}	0.2535
T4LpWT 72R1f Biotin-Streptavidin-Ficoll	0.50	2.2×10^{-5}	0.22	1.1×10^{-5}	0.64	8.1×10^{-5}	0.3391
T4LpWT 72R1f 6His-Ni-NTA-Buffer	0.34	7.4×10^{-6}	-0.46	1.3×10^{-6}	0.46	3.6×10^{-5}	0.0307
T4LpWT 72R1f 6His-Ni-NTA-Sucrose	0.31	5.8×10^{-6}	-0.76	2.0×10^{-7}	0.39	2.3×10^{-5}	0.0338
T4LpWT 72R1f 6His-Ni-NTA-Ficoll	0.54	2.6×10^{-5}	0.26	1.2×10^{-5}	0.51	4.6×10^{-5}	0.2137
T4LpWT 72R1f 6His-Zn-IDA	0.19	9.8×10^{-8}	-1.08		0.24	8.5×10^{-6}	0.0418
T4LpWT 72RY CNBr	0.64	3.9×10^{-5}	0.29	1.3×10^{-5}	0.79	1.4×10^{-4}	0.2538
T4LpWT 72RY Biotin-Streptavidin-Buffer	0.47	1.8×10^{-5}	-0.02	5.3×10^{-6}	0.50	4.5×10^{-5}	0.2237
T4LpWT 72RY Biotin-Streptavidin-sucrose	0.39	1.1×10^{-5}	0.04	6.4×10^{-6}	0.42	3.0×10^{-5}	0.2637
T4LpWT 72RY Biotin-Streptavidin-Ficoll	0.50	2.1×10^{-5}	0.36	1.6×10^{-5}	0.51	4.6×10^{-5}	0.4791
T4LpWT 72RY 6His-Ni-NTA	0.23	1.6×10^{-6}	-0.45	1.4×10^{-6}	0.36	2.1×10^{-5}	0.0434
T4LpWT 72RY 6His-Zn-IDA	0.15		-0.69	4.0×10^{-7}	0.17	3.4×10^{-6}	0.0919

8. Signal noises

	L”/L±Noise	τ_R±Noise/sec	H”/H±Noise	τ_R±Noise/sec
HoloMb 66R1f CNBr-Buffer	0.55±0.01	$2.7 \pm 0.2 \times 10^{-5}$	0.86±0.07	$1.8 \pm 0.4 \times 10^{-4}$
HoloMb 66RY CNBr-Buffer	0.50±0.03	$2.2 \pm 0.4 \times 10^{-5}$	0.67±0.15	$9.2 \pm 4.4 \times 10^{-5}$
HoloMb 113R1f CNBr-Buffer	0.31±0.01	$5.8 \pm 0.9 \times 10^{-6}$	0.41±0.06	$2.8 \pm 0.8 \times 10^{-5}$
HoloMb 132R1f CNBr-Buffer	0.38±0.02	$1.1 \pm 0.2 \times 10^{-5}$	0.56±0.08	$5.8 \pm 1.6 \times 10^{-5}$
HoloMb 132RY CNBr-Buffer	0.46±0.01	$1.8 \pm 0.2 \times 10^{-5}$	0.55±0.05	$5.5 \pm 0.9 \times 10^{-5}$
T4LpWT 72RY precipitation	1.08±0.01	$1.6 \pm 0.1 \times 10^{-4}$	2.80±0.15	∞
T4LpWT 72RY CNBr-glutaraldehyde	0.85±0.01	$8.0 \pm 0.2 \times 10^{-5}$	1.00±0.02	$2.7 \pm 0.2 \times 10^{-4}$
T4LpWT 72RY CNBr-Ficoll	0.61±0.01	$3.5 \pm 0.1 \times 10^{-5}$	0.77±0.03	$1.3 \pm 0.1 \times 10^{-4}$
T4LpWT 72RY CNBr-sucrose	0.61±0.01	$3.5 \pm 0.1 \times 10^{-5}$	0.71±0.02	$1.1 \pm 0.1 \times 10^{-4}$
T4LpWT 72RY CNBr-Buffer	0.65±0.01	$4.0 \pm 0.2 \times 10^{-5}$	0.79±0.02	$1.4 \pm 0.1 \times 10^{-4}$
T4LpWT 131RY CNBr-Buffer	0.66±0.02	$4.1 \pm 0.1 \times 10^{-5}$	0.80±0.04	$1.4 \pm 0.2 \times 10^{-4}$
T4LpWT 72R1f precipitation	0.94±0.02	$1.0 \pm 0.1 \times 10^{-4}$	2.44±0.12	∞
T4LpWT 72R1f CNBr-glutaraldehyde	0.72±0.01	$5.1 \pm 0.1 \times 10^{-5}$	0.92±0.04	$2.1 \pm 0.3 \times 10^{-4}$
T4LpWT 72R1f CNBr-Buffer	0.59±0.02	$3.1 \pm 0.1 \times 10^{-5}$	0.87±0.05	$1.8 \pm 0.3 \times 10^{-4}$
T4LpWT 72R1f CNBr-5.1°C	0.58±0.01	$3.0 \pm 0.1 \times 10^{-5}$	1.21±0.06	$5.1 \pm 0.9 \times 10^{-4}$
T4LpWT 72R1f CNBr-34.8°C	0.52±0.02	$2.3 \pm 0.1 \times 10^{-5}$	0.71±0.05	$1.1 \pm 0.2 \times 10^{-4}$
T4LpWT 115R1f CNBr-Buffer	0.54±0.01	$2.6 \pm 0.1 \times 10^{-5}$	0.66±0.03	$8.6 \pm 0.9 \times 10^{-5}$
T4LpWT 131R1f CNBr-Buffer	0.53±0.01	$2.5 \pm 0.2 \times 10^{-5}$	0.66±0.04	$8.8 \pm 1.4 \times 10^{-5}$

(continued)

	L”/L±Noise	τ_R±Noise/sec	H”/H±Noise	τ_R±Noise/sec
T4LpWT-128R1f CNBr-Buffer	0.56±0.02	$2.8 \pm 0.2 \times 10^{-5}$	0.62±0.05	$7.5 \pm 1.3 \times 10^{-5}$
T4L 121A/133A 128R1f CNBr-Buffer	0.69±0.01	$4.7 \pm 0.2 \times 10^{-5}$	0.79±0.03	$1.4 \pm 0.1 \times 10^{-4}$
T4LpWT-130R1f CNBr-Buffer	0.56±0.01	$2.8 \pm 0.1 \times 10^{-5}$	0.66±0.04	$8.7 \pm 1.1 \times 10^{-5}$
T4L 121A/133A 130R1f CNBr-Buffer	0.80±0.01	$6.7 \pm 0.1 \times 10^{-5}$	0.97±0.03	$2.5 \pm 0.2 \times 10^{-4}$
T4LpWT-132R1f CNBr-Buffer	0.45±0.01	$1.6 \pm 0.1 \times 10^{-5}$	0.58±0.04	$6.4 \pm 1.1 \times 10^{-5}$
T4L 121A/133A 132R1f CNBr-Buffer	0.66±0.01	$4.2 \pm 0.1 \times 10^{-5}$	0.72±0.04	$1.1 \pm 0.2 \times 10^{-4}$
T4LpWT 128RY CNBr-Buffer	0.69±0.02	$4.6 \pm 0.2 \times 10^{-5}$	0.78±0.05	$1.3 \pm 0.2 \times 10^{-4}$
T4L 121A/133A 128RY CNBr-Buffer	0.86±0.01	$8.3 \pm 0.2 \times 10^{-5}$	0.84±0.02	$1.7 \pm 0.2 \times 10^{-4}$
T4LpWT 130RY CNBr-Buffer	0.69±0.02	$4.7 \pm 0.3 \times 10^{-5}$	0.67±0.05	$9.2 \pm 1.7 \times 10^{-5}$
T4L 121A/133A 130RY CNBr-Buffer	0.88±0.01	$8.8 \pm 0.3 \times 10^{-5}$	0.83±0.02	$1.6 \pm 0.1 \times 10^{-4}$
T4LpWT 132RY CNBr-Buffer	0.80±0.02	$6.8 \pm 0.4 \times 10^{-5}$	0.81±0.06	$1.5 \pm 0.3 \times 10^{-4}$
T4L 121A/133A 132RY CNBr-Buffer	0.92±0.01	$9.9 \pm 0.3 \times 10^{-5}$	0.94±0.02	$2.3 \pm 0.2 \times 10^{-4}$

(continued)

	L”/L±Noise	τ_R±Noise/sec	H”/H±Noise	τ_R±Noise/sec
T4LpWT 72R1f Biotin-Streptavidin-Buffer	0.43±0.02	$1.5 \pm 0.2 \times 10^{-5}$	0.57±0.07	$6.1 \pm 1.6 \times 10^{-5}$
T4LpWT 72R1f Biotin-Streptavidin-sucrose	0.40±0.02	$1.2 \pm 0.1 \times 10^{-5}$	0.44±0.06	$3.3 \pm 0.9 \times 10^{-5}$
T4LpWT 72R1f Biotin-Streptavidin-Ficoll	0.50±0.02	$2.2 \pm 0.3 \times 10^{-5}$	0.64±0.09	$8.1 \pm 2.5 \times 10^{-5}$
T4LpWT 72R1f 6His-Ni-NTA-Buffer	0.34±0.02	$7.4 \pm 1.4 \times 10^{-6}$	0.46±0.09	$3.6 \pm 1.4 \times 10^{-5}$
T4LpWT 72R1f 6His-Ni-NTA-Sucrose	0.31±0.02	$5.8 \pm 1.3 \times 10^{-6}$	0.39±0.09	$2.3 \pm 0.9 \times 10^{-5}$
T4LpWT 72R1f 6His-Ni-NTA-Ficoll	0.54±0.01	$2.6 \pm 0.2 \times 10^{-5}$	0.51±0.05	$4.6 \pm 0.9 \times 10^{-5}$
T4LpWT 72R1f 6His-Zn-IDA	0.19±0.02		0.24±0.07	$8.5 \pm 5.3 \times 10^{-6}$
T4LpWT 72RY Biotin-Streptavidin	0.47±0.03	$1.8 \pm 0.2 \times 10^{-5}$	0.50±0.07	$4.5 \pm 1.4 \times 10^{-5}$
T4LpWT 72RY 6His-Ni-NTA	0.23±0.01	$1.6 \pm 0.6 \times 10^{-6}$	0.36±0.13	$2.1 \pm 1.4 \times 10^{-5}$
T4LpWT 72RY 6His-Zn-IDA	0.15±<0.01		0.17±0.03	$3.4 \pm 1.7 \times 10^{-6}$

6.6 Discussion

This work aims to demonstrate the methodology based on ST-EPR for monitoring dynamics in the time range of μs-ms by introducing new spin labels with higher rigidity. It has always been attractive to find new spin labels possessing less internal motions and fewer rotamers for applications in both distance and dynamic measurements. Ever since the understanding that internal motions of R1 are dominated by rotations about the two terminal single bonds: χ_4 and χ_5, strategies have been designed to restrict the χ_4 and χ_5. One is to introduce a bulky substituent on the side chain, while an alternative approach is to generate additional interactions between the nitroxide ring and the protein. Progress has been made in previous studies: Bulky substituents on

position 4 of nitroxide rings are introduced in structures of R1b and R1p, while V1 interacts with the S_γ of the disulfide bond through its nitrogen atom at position 4. Characterizations have shown the improvement in rigidity of these labels, implying the effectiveness of functionalizing position 4.

Inspired by these results, R1f and RY side chains are designed with slightly more hydrophobic and more bulky substituents on position 4. For the first time, one additional substituent is introduced to the α-carbon position to further restrict χ_4 and χ_5, which has been proven to be effective by the results of this work. RY is generally more immobilized than R1f or even RX on some sites on characteristic timescales of both CW-EPR and ST-EPR, making it an ideal label for investigating real slow protein dynamics in the time domain of 10^{-4}~10^{-3}s.

While the inherent flexibility of R1 allows for introduction at virtually any site within a protein, there is always concern about the accessibility of bulky side chains to proteins. As compared to RY which is more steric, R1f has achieved a practical balance between its rigidity and flexibility. On residue 130C in T4L L121A/L133A cavity mutant, results imply that R1f resides properly inside the interior cavity, which requires certain flexibility during the labeling. In the meanwhile, R1f has sufficiently restricted internal motions to detect submillisecond dynamics in ST-EPR spectra. Though it is hard to directly compare the rigidity of new labels with TOAC or conventional labels like iodoacetamide derivatives and maleimide derivatives because different proteins have been used. However, by using R1 and RX as references, it can be concluded that R1f and RX are no less rigid. Moreover, benefiting from using disulfide bonds as the linkage to proteins, both the labeling efficiency and stability are promised, suggesting a wider range of applications than conventional labels.

The purpose of this work is to show the capacity of new rigid labels and the feasibility of the

methodology in actual ST-EPR measurements, rather than give quantitatively accurate values of correlation times. Obtained from calibration curves, the accuracy of τ_R values is decided by the selection of standard systems. It is essential to control all other variables when directly comparing the rate of detected dynamics (correlation times) between samples from ST-EPR spectra. However, different variables are usually coupled together in actual motional processes, and the way how they couple is dependent on many aspects.

Supported by results from both simulations of CW-EPR spectra and structural characterizations, it can be confirmed that every R1-derivatized spin label possesses its particular anisotropic motional mode. Since either the anisotropy of spin labels or the amplitude of motions influences the angular extent during the transfer of saturation, the intensity at the same field position (the line-height) does not necessarily consist of the same angular contribution when measured with different spin labels. As a result, a numeric difference in their line-height ratios does not necessarily represent the pure difference in the rate of motion when different labels are used. In practical ST-EPR measurements, these influences can be qualitatively distinguished when comparing parameter correlation plots (Figure 6.21) of different labels[50–53]. As it can be judged from plots, these nitroxide spin labels have qualitatively similar behaviors so that calibration curves can still be used qualitatively to determine orders of timescales. However, a whole series of calibration curves should be measured under the specific condition and with a specific label if more accurate values of correlation times are needed, which is not practically efficient.

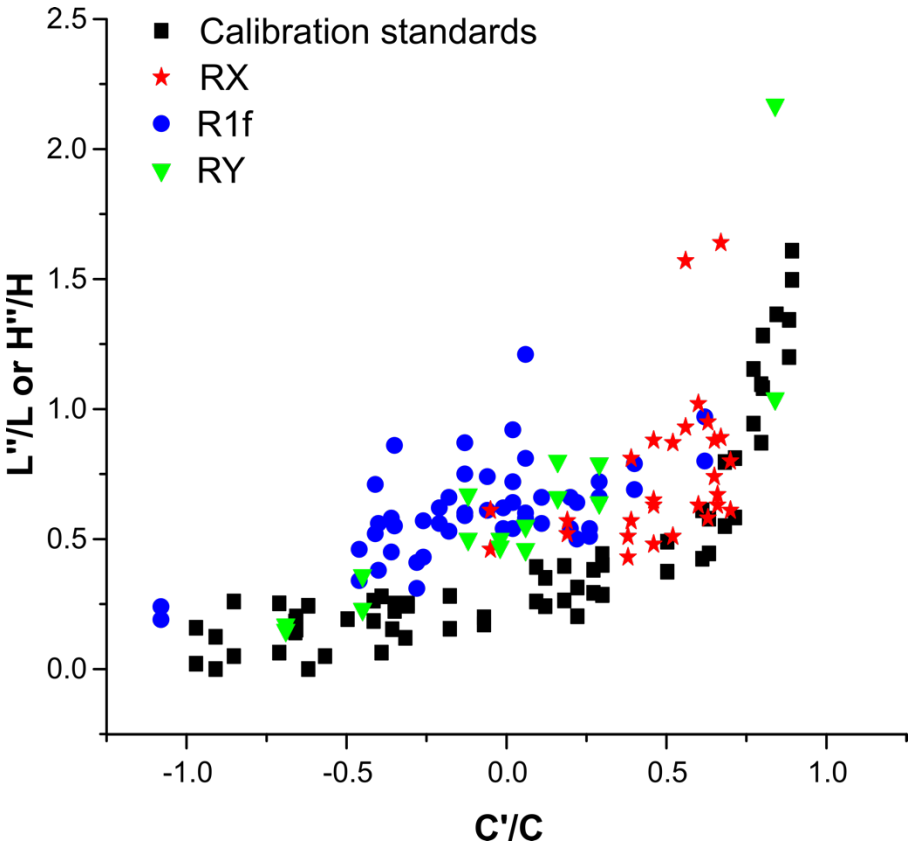

Figure 6.21 Parameter correlation plots of L''/L and H''/H vs. C'/C and for data of RX, RY, and R1f in section 6.5, and data of standards used in calibration curves of reference.

While line-height ratios are dependent on the coupling between variables describing the motion, the integrated spectral intensities are dependent on the coupling between variables and surroundings. When possibly sequestered in the hydrophobic cavity (L121A/L133A/130C) or surrounded by macromolecules (Ficoll), the sample has shown a larger value of IST than values obtained from fully immobilized samples (precipitation). However, there are still residual motions reflected from spectral lineshapes. It is hard to conclude the mechanism from these results only, but it is clear that the sample has responded heterogeneously to different perturbations rather than simply slowing down motions globally.

On the basis of such an understanding of ST-EPR results, the fact that there is a certain type of microsecond motion generally detected on helical sites seems to be inspiringly interesting. As

the X-ray crystallographic structure provides at best a single conformation confined by lattice interaction from the conformational ensemble, there are more conformational states permitted in the solution. At physiological temperature, timescales of microseconds and slower correspond to energy barriers of several k_BT (the product of the Boltzmann constant and the absolute temperature), which sets up a limited number of conformational states with such long lifetimes. Moreover, sufficient angular amplitudes are necessary for motions to be effectively reflected from lineshapes according to the mechanism of ST-EPR. While there should be no fast and large backbone dynamics in well-packed helical regions, all rigid spin labels used in this work have highly restricted anisotropic internal motions. It can be concluded that either can contribute significantly to dynamics revealed by ST-EPR lineshapes. Collectively, all results support the contention that detected motions should be large-amplitude collective motions involving conformational states that are likely to be functionally relevant. Some insights about the structural origin of motions are already implied from the perturbation experiments using sucrose and Ficoll. To further understand the essence of these internal dynamics, measurements of magnitudes in both distance and angle are necessary to complement the timescale information obtained in this work.

6.7 References

1. Thomas, D. D., Seidel, J. C., Hyde, J. S. & Gergely, J. Motion of subfragment-1 in myosin and its supramolecular complexes: saturation transfer electron paramagnetic resonance. *Proc. Natl. Acad. Sci.* **72**, 1729–1733 (1975).
2. Thomas, D. D., Dalton, L. R. & Hyde, J. S. Rotational diffusion studied by passage saturation transfer electron paramagnetic resonance. *J. Chem. Phys.* **65**, 3006–3024 (1976).

3. Thomas, D. D., Ishiwata, S., Seidel, J. C. & Gergely, J. Submillisecond rotational dynamics of spin-labeled myosin heads in myofibrils. *Biophys. J.* **32**, 873–889 (1980).
4. Lewis, S. M. & Thomas, D. D. Effects of vanadate on the rotational dynamics of spin-labeled calcium adenosinetriphosphatase in sarcoplasmic reticulum membranes. *Biochemistry* **25**, 4615–4621 (1986).
5. Horváth, L. I., Dux, L., Hankovszky, H. O., Hideg, K. & Marsh, D. Saturation transfer electron spin resonance of Ca2(+)-ATPase covalently spin-labeled with beta-substituted vinyl ketone- and maleimide-nitroxide derivatives. Effects of segmental motion and labeling levels. *Biophys. J.* **58**, 231–241 (1990).
6. Esmann, M., Sar, P. C., Hideg, K. & Marsh, D. Maleimide, Iodoacetamide, Indanedione, and Chloromercuric Spin Label Reagents with Derivatized Nitroxide Rings as ESR Reporter Groups for Protein Conformation and Dynamics. *Anal. Biochem.* **213**, 336–348 (1993).
7. Esmann, M., Hankovszky, H. O., Hideg, K., Pedersen, J. A. & Marsh, D. Vinyl ketone reagents for covalent protein modification. Nitroxide derivatives suited to rotational diffusion studies by saturation transfer electron spin resonance, using membrane-bound Na,K-ATPase as an example. *Anal. Biochem.* **189**, 274–282 (1990).
8. Esmann, M., Hankovszky, H. O., Hideg, K. & Marsh, D. A novel spin-label for study of membrane protein rotational diffusion using saturation transfer electron spin resonance. Application to selectively labelled Class I and Class II -SH groups of the shark rectal gland Na+/K+-ATPase. *Biochim. Biophys. Acta BBA - Biomembr.* **978**, 209–215 (1989).
9. James, Z. M., McCaffrey, J. E., Torgersen, K. D., Karim, C. B. & Thomas, D. D. Protein-Protein Interactions in Calcium Transport Regulation Probed by Saturation Transfer Electron Paramagnetic Resonance. *Biophys. J.* **103**, 1370–1378 (2012).

10. Mello, R. N. & Thomas, D. D. Three Distinct Actin-Attached Structural States of Myosin in Muscle Fibers. *Biophys. J.* **102**, 1088–1096 (2012).
11. Thompson, A. R., Naber, N., Wilson, C., Cooke, R. & Thomas, D. D. Structural Dynamics of the Actomyosin Complex Probed by a Bifunctional Spin Label that Cross-Links SH1 and SH2. *Biophys. J.* **95**, 5238–5246 (2008).
12. Columbus, L., Kálai, T., Jekö, J., Hideg, K. & Hubbell, W. L. Molecular Motion of Spin Labeled Side Chains in α-Helices: Analysis by Variation of Side Chain Structure. *Biochemistry* **40**, 3828–3846 (2001).
13. Fleissner, M. R., Cascio, D. & Hubbell, W. L. Structural origin of weakly ordered nitroxide motion in spin-labeled proteins. *Protein Sci.* **18**, 893–908 (2009).
14. Bank, R. P. D. RCSB PDB - 1ZWN: Crystal structure of spin labeled T4 Lysozyme (V131R1B). https://www.rcsb.org/structure/1ZWN.
15. Guo, Z., Cascio, D., Hideg, K., Kálái, T. & Hubbell, W. L. Structural determinants of nitroxide motion in spin-labeled proteins: Tertiary contact and solvent-inaccessible sites in helix G of T4 lysozyme. *Protein Sci.* **16**, 1069–1086 (2007).
16. Bank, R. P. D. RCSB PDB - 1ZUR: Crystal structure of spin labeled T4 Lysozyme (V131R1F). https://www.rcsb.org/structure/1ZUR.
17. Fawzi, N. L. *et al.* A rigid disulfide-linked nitroxide side chain simplifies the quantitative analysis of PRE data. *J. Biomol. NMR* **51**, 105 (2011).
18. López, C. J., Fleissner, M. R., Brooks, E. K. & Hubbell, W. L. Stationary-Phase EPR for Exploring Protein Structure, Conformation, and Dynamics in Spin-Labeled Proteins. *Biochemistry* **53**, 7067–7075 (2014).

19. McCoy, J. & Hubbell, W. L. High-pressure EPR reveals conformational equilibria and volumetric properties of spin-labeled proteins. *Proc. Natl. Acad. Sci.* **108**, 1331–1336 (2011).
20. Hubbell, W. L., López, C. J., Altenbach, C. & Yang, Z. Technological advances in site-directed spin labeling of proteins. *Curr. Opin. Struct. Biol.* **23**, 725–733 (2013).
21. Sale, K., Sár, C., Sharp, K. A., Hideg, K. & Fajer, P. G. Structural Determination of Spin Label Immobilization and Orientation: A Monte Carlo Minimization Approach. *J. Magn. Reson.* **156**, 104–112 (2002).
22. Fleissner, M. R. X-ray structures of nitroxide side chains in proteins: A basis for interpreting distance measurements and dynamic studies by electron paramagnetic resonance. (University of California, Los Angeles).
23. Hubbell, W. L., Altenbach, C., Hubbell, C. M. & Khorana, H. G. Rhodopsin structure, dynamics, and activation: A perspective from crystallography, site-directed spin labeling, sulfhydryl reactivity, and disulfide cross-linking. in *Advances in Protein Chemistry* vol. 63 243–290 (Academic Press, 2003).
24. Papermaster, D. S. & Dreyer, W. J. Rhodopsin content in the outer segment membranes of bovine and frog retinal rods. *Biochemistry* **13**, 2438–2444 (1974).
25. Daemen, F. J. M. Vertebrate rod outer segment membranes. *Biochim. Biophys. Acta BBA - Rev. Biomembr.* **300**, 255–288 (1973).
26. Ryba, N. J. P. *et al.* Rhodopsin mobility, structure, and lipid-protein interaction in squid photoreceptor membranes. *Biochemistry* **32**, 3298–3305 (1993).
27. Kusnetzow, A. K., Altenbach, C. & Hubbell, W. L. Conformational States and Dynamics of Rhodopsin in Micelles and Bilayers. *Biochemistry* **45**, 5538–5550 (2006).

28. Matthews, R. G., Hubbard, R., Brown, P. K. & Wald, G. Tautomeric Forms of Metarhodopsin. *J. Gen. Physiol.* **47**, 215–240 (1963).
29. Mchaourab, H. S., Lietzow, M. A., Hideg, K. & Hubbell, W. L. Motion of Spin-Labeled Side Chains in T4 Lysozyme. Correlation with Protein Structure and Dynamics. *Biochemistry* **35**, 7692–7704 (1996).
30. Ando, N. *et al.* Structural and Thermodynamic Characterization of T4 Lysozyme Mutants and the Contribution of Internal Cavities to Pressure Denaturation. *Biochemistry* **47**, 11097–11109 (2008).
31. Royer, C. A., Mann, C. J. & Matthews, C. R. Resolution of the fluorescence equilibrium unfolding profile of trp aporepressor using single tryptophan mutants. *Protein Sci.* **2**, 1844–1852 (1993).
32. Myers, J. K., Nick Pace, C. & Martin Scholtz, J. Denaturant m values and heat capacity changes: Relation to changes in accessible surface areas of protein unfolding. *Protein Sci.* **4**, 2138–2148 (1995).
33. Pantazatos, D. P. & MacDonald, R. I. Site-directed Mutagenesis of Either the Highly Conserved Trp-22 or the Moderately Conserved Trp-95 to a Large, Hydrophobic Residue Reduces the Thermodynamic Stability of a Spectrin Repeating Unit *. *J. Biol. Chem.* **272**, 21052–21059 (1997).
34. Tang, C., Lew, S. & He, D. Using a second-order differential model to fit data without baselines in protein isothermal chemical denaturation. *Protein Sci.* **25**, 898–904 (2016).
35. Lu, J. & Dahlquist, F. W. Detection and characterization of an early folding intermediate of T4 lysozyme using pulsed hydrogen exchange and two-dimensional NMR. *Biochemistry* **31**, 4749–4756 (1992).

36. Matthews, B. W. Studies on Protein Stability With T4 Lysozyme. in *Advances in Protein Chemistry* (eds. Anfinsen, C. B., Richards, F. M., Edsall, J. T. & Eisenberg, D. S.) vol. 46 249–278 (Academic Press, 1995).
37. Timofeev, V. P. & Tsetlin, V. I. Analysis of mobility of protein side chains by spin label technique. *Biophys. Struct. Mech.* **10**, 93–108 (1983).
38. Squier, T. C. & Thomas, D. D. Methodology for increased precision in saturation transfer electron paramagnetic resonance studies of rotational dynamics. *Biophys. J.* **49**, 921–935 (1986).
39. Kirino, Y., Ohkuma, T. & Shimizu, H. Saturation Transfer Electron Spin Resonance Study on the Rotational Diffusion of Calcium- and Magnesium-Dependent Adenosine Triphosphatase in Sarcoplasmic Reticulum Membranes1. *J. Biochem. (Tokyo)* **84**, 111–115 (1978).
40. King, M. D. & Quinn, P. J. A passage saturation transfer paramagnetic resonance study of the rotational diffusion of the sarcoplasmic reticulum calcium-ATPase. *J. Bioenerg. Biomembr.* **15**, 135–150 (1983).
41. Kaizu, T., Kirino, Y. & Shimizu, H. A Saturation Transfer Electron Spin Resonance Study on the Break in the Arrhenius Plot for the Rotational Motion of Ca2+ Adenosine Triphosphatase Molecules in Purified and Lipid-Replaced Preparations of Rabbit Skeletal Muscle Sarcoplasmic Reticulum1. *J. Biochem. (Tokyo)* **88**, 1837–1843 (1980).
42. Inesi, G., Millman, M. & Eleter, S. Temperature-induced transitions of function and structure in sarcoplasmic reticulum membranes. *J. Mol. Biol.* **81**, 483–504 (1973).

43. Hoffmann, W., Sarzala, M. G. & Chapman, D. Rotational motion and evidence for oligomeric structures of sarcoplasmic reticulum Ca2+-activated ATPase. *Proc. Natl. Acad. Sci.* **76**, 3860–3864 (1979).

44. Squier, T. C. & Thomas, D. D. Applications of new saturation transfer electron paramagnetic resonance methodology to the rotational dynamics of the Ca-ATPase in sarcoplasmic reticulum membranes. *Biophys. J.* **49**, 937–942 (1986).

45. Moore, B. M., Lentz, B. R. & Meissner, G. Effects of sarcoplasmic reticulum Ca2+ ion-stimulated ATPase on phospholipid bilayer fluidity: boundary lipid. *Biochemistry* **17**, 5248–5255 (1978).

46. Howard, E. C., Lindahl, K. M., Polnaszek, C. F. & Thomas, D. D. Simulation of saturation transfer electron paramagnetic resonance spectra for rotational motion with restricted angular amplitude. *Biophys. J.* **64**, 581–593 (1993).

47. Weber, P. C., Ohlendorf, D. H., Wendoloski, J. J. & Salemme, F. R. Structural Origins of High-Affinity Biotin Binding to Streptavidin. *Science* **243**, 85–88 (1989).

48. Grubmüller, H., Heymann, B. & Tavan, P. Ligand Binding: Molecular Mechanics Calculation of the Streptavidin-Biotin Rupture Force. *Science* **271**, 997–999 (1996).

49. López, C. J., Yang, Z., Altenbach, C. & Hubbell, W. L. Conformational selection and adaptation to ligand binding in T4 lysozyme cavity mutants. *Proc. Natl. Acad. Sci.* **110**, E4306–E4315 (2013).

50. Fung, L. W.-M. & Johnson, M. E. Multiple motions of the spectrin-actin complex in the saturation transfer EPR time domain. *J. Magn. Reson. 1969* **51**, 233–244 (1983).

51. Gaffney, B. Jean. Spin label-thiourea adducts. A model for saturation transfer ESR studies of slow anisotropic rotation. *J. Phys. Chem.* **83**, 3345–3349 (1979).

52. Johnson, M. E., Lee, L. & Fung, L. W. M. Models for slow anisotropic rotational diffusion in saturation transfer electron paramagnetic resonance at 9 and 35 GHz. *Biochemistry* **21**, 4459–4467 (1982).
53. Thiyagarajan, P. & Johnson, M. E. Saturation-transfer electron paramagnetic resonance detection of anisotropic motion by sickle hemoglobin molecules in the polymer state. *Biochemistry* **26**, 1903–1909 (1987).

Chapter 7: Structure and dynamics of R9, a nitroxide spin label with non-reducible linkage suitable for distance mapping and monitoring protein dynamics

7.1 Introduction

Methanethiosulfonate nitroxides have enjoyed extensive use for spin labeling cysteines in proteins due to their high reactivity and specificity, allowing facile reaction of the reagents even with partially and fully buried cysteine residues. The H-bonding interaction[1] (Figure 7.1 (A)) of the S_δ sulfur of the disulfide linkage with the C_α-H hydrogen atom of the residue gives rise to the anisotropic motion which in turn averages the magnetic tensor parameters of the nitroxide in such a manner as to make the CW-EPR spectral lineshape exquisitely sensitive ns time scale internal motions of the protein, and to modulation of the side chain motion by local interactions. Thus, R1 has become the sensor of choice for monitoring fast backbone fluctuations and mapping secondary and tertiary structures.

However, the internal motional modes of R1 that make it useful to map local interactions and backbone dynamics on the ns time scale also limit its use for monitoring slow protein internal motions (μs-ms), and complicate the interpretation of inter-spin distance distributions determined from dipolar spectroscopy. To limit the conformational space and restrain the motion of the spin label, internally constrained disulfide-linked side chains have been introduced.

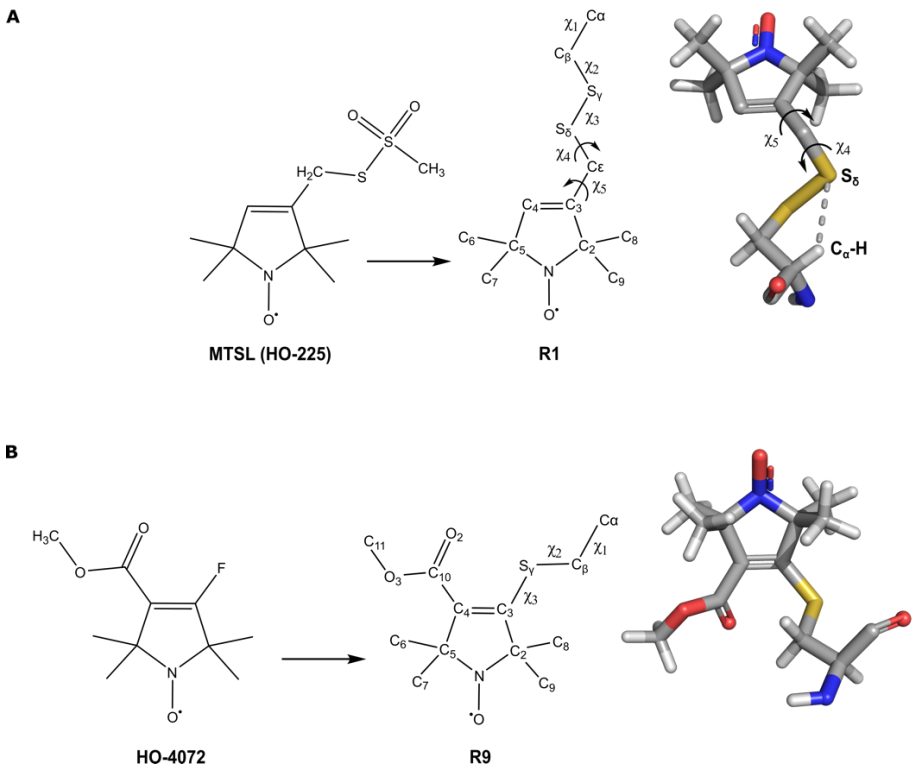

Figure 7.1 (A) Structure of the reagent 1-oxyl-2,2,5,5-tetramethypyrroline-3-methyl (MTTSL, HO-225), the R1 side chain with designations of atoms and dihedral angles used in the text, and the molecular model (from PDB code 2CUU). The C_α-H···S_δ interaction that restricts the motion of the disulfide linkage is shown. (B) Structures of the reagent HO-4072, the R9 side chain with designations of atoms and dihedral angles used in the text, and the molecular model (from the crystal structure of T4L 65R9/76R9, see next sections).

However, in addition to their positive features such as strong ordering and localization, they have some disadvantages. The disulfide is readily cleaved by reducing agents that are necessary for the stability of some proteins. In the case of the V1 side chain[2], the reactive disulfide is unstable and susceptible to spontaneous hydrolytic cleavage in the aqueous solution. The high reactivity of methanethiosulfonate reagents to even buried cysteine residues[3] makes it essential to remove at least some of the native cysteines which might be functionally important to the protein.

In this study, another novel nitroxide reagent (HO-4072, Figure 7.1 (B)) was introduced that reacts exclusively with solvent-exposed cysteine residues, making it unnecessary to remove native buried cysteine residues. The nitroxide side chain formed by the reaction, designated R9, has a stable thioether linkage that is not cleavable by the usual reducing reagents. Moreover, R9 has the shortest linkage of any nitroxide side chain introduced at cysteine, and the nitroxide resides close to the protein backbone. Finally, R9 is generally relatively immobilized, and crystal structures are presented that identify the unique interactions that lead to high ordering of the side chain.

The R9 side chain has been introduced at solvent-exposed sites in regular α-helices in T4L. In the sections below we: (1) explore the internal dynamics of R9 and evaluate the potential of the side chain for use as a monitor of slow protein motions; (2) characterize the reaction of reagent HO-4072 with solvent-exposed cysteine residues with respect to mechanism and rate, and evaluate the degree of destabilization to T4L that might be brought by the substitution for R9 side chains; and (3) present X-ray crystal structures of R9 on helical sites and identify the structural origin of the strongly ordered motion. Applications to determine inter-residue distance with DEER, and to monitor slow protein dynamics with ST-EPR are briefly presented. The possible use of R9 for distance determination using T_1 relaxation is also discussed.

7.2 Results

7.2.1 CW-EPR studies of R9

7.2.1.1 Internal dynamics of the R9 side chain on solvent-exposed α-helical sites

To isolate the side chain and protein dynamic modes, the spin-labeled protein is either

investigated in a high viscosity medium (sucrose and/or Ficoll) or attached to the solid support functionalized by cyanogen bromide (CNBr) to eliminate uniform rotational diffusion. To further isolate just the internal motion of the side chain a reference site is selected where protein structural fluctuations do not contribute significantly to the nitroxide motion, and where the side chain is fully solvent exposed and does not contact other amino acid residues in the protein. Site 72 in T4L, in the center of the long rigid helix C, meets all these criteria, and has been used as a reference for R1 and other side chains.

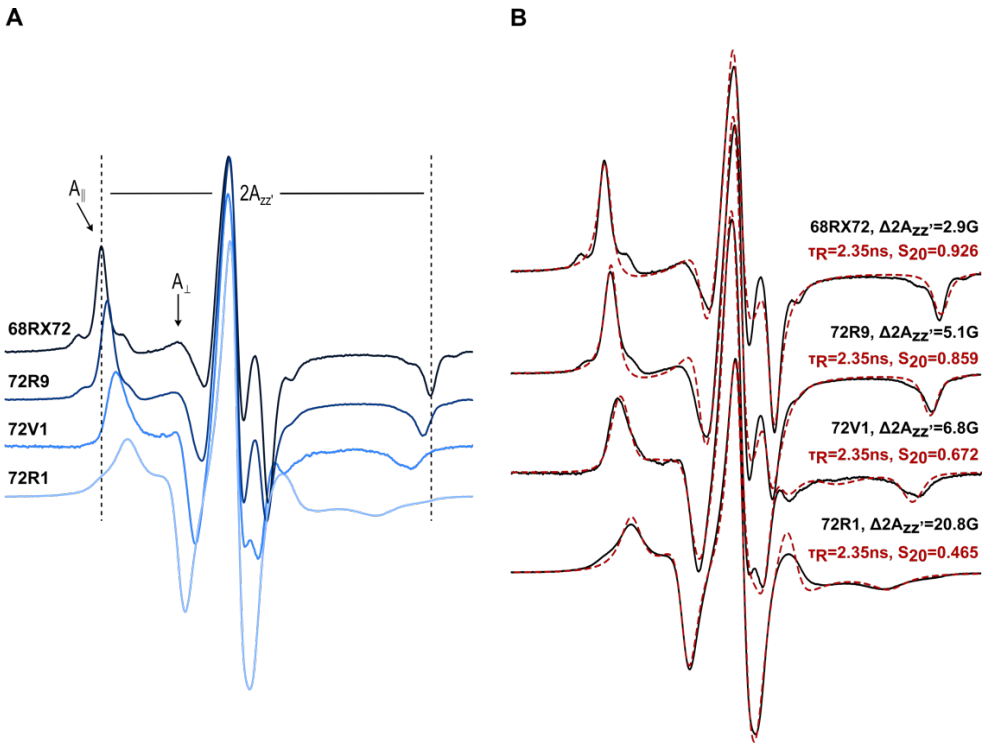

Figure 7.2 CW-EPR spectrum and simulation of spin-labeled T4L72C attached to CNBr-Sepharose. The magnetic field scan width is 100 G. (A) Experimental spectra of T4L 68RX72, 72R9, 72V1, and 72R1 at room temperature. The parallel ($A_{\parallel}$) and perpendicular ($A_{\perp}$) components of the axially symmetric hyperfine tensor, and the effective hyperfine splitting, $2A_{zz'}$ are shown. The vertical lines are drawn and fixed to the value corresponding to the $2A_{zz'}$ of the T4L 68RX72 spectrum as a reference for comparison. (B) The MOMD simulated (red dash) spectra were obtained by reducing the order parameter of motion, and corresponding experimental (black solid) spectra of T4L

68RX72, 72R9, 72V1, and 72R1 attached to CNBr-Sepharose (red dash). Values of the hyperfine splitting difference ($\Delta 2A_{zz'}$), the correlation time (τ_R), and the order parameter (S_{20}) are shown.

Figure 7.2 (A) presents CW-EPR spectra of nitroxide side chains with single site attachment to 72C (R1, V1, R9) or doubly attached via 68C/72C (RX^4) in T4L attached to CNBr-Sepharose. Unsurprisingly, the most highly ordered side chain observed for any spin label is the crosslinking nitroxide RX, shown here attached to the double cysteine T4L mutant 68C/72C. The CW spectrum is striking with well-resolved parallel ($A_{\parallel}$) and perpendicular ($A_{\perp}$) components of the hyperfine tensor, narrow linewidths of the outer hyperfine extrema, and a large hyperfine splitting $2A_{zz'}$. The previous simulation of the lineshape indicates that the spectrum arises from a highly ordered but rapid anisotropic motion of the nitroxide. The high order is due to both the backbone rigidity of the protein near residue 72 and the highly constrained internal motion of the crosslinked side chain.

The spectra of the other nitroxide side chains shown have a common feature: they all can be accounted for reasonably well by a similar rapid anisotropic motion of the nitroxide with varying degrees of order. Simulations according to this model are shown for each as a dotted trace, obtained by just reducing the order parameter for the motion, proceeding from RX to R1 (Figure 7.2 (B)). The similarity to the experimental lineshapes is remarkably good for such a simple model. The corresponding values of the S_{20} order parameter that characterizes the amplitude of the motion are provided next to each spectrum. Small variations in other parameters can optimize the fit to each data set, but differences in order dominate.

A more explicit spectral simulation (Table 7.1) using the MOMD model shows a best-fit to the spectrum of T4L72R9 on CNBr for a simple anisotropic motion of the nitroxide in a cone, which requires a fast internal motion with a correlation time $\tau_R \approx 2.3$ ns, with a high degree of

order (S=0.87) that can be described as motion confined within a cone of half-angle ≈ 17.4°. Recall that at the same location, a best-fit to the spectrum of T4L 68RX72 attached to CNBr-Sepharose indicates a motion confined within a cone of half-angle≈15°, while for 72R1 the half-angle ≈ 37°.

Table 7.1 Parameters for simulations

	A_{xx}/G	A_{yy}/G	A_{zz}/G	<R>/s^{-1}	τ_R/ns	S	c_0^2
68RX72	6.31	5.40	36.68	7.85	2.35	0.926	13.69
72R9	5.73	5.30	36.29	7.85	2.35	0.859	7.51
72R9 (explicit)	5.73	5.30	36.29	7.85	2.35	0.866	7.84
72V1	5.90	5.18	34.97	7.85	2.35	0.672*	1.91
72R1	6.31	5.37	37.09	7.85	2.35	0.465	2.13

The magnetic parameters used for simulations are as follows: $g_{xx} = 2.00800, g_{yy} = 2.00586, g_{zz} = 2.00199$; for the explicit MOMD simulation of 72R9, $\alpha_D = 0$, $\beta_D = 6.80°$, $\gamma_D = 0$, $\Delta^{(0)} = \Delta^{(2)} = 0$ G; for the simulation of 72V1, a $c_0^4 = 2.76$ is required, and $g_{xx} = 2.00873, g_{yy} = 2.00604, g_{zz} = 2.00230$ (reported by Warshaviak et al.[2]).

Within the context of this motional model, the value of $2A_{zz'}$ is a direct measure of the amplitude of motion, i.e., the order for the model under consideration. The value of $2A_{zz'}$ under ambient conditions depends on the electronic structure of the nitroxide and local polarity in the protein as well as the motion of the nitroxide. The rigid limit value of $2A_{zz'}$ is determined in frozen solution first ($2A_{zz'}$ (0)), and the difference $\Delta 2A_{zz'} = 2A_{zz'}(0) - 2A_{zz'}$ is a metric that can be used to compare the relative mobilities of the different labels. This value is provided for each label along with the S_{20}. The reference of maximum rigidity, RX, has a $\Delta 2A_{zz'} = 2.9$G, indicating a limited amplitude of internal motions. 72R9 has a larger decrease of 5.1G, revealing more inherent mobility of the R9 side chain compared with RX, while spectra for 72V1 and 72R1 have further increases in a $\Delta 2A_{zz'} = 6.8$ and 20.8G, respectively.

Of this family of internally ordered side chains, R9 has the highest order of singly attached side chains. In addition to differences in a $\Delta 2A_{zz'}$, we also note that there is a systematic increase

in spectral linewidths proceeding from RX to R1. This is consistent with the corresponding increases in amplitude of motion on the ns time scale, which would be expected to produce an increasing magnitude of relaxation effects.

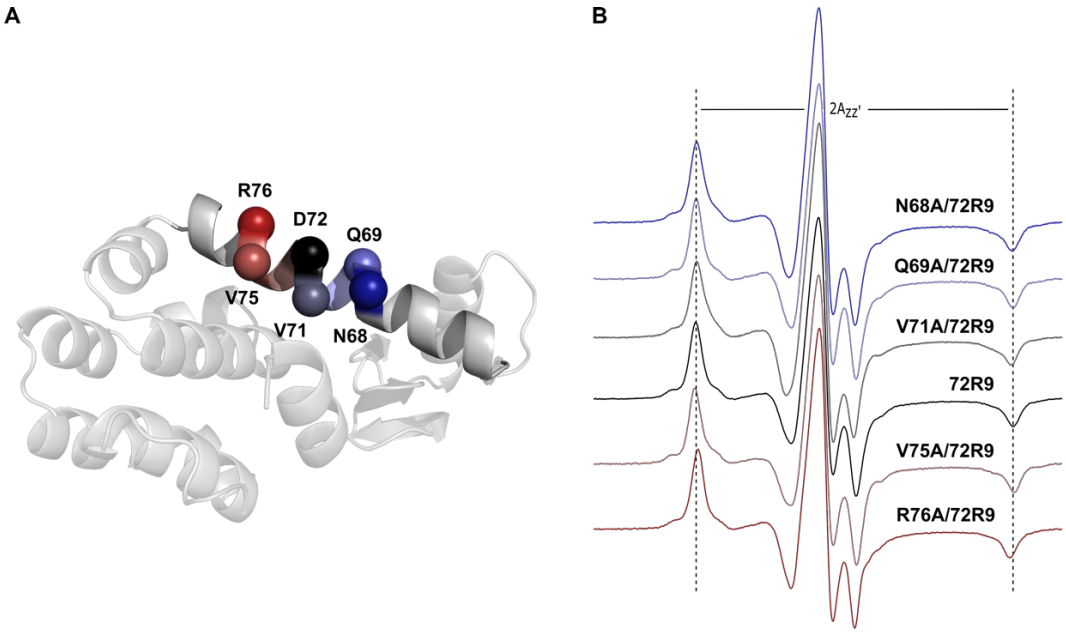

Figure 7.3 (A) Ribbon diagram of helix C on T4L (PDB code: 1L63) showing the residue 72C where R9 is introduced and neighboring Alanine replacements. The helix is colored as a transition from blue at its N-terminus to red at its C-terminus. Space-filling CPK models are shown for each native residue that is mutated to alanine. (B) Corresponding CW-EPR spectra of R9-labeled T4L mutants attached to CNBr-Sepharose at room temperature. The vertical lines are drawn and fixed to the value corresponding to the $2A_{zz'}$ of the 72R9 spectrum as a reference for comparison.

To investigate the possibility that this high ordering of R9 could be caused by interaction with neighboring residues, the T4L construct 72C was subjected to various mutations of residues around site 72 to alanines. Five residues (N68, Q69, V71, V75, R76, in Figure 7.3 (A)) with potential for interaction with R9 are individually mutated. These chosen mutations have been shown by corresponding CW-EPR spectra of R1-labeled samples to not have significant effects on the secondary structure/native local fold of the helix C (see chapter 6). Clearly, spectra

(Figure 7.3 (B)) of all alanine mutants (attached to CNBr-Sepharose) are essentially identical to the spectrum of the original T4L construct 72C, supporting the conclusion that specific local side chain interactions are not responsible for the high degree of immobilization. Of course, this does not eliminate the possibility that the methyl groups of alanine could be involved in an interaction with R9, a possibility that will be revisited below.

7.2.1.2 Dependence of the R9 side chain mobility on protein local structures

To explore the generality of labeling and the information content of R9 EPR spectra in a helical protein, the side chain was introduced, one at a time, at sites in distinct structural elements of T4L, namely solvent-exposed sites in the interior of regular helices (sites 68, 72, 76, 131), helix N-terminal sites (sites 82, 109), a C-terminal helix site (site 80), an interhelical loop site (site 81), tertiary contact sites (sites 65, 115, 134), and buried sites (site 99, 118, 133, 153). Figure. 7.4 (A) shows the location of the above sites in T4L with the backbone color-coded according to crystallographic B-factors.

The EPR spectra of all labeled mutants were measured in a 30% (wt/wt) sucrose solution to minimize the contribution from the rotational diffusion of the protein. The solid-support attachment was not used considering the variety of topographical regions involved and the likelihood that direct nitroxide/solid support interactions will contribute to the side chain dynamics at some sites. Thus, the spectra reflect a small contribution from rotational diffusion of the protein that is absent in solid support attachment, but differences between the sites can be reliably interpreted as contributions from internal modes of motion. The spectra are shown in Figure 7.4 (B).

Firstly, the data reveal that the R9 side chain can be introduced with good yields at sites in

any of the structural elements tested (Figure 7.4 (B)), except for the buried sites where there is essentially no labeling. On the other hand, the methanethiosulfonate R1 reagent (and the disulfide IDSL V1 reagent at site 118) react readily with these sites as previously reported[2,3,5]. The apparent selectivity for solvent-exposed sites can be an important advantage of the R9 labeling scheme, which will be explored in the following sections.

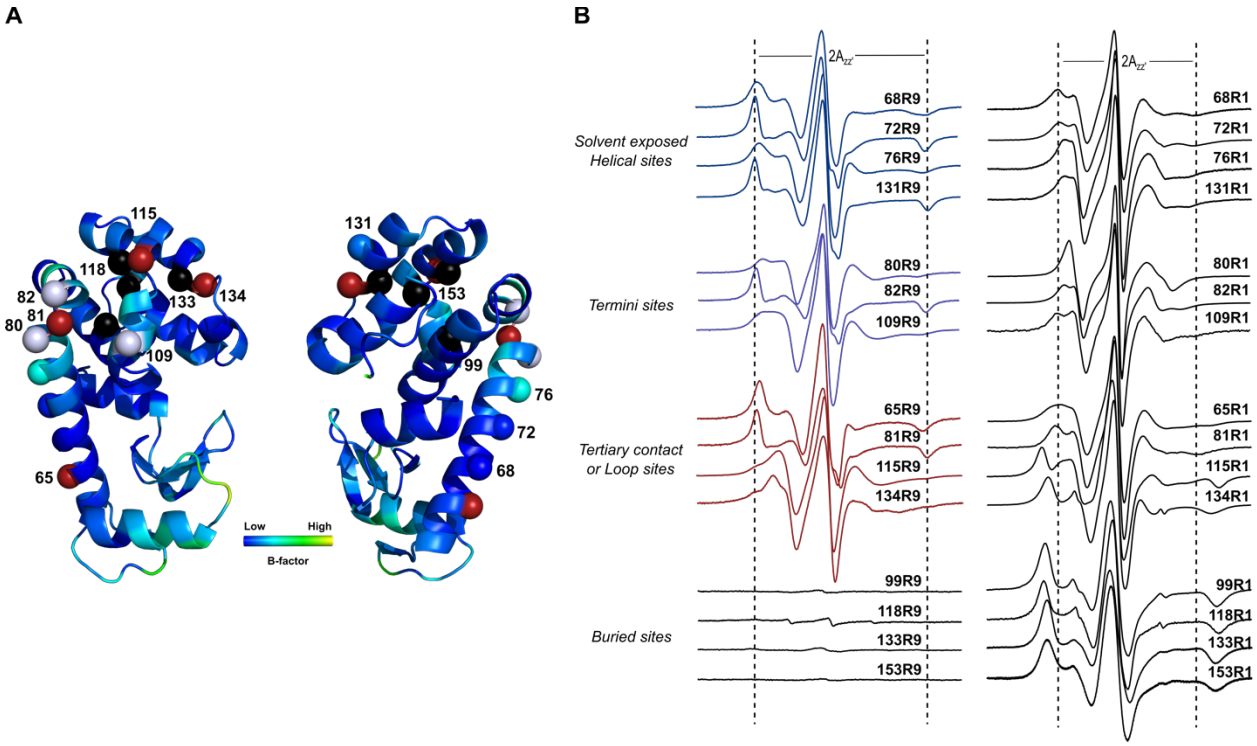

Figure 7.4 Comparison of CW-EPR spectra of R9 and R1 at various sites of T4L. (A) Ribbon diagram of T4L (PDB code: 1L63) showing all the sites used in this study, of which each residue is colored based on the value of B-factor. The blue spheres (non-interacting helical sites), blue-white spheres (helical termini sites), red spheres (tertiary contact sites), and black spheres (buried sites) at the Cα indicate where spin labels are introduced. (B) CW-EPR spectra of R1 and R9 at room temperature in 30% (wt/wt) sucrose solution. The vertical lines are drawn and fixed to the value corresponding to the $2A_{zz'}$ of the 72R1 or 72R9 spectrum as a reference for comparison. Spectra of helical sites are sequentially ordered. Spectra of buried sites were measured under the same experimental conditions to reveal how negligible the amount of a buried site can be labeled by R9.

Based on larger $2A_{zz'}$ values, the R9 side chain is generally more immobilized at each site

compared to R1. As compared to R1 or V1, its unique short linkage enables fewer oscillating bonds and closeness to the backbone. Benefiting from its higher rigidity, R9 is able to monitor dynamics with effectively fewer complications arising from its own internal modes. At non-interacting helix surface sites, the spectra of R9 reflect the mobility variation between the center and the termini, which resembles what has been revealed by R1.

Nevertheless, the spectra of R9 reflect a striking site-specific variation in mobility that encodes information on local backbone dynamics and interactions in regular helical structures. It has been known that local interactions of the nitroxide with other groups in the protein can give rise to multicomponent spectra that can be modulated in complex ways by exchange events. Both RX and V1 show strong immobilization and therefore a high similarity generally on almost all sites. Although there are still site-dependent differences, such as the value of $2A_{zz'}$, the variations are often subtle and not intuitive. The R9 side chain might be able to provide unique information on protein backbone dynamics.

Although an analysis of the structural and dynamic origin for the site-dependent mobility is beyond the scope of this work, crystal structures that will be presented below identify the unique interactions of R9, which give rise to relative immobilization and offer clues to the origin of the site-dependent variation.

7.2.2 Reaction of HO-4072

7.2.2.1 The reaction mechanism and kinetics

The reaction of HO-4072 with cysteine is anticipated to proceed via a Michael addition followed by E1 elimination (Figure 7.5 (A)). The nucleophile in the Michael addition is RS-, so the reaction should proceed most rapidly in an alkaline solution. This is readily confirmed by

monitoring the decrease in EPR signal (Figure 7.5 (B)) corresponding to the unreacted HO-4072 during the reaction under pseudo-first order conditions (large excess of protein). Figure 7.5 (C) shows the pseudo-first order rate constant determined in this manner as a function of pH for T4L 131C. The apparent pK determined by fitting is 8.35±0.2, a reasonable value for the pK_a of cysteine in a protein[6].

However, these data do not identify the product, and it could be the Michael addition intermediate preceding the elimination of the HF molecule (Figure 7.5 (A)). Moreover, the 4-ester could be partially or fully hydrolyzed in the alkaline solutions in which the reaction is most favorably carried out (pH 8 to 9). Thus, a mixture of products is possible. However, mass spectrometry of the final product indicates a single species with the expected mass increase corresponding to the R9 side chain (196±1 Da), readily distinguishable from the intermediate with (181±1 Da increase) ester hydrolysis. Examples of single- and double-site reactions are illustrated in Figure 7.5 (D). Mass spectra were also recorded during the reaction, and no evidence of accumulation of the Michael intermediate (216±1 Da increase) was observed (Figure 7.6). Apparently, the elimination step is rapid.

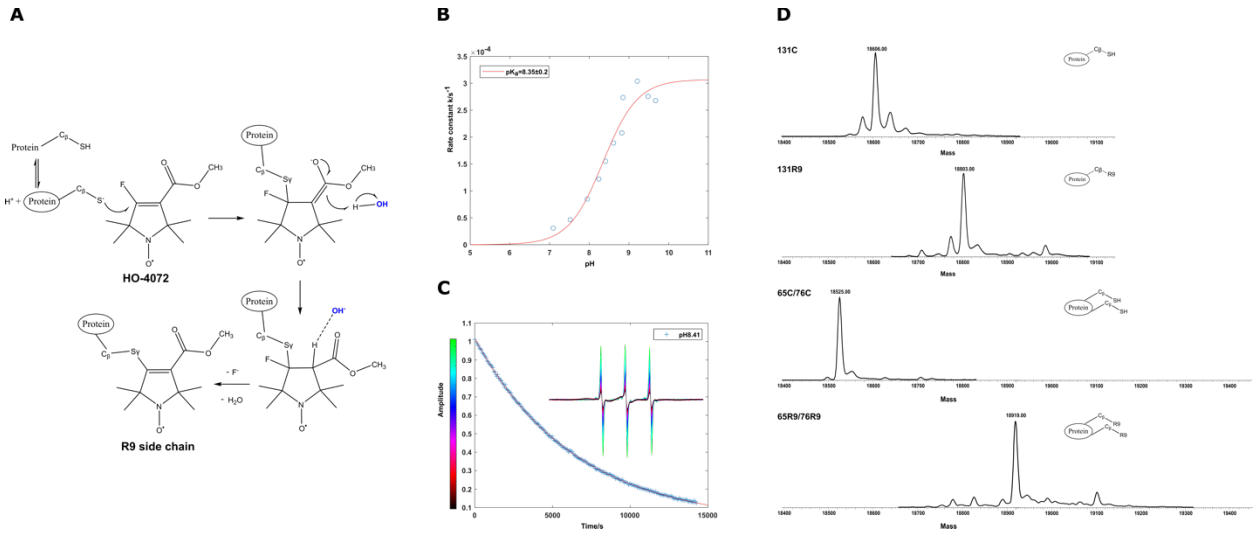

Figure 7.5 The SDSL strategy and kinetics based on cysteine. (A) Proposed spin-label reaction mechanism with HO-4072 to generate the R9 side chain. (B) The fitting for the pH dependence of reaction rate constants to the Henderson–Hasselbalch equation. (C) The reaction kinetic curve was obtained by fitting the decreased CW-EPR high field signal amplitudes of HO-4072 reaction to an exponential function under pH=8.41 in solution. (D) Deconvoluted ESI mass spectra before and after the spin-label reaction between HO-4072 and T4L mutant with a single solvent-exposed cysteine (131C) or double solvent-exposed cysteines (65C/76C).

In a separate experiment, it was also found that ester hydrolysis of the reagent itself does not take place at measurable rates even at pH = 8.7 at 28°C for 48h (personal communication from Dr. Támás Kálai). The cysteine-less pseudo wild-type T4L was also incubated with the HO-4072 under the same reaction conditions. It was determined that background labeling of groups other than cysteine contributed less than 1% of the total EPR signal of the labeled cysteine mutants when pH<9.

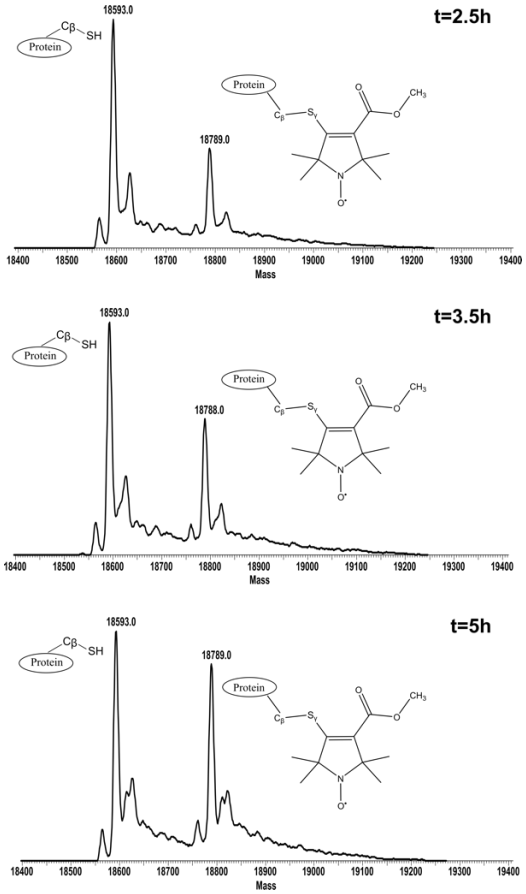

Figure 7.6 Deconvoluted ESI mass spectra of a reaction mixture of T4L mutant with a single solvent-exposed cysteine (72C) with HO-4072 after 2.5, 3.5, or 5 h.

7.2.2.2 Degree of destabilization to T4L by the substitution for the R9 side chain

The urea denaturation curves (Figure 7.7) were also determined for T4L72R9 using tryptophan fluorescence to quantitatively assess its possible influence exerting on the stability of the protein. The fit to the two-state model (Table 7.2) showed a decrease in the free energy of unfolding relative to the mutant 72C, revealing the destabilization effect brought by the side chain R9. As compared to R1 (and even the hydrophobic RY), although it is still within the typical values for single amino acid substitutions as 2-5 kcal/mol, a roughly 4 kcal/mol decrease clearly implies that R9 interacts distinctively differently with the protein from disulfide-linked side chains.

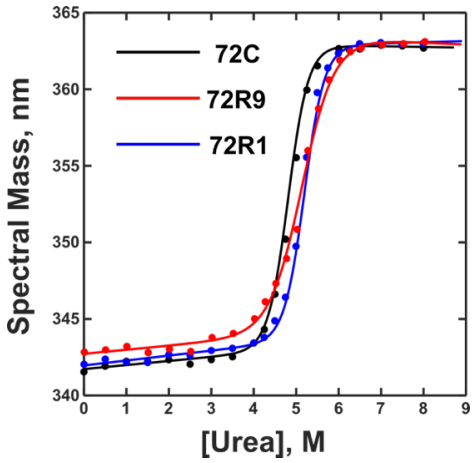

Figure 7.7 Urea denaturation curves of T4L72C, T4L72R1, and T4L72R9 based on the center of spectral mass of tryptophan fluorescence emission, fit to the equation describing a two-state, reversible unfolding process at equilibrium (details are described in chapter 8, materials and methods).

Table 7.2 Thermodynamic properties derived from the two-state model fit of urea denaturation curves.

	T4L72C	T4L72R1	T4L72R9
ΔG_0 (kcal/mol)	12.0 ± 0.91	11.6 ± 1.6	7.92 ± 1.8

$\Delta\Delta G_0$ (kcal/mol)		-0.4	-4.08
m (kcal·L/mol^2)	2.47 ± 0.19	2.26 ± 0.33	1.56 ± 0.36
$[Urea]_{1/2}$ (mol/L)	4.87	5.13	5.07

An obvious shift (almost one unit less) was also observed for the m-value, which might be able to provide some insight into understanding the change in the free energy. Over years of studying[7–9], it now appears that urea denatures proteins because it favors conformations that expose more solvent-accessible surface area (ASA). As urea is added to a protein solution, the denatured state is energetically more favored as more peptide groups can be exposed to the solution in which the urea principally acts as a preferred solvent for these groups. The conformational equilibrium is consequently shifted towards the unfolded state, of which the population is dependent on the concentration of urea, producing measurable responses that can be used for thermodynamic analysis.

Experimentally defined in this analysis, the thermodynamic m-value is generally considered as a parameter reporting on the difference in ASA between the folded and denatured states. The apparently decreased m-value indicates that such a difference in ASA for 72R9 is smaller than what it is for 72R1. One possible reason is that the denatured state is somehow more compact when the side chain R9 is attached to site 72C, as compared to when the side chain R1 is attached.

However, considering that the protein mutant is essentially the same, a rather uncommon but seemingly reasonable possibility could be proposed. While the accurate description of the urea-induced denaturation mechanism is still under debate, a widely-accepted point of view is that urea preferentially and efficiently solvates the protein backbone via hydrogen bonding, which serves as one of the key steps through which urea intrudes the hydrophobic core of the protein and denatures it. When attached to the solvent-accessible surface of the protein (site 72), the R9 side chain likely competes against urea to develop noncovalent interactions (e.g., hydrogen

bonding) with backbone atoms, leading to a reduction of the apparent solvent-accessible surfaces and less effectiveness of urea.

More experiments are needed to justly explain the effects detected in the urea denaturation and to understand the mechanism, which seems to be relevant to the interactions between the R9 side chain and the protein. In this context, a crystal structure could fundamentally advance comprehension by offering a structural basis at the atomic level. Some results will be shown below.

7.2.3 Crystal structure of T4L 65R9/76R9

To identify the interactions of the R9 side chain that constrain the internal motion at helical sites, a 1.6Å crystal structure of T4L containing R9 side chains at positions 65 and 76 in the long helix C (T4L 65R9/76R9) was solved and refined to an R-factor of 21% (Table 7.3, more detailed statistics will be reported in a future publication). A structure of R9 at reference site 72 was not obtained since this site is involved in crystal contacts.

At the level of the backbone fold, the structure of T4L 65R9/7R9 is essentially identical to pseudo-WT (PDB code: 1L63). In particular, there is little difference between the backbone dihedral angles along helix C in T4L 65R9/76R9 and the pseudo-WT structures from Ramachandran plots, showing that the spin labels do not distort the local helical geometry (Figure 7.8).

Table 7.3 X-ray data collection and refinement statistics for the T4L 65R9/76R9 crystal

Data Collection	
Temperature, K	100
Wavelength, Å	1.5418
Resolution, Å	80-1.60

Highest resolution shell		1.66-1.60
Space group		$P3_221$
Completeness, %		97.64
Unit cell dimensions		
	a, Å	60.390
	b, Å	60.390
	c, Å	95.430
Refinement		
Resolution, Å		45.86-1.60
Reflections used		26610
R_{cryst}, %		20.64
R_{free}, %		22.93
R. M. S. deviations		
	Bond lengths, Å	0.007
	Bond angles, °	0.874
Mean B factor, Å		
	Protein atoms	22.94
	Overall atoms	23.81
Estimated coordinate error, Å		0.15

Figure 7.9 shows the electron density map for 65R9 and 76R9; electron densities of native side chains at other positions in the helix C are also shown to indicate the quality of the structure. Remarkably, the $2F_O–F_C$ electron density map reveals a single conformation of the side chain at both sites 65 and 76, with nearly all non-hydrogen atoms resolved. This is consistent with the high order of R9 reflected in the CW-EPR spectra. In contrast, electron density maps of the more mobile R1 at solvent-exposed helical sites are generally not resolved for the nitroxide ring due to disorder about the final two single bonds (χ_4 and χ_5) (Figure 7.1).

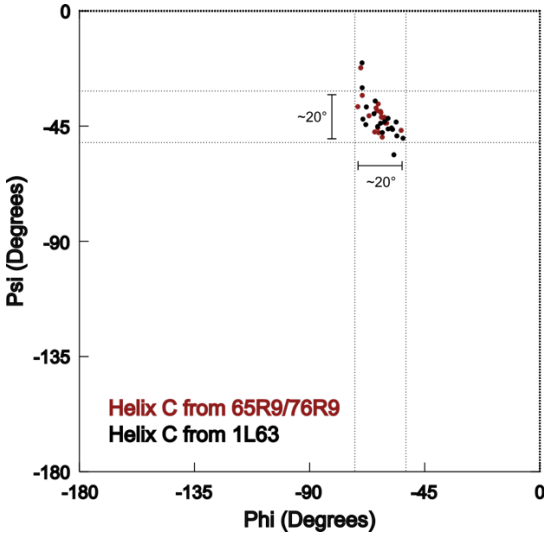

Figure 7.8 Ramachandran plot of the backbone dihedral angles for the T4L pseudo-wild type (PDB code: 1L63) and 65R9/76R9 crystal structures, showing that R9 does not substantially perturb the local protein structure from the wild type.

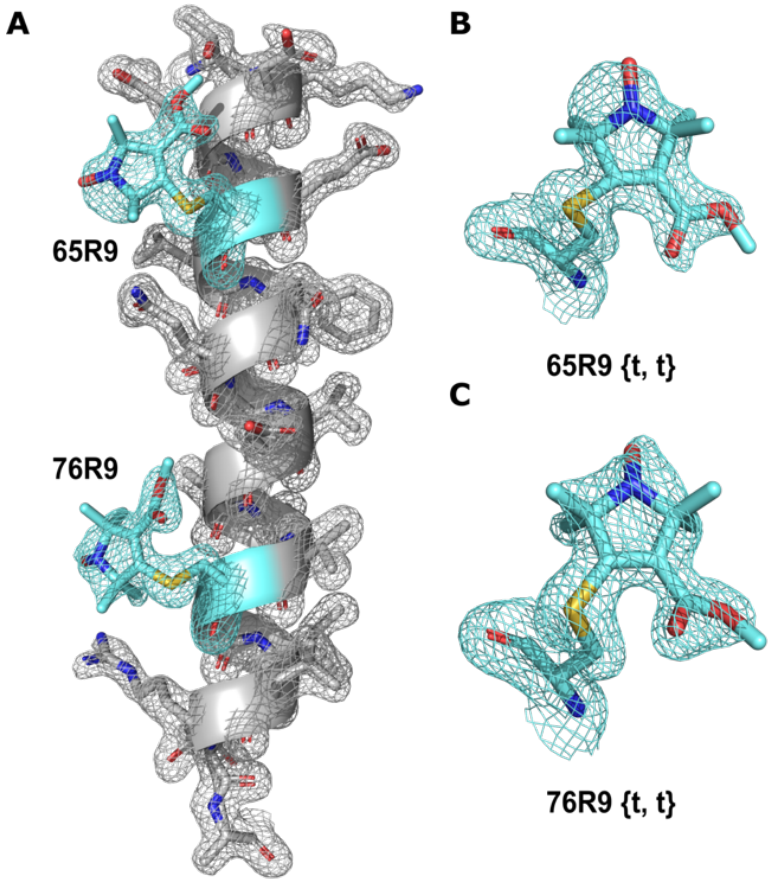

Figure 7.9 Crystal structure of T4L 65R9/76R9 at 100 K. (A) Electron density map for R9 and neighboring side chains are shown for the C helix. The electron density (cyan mesh) was calculated as an unweighted $2F_o$-F_c map contoured at 1.0 σ. (B and C) Electron density maps of 65R9 and 76R9, respectively.

Rotamers of a side chain with respect to dihedral angles $\{\chi_1, \chi_2\}$ are designated t (trans), p (plus), or m (minus). For native amino acid side chains, nominal values of t, p, m are ±180°, +60° and -60°, but variations of ±30° are commonly observed. For R1, V1, and RX, {m, m}, {t, p}, and {t, m} are the predominant rotamers observed in crystal structures on α-helices[2,10]. These rotamers are apparently stabilized by intra-residue interactions between the disulfide moiety and the peptide backbone, especially the C_α-H···S_δ interaction.

At both sites 65 and 76, the R9 side chain adopts the {t, t} conformation (Table. 7.4) that has not so far been observed in any structures of disulfide-linked spin labels at α-helical sites[11–14].

The non-covalent interactions that likely stabilize this rotamer and constrain the motion are identified from the structure as pairwise interactions at a distance less than the sum of the van der Waals radii of the atoms. Due to the short nitroxide-protein linkage in the R9 side chain, the nitroxide ring resides close to the backbone and numerous interactions unique to R9 are found. These may be grouped into two classes: (1) internal interactions within the R9 amino acid, and (2) inter-residue interactions with the i-3 and i-4 residues. The key interactions meeting the criterion and involved in stabilizing the rotamer and hindering rotation of the nitroxide are shown in Figure 7.10 and tabulated in Table 7.5.

Table 7.4 Structures of the T4L 65R9 and 76R9 side chains.

Dihedral angle (χ)(°) or Bond angle ($\angle$)(°) or Distance (d)(Å)	T4L 65R9 {t, t}	T4L 76R9 {t, t}
χ_1	-176.55	-177.55
χ_2	-174.45	-142.95
χ_3	+138.30	+114.46
$\angle C_\beta\text{-}S_\gamma\text{-}C_3$	+95.64	+106.78
d ($C_\beta\text{-}S_\gamma$)	1.765	1.799

Primary interactions that stabilize the χ_1 configuration as {t} are the $C_\alpha\text{-}H\cdots S_\gamma$ interaction, the two $C_\beta\text{-}H\cdots O{=}C$ interactions with backbone peptides (residue i-3 and i-4), and the relative weak $S_\gamma\cdots O{=}C$ internal interaction[15–18]. Such inter-atomic interactions, including the C_β-H interactions with oxygen, have been previously documented in proteins[19,20]. It needs to be noted that although the C_β-H is usually not considered as the H-bond donor, due to the adjacent sulfur, it is in principle more prone to develop such interaction with a nice H-bond acceptor, such as the carbonyl oxygen.

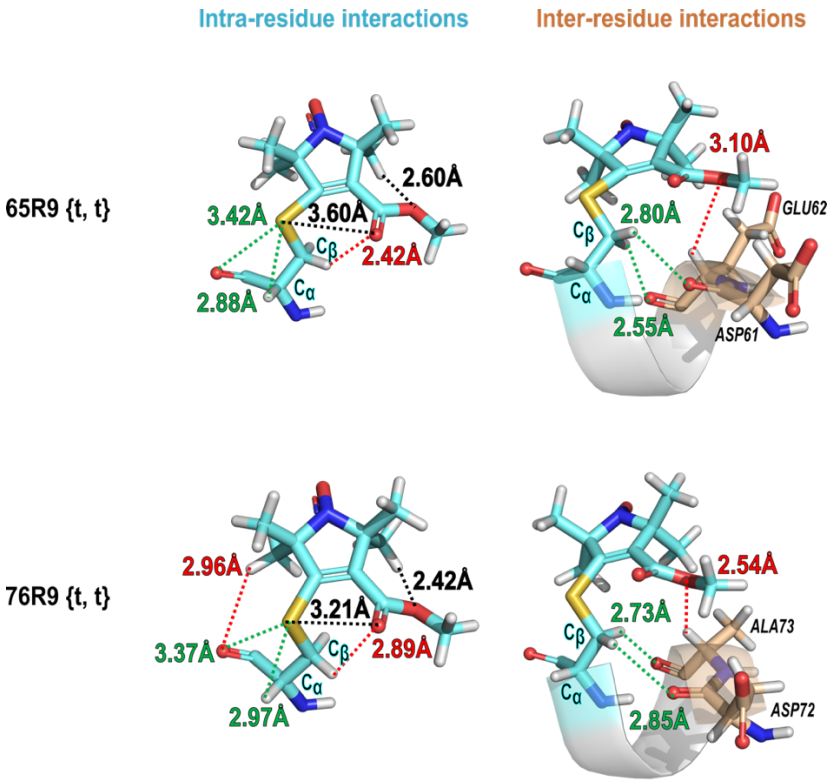

Figure 7.10 Intra-residue and inter-residue interactions that stabilize the structure of 65R9 {t, t} and 76R9 {t, t} on helix C determined from the crystal structure. Interactions stabilizing the χ_1 and χ_2 are colored green, the ones restricting the χ_3 are colored red, and the ones stabilizing the internal structure but not the dihedrals of the thioether linkage are colored black.

However, these interactions will not restrict values of χ_2 and χ_3, and the motion of the nitroxide ring relative to the protein. Apparently, the ester group plays an essential role in restricting the internal motion of the R9 side chain. Again, though the sp^3 hybridization ester oxygen is not often seen as the H-bond acceptor, it is not impossible. Taking account of the fact that C_α-H has been widely known to form stable interaction due to its acidity, it is convincing that the ester group can help R9 to be relatively immobilized on the protein surface.

The 4-substituent ester group is approximately co-planar with the unsaturated nitroxide ring presumably due to conjugation. The small tilt angle (approximately 30°-35°) between two conjugation planes optimizes intramolecular interactions of the oxygen atoms in the ester with S_γ

and C_α-H, and avoids a possible repulsive interaction between the ester methyl group with C_β. The close apposition of the nonpolar surface of the nitroxide ring with the backbone surface leads to the de-solvation of the ring and suggests an additional, perhaps dominant, contribution from the hydrophobic effect (Figure 7.11).

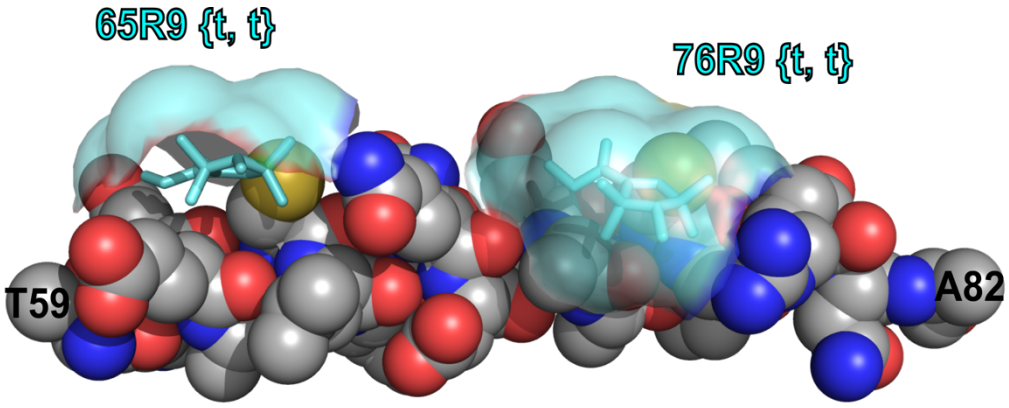

Figure 7.11 Illustration of the de-solvation by nonpolar surfaces. The stick models of the nitroxide ring structures from 65R9 and 76R9 are shown with their nonpolar surfaces (cyan), while the backbone atoms under the surfaces that become solvent inaccessible are shown as space-filling models.

Importantly, the interactions in Table. 7.5 do not rely on the identity of any neighboring side chain (unless glycine) since only C_β-H interactions are involved with peptide atoms of nearest neighbors. Moreover, the intra-R9 interactions are general and site independent. Thus, it is reasonable to assume that for R9 at helical sites, the above interactions would be retained, and one would expect internal immobilization of the nitroxide. However, collective motions of the helix would still modulate the motion of the nitroxide, suggesting the possibility that R9 may be a sensor for slow protein motions, as discussed further below.

Table 7.5 Apparent attractive interactions with the R9 side chain in the {t, t} configuration at sites 65 and 76.

Distances (Å)	T4L 65R9 {t, t}	T4L 76R9 {t, t}
Intra-residue interactions		
C_γ-H···O (ester oxygen)	2.60	2.42
S_γ···O (carbonyl oxygen)	3.60*	3.21
C_β-H···O (carbonyl oxygen)	2.42	2.89*

C_α-H···S_γ	2.88	2.97
S_γ···O (peptide oxygen)	3.42	3.37
C_8-H···O (peptide oxygen)	n.a.	2.96*
Inter-residue interactions		
O (ester oxygen) ···$C_{\alpha,\ i\text{-}3}$-H	n.a.	2.54
C_β-H···$O_{i\text{-}3}$ (peptide oxygen)	2.55	2.73
C_β-H···$O_{i\text{-}4}$ (peptide oxygen)	2.80	2.85*

* The sum of hydrogen and oxygen van der Waals radii[21] which is 2.7~2.8 Å, but the weak interactions (distance < 3.0 Å) are still included, n.a.: the distance is larger than 3.0 Å; the sum of the hydrogen and sulfur van der Waals radii which is 3.0~3.1 Å; the sum of the oxygen and sulfur van der Waals radii which is 3.3~3.4 Å.

Although the {t, t} rotamer is the only one observed here, other rotamers can be modeled with a similar set of attractive interactions and without steric collisions (see below). The selection of the {t, t} rotamer may be the result of the environment in the crystal lattice, particularly at site 65 (Figure 7.12), the nitroxide is at a distance of 3.2-3.3Å with several atoms spatially surrounded: the peptide oxygen of Ile50 from the same protein molecule; the C_δ-H, and the N_ε-H of Arg137 from a symmetry-related protein molecule in the crystal lattice.

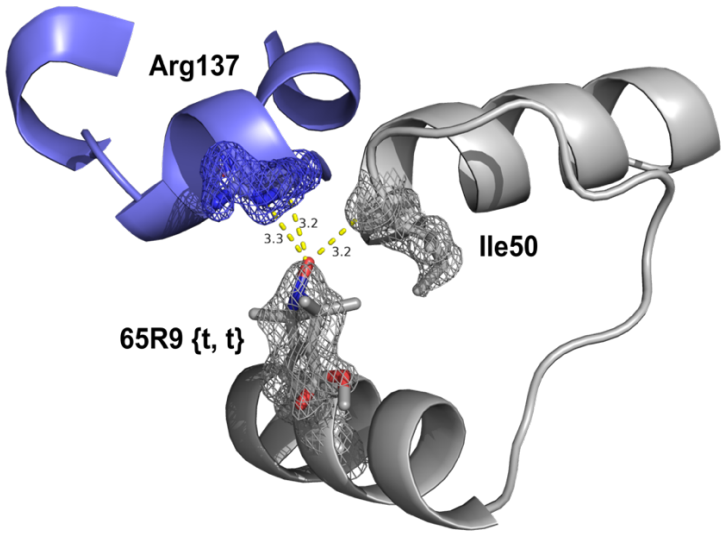

Figure 7.12 Interactions determined from the crystal structure between 65R9 {t, t} with Ile50 from the same protein molecule (grey), and Arg137 from a symmetry-related protein molecule in the crystal lattice (blue).

It seems that the short linkage of R9 also plays a role in populating the {t, t} rotamer. As a comparison, there is no such interaction around V1 that instead adopts the rotamer {t, p} at the

same site (site 65). The fact that the disulfide linkage of V1 is longer than R9 is very likely to force V1 to point toward another direction, otherwise, it would not be able to fit into the fairly narrow space surrounded by Ile50 and Arg137 in the lattice. Similar to V1 but with an even longer length, R1 has been forced to interact repulsively with another symmetry-related protein molecule in the crystal lattice, leading to internal strain and thus its non-nominal values of χ_1 and χ_2 (153° and 89°)[22].

In addition to the potential influences from symmetry-related molecules, more generally, the unusual solvent conditions in the crystal can also play a role in determining the rotamer(s) of any side chain, such as R9, where solvation is an important energetic feature. Indeed, DEER distance mapping of the protein in frozen solution indicates the existence of at least one other preferred rotamer of R9. The results are presented in the following section.

Shortly, for R1, the C_α-H$\cdots S_\delta$ interaction essentially determines that the χ_4/χ_5 model[23] is sufficient for describing its mobility, in which the last two terminal bonds matter the most. While for V1, the mobility of the whole side chain is effectively restricted with the internal strain accomplished via N$\cdots S_\gamma$ interaction to the torsional oscillation about the terminal χ_4 dihedral angle bond. Due to the fact that R9 has only three bonds as the linkage, it is natural to assume that its terminal bond would be more accessible to various non-covalent interactions. Details will be analyzed below.

7.2.4 Interspin distance mapping by DEER

Double electron–electron resonance (DEER) spectroscopy[24] is well-established for measuring long-range distance (20–80 Å) between pairs of spin labels selectively introduced in proteins. An important feature of DEER is that it provides analytical probability distributions, not

just average distances, making this technique a superior tool for revealing not only the structural heterogeneity of protein, but also the magnitude of structural differences.

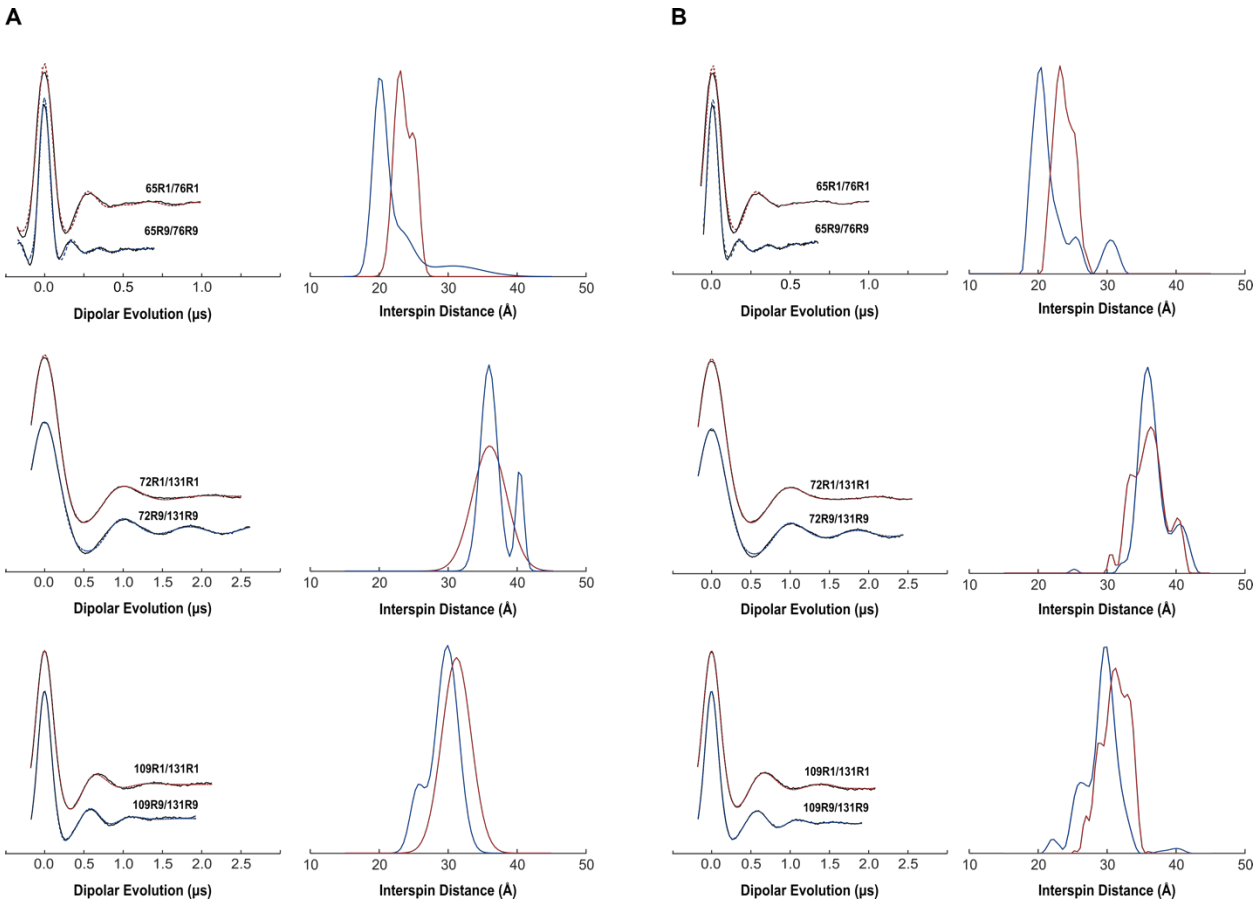

Figure 7.13 DEER data of T4L mutants bearing either two R9 side chains (blue traces) or two R1 side chains (red traces). Background-subtracted dipolar evolution functions (left) of the indicated mutants and their corresponding area-normalized distance probability distributions (right) obtained from (A) multiple Gaussian-based fits; (B) Tikhonov regularization (model-free) fits, for T4L 65R9/76R9, T4L 72R9/131R9, and T4L 109R9/131R9.

The distances determined by DEER will of course depend on the structure of the protein, but in addition on the $\{\chi_1, \chi_2\}$ rotamer of each side chain. The width of a distribution is determined by the spatial disorder of the nitroxide in the state populated, and this is determined both by the disorder of the protein structure and of the side chain itself. Therefore, the internal flexibility (disorder) of R1 makes it problematic to directly translate interspin distances into structural

information of proteins. It is therefore of interest to discover rigid nitroxide side chains for which the internal flexibility has minimal contribution to the overall distribution width.

Though many efforts have been made through crystallization and simulation to model the state of R1 and thereby deconvolute its contribution in DEER measurements, finding an alternative side chain with more restricted internal motions has always been considered a neater way to simplify this problem. The crosslinker RX has proven useful for its significantly narrow linewidth compared to R1. However, it would require 4 cysteine mutations per one distance measurement, which unquestionably casts a shadow on whether the folding of proteins would be influenced in some regions. Moreover, the formation of the crosslink would likely lead to strain in forming a proper helix extending to the i+3 or i+4 position, thereby potentially modifying the local structure and dynamics.

As already shown by CW-EPR spectra at various sites, the R9 side chain has the highest order of motion of any single-site attachment label, making it a potential candidate for DEER distance measurements that would reflect primarily protein disorder. To evaluate this point, pairs of R9 labels were introduced at T4L sites in regular, stable helices.

Table 7.6 Results of multiple Gaussian-based fits.

	Distance (Å)	Width (Å)	Population
65R9/76R9	20.08 ± 0.16	2.41 ± 0.34	61.32%
	23.04 ± 1.62	4.27 ± 3.04	24.73%
	30.70 ± 2.73	9.76 ± 4.23	13.95%
65R1/76R1	22.98 ± 0.21	2.28 ± 0.37	69.51%
	25.17 ± 0.27	1.65 ± 0.42	30.49%
72R9/131R9	35.91 ± 0.05	2.92 ± 0.13	81.22%
	40.39 ± 0.16	1.34 ± 1.09	18.78%
72R1/131R1	36.01 ± 0.08	5.85 ± 0.21	100.00%
109R9/131R9	25.56 ± 0.18	2.50 ± 0.44	16.40%
	29.90 ± 0.06	3.82 ± 0.12	83.60%
109R1/131R1	31.22 ± 0.07	5.00 ± 0.19	100.00%

Previous DEER studies have shown that analysis using a multiple-Gaussian model provides a way to distinguish 'states' in equilibrium and to obtain the fractional populations of each component from the distance distributions. For results obtained in this experiment, fits of dipolar evolution functions (DEF) to a multiple-Gaussian model for the distance distribution

were found to be equivalent to the model-free analysis in reproducing the details of the distance distributions (Figure 7.13), therefore the analysis is based mainly on the multiple-Gaussian model.

Remarkably, in each pair, each component from the distance distribution of R9-labeled mutants has narrower widths (Table 7.6) than R1-labeled analogs, reflecting a better localization of nitroxide within R9 (Figure 7.13). The dominant component of in each distribution has a shorter most probable distance value compared to what R1-labeled analogs measure. Both the shorter distance and narrower peak width could presumably be attributed to the short linkage and restricted mobility of R9, though there is still residual motion that must account for the width of the interspin distance distribution.

As mentioned, the structural heterogeneity in both the side chain and the protein itself would contribute to the width of distance distributions. Among 3 pairs of R9-labeled mutants, 109R9/131R9 shows the most complex structure in the distance distribution, consistent with the fact that site 109 resides in the short helix F that is known to have a high degree of flexibility[25]. As a comparison, the distance distribution of 65R9/76R9 is essentially dominated by a single distance of ~20.1Å, which is consistent with the fact that both sites are located within the stable helix C.

Of significant interest is that the 20.1Å distance determined by DEER for 65R9/76R9 is 3Å longer than the 17.3Å interspin distance measured from the crystal structure (Figure 7.14 (A)). Considering that there is no second R9 rotamer except for the rotamer {t, t} resolved at the same time from the crystal structure, it is reasonable to assume that a different rotamer must be populated in the aqueous solution instead.

While it is known that only the most energetically favored conformational structure will be

stabilized during crystallization, the selection of molecular rotamers can be severely affected by the crystal environment. Both the difference in temperature and the degree of hydration could theoretically modulate the rotameric equilibria, leading to the deviation between the crystal and solution structures. In a contrast, DEER experiments can presumably capture and resolve all co-existing distances under the equilibrium in the aqueous solution. Less observed in previous works, it is actually intriguing that the attached spin labels report the same physical distance differently under different environments (as large as 3Å).

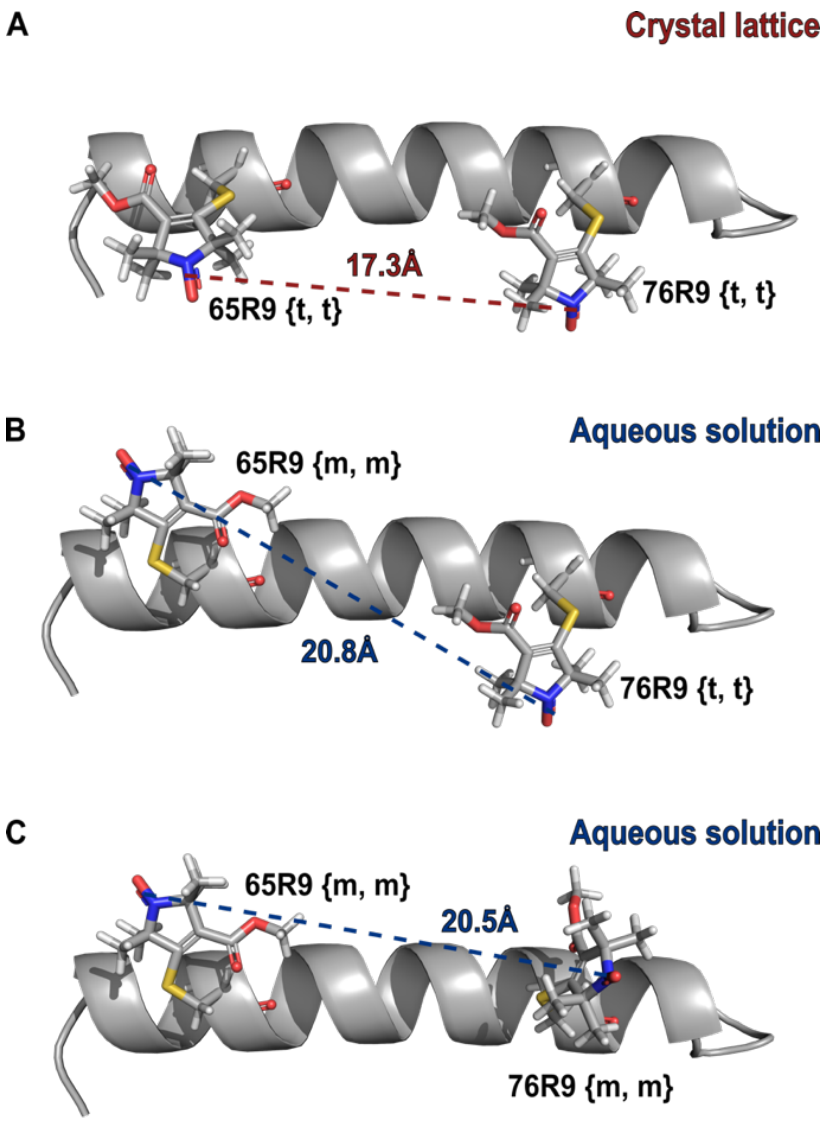

Figure 7.14 Models of the C helix containing 65R9 and 76R9, showing the interspin distance between: (A) 65R9 {t, t} and 76R9 {t, t}; (B) 65R9 {m, m} and 76R9 {t, t}; (C) 65R9 {m, m} and 76R9 {m, m}.

To further understand this difference, other possible rotamers that would be sterically allowed were modeled[26] at both sites based on the crystallographically determined configuration of R9 (bond angles, lengths, etc.) to see if the DEER-measured distance can thus be satisfied. While this distance difference cannot be compensated by only adjusting the χ_3, it is required for the R9 side to adopt a different $\{\chi_1, \chi_2\}$ rotamer that is not {t, t} at site 65. Among all models, using an {m, m, +170°} rotamer at site 65 and keeping the {t, t, +114°} rotamer at site 76, an interspin distance of ~20.7Å can be obtained (Figure 7.14 (B)). Another feasible combination is to also propose an {m, m} rotamer for 76R9, giving a distance of ~20.5Å (Figure 7.14 (C)).

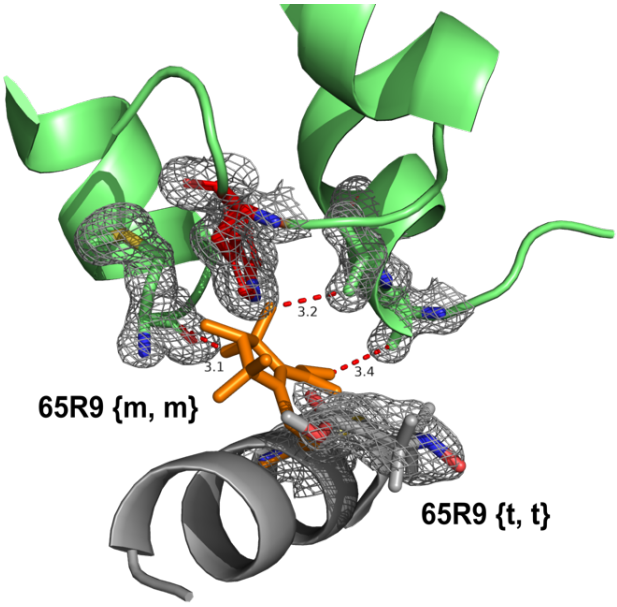

Figure 7.15 A model of interactions between 65R9 {m, m} (orange) with Trp158, Met1, Ala93, and Val94 from a symmetry-related protein molecule in the crystal lattice (green). The original 65R9 {t, t} rotamer is also displayed to show the relative orientation.

Either the unique short linkage or the chemical composition (ester group), or both have potentially enabled a virtually different rotameric library for R9. When building up the model of

the {m, m, +170°} rotamer in the crystal lattice, which is compatible with the DEER distance, there shows several potentially unfavorable repulsive interactions, even collisions, between this rotamer (colored as orange) with another (different from the one in Figure 7.12) symmetry-related molecule. The hydrophobic patch (Figure 7.15) formed by Trp158, Met1, Ala93, and Val94 from this molecule could essentially eliminate the possibility of populating the {m, m} rotamer at site 65 in the crystal lattice.

In summary, the {t, t} rotamer is more energetically favored under the crystal environment, which could not be achieved similarly in the aqueous solution. Instead, another rotamer is populated, suggesting that this configuration would be more stable when there is no interaction imposed from symmetry-related molecules. It needs to be emphasized that the {m, m} is just one of the possible rotamers that are energetically reasonable in the solution, but other alternatives are not certainly excluded. The fact that there is more than one single component in each of the three DEER distance distributions of R9 pairs implies the existence of rotameric equilibria.

In fact, it has been shown in the modeling tests (results not included here) that combinations using different rotamers can account for all of the probable distances resolved in distributions except for the minor one (14%) at 30.7Å in 65R9/76R9, which might be rationalized to fluctuations of the backbone. The feature of the R9 side chain that it possesses the shortest linkage and thus the closeness to the surface suggests that it might be able to provide a unique perspective in describing backbone dynamics that is not detectable to other disulfide-linked labels.

Collectively, the R9 side chain has shown to be a practically applicable alternative for DEER measurements, exhibiting narrower and discrete components in distance distributions, which would help simplify the consequent analysis. Although it has always been debated whether

DEER measurements can faithfully retain the conformation under ambient conditions upon flash-freezing, it is unquestionable that the distance measurement of 65R9/76R9 identifies a distinction between crystal lattice and aqueous solution under cryogenic temperatures. Further analysis will be given and discussed below.

7.2.5 Structural origin of the highly ordered motion of the R9 side chain

As supported by the characteristic CW-EPR lineshapes, the narrow DEER distribution, and the resolved nitroxide ring in the crystal structure, it is reasonable to believe that the R9 side chain is strongly immobilized to the backbone on the protein surface. For possible applications and a further understanding of the spin label, it is vital to comprehend and eventually elucidate the structural origin of its rigidity.

It has already been revealed *via* the analysis about the {t, t} rotamer that the R9 side chain is able to adopt the configuration so that energetically favored interactions around it can be satisfied, and thus the side chain can be effectively immobilized relative to the protein. The closeness of R9 to the surface ensures that necessary interaction can be formed with 'conserved' atoms (C_α, C_β, or peptide carbonyl oxygen) in the backbone. At the same time, the short linkage also helps minimize potential hydrophobic collision so that the ester group can extend and approach other atoms to develop non-covalent interactions.

Analogously, when modeling the {m, m} rotamers, all χ_1, χ_2, and χ_3 angles are approximately optimized so that as much as attractive interactions could be satisfied. In general, sufficient interactions are accessible for this rotamer to be energetically stable at the sites being examined, further supporting the presumption that this rotamer would be more favored in the aqueous solution.

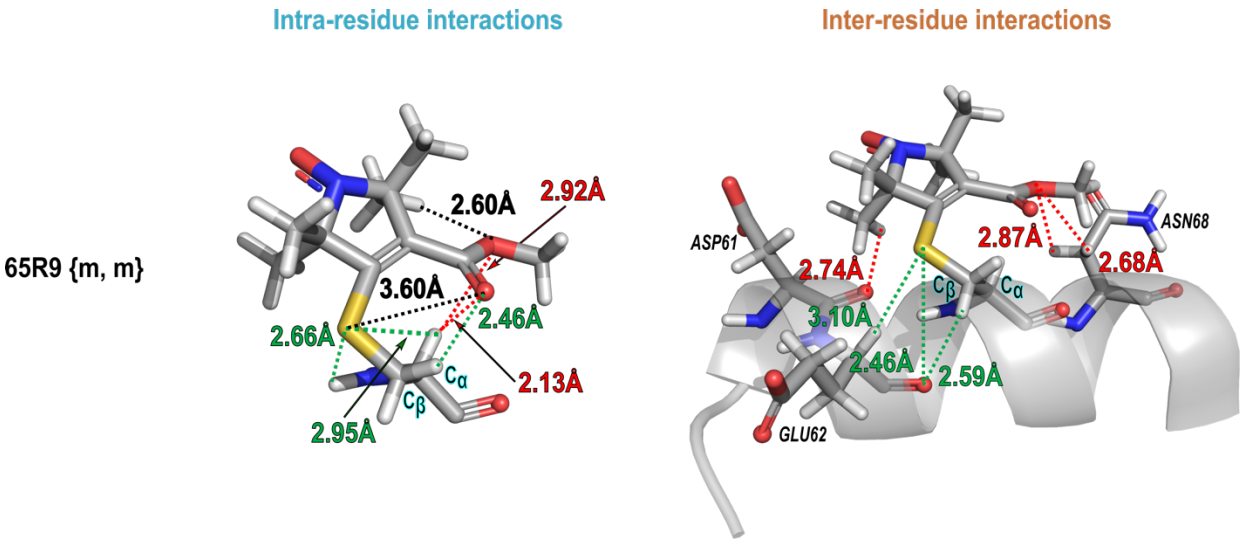

Figure 7.16 Intra-residue and inter-residue interactions that stabilize the structure of 65R9 {m, m} on helix C from the molecular modeling.

Common interactions are found for both configurations, including the C_α-H···S_γ and C_β-H···O_{i-3}/O_{i-4} (peptide) interactions. Attractive interactions observed previously from only the {m, m} rotamer of R1, such as the (peptide) N-H···S_γ interaction and the C_β-H···O (peptide) interaction, are also found. Instead of the $C_{\alpha,\, i-3}$-H···O (ester oxygen) interaction, the {m, m} rotamer has a similar but also more or less weak attractive interaction between the $C_{\beta,\, i+3}$-H and the carbonyl sp^2 oxygen (peptide) to help immobilize the side chain to the backbone. Even though, due to the carboxamide side chain of Asn68, such interaction at site 65 could be enhanced by its more acidic $C_{\beta,\, i+3}$-H.

Among all the interactions that the proposed model of the {m, m} rotamer has enabled, the most important one is the strong attractive interaction between C_α-H and the carbonyl sp^2 oxygen (Table. 7.7 and Figure 7.16). Instead of forming the potentially weak hydrogen-bonding with the C_β-H in {t, t} rotamers, the ester group is positioned within the accessible range of the more acidic C_α-H to make internal interaction when the side chain adopts the {m, m} configuration.

The {m, m} rotamer was found in previous publications to be the most probable of all

sterically allowed rotamers according to both experimental results and quantum mechanical computation of disulfide-linked side chains. Both the S_γ and S_δ atoms form interactions with the backbone C_α-H facilely, making this rotamer likely the most energetically favored configuration on surface-accessible helix regions. Similarly (also with the C_α-H$\cdots S_\gamma$ interaction), but also differently (no atom S_δ), it is reasonable to speculate that at the same topographic regions (solvent exposed helical sites), the {m, m} configuration will be the most prospective rotamer for R9 side chains to adopt. The C_α-H interactions with oxygen have been widely documented in proteins, which could play the key role in sufficiently restricting the mobility of R9 relative to the protein.

Table 7.7 Attractive interactions with the R9 side chain in the {m, m} configuration at sites 65 and 72.

Distances (Å)	65R9 {m, m}	72R9 {m, m}
Intra-residue interactions		
C_7-H$\cdots$O (ester oxygen)	2.60	2.42
C_α-H$\cdots$O (ester oxygen)	2.92*	n.a.
$S_\gamma\cdots$O (carbonyl oxygen)	3.60*	3.21
C_β-H$\cdots$O (carbonyl oxygen)	2.46	n.a.
C_α-H$\cdots$O (carbonyl oxygen)	2.13	2.20
C_α-H$\cdots S_\gamma$	2.95	2.67
N (peptide nitrogen)-H$\cdots S_\gamma$	2.66	3.19*
Inter-residue interactions		
O (ester oxygen) $\cdots C_{\beta,\, i+3}$-H	2.87*	n.a.
O (ester oxygen) $\cdots C_{\beta,\, i+3}$-H (another)	2.68	n.a.
C_β-H$\cdots O_{i-3}$ (peptide oxygen)	2.59	2.82*
C_β-H$\cdots O_{i-4}$ (peptide oxygen)	n.a.	2.72
$S_\gamma\cdots C_{\alpha,\, i-3}$-H	3.10	n.a.
$S_\gamma\cdots O_{i-4}$ (peptide oxygen)	2.46	3.50*
C_8-H$\cdots O_{i-4}$ (peptide oxygen)	1.40*	n.a.
C_8-H (another)$\cdots O_{i-4}$ (peptide oxygen)	2.74	n.a.

*The sum of the hydrogen and oxygen van der Waals radii which is 2.7~2.8 Å, but the weak interactions (distance < 3.0 Å) are still included; the sum of the hydrogen and sulfur van der Waals radii which is 3.0~3.1 Å; the sum of the oxygen and sulfur van der Waals radii which is 3.3~3.4 Å

While the existence of other rotamers cannot be excluded with certainty, the {m, m}

rotamers were found to be successfully modeled (results were not shown) at most helical sites tested for R9 in this work, including sites 68, 72, 76, 80, 82, 109, 115, and 131. The modeling tests for 72R9/131R9 have offered other supportive evidence. It turns out to be that any model built with the {t, t} rotamer at site 72 actually cannot explain the dominant interspin distance of ~35.9Å reported by DEER measurement for the 72R9/131R9 pair, regardless of which rotamer is used at site 131. In the meantime, both the DEER result of the 72R9/131R9 pair and 109R9/131R9 pair are compatible with models using {m, m} rotamers of R9 at sites 72, 109, and 131 (Figure 7.17).

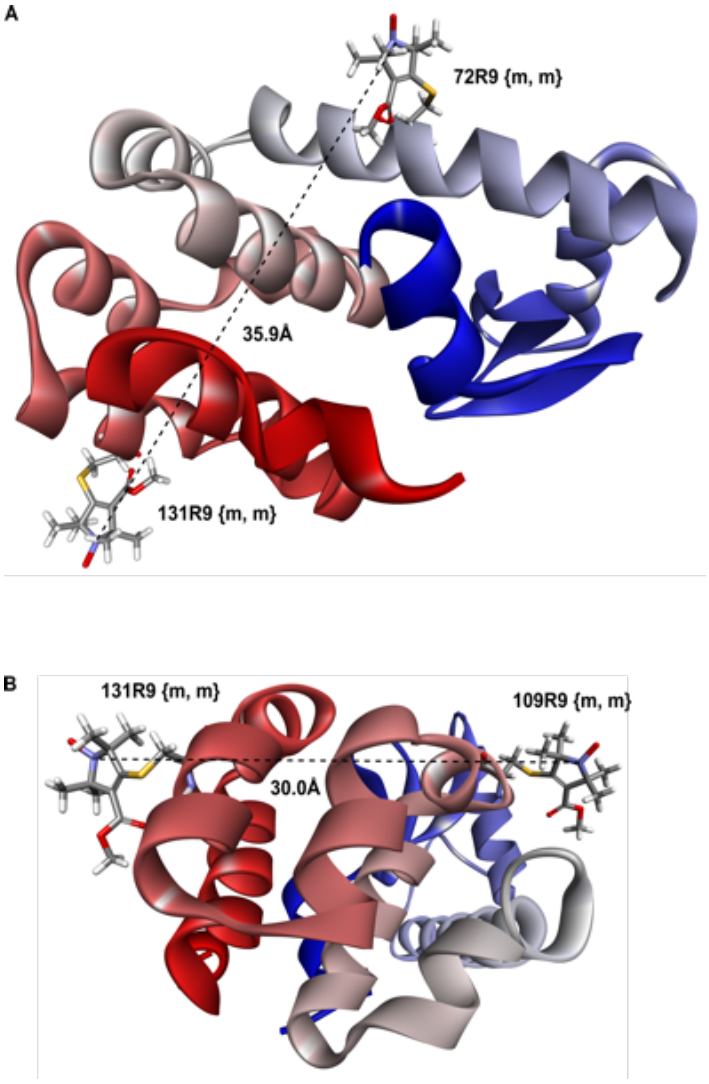

Figure 7.17 Models of T4L containing 72R9, 109R9, and 131R9, showing the interspin distance corresponding to DEER measurements. (A) 72R9/131R9; (B) 109R9/131R9. The protein is colored as a transition from blue at its N-terminus to red at its C-terminus.

Among three rotamers previously observed for R1, the {t, m} rotamer is not sterically allowed for 72R9 (also {m, p}, {p, m}, {p, p}, {p, t}). Even though it is theoretically possible to build the {t, p} or {m, t} rotamers for 72R9, both rotamers would orient the ester group away from the protein but into the solution. Instead, {m, m} can keep the structure closer to the backbone and thus effectively immobilize the side chain by being able to pick up more interactions, which is consistent with what the CW-EPR spectrum of 72R9 shows: the strongly restricted, highly ordered motion.

It needs to be noted that although at both sites the same rotamer is adopted, the 65R9 {m, m} resides differently from 72R9 {m, m}. Around 72R9, there are two hydrophobic Valine residues at the i-1 and i+3 positions prohibiting the 4 methyl groups of the nitroxide ring from getting closer. While their coherent (a single Val is not enough as proved by the alanine substitution experiment) steric hindrance could be the reason why the R9 side chain could be so strongly immobilized at this site, such orientation has disabled additional interactions between the hydrogen atoms from the nitroxide ring with the peptide oxygen at the i-4 position, which were observed in the 65R9. However, the mobility of 65R9 is indeed less restricted than 72R9 judging from their CW-EPR spectra, which could be a result of the backbone fluctuation near site 65 located near the termini of the helix.

7.2.6 Applications

7.2.6.1 Spin-lattice relaxation rate (T_1) of T4L72R9 attached to Sepharose

It is well established that the EPR spectrum is modulated by the relaxation effects. By measuring saturation-relaxation dependent behaviors of the spin label, several EPR techniques extend the detection limit of structure and dynamics.

Reflected from the narrow linewidth of CW spectra, it can be inferred that R9 has a long relaxation time as compared to R1 due to its restricted amplitude of internal motion. In order to quantitatively evaluate R9 for further application, its value of T_1, the spin-lattice relaxation time on T4L 72C attached to CNBr-Sepharose is measured by the pulsed saturation recovery EPR (SR-EPR)[27]. Briefly, SR measures the recovery of the EPR signal following a saturating microwave pulse applied to the maximum absorbance of the nitroxide $m_I = 0$ resonance. Under similar conditions, the longer T_1 usually correlates with the more restricted motion. On solvent-exposed sites of proteins, R1 typically has $T_1 \approx 3\mu s$ (2.9μs for 72R1 on CNBr), while RX has T_1 of 6~9μs (7.7μs for 68RX72 on CNBr).

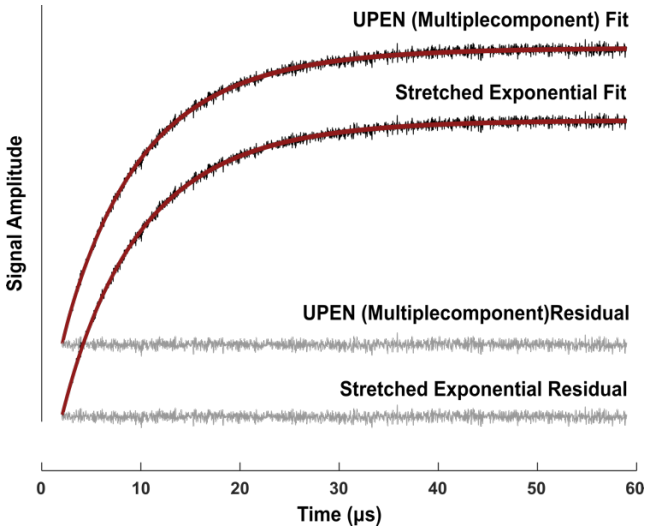

Figure 7.18 SR curves for 72R9 on CNBr-Sepharose. The plot shows the signal intensity recorded at the nitroxide $m_I = 0$ resonance position in the first derivative CW spectrum as a function of time following a saturating microwave pulse delivered at the same position (black traces). Also shown are the fit to a Stretched Exponential model and UPEN[28] (Multiplecomponent) model (red traces). The residuals for both fits are shown as gray traces, respectively.

When the extent of motional averaging is effectively limited, it is important to carefully select the proper mathematical model as the heterogeneity of the environment may play a more prominent role. Recently, the stretched exponential function (SEF) has been proposed by Subczynski and coworkers [29–32] to adequately describe such systems by a continuous sum of exponential decays. The stretching parameter (β) in SEF which ranges between zero and one, can be interpreted as a measure of environmental heterogeneity. The smaller the β, the more heterogeneous and less ordered the environment.

Indeed, the SR-EPR data of T4L 72R9 can be nicely fitted using the SEF with a $\beta = 0.91$ and $T_1 = 7.56\mu s$, suggesting a slightly heterogeneous and highly restricted mobility. Though the residuals from the conventional fit using three distinct exponential functions show comparable goodness to the fit residuals using the SEF (Figure 7.18), fitting with SEF is a more reasonable model that is consistent with the analysis based on the motional model determined from the spectral lineshape simulation: a single motional component of a high order.

With its $T_1 = 7.56\mu s$, R9 has exhibited its potential of serving as the probe candidate not only in slow motion detection (will be shown below) but also in relaxation enhancement measurements[33–35] for providing long-range distances (20~60Å) on the nm scale in biological systems. Under physiological temperature, the upper limit of the accessible distance of this method can be theoretically extended to 40~45Å with such a long T_1 value[33,34].

7.2.6.2 Detecting dynamics on the microsecond time scale with the R9 side chain in ST-EPR

As extensively discussed in previous chapters of this dissertation, due to the uncommon sensitivity of ST-EPR to all motions on time scales from ns to ms, it is crucial to exclude the contribution from ps-ns fast motions when measuring slower dynamics. The fast internal motion

of the spin label side chain itself can also bring in significant perturbance to the measurement using ST-EPR. A rigid spin label side chain with more restricted internal motion is essential for measuring slow dynamics. Here, we show that as a monofunctional spin label with the more chemically stable thioether linkage, R9 is sufficiently immobilized on helical sites to detect microsecond dynamics in protein with ST-EPR.

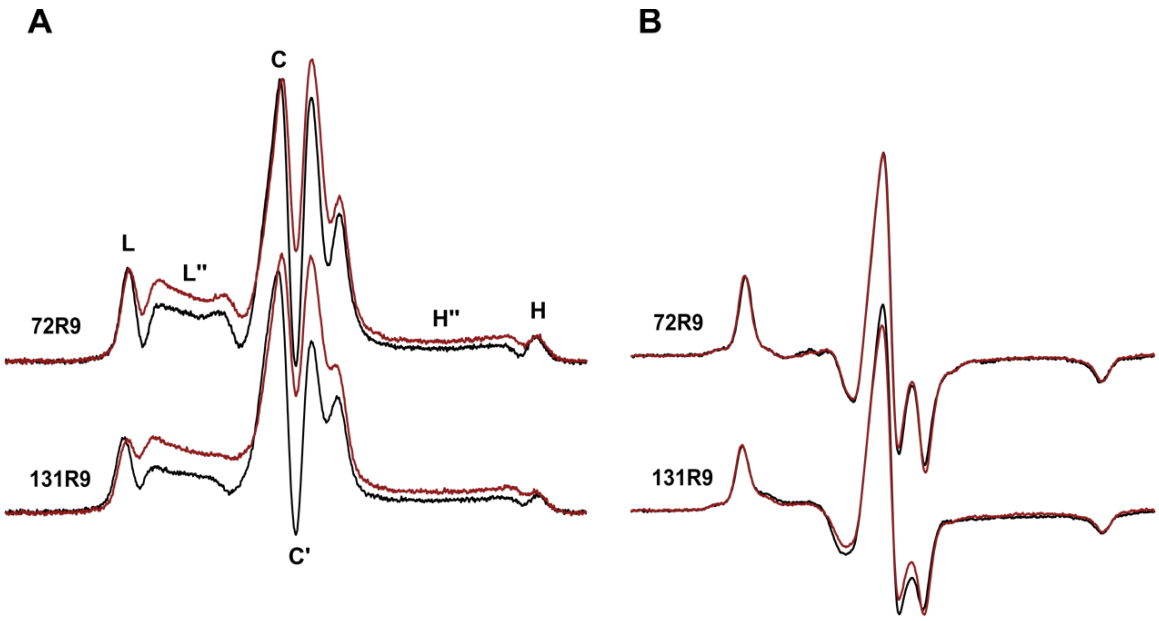

Figure 7.19 (A) ST-EPR and (B) CW-EPR spectra of T4L72R9 and T4L131R9 at room temperature, before (black traces) and after (red traces) being crosslinked by glutaraldehyde. All mutants attached to CNBr-activated Sepharose. The magnetic field scan width is 100 G. Line-heights used to calculate parameters are defined as shown, with the following explanations: All line-heights are measured with respect to the baseline. L is the resolved peak in the low field. L" is defined as the line-height at the field position 10 Gauss to the right of L. Similarly, H is the resolved peak in the high field, and H" is 15 Gauss to the left. The C and C' are the first peak and trough in the center.

Figure 7.19 (A) shows the ST-EPR spectra (black traces) measured for T4L72R9 and T4L131R9 at room temperature. Both samples are attached to solid supports to exclude Brownian rotational diffusion of proteins. Lineshapes of the two sites are qualitatively similar, and both L”/L (Table 7.8) report dynamics with correlation times around 23μs (calibration curves

of standards are from published results[36]) With higher sensitivity to the angular change of motions, the H''/H of 72R9 shows dynamics ~50μs, while 131R9 shows dynamics ~100μs. The result that τ_R values obtained from different line-height ratios are different suggests the anisotropic nature of detected dynamics. It is reasonable to suppose that either the motional mode of protein is anisotropic, or it is coupled to the intrinsic anisotropy of the sensor, R9 itself.

In order to better understand the motional origin of the microsecond dynamics observed in ST-EPR measurement, labeled proteins were crosslinked on the solid support by a sufficient amount of glutaraldehyde. For crosslinked samples (red traces), the H''/H of 72R9 shows dynamics >100μs, while 131R9 shows dynamics >200μs. As each protein molecule was already separately tethered to CNBr-Sepharose, extensive crosslinking should only be able to exert influences on protein internal motions. Like what has been observed for RX and RY side chains, the CW-EPR spectra at both sites are hardly distinguishable before and after the crosslinking reaction, especially site 72 (Figure 7.19 (B)), which confirms again that the R9 side chain is so strongly immobilized that the CW-EPR lineshapes are not sensitive anymore. On the contrary, the ST-EPR spectra show apparent changes (Figure 7.19 (A)).

Table 7.8 Parameters of ST-EPR (Line-height ratios) and correlation times of T4L72R9 and T4L131R9.

	L''/L	τ_R/sec	C'/C	τ_R/sec	H''/H	τ_R/sec
T4L72R9 CNBr glutaraldehyde	0.72	5.2×10^{-5}	0.39	1.8×10^{-5}	0.77	1.3×10^{-4}
T4L72R9 CNBr Buffer	0.52	2.3×10^{-5}	0.02	5.9×10^{-6}	0.52	5.0×10^{-5}
T4L131R9 CNBr glutaraldehyde	0.85	8.0×10^{-5}	0.45	2.3×10^{-5}	0.93	2.2×10^{-4}
T4L131R9 CNBr Buffer	0.53	2.4×10^{-5}	-0.09	4.3×10^{-6}	0.69	9.9×10^{-5}

The fact that the microsecond motions are susceptible to crosslinking reaction implies that it is mainly the internal dynamics of proteins that are detected by ST-EPR before crosslinking. Based on ST-EPR results, it can be confirmed that there are faster motional modes existing in the

non-crosslinked proteins. Possibilities of the origin of such dynamics have been discussed in previous chapters. Here, the qualitative ST-EPR results, as well as the determined T_1 value, are to demonstrate the ability to use the monofunctional R9 to detect dynamics in the challenging submillisecond time domain. The highly restricted motion of R9 on helical sites is promising for measurements even beyond the CW-EPR rigid limit.

7.2.6.3 Hetero-double electron resonance

There is great potential for the reaction selectivity of reagent HO-4072. In fact, the likelihood of having more cysteine residues that are functionally relevant also increases with the increase in size and structural complexity of protein. Although rounds of mutagenesis or the use of another spin label reagent targeting other amino acids could theoretically serve as the solution, the accompanying costs essentially make the spin labeling approach practically less preferred for large and complex proteins. In the experiments with T4L, R9 was found to be selective for surface sites only, which could enable measurements using SDSL-EPR techniques for proteins carrying unfavorable buried cysteines.

On the basis of the reaction selectivity of reagent HO-4072 for solvent-exposed sites, the possibility of introducing a hybrid of two different spin labels to the same mutant sample has been explored. As a proof of concept, four T4L mutants carrying a pair of cysteines were designed of which the interspin distances are detectable in DEER measurements, consisting of a solvent-exposed site (68C, 72C, 76C, 131C), and a buried site (118C). It is clear from both CW-EPR spectra (Figure 7.20) and DEER distances (Figure 7.21) that such a labeling scheme is accomplished, by direct comparing with the results collected for mutants labeled with two R1 side chains instead.

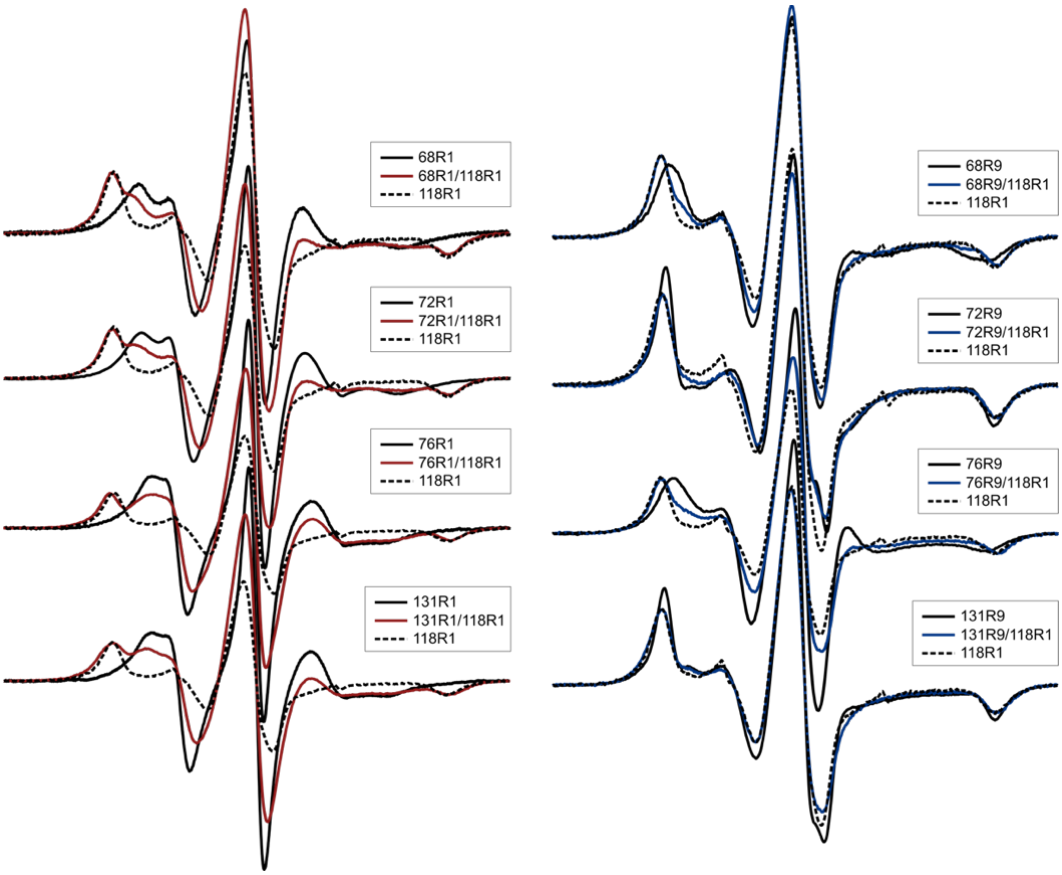

Figure 7.20 CW-EPR spectra at room temperature in 30% (wt/wt) sucrose solution of T4L mutants bearing either two R1 side chains (red traces) or the hybrid (blue traces) of R9 side chains.

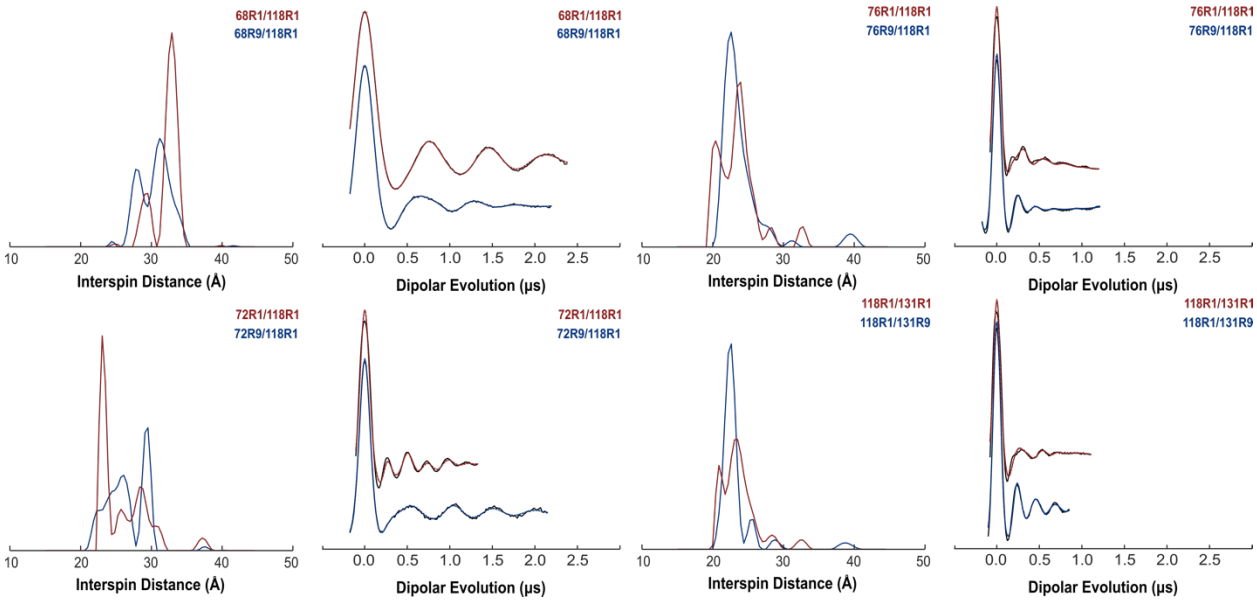

Figure 7.21 DEER data of T4L mutants bearing either two R1 side chains (red traces) or the hybrid (blue traces) of R9 side chains on solvent-exposed sites (68C, 72C, 76C, 131C) and R1 side chains on the buried site 118C. Background-subtracted dipolar evolution functions and corresponding area-normalized distance probability distributions are obtained from Tikhonov regularization (model-free) fits.

More experiments are needed to fully uncover the potential of this scheme in actual applications. Current results actually lay a foundation for practicing Hetero-double electron resonance experiments in the future. Theoretically, any R1-derivatized side chain might be used to substitute R1 in this scheme if sterically allowed, potentially enabling a large variety of spin-pair combinations. A such possibility might be uniquely advantageous for studies involving the exploration of spin label properties, or requiring varied EPR responses from topographically different regions.

7.3 Discussions and conclusion

The results presented here show that the internal motion of the thioether-linked R9 side chain is strongly ordered. The reaction mechanism implies that the side chain is only selectively attached to solvent-exposed sites. As compared to previously published thioether-linked spin labels (such as the BASL[37]), the existence of an ester functional group in structure improves its performance by minimizing unfavored interactions and restricting internal flexibility.

It is particularly interesting that the high ordering is not a result of any single, isolated intra-side chain interaction (like the sulfur-nitrogen interaction in V1). Rather, it seems that with its shorter length and the ester group, the R9 side chain is able to adopt the configuration so that all possible interactions around it can be satisfied maximally, and thus it can be effectively immobilized relative to the protein backbone.

Several attractive intra-residue and inter-residue interactions, as well as hydrophobic interactions, were identified from the crystal structure and molecular modeling. Furthermore, the smaller m-value obtained in the urea denaturation experiment is actually consistent with what was observed in the crystal structure, that there are collective interactions between the R9 side chain with the backbone to immobilize it on the surface. The existence of such interactions might compete with urea which acts as a preferred solvent for exposed protein side chains during the denaturation, thus leading to a decrease in m-value.

Unlike the majority of previously published immobilized spin label side chains (R1p[38], V1, RX, etc.), the spectra of R9 reflect distinctive site-specific variations in the ps-ns time range that encodes information on local backbone dynamics and interactions. Moreover, its high degree of internal motional order is expected to extend the dynamic range in the microsecond scale, as well as the resolution in distance measurements, which has been proved by the results shown in this chapter. Collectively, such uniqueness undoubtedly makes the R9 side chain valuable addition to SDSL-EPR technology.

7.4 References

1. Fleissner, M. R., Cascio, D. & Hubbell, W. L. Structural origin of weakly ordered nitroxide motion in spin-labeled proteins. *Protein Sci.* **18**, 893–908 (2009).
2. Toledo Warshaviak, D., Khramtsov, V. V., Cascio, D., Altenbach, C. & Hubbell, W. L. Structure and dynamics of an imidazoline nitroxide side chain with strongly hindered internal motion in proteins. *J. Magn. Reson.* **232**, 53–61 (2013).

3. Mchaourab, H. S., Lietzow, M. A., Hideg, K. & Hubbell, W. L. Motion of Spin-Labeled Side Chains in T4 Lysozyme. Correlation with Protein Structure and Dynamics. *Biochemistry* **35**, 7692–7704 (1996).
4. Fleissner, M. R. *et al.* Structure and dynamics of a conformationally constrained nitroxide side chain and applications in EPR spectroscopy. *Proc. Natl. Acad. Sci.* **108**, 16241–16246 (2011).
5. Columbus, L. M. Investigating backbone and side chain dynamics of α-helices in the nanosecond regime with site -directed spin labeling. (University of California, Los Angeles).
6. Fasman, G. D. *Handbook of Biochemistry: Section D Physical Chemical Data, Volume I*. (CRC Press, 2018).
7. Das, A. & Mukhopadhyay, C. Urea-Mediated Protein Denaturation: A Consensus View. *J. Phys. Chem. B* **113**, 12816–12824 (2009).
8. Myers, J. K., Nick Pace, C. & Martin Scholtz, J. Denaturant m values and heat capacity changes: Relation to changes in accessible surface areas of protein unfolding. *Protein Sci.* **4**, 2138–2148 (1995).
9. Tang, C., Lew, S. & He, D. Using a second-order differential model to fit data without baselines in protein isothermal chemical denaturation. *Protein Sci.* **25**, 898–904 (2016).
10. Balo, A. R., Feyrer, H. & Ernst, O. P. Toward Precise Interpretation of DEER-Based Distance Distributions: Insights from Structural Characterization of V1 Spin-Labeled Side Chains. *Biochemistry* **55**, 5256–5263 (2016).
11. Cunningham, T. F. *et al.* High-Resolution Structure of a Protein Spin-Label in a Solvent-Exposed β-Sheet and Comparison with DEER Spectroscopy. *Biochemistry* **51**, 6350–6359 (2012).

12. Freed, D. M., Horanyi, P. S., Wiener, M. C. & Cafiso, D. S. Conformational Exchange in a Membrane Transport Protein Is Altered in Protein Crystals. *Biophys. J.* **99**, 1604–1610 (2010).
13. Lietzow, M. A. & Hubbell, W. L. Motion of Spin Label Side Chains in Cellular Retinol-Binding Protein: Correlation with Structure and Nearest-Neighbor Interactions in an Antiparallel β-Sheet. *Biochemistry* **43**, 3137–3151 (2004).
14. Stoll, S. *et al.* Double electron–electron resonance shows cytochrome P450cam undergoes a conformational change in solution upon binding substrate. *Proc. Natl. Acad. Sci.* **109**, 12888–12893 (2012).
15. Kříž, K., Fanfrlík, J. & Lepšík, M. Chalcogen Bonding in Protein−Ligand Complexes: PDB Survey and Quantum Mechanical Calculations. *ChemPhysChem* **19**, 2540–2548 (2018).
16. Bleiholder, C., Werz, D. B., Köppel, H. & Gleiter, R. Theoretical Investigations on Chalcogen−Chalcogen Interactions: What Makes These Nonbonded Interactions Bonding? *J. Am. Chem. Soc.* **128**, 2666–2674 (2006).
17. Brezgunova, M. E. *et al.* Chalcogen Bonding: Experimental and Theoretical Determinations from Electron Density Analysis. Geometrical Preferences Driven by Electrophilic–Nucleophilic Interactions. *Cryst. Growth Des.* **13**, 3283–3289 (2013).
18. Pascoe, D. J., Ling, K. B. & Cockroft, S. L. The Origin of Chalcogen-Bonding Interactions. *J. Am. Chem. Soc.* **139**, 15160–15167 (2017).
19. Manikandan, K. & Ramakumar, S. The occurrence of C-H…O hydrogen bonds in α-helices and helix termini in globular proteins. *Proteins Struct. Funct. Bioinforma.* **56**, 768–781 (2004).

20. Yesselman, J. D., Horowitz, S., Brooks III, C. L. & Trievel, R. C. Frequent side chain methyl carbon-oxygen hydrogen bonding in proteins revealed by computational and stereochemical analysis of neutron structures. *Proteins Struct. Funct. Bioinforma.* **83**, 403–410 (2015).
21. Bondi, A. van der Waals Volumes and Radii. *J. Phys. Chem.* **68**, 441–451 (1964).
22. Langen, R., Oh, K. J., Cascio, D. & Hubbell, W. L. Crystal Structures of Spin Labeled T4 Lysozyme Mutants: Implications for the Interpretation of EPR Spectra in Terms of Structure. *Biochemistry* **39**, 8396–8405 (2000).
23. Columbus, L., Kálai, T., Jekö, J., Hideg, K. & Hubbell, W. L. Molecular Motion of Spin Labeled Side Chains in α-Helices: Analysis by Variation of Side Chain Structure. *Biochemistry* **40**, 3828–3846 (2001).
24. Jeschke, G. DEER Distance Measurements on Proteins. *Annu. Rev. Phys. Chem.* **63**, 419–446 (2012).
25. Guo, Z., Cascio, D., Hideg, K., Kálái, T. & Hubbell, W. L. Structural determinants of nitroxide motion in spin-labeled proteins: Tertiary contact and solvent-inaccessible sites in helix G of T4 lysozyme. *Protein Sci.* **16**, 1069–1086 (2007).
26. *Molecular materials with specific interactions: modeling and design*. (Springer, 2007).
27. Bridges, M. D., Hideg, K. & Hubbell, W. L. Resolving Conformational and Rotameric Exchange in Spin-Labeled Proteins Using Saturation Recovery EPR. *Appl. Magn. Reson.* **37**, 363–390 (2010).
28. Bridges, M. D., Yang, Z., Altenbach, C. & Hubbell, W. L. Analysis of Saturation Recovery Amplitudes to Characterize Conformational Exchange in Spin-Labeled Proteins. *Appl. Magn. Reson.* **48**, 1315–1340 (2017).

29. Phillips, J. C. Stretched exponential relaxation in molecular and electronic glasses. *Rep. Prog. Phys.* **59**, 1133 (1996).
30. Klafter, J. & Shlesinger, M. F. On the relationship among three theories of relaxation in disordered systems. *Proc. Natl. Acad. Sci.* **83**, 848–851 (1986).
31. Johnston, D. C. Stretched exponential relaxation arising from a continuous sum of exponential decays. *Phys. Rev. B* **74**, 184430 (2006).
32. Stein, N., Mainali, L., Hyde, J. S. & Subczynski, W. K. Characterization of the Distribution of Spin–Lattice Relaxation Rates of Lipid Spin Labels in Fiber Cell Plasma Membranes of Eye Lenses with a Stretched Exponential Function. *Appl. Magn. Reson.* **50**, 903–918 (2019).
33. Yang, Z. *et al.* Long-Range Distance Measurements in Proteins at Physiological Temperatures Using Saturation Recovery EPR Spectroscopy. *J. Am. Chem. Soc.* **136**, 15356–15365 (2014).
34. Yang, Z. *et al.* A triarylmethyl spin label for long-range distance measurement at physiological temperatures using T1 relaxation enhancement. *J. Magn. Reson.* **269**, 50–54 (2016).
35. Hubbell, W. L., López, C. J., Altenbach, C. & Yang, Z. Technological advances in site-directed spin labeling of proteins. *Curr. Opin. Struct. Biol.* **23**, 725–733 (2013).
36. Squier, T. C. & Thomas, D. D. Methodology for increased precision in saturation transfer electron paramagnetic resonance studies of rotational dynamics. *Biophys. J.* **49**, 921–935 (1986).
37. Heaven, G., Hollas, M. A., Tabernero, L. & Fielding, A. J. Spin Labeling of Surface Cysteines Using a Bromoacrylaldehyde Spin Label. *Appl. Magn. Reson.* **52**, 959–970 (2021).

38. Fawzi, N. L. *et al.* A rigid disulfide-linked nitroxide side chain simplifies the quantitative analysis of PRE data. *J. Biomol. NMR* **51**, 105 (2011).

Chapter 8: Materials and Methods

8.1 Synthesis of nitroxide spin labels

The nitroxide spin labels used in Chapters 5-7 were synthesized in Dr. Kálmán Hideg and Dr. Támás Kálai's laboratory in Pécs, Hungary. The syntheses were published previously (for HO-225[1], HO-1944[2], HO-2101[3], and HO-3606[4]) or will be published in collaborative papers in the future (for HO-3292 and HO-4072, etc.).

8.2 Construction, expression, and purification of T4L mutants

The construction of the following cysteine mutants has been described elsewhere[5–11]: K65C, K65C/R76C, K68C, N68C/D72C, N68C/N81C, D72C, D72C/V131C, D72C/R76A, R76C, R80C, N81C, A82C, L99C, T109C, T109C/V131C, T115C, L118C, R119C, D127C/V131C, E128C (in the construct of pseudo-wild type and L121A/L133A), A130C (in the construct of pseudo-wild type and L121A/L133A), V131C, V131C/D127A, V131C/E128A, V131C/N132A, V131C/K135A, V131C/R154A, N132C (in the construct of pseudo-wild type and L121A/L133A), L133C, A134C, T151C, and F153C.

New mutants were generated using the QuickChange site-directed mutagenesis method (Stratagene) in the pseudo-wild type T4 lysozyme construct containing the substitutions C54T and C97A: N68C/L118C, D72/N68A, D72/Q69A, D72/V71A, D72/V75A, D72C/L118C, R76C/R80A, R76C/L118C, V131C/L118C. All mutations were confirmed by sequencing (Genewiz Inc. (South Plainfield, NJ) and Laragen Inc. (10601 Virginia Ave, CA)). The mutants in the pHSe5 vector and pET11a vector were transformed into *Escherichia coli* BL21(DE3) expression strain (Stratagene), respectively, and expressed as described previously.

Soluble T4L mutants were purified as described by Mchaourab et al.[11], and the isolation of

T4L cavity mutants (L121A/L133A) from inclusion bodies was described by Lopez et al[12]. Briefly, cell cultures were grown to an OD (600nm) ≈ 1.0 AU, and protein expression was induced by adding IPTG (1 mM). The cells were harvested by centrifugation and the cell pellets were resuspended and sonicated. Supernatants or resuspended inclusion bodies were loaded respectively into ion exchange columns (GE Healthcare, now Cytiva) and eluted with a gradient of NaCl.

Sample purity was greater than 95 % as judged by SDS-PAGE electrophoresis. To exclude the possible co-existence of misfolded soluble-oligomeric species in some samples, the eluted fraction was further injected into a Superdex 75 (GE Healthcare, now Cytiva) gel filtration column. In all cases, there was a single peak with a retention volume of ~ 15.1 mL corresponding to monomeric T4 lysozyme.

8.3 Spin labeling of T4L mutants

The reducing agent (DTT or TCEP) was removed by using a Hi-Trap Desalting column (GE Healthcare, now Cytiva) equilibrated with buffer consisting of 50 mM MOPS, 25 mM NaCl pH 6.8. The eluted protein was incubated immediately with 5- to 10-fold molar excess (1- to 3-fold for HO-1944 to avoid double labeling) of nitroxide reagent. The sample was incubated for at least 1h at room temperature for stable mutants and/or reacting with R1, or overnight at 4°C for less stable mutants and/or reacting with bulky labels such as HO-3292. A second aliquot of 5- to 10-fold molar excess of nitroxide reagent may be added after 3-6h incubation when the labeling reaction is slow. Excess nitroxide reagents were removed with the same desalting column. The spin-labeled protein was concentrated with Amicon Ultra 10 kDa MWCO (Millipore).

For generating the thioether-linked side chain R9 with HO-4072, the sample was eluted with the buffer consisting of 10 mM MES, 100 mM NaCl pH 6.0 instead. The eluted protein was

incubated with nitroxide reagent and the reaction was initiated by adjusting the pH to 8~9 with appropriate volumes of Bis-tris propane pH 11 buffer or sodium borate pH 11 buffer. After the reaction, excess nitroxide reagents were removed by eluting the labeled proteins with a buffer consisting of 50 mM MOPS, 25 mM NaCl pH 6.8.

8.4 Construction, expression, and purification of sperm whale myoglobin mutants

The complete protocol was described and published by Lopez et al.[13] The plasmid pET17b (Novagen, Madison WI) carrying the WT gene of sperm whale myoglobin was kindly provided by Steven Boxer (Stanford University, Ca). Briefly, the individual cysteine substitutions were introduced by using the QuickChange site-directed mutagenesis method (Stratagene). The construction of some cysteine mutants (D27C/R31C, E54C, V66C, E109C/H113C, H113C, N132C) has been described by Lopez et al., and some new mutants (Q8C/H12C, V66C/T70C, N132C/E136C) were generated. All mutations were confirmed by DNA sequencing. Mutant plasmids were transformed into the expression cells E. coli BL21(DE3).

The protein was forced to over-express in inclusion bodies by incubating the culture at 42°C for 3-4 hours after the addition of IPTG. The inclusion bodies were washed and resuspended, and the protein was purified by reverse-phase HPLC (Shimadzu Biotech) using a linear gradient of an acetonitrile solution containing 0.1% trifluoroacetic acid as a mobile phase. Following HPLC purification, the protein fractions containing apomyoglobin (as judged by SDS-PAGE) were lyophilized and stored at 4°C until needed.

8.5 Spin labeling of myoglobin mutants and reconstitution of apomyoglobin with hemin

The reconstitution of apomyoglobin cysteine mutants was required to obtain Holomyoglobin samples and was done as previously described[14,15] with some modifications. Lyophilized protein

was resuspended in a urea buffer, and the in vitro refolding was achieved by overnight dialysis of the urea-denatured protein into a refolding buffer (10 mM sodium acetate, 5 mM DTT, pH 6.1). The reducing agent was removed by using a Hi-Trap Desalting column (GE Healthcare, now Cytiva) equilibrated with buffer consisting of 10 mM sodium acetate, 100 mM NaCl pH 6.1. The eluted protein was incubated immediately with 5- to 10-fold molar excess (1- to 3-fold for HO-1944) of nitroxide reagent. The sample was incubated overnight at 4℃.

The labeled apomyoglobin was then incubated overnight at 4℃ in the dark with a 1- to 3-fold molar excess of bovine hemin (Sigma). The powder hemin was solubilized in DMSO to saturation. The mixture was then filtered and the actual solution concentration was determined by measuring the absorbance at 406 nm using an extinction coefficient of 170,000 $M^{-1}cm^{-1}$. After incubation, excess hemin was removed using the Amicon ultra concentrator and the binding of heme was assessed *via* the UV-Vis spectra. The holomyoglobin reconstituted in this manner auto-oxidizes into the aquomet form (Fe^{+3}–H_2O) as judged by the soret band at 409 nm[16–18]. The A_{409}/A_{280} ratio was measured to ensure that the protein was fully reconstituted (A_{409}/A_{280} = 4.6 ~5.1).

8.6 Protein immobilization

8.6.1 Attachment to solid supports

8.6.1.1 On CNBr-Sepharose

Corresponding mutants were covalently attached to CNBr-activated Sepharose 4B as previously described for R1 mutants (ref). CNBr-activated Sepharose 4B was purchased from GE Healthcare (now Cytiva). The lyophilized media was suspended and washed several times with 1 mM HCl pH 2.0 following manufacturer instructions. HCl was removed with several

medium volumes of coupling buffer (0.1M $NaHCO_3$, 0.5M NaCl at pH 8.3). The spin-labeled proteins (2–4 mg) were diluted (~400 μL) in the appropriate coupling buffer and added to the beads in a 2:1 protein solution/medium ratio. The coupling reaction was incubated overnight at 4°C.

Any uncoupled protein was eluted with coupling buffer and the coupling efficiency was assessed by UV_{280} absorption. The coupling reaction typically yielded estimated adsorption of 25-60 mg of protein per milliliter of medium according to the manufacturer. The immobilized protein was equilibrated with the appropriate buffers and loaded in glass capillaries (0.60 mm ID x 0.84 mm OD, VitroCom Inc, N. J.) before EPR measurements.

8.6.1.2 On streptavidin-resin

Corresponding mutants carrying the UAA group were expressed, purified, spin-labeled, biotinylated, and attached to streptavidin-functionalized resin (Thermo Scientific) as previously described by Lopez et al.[19] for R1 mutants (ref). Briefly, the amber codon (TAG) was introduced to the T4L gene (pET11a vector) site specifically using the QuikChange site-directed mutagenesis method. In this dissertation, only the p-AzF was used and introduced to the N-terminus of the pseudo wild-type T4L as the second residue after the methionine. The sequence -Gly-Ser-Gly-Ser-Gly- was also inserted after the p-AzF residue using the Q5 site-directed mutagenesis method, serving as a short and flexible spacer between the attachment and the folded protein. The mutations were verified by DNA sequencing.

The reagent Dibenzylcyclooctyne (DBCO)-biotin was obtained from ClickChemistry Tools (Scottsdale, Az). Pierce® High Capacity Streptavidin Agarose Resin was purchased from Thermo Scientific. Affinity-purified streptavidin is isolated from *Streptomyces avidinii* and has been immobilized on 6% crosslinked beaded agarose. The coupling reaction typically yielded an

estimated 10 mg of protein per milliliter of medium according to the manufacturer. The immobilized protein was equilibrated with the appropriate buffers and loaded in glass capillaries before EPR measurements.

8.6.1.3 On immobilized metal affinity chromatography (IMAC) resin

The 6×His-tag was introduced to the N-terminus of pseudo wild-type T4L using the Q5 site-directed mutagenesis method, together with two sequences serving as spacers: the -Gly-Ser-Gly- after the methionine but before the 6×His, and the -Gly-Ser-Gly-Ser-Gly- after the 6×His. Corresponding mutants carrying the 6×His-tag were expressed similarly as the pseudo wild-type T4L, but purified over HisTrap™ High Performance columns (Cytiva) and eluted with a gradient of imidazole. The eluted His-tagged protein was added with reducing agents, and desalted over the Hi-Trap Desalting column (GE Healthcare, now Cytiva) equilibrated with buffer consisting of 50 mM MOPS, 25 mM NaCl pH 6.8 to be spin labeled accordingly (see 8.3). After labeling, excess nitroxide reagents were removed with the same desalting column, and the protein was desalted into the equilibration buffer (20 mM sodium phosphate, 300 mM sodium chloride, 10 mM imidazole, pH 7.4).

The desired quantity of IMAC resin was equilibrated in the equilibration buffer and washed 3X by centrifugation with a 5-fold excess of the same buffer. After the final wash and removal of the supernatant, the His-tagged, spin-labeled protein was added to the resin in an amount equivalent to the stated capacity of the resin and the suspension was mixed at room temperature for at least 2 hours at room temperature or 4 °C overnight. The supernatant was removed and the resin was washed with a buffer consisting of 50 mM MOPS, 25 mM NaCl at pH 6.8 prior to EPR measurements.

HisPur^{TM} Ni-NTA Resin was purchased from Thermo Scientific. This resin is composed of

nickel-charged nitrilotriacetic acid (NTA) chelate immobilized onto 6% crosslinked agarose. The coupling reaction typically yielded an estimated 60 mg of protein per milliliter of medium according to the manufacturer. Zinc Chelating Resin was purchased from Geno Technology, Inc. This resin is composed of zinc-charged iminodiacetate (IDA) chelate immobilized onto 6% crosslinked agarose. The coupling reaction typically yielded an estimated 20 mg of protein per milliliter of medium according to the manufacturer.

8.6.2 Using glutaraldehyde crosslinking

300-700 μM of spin label protein on 5μL of CNBr-Sepharose was incubated with >25-fold molar excess of ice-cold glutaraldehyde solution (Electron Microscopy Sciences, Hatfield, PA) at 4℃. The mixture was immediately loaded into a sealed 0.60 mm ID x 0.84 mm OD, VitroCom Inc, N. J., and subjected to quick centrifugation at 800 rpm for 1 minute to facilitate the settlement of beads at bottom of the capillary tube. The crosslinking reaction was allowed to proceed at room temperature. The crosslinked mixture formed a yellowish color over the beads after ~15 minutes of incubation time.

8.6.3 Ammonia sulfate precipitation

As a model system for studying isotropic Brownian rotational diffusion, human oxyhemoglobin (Hb) was labeled specifically at both β-93 residues with a maleimide spin label (MSL), N-(1-oxyl-2, 2, 6, 6- tetramethyl-4-piperidinyl)-maleimide, as described previously[20]. In order to obtain reference spectra corresponding to no motion, a 50 mg/ml solution of MSL-Hb was diluted 3:1 with a 50 mg/ml solution of unlabeled Hb to avoid dipolar interaction and Heisenberg exchange. A portion of the diluted MSL-Hb was precipitated in saturated ammonium sulfate (approximately 75 mg ammonium sulfate plus 100 ml solution, undissolved solids were

observed at the bottom) overnight at 4°C, yielding a precipitate that contained (by weight) approximately 10% Hb, 40% ammonium sulfate, and 50% water.

Accordingly, a 30 mg/ml solution of spin-labeled T4L (with R1/R1f/RY/RX) was serially diluted from 3:1 to 1:1, to 1:5 with a 30 mg/ml solution of unlabeled pseudo wild-type T4L (roughly 2.6-fold lighter in weight than Hb). The CW-EPR spectrum of each was determined so that an acceptable ratio (without dipolar interaction and Heisenberg exchange) can be selected (by lineshapes). The results showed that for most T4L samples 1:3 was a compatible choice. A portion was precipitated also in the saturated ammonium sulfate overnight at 4°C, yielding the precipitated samples.

8.7 Crystallization of T4L mutants and X-ray Crystallography

T4L 65R9/76R9 was crystallized using the hanging drop vapor diffusion method. Reservoir buffers were prepared in twelve different concentrations of the precipitant (1.85-2.40 M Na/KPO_4) all having 0.15 M NaCl and 100 mM 1,6 hexanediol at eight different pHs (6.7-7.4) with or without the additive 3% 2-propanol. Crystallization trials were prepared by mixing purified labeled protein (15 mg/ml in 50 mM MOPS, 25 mM NaCl, pH 6.8) with reservoir buffer by ratios of 1:2, 1:1, and 2:1, and by suspending the drops over 100μL of the same buffer. The final crystallization condition was 2.35 M Na/KPO_4, pH 7.4 with 3% 2-propanol. Crystals appeared in 1 week under 4°C.

The crystals of T4L 65R9/76R9 were cyro-protected using mineral oil and were flash-frozen at 100 K with a nitrogen gas stream. Data were collected at 100 K on a RAXIS-IV++ image plate detector (RIGAKU), processed with DENZO, and reduced with SCALEPACK[21]. T4L 65R9/76R9 crystals grew in space group $P3_221$ and were isomorphous with the pseudo-wild type T4 Lysozyme crystals with similar cell dimensions[22]. The data sets showed only one molecule in

the asymmetric unit. The structure was determined by molecular replacement method using PHASER[23]. PDB accession code 1C6T[24] was used as a starting model. A randomly selected 5% of the data was set aside before the start of the refinement to calculate R_{free}. Models were refined using REFMAC[25] or PHENIX[26] and rebuilt using COOT[27]. The refinement quality was monitored using the R_{free}. After each model was refined to a R_{free} of less than 22%, the spin label side chain was built-in and subject to further refinement iterations. The final structures were validated with COOT.

8.8 EPR spectroscopy

8.8.1 Conventional CW-EPR (V_1 spectra)

Conventional CW-EPR spectra were measured on a Varian E-109 spectrometer fitted with a two-loop one-gap resonator[28]. Protein samples of 5 μL (100μM ~1mM) were loaded in glass capillaries (0.60 mm ID x 0.84 mm OD, VitroCom Inc, N. J.) sealed on one end. Spectra were acquired using either a 2mW incident microwave power for a stronger signal intensity, or 0.02mW power to avoid any saturation for accurately measuring V_1 spectra. Spectra were recorded at X-band frequency with a scan width of 100G and Q-band frequency with a width of 160G, using ca. 1G field modulation amplitude at 100 kHz.

Temperature control was achieved with a commercial Bruker temperature control unit, which employs nitrogen flow from a liquid nitrogen boiler and heater apparatus. A dewar insert (Wilmad, Dallas, TX) equipped with a thermocouple monitoring the in-situ temperatures was placed around the loop-gap resonator.

8.8.2 ST-EPR (V_2' spectra)

Thomas et al.[20,29,30] reported the detailed calibration procedure, the instrumental parameter

settings, and the reference curves for obtaining apparent correlation times. Some modifications were made for the specific apparatus in-use.

ST-EPR spectra were also measured on the Varian E-109 spectrometer fitted with a two-loop one-gap resonator. Protein samples were loaded also in glass capillaries (0.60 mm ID x 0.84 mm OD, VitroCom Inc, N. J.) sealed on one end. An exact same sample can be used in concert for CW and ST measurements. A 'blank' sample was prepared separately using the same type of capillaries filled with the same medium (buffer/viscogen added/solid supports, etc.), loaded with spin reagent molecules at a similar concentration as the labeled protein sample. Due to the fast-tumbling dynamics of spin molecules, an assuredly unsaturated but intense signal can be acquired.

The accurate B_1 (or designated as H_1 in some publications) value of the resonator was determined and calibrated as described by Squire et al.[29] using the peroxylamine disulfonate in deoxygenated solution. All ST-EPR spectra (V_2' scheme) were acquired using a 1.25mW incident microwave power, at which the strength of the magnetic field, B_1, equals 0.25G for this resonator. The field was modulated at 50kHz with a modulation amplitude of 5G. A 0.02mW power was used to obtain the unsaturated V_1 spectra, at which the B_1 = 0.032G. Both spectra were recorded at X-band frequency with a scan width of 100G.

For each measurement, the V_2' spectrum was firstly acquired using the 1.25mW incident microwave power at an approximate null value of the reference phase to determine the gain value needed for obtaining an acceptable signal intensity. Once the gain was determined, the power was adjusted down to 0.02mW to set the accurate value of the reference phase, with all the other parameters at the same values to be used in the actual V_2' measurement.

The value corresponding to a null signal under the in-phase setting was firstly estimated by

linear extrapolation method for the 'blank' sample, of which the unsaturated and intense signal helped to save time for signal averaging and thus decrease the error from readings. This estimated value was examined for the actual sample by checking whether an acceptable null signal can be obtained. If not, the phase would be adjusted again by the linear extrapolation method until the null was achieved. The power was then tuned up to 1.25mW for measuring the actual ST-EPR signal.

8.8.3 DEER

The four-pulse DEER experiments for the double spin-labeled proteins were conducted at 80K on the Bruker ELEXSYS 580 spectrometer equipped with a SuperQFT Q-band bridge and a 10-W AmpQ Q-band amplifier, and fitted with an ER 5107 D 2 Q-band resonator (Bruker Siospin). The protein concentration during the DEER experiments was maintained at or below 200 μM. 20 μL of samples in D_2O-based buffer containing 10-20 % v/v deuterated-glycerol as cryoprotectant was loaded into a quartz capillary tube (2.0 mm ID x 2.4 mm OD; VitroCom Inc., NJ) and then flash-frozen in liquid nitrogen. A 36 ns π–pump pulse was set at the maximum of the center-line absorption spectra and the observer π/2 (16 ns) and π (32 ns) pulses were positioned 80 MHz less than the pulse frequency, which corresponds to the absorption maxima of the low-field line. Additional parameters were set to the following values: d1 = 300 ns, d2 = variable (1500 – 3000 ns), d3 = 100 ns, d30 = 8-16 ns, phase cycling = 2-step.

Distance distributions were obtained from the raw dipolar evolution time raw data using a custom program, LongDistances (available at https://sites.google.com/site/altenbach/labview-programs/epr-programs), written in the LabView software package (National Instruments, Austin, TX) by Christian Altenbach (Stein Eye Institute, UCLA). A dipolar evolution function was obtained after an exponentially decaying background function was applied to correct for

random inter-molecular dipolar interactions. Fourier transformation of the dipolar evolution function generated a dipolar spectrum, which was fit using either the Tikhonov regularization[31] techniques or Gaussian distributions to get the interspin distance distribution.

8.9 Spectral simulation of CW-EPR spectra

EPR spectra were fit to the MOMD model of Freed and co-workers using a modified Levenberg-Marquardt algorithm. The paper of Budil et al.[32] provides a detailed description of the model, simulation parameters, and fitting procedures. A brief description specific to the implementation used in the present work is given below. For consistency, the notation used is that of Budil et al. Spectral simulations were carried out using the MOMD fitting program, MuitiComponent, as implemented by Christian Altenbach (https://sites.google.com/site/altenbach/labview-programs/epr-programs).

For fitting experimental spectra to the MOMD model, published values for the elements of the g tensors (g_{xx}, g_{yy}, g_{zz}) for MTSSL in water were used as starting values[33]. The values of the apparent hyperfine splitting $2A_{zz}$, that measured from the liquid nitrogen frozen spectra of each side chain were used as the $2A_{zz}$. The final values of the A and g tensor elements were very similar to the previously published values.

The fit was then optimized with the rotational diffusion rates (R_{xx}, R_{yy}, R_{zz}), the coefficient of the ordering potential (c_{20} and c_{40}) from which the order parameter S_{20} was computed. In specific conditions (see chapter 5-7), the tilt angles of diffusion tensors, mostly the β_D for z-axis anisotropic motions, were also allowed to vary. After the above parameters were optimized, the director-frame-dependent Gaussian inhomogeneous broadening ($\Delta^{(0)}$ and $\Delta^{(2)}$), and the values of Lorentzian linewidth tensors (W_{xx}, W_{yy}, W_{zz}) were allowed to vary reasonably to improve the fits.

8.10 Urea denaturation and fluorescence spectroscopy

Three tryptophan residues are present in the C-terminal lobe of T4 lysozyme (Trp126, Trp138, and Trp158). 10 M stock solutions of urea were made on the day of use by dissolving the urea in 50 mM MOPS, 25 mM NaCl pH 6.8, the same buffer used in purified protein stock solutions. By preparing a series of solutions of protein in various concentrations of urea, the mixtures were further diluted to a final concentration of < 3 μM and a constant concentration of protein is used for the whole series. No contaminants were detected spectroscopically.

Samples were excited at 280 nm with a bandwidth of 5 nm to minimize tyrosine excitation, and emission from 300 to 500 nm was collected at 90° with a bandwidth of 5 nm. All protein solutions were allowed to equilibrate at room temperature for 60 to 90 min after mixing with urea to different concentrations and before the measurement, as no spectral changes were detected, which suggested that all samples appeared to have attained equilibrium at room temperature. Data were analyzed[34] with MATLAB (The MathWorks, Natick, MA). The center of spectral mass, ⟨λ⟩, of each spectrum was calculated in the region 300 to 500 nm with the following equation:

$$\langle\lambda\rangle = \sum_{i=1}^{N} \lambda_i I_i \Big/ \sum_{i=1}^{N} I_i$$

where I_i is the fluorescence intensity at the wavenumber, λ_i, and N is the number of data points collected in the spectrum. The weighted average was then converted to wavelength, ⟨λ⟩. For two-state denaturation, the thermodynamic stability of the protein is evaluated by the free energy difference between the native/folded (F) and denatured/unfolded (U) states.

$$\Delta G = -RTlnK$$

$$K = \frac{[Protein]_{unfolded}}{[Protein]_{folded}} = \frac{f_U}{f_F}$$

$$f_U + f_F = 1$$

$$\Upsilon = \Upsilon_U f_U + \Upsilon_F f_F$$

$$\Upsilon_U = \alpha_U + \beta_U \cdot [Urea]$$

$$\Upsilon_F = \alpha_F + \beta_F \cdot [Urea]$$

$$\Upsilon = (\alpha_F + \beta_F \cdot [Urea]) + [(\alpha_U + \beta_U \cdot [Urea]) - (\alpha_F + \beta_F \cdot [Urea])] \times \frac{exp^{\frac{m[Urea]-\Delta G_0}{RT}}}{1 + exp^{\frac{m[Urea]-\Delta G_0}{RT}}}$$

$$\Delta G = \Delta G_0 - m \cdot [Urea]$$

$$[Urea]_{1/2} = \Delta G_0 / m$$

where: the signal (Υ) is the intensity-averaged emission wavelength, ⟨λ⟩; K is the apparent equilibrium constant under each individual urea concentration; ΔG is the Gibbs free-energy change of protein unfolding at each urea concentration while ΔG_0 is the unfolding free-energy in buffer without denaturants; m is experimentally defined as the positive slope of the relationship of ΔG with denaturant concentration; $[Urea]_{1/2}$ is the concentration of denaturant at 50% denaturation; f_F and f_U are fractions of unfolded and folded protein at each measurement point respectively, R is the gas constant (8.314 $J \cdot K^{-1} \cdot mol^{-1}$) and T is the experimental temperature which was selected at 295 K (22℃, the room temperature).

The baselines in the pre-transition (0~2 mol/L urea) and post-transition (7~8 mol/L urea) stages are fitted linearly to obtain the factors $\alpha_{F/U}$ (slopes) and $\beta_{F/U}$ (intercepts), which is attributed to solvent effects on the signal in the folded or unfolded states respectively. Between the two baselines, the region is defined as the transition stage and fitted the signal (Υ) to a two-state model, where the ΔG_0, m, and $[Urea]_{1/2}$ are derived as independent parameters.

8.11 References

1. Sár, C. P., Jekö, J. & Hideg, K. Synthesis of 3,4-Disubstituted 2,5-Dihydropyrrol-1-yloxyl Spin Label Reagents. *Synthesis* **1998**, 1497–1500 (1998).
2. Fleissner, M. R. *et al.* Structure and dynamics of a conformationally constrained nitroxide side chain and applications in EPR spectroscopy. *Proc. Natl. Acad. Sci.* **108**, 16241–16246 (2011).
3. Columbus, L., Kálai, T., Jekö, J., Hideg, K. & Hubbell, W. L. Molecular Motion of Spin Labeled Side Chains in α-Helices: Analysis by Variation of Side Chain Structure. *Biochemistry* **40**, 3828–3846 (2001).
4. Fawzi, N. L. *et al.* A rigid disulfide-linked nitroxide side chain simplifies the quantitative analysis of PRE data. *J. Biomol. NMR* **51**, 105 (2011).
5. Lopez, C. J. Mapping molecular flexibility of spin labeled proteins on the nanosecond and longer time scales via CW lineshape analysis and osmolyte-perturbation EPR. (University of California, Los Angeles).
6. Guo, Z. Correlation of spin label side-chain dynamics with protein structure: Studies of T4 lysozyme with site-directed mutagenesis and x-ray crystallography. (University of California, Los Angeles).
7. Fleissner, M. R. X-ray structures of nitroxide side chains in proteins: A basis for interpreting distance measurements and dynamic studies by electron paramagnetic resonance. (University of California, Los Angeles).
8. Columbus, L. M. Investigating backbone and side chain dynamics of α-helices in the nanosecond regime with site -directed spin labeling. (University of California, Los Angeles).

9. Warshaviak, D. T. Modeling the structure and dynamics of biological molecules. Part A: Quantum mechanical and experimental studies of nitroxide side chains in proteins. Part B: Molecular modeling of actin and its interactions with cofilin. (University of California, Los Angeles).
10. Langen, R., Oh, K. J., Cascio, D. & Hubbell, W. L. Crystal Structures of Spin Labeled T4 Lysozyme Mutants: Implications for the Interpretation of EPR Spectra in Terms of Structure. *Biochemistry* **39**, 8396–8405 (2000).
11. Mchaourab, H. S., Lietzow, M. A., Hideg, K. & Hubbell, W. L. Motion of Spin-Labeled Side Chains in T4 Lysozyme. Correlation with Protein Structure and Dynamics. *Biochemistry* **35**, 7692–7704 (1996).
12. López, C. J., Yang, Z., Altenbach, C. & Hubbell, W. L. Conformational selection and adaptation to ligand binding in T4 lysozyme cavity mutants. *Proc. Natl. Acad. Sci.* **110**, E4306–E4315 (2013).
13. López, C. J., Oga, S. & Hubbell, W. L. Mapping Molecular Flexibility of Proteins with Site-Directed Spin Labeling: A Case Study of Myoglobin. *Biochemistry* **51**, 6568–6583 (2012).
14. Jennings, P. A., Stone, M. J. & Wright, P. E. Overexpression of myoglobin and assignment of its amide, Cα and Cβ resonances. *J. Biomol. NMR* **6**, 271–276 (1995).
15. Springer, B. A. & Sligar, S. G. High-level expression of sperm whale myoglobin in Escherichia coli. *Proc. Natl. Acad. Sci.* **84**, 8961–8965 (1987).
16. Antonini, E. & Brunori, M. *Hemoglobin and myoglobin in their reactions with ligands*. (North-Holland Publishing Company, 1971).

17. van Kampen, E. J. & Zijlstra, W. G. Spectrophotometry of Hemoglobin and Hemoglobin Derivatives. in *Advances in Clinical Chemistry* (eds. Latner, A. L. & Schwartz, M. K.) vol. 23 199–257 (Elsevier, 1983).
18. Kampen, E. J. van & Zijlstra, W. G. Determination of Hemoglobin and Its Derivatives. in *Advances in Clinical Chemistry* (eds. Sobotka, H. & Stewart, C. P.) vol. 8 141–187 (Elsevier, 1966).
19. López, C. J., Fleissner, M. R., Brooks, E. K. & Hubbell, W. L. Stationary-Phase EPR for Exploring Protein Structure, Conformation, and Dynamics in Spin-Labeled Proteins. *Biochemistry* **53**, 7067–7075 (2014).
20. Thomas, D. D., Dalton, L. R. & Hyde, J. S. Rotational diffusion studied by passage saturation transfer electron paramagnetic resonance. *J. Chem. Phys.* **65**, 3006–3024 (1976).
21. Otwinowski, Z. & Minor, W. Processing of X-ray diffraction data collected in oscillation mode. in *Methods in Enzymology* vol. 276 307–326 (Academic Press, 1997).
22. Weaver, L. H. & Matthews, B. W. Structure of bacteriophage T4 lysozyme refined at 1.7 Å resolution. *J. Mol. Biol.* **193**, 189–199 (1987).
23. McCoy, A. J. *et al.* Phaser crystallographic software. *J. Appl. Crystallogr.* **40**, 658–674 (2007).
24. Quillin, M. L., Breyer, W. A., Griswold, I. J. & Matthews, B. W. Size versus polarizability in protein-ligand interactions: binding of noble gases within engineered cavities in phage T4 lysozyme11Edited by B. Honig. *J. Mol. Biol.* **302**, 955–977 (2000).
25. Murshudov, G. N., Vagin, A. A. & Dodson, E. J. Refinement of Macromolecular Structures by the Maximum-Likelihood Method. *Acta Crystallogr. D Biol. Crystallogr.* **53**, 240–255 (1997).

26. Adams, P. D. *et al.* PHENIX: building new software for automated crystallographic structure determination. *Acta Crystallogr. D Biol. Crystallogr.* **58**, 1948–1954 (2002).
27. Emsley, P. & Cowtan, K. Coot: model-building tools for molecular graphics. *Acta Crystallogr. D Biol. Crystallogr.* **60**, 2126–2132 (2004).
28. Hubbell, W. L., Froncisz, W. & Hyde, J. S. Continuous and stopped flow EPR spectrometer based on a loop gap resonator. *Rev. Sci. Instrum.* **58**, 1879–1886 (1987).
29. Squier, T. C. & Thomas, D. D. Methodology for increased precision in saturation transfer electron paramagnetic resonance studies of rotational dynamics. *Biophys. J.* **49**, 921–935 (1986).
30. Hyde, J. S. & Thomas, D. D. New Epr Methods for the Study of Very Slow Motion: Application to Spin-Labeled Hemoglobin. *Ann. N. Y. Acad. Sci.* **222**, 680–692 (1973).
31. Jeschke, G. & Polyhach, Y. Distance measurements on spin-labelled biomacromolecules by pulsed electron paramagnetic resonance. *Phys. Chem. Chem. Phys.* **9**, 1895–1910 (2007).
32. Budil, D. E., Lee, S., Saxena, S. & Freed, J. H. Nonlinear-Least-Squares Analysis of Slow-Motion EPR Spectra in One and Two Dimensions Using a Modified Levenberg–Marquardt Algorithm. *J. Magn. Reson. A* **120**, 155–189 (1996).
33. Owenius, R., Engström, M., Lindgren, M. & Huber, M. Influence of Solvent Polarity and Hydrogen Bonding on the EPR Parameters of a Nitroxide Spin Label Studied by 9-GHz and 95-GHz EPR Spectroscopy and DFT Calculations. *J. Phys. Chem. A* **105**, 10967–10977 (2001).
34. Tang, C., Lew, S. & He, D. Using a second-order differential model to fit data without baselines in protein isothermal chemical denaturation. *Protein Sci.* **25**, 898–904 (2016).